3rd JOGJA INTERNATIONAL CONFERENCE ON PHYSICS 2012

ISBN : 979-95620-2-3

FACULTY OF MATHEMATICS AND NATURAL SCIENCES
UNIVERSITAS GADJAH MADA

Yogyakarta, 18-19 September 2012

http://www.jipc.ugm.ac.id/2012/

PROCEEDINGS

ORGANIZED BY :

PHYSICS DEPARTMENT
FACULTY OF MATHEMATICS AND NATURAL SCIENCE
UNIVERSITAS GADJAH MADA

3rd JOGJA INTERNATIONAL CONFERENCE ON PHYSICS 2012

ISBN : 979-95620-2-3

FACULTY OF MATHEMATICS AND NATURAL SCIENCES
UNIVERSITAS GADJAH MADA

Yogyakarta, 18-19 September 2012

http://www.jipc.ugm.ac.id/2012/

PROCEEDINGS

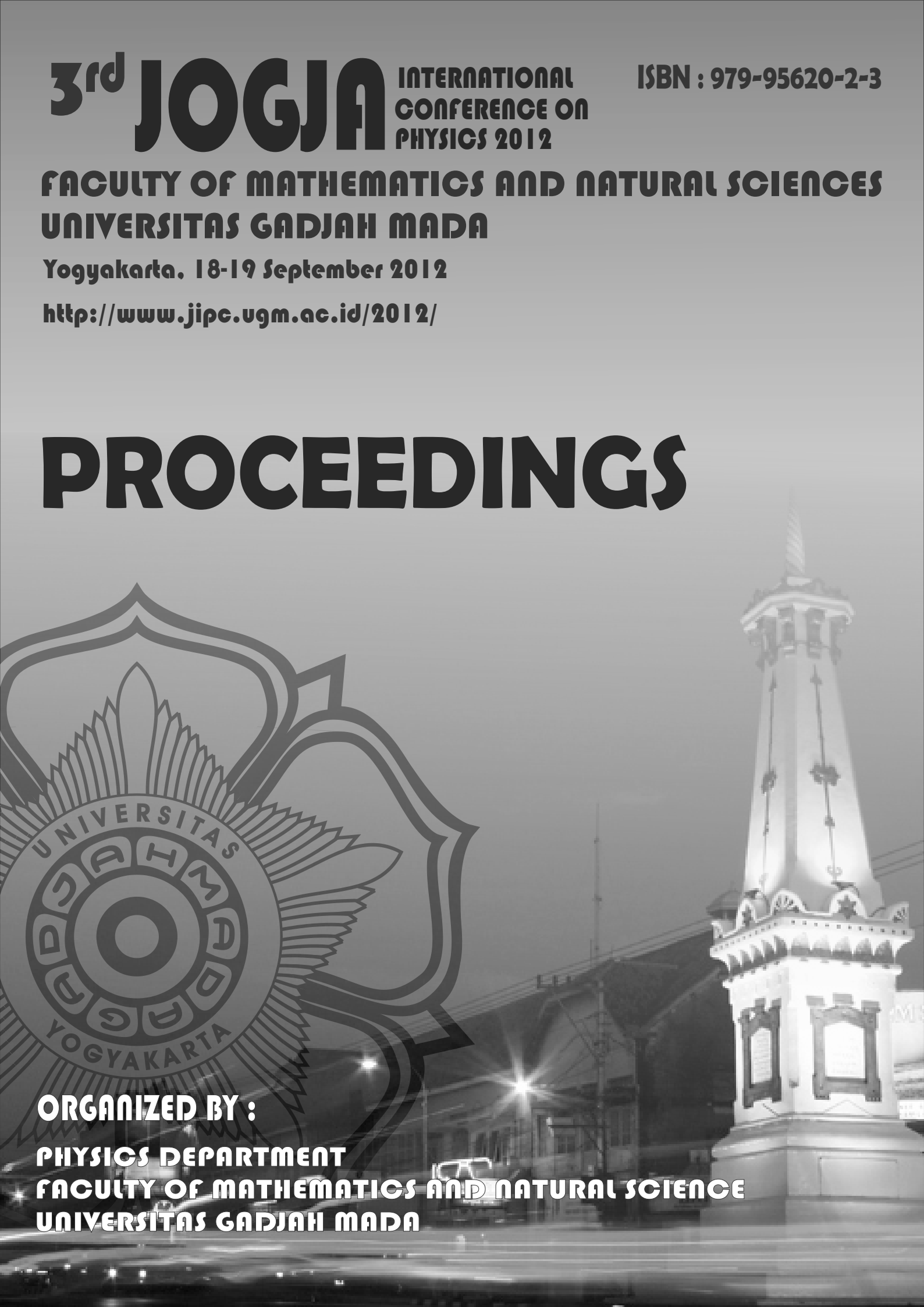

ORGANIZED BY :

PHYSICS DEPARTMENT
FACULTY OF MATHEMATICS AND NATURAL SCIENCE
UNIVERSITAS GADJAH MADA

Foreword

Welcome to the International Conference on Physics 2012, this conference is the continuation of the previous Jogja International Physics Conference 2007 and the Jogja Regional Physics Conference 2005. This conference is organized by the Physics Department Universitas Gadjah Mada to enhance networking, cooperation, the development of research, and education in physics. We are very happy for the enthusiastic participations on this conference. We welcome you also to Jogjakarta, the most beautiful cultural based city in Indonesia.

The Department of Physics would like to appreciate and recognize all of the keynote speakers in this conference, Prof. Dr. Shoichi Kai (Kyushu University), Prof. Dr. Makoto Notomi (Waseda University), Dr Isao Watanabe (RIKEN, Japan), Prof. Frans. J.M.Harren (Radboud Nijmegen University), Dr. Hirotaka Sato (Nanyang Technological University), Dr. Nurul Taufiqurrahman (Chairman Indonesian Nanotechnology Society), and Prof. Dr. Kamsul Abraha (Universitas Gadjah Mada University).

On behalf of the Physics Department I would like to express sincere gratitude to the Organizing Committee members of the conference, all Laboratories, and Study Programs for their hospitalities and supports. Last but not least I would to give my thanks to the Faculty of Mathematics and Natural Sciences Universitas Gadjah Mada for their continuous supports. I hope this conference will give significant contributions to physics development in Indonesia.

With sincere gratitude
Head of Physics Department
Gadjah Mada University, Yogyakarta Indonesia

Dr.-Ing. Ari Setiawan

Foreword

International Conference on Physics 2012 is the third physics conference organized by department of Physics, Gadjah Mada University. The conference is intended for physicist-research sharing forum all over the world to increase their interaction toward enhancing the progress in the field of physics.

This year there are six papers in the plenary session, which are presented by sex invited speakers. The committee also received 92 papers. The papers consist of Condensed Matter (34 papers), Geophysics, Atomic and Molecular Physics, and Interdisciplinary Physics (18 papers), Computational and Theoretical Physics (18 papers), Instrumentation and Applied Physics (15 papers), and posters (7 papers). There will be five different concurrent sessions can be attended at any time during the conference.

The committee has done an admirable job of arranging the program for thr benefit of participants. The committee hopes that this conference can enrich, enhance the physics knowledge, and serves as a forum for individual to meet and discuss physics current issue.

Dr. Edi Suharyadi
Chair person

List of Committee Members

Steering Committee:

Dr. Ari Setiawan
Dr. Mitrayana
Dr. Mirza Satriawan
Dr. Kuwat Triyana
Dr. Gede Bayu Suparta

Organizing Committee:

Chair : Dr. Edi Suharyadi
Secretary : Dr. Wiwit Suryanto
Treasurer : Dra. Chotimah, M.S.
Rini Nurharini

Technical Committee:

Dr. Rinto Anugraha
Dr. Fachrudin Nugroho
Eddy Hartantyo, S.Si., M.Si.
Moh. Adhib Ulil Absor, M.Sc.
Drs. Eko Sulistya, M.Si
Dwi Satya Palupi, S.Si, M.Si
Sholihun Ahmad, M.Sc.
Sudarmaji, S.Si., M.Sc.
Muhammad Darwis, M.Sc.
Afif Rakhman, S.Si., M.T.
Romy Hahang SB, M.Si
Eko Tri Sulisyani, S.Si, M.Sc.
Juliasih Partini, S.Si, M.Si
La Aba, M.Si.
Saptono
Darsono

Reviewers:

Prof. Dr. Kirbani SB
Prof. Dr. Kusminarto
Prof. Dr. Sismanto
Prof. Dr. Kamsul Abraha
Prof. Dr. Agung Bambang Setio Utomo
Dr. Waluyo
Dr. Dr. rer. nat.. M.Farchani Rosyid
Dr. Pekik Nurwantoro
Dr. Kuwat Triyana
Dr. Yusril Yusuf
Dr. Edi Suharyadi

Table of Contents

Section C: Geophysics, Atomic and Molecular Physics, and Interdisciplinary Physics

Section D: Instrumentation and Applied Physics

Section E: Poster Session

Atomic Structures of Liquid and Amorphous $(GeTe_4)_{100-x}In_x$ Phase Change Material: an Ab Initio Molecular Dynamics Study

***A. Zaidan*[1,2,*], *Vl. Ivanova*[1], *and P. Petkov*[1]**

[1]*Department of Physics, Thin Film Technology Lab, University of Chemical Technology and Metallurgy, 8 "Kl. Ohridski" Blvd., 1756 Sofia, Bulgaria*

[2] *Department of Physics, Faculty of Science and Technology, Universitas Airlangga, Surabaya 60115, Indonesia*

Abstract

Chalcogenide based on Ge-Te has been regarded as potential candidate of phase change materials due to its fast transition between crystalline and amorphous form. In this study, ab initio molecular dynamics (AIMD) were used to investigate structures of $GeTe_4$ with indium dopant (5, 10, 15 and 20 at %). Pair distribution functions, bond angle distributions and ring statistics were calculated and discussed for amorphous and liquid state. Calculation result of bond angle distribution suggest that structure of our system should be partially tetrahedral. Ring statistics of our samples shown that four member square rings 'seed' is dominant ring size. This 'seed' is basic building block for crystal growth in amorphous-crystal transition which is one of important properties for phase change materials.

Keywords: *Phase Change Materials, Ab Initio Molecular Dynamics, Chalcogenide.*

* Corresponding author.
E-mail address: zaidan@unair.ac.id

I. Introduction

Chalcogenide glasses are interesting materials because of their technological applications and commercial importance. Due to their unique properties (low phonon energies, optical transparency in IR region, high index of refraction), chalcogenide glasses have many important applications in optics, optoelectronics, and electronics. These applications including phase change material [1, 2, 3, 4], sensor [5, 6], optical circuits, gratings, waveguides [7, 8, 9], and many others.

Phase change materials have have been extensively studied by many authors because it is expected to be the future of non-volatile memories [10,11]. Chalcogenide based on Ge-Te has been regarded as a potential candidate of phase change materials due to its fast transition between crystalline and amorphous form. However, very little theoretical guidance is available for this alloy, especially for Ge-Te-In system.

With these motivations, theoretical study of chalcogenide $GeTe_4$ doped with Indium 5, 10, 15, and 20 at % structures in liquid and amorphous form have been done. Models reported in this work is generated through melt quenching ab initio molecular dynamics simulations. This approach, first pioneered by Car and Parrinello, which combines density functional theory (DFT) with (MD) into a powerful tool for investigating liquid and amorphous structures.

II. Calculation Details

As in our earlier work of Ge-Te-In chalcogenide systems [12, 13], relaxed structure of $(GeTe_4)_{100-x}In_x$ with x = 5, 10, 15, 20 were generated by first-principles MD simulation. The calculations were performed with the SIESTA program [14] using a linear combination of numerical atomic orbitals as the basis set and norm-conserving pseudopotentials. The total energy is approximated in the non-self consistent Harris functional.

In this work we propose 300 atoms models. As strating point is 240 atoms of $GeTe_4$ which is placed randomly inside cubic lattice with boundary and lattice constant depend on system mass density. AIMD is used because this method is more accurate than classical MD. Relaxed model of $GeTe_4$ then doped with Indium atoms so we get 300 atoms of $(GeTe_4)_{100-x}In_x$ with x = 5, 10, 15, 20.

Using relaxed structures, pair distribution functions, bond angle distributions and ring

statistics were calculated and discussed for amorphous and liquid state.

Unfortunately up to now there is no standard procedure to do amorphous structure modeling using MD method. Although several amorphous systems were successfully generated from so called melt quenching technique, but this technique itself is vary in detail. Melt quenching can be done using classical or ab initio MD or even both of them. The melt and quench simulation scheme proceeds by carrying out a series of MD simulations. At each step, the structure obtained from the previous MD simulation is used as the starting point for the next one. In this work, process of melt quenching technique contains four ab initio MD steps, two annealing processes, one canonical MD, and one relaxation process. First, system is annealed at 1500 K which is higher than melting temperature of systems and then system is allowed to reach thermodynamic equilibrium in this temperature using canonical MD. The process is then reversed to quench the system back to room temperature and followed by relaxation to zero temperature. Then relaxed structures were equilibrated for 2 ps at 300 K and 1400 K.

For each MD simulation, system is given enough time to reach its thermal equilibrium in order to eliminate its correlation to the previous structure. At each step, system is allowed to run for 2 ps to reach its thermodynamic equilibrium. The time step for the simulations is set to be 2 fs in order to suppress numerical error.

III. Results and discussion

One of melt quenching ab initio molecular dynamics relaxed structure is shown in figure 1. Figure 1(a) shows 300 atoms configuration of amorphous $(GeTe_4)_{90}In_{10}$ in each element Germanium, Tellurium and Indium are displayed by orange, blue and green ball respectively. Figure 1(b) gives information about distribution of coordination number. From 1(b) it is known that amorphous $(GeTe_4)_{90}In_{10}$ is dominated by atoms with coordination number 3 and 4.

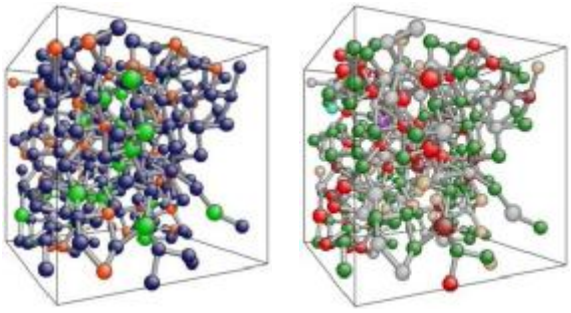

(a) (b)

Figure 1. Atomic configuration of amorphous $(GeTe_4)_{100-x}In_x$. (a) Element display (orange: Ge, blue: Te, green: In), (b) Coordination number display (turquoise: 1, burlywod: 2, Forest green: 3, gray: 4, red: 5, brown: 6, purple: 7)

Pair distribution function

Pair distribution function (PDF) is an important parameter to study structural characteristics. PDF is the key to investigate especially short and medium range order of material. The method can be applied to amorphous, liquid and crystalline.

PDF describes a probability of finding an atom or molecule at given inter-atomics distance. The main application of PDF is to study materials that do not have long range order of material (amorphous or liquid).

Experimentally, PDF can be obtained directly from diffraction data by Fourier transforming normalized total structure factor. PDF from atomic configuration can be obtained by two methods: first, calculation of probability to find an atom in a shell *dr* at the distance *r* of another atom chosen as a reference point and second, the experiment-like calculation using Fourier transform of the structure factor obtained using the Debye equation.

Calculated pair distribution function for system $(GeTe_4)_{100-x}In_x$ shown in figure 2. From figure 2(a) for amorphous system and figure 2(b) for liquid, it is known that the first peak position of PDF for amorphous and liquid state generally slight increase with addition of indium. It means that total cut-off distance between atoms increase with indium addition. Shallow first peak in amorphous system imply that first peak location is sensitive to the atoms cut-off value selected. Liquid $(GeTe_4)_{100-x}In_x$ has broader PDF and lower peak intensity.

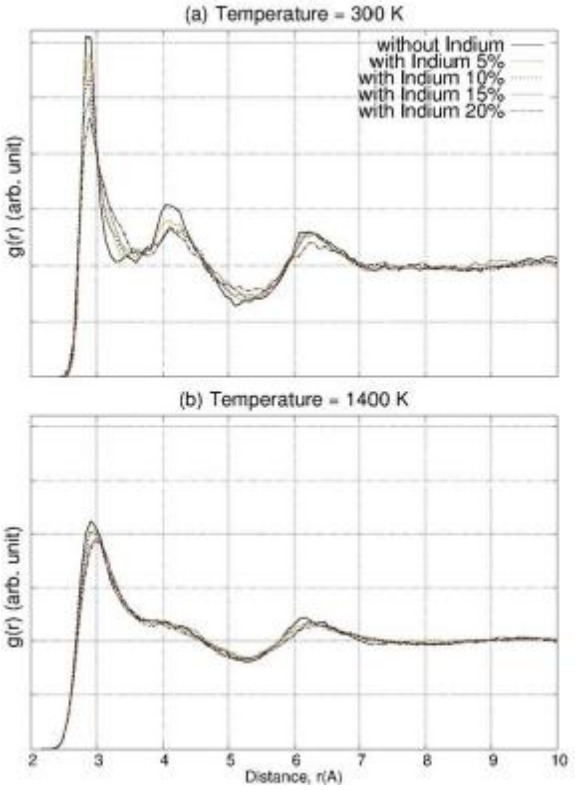

Figure 2. Calculated pair distribution function of system $(GeTe_4)_{100-x}In_x$. (a) For temperature 300 K (amorphous) (b) for temperature 1400 K (liquid)

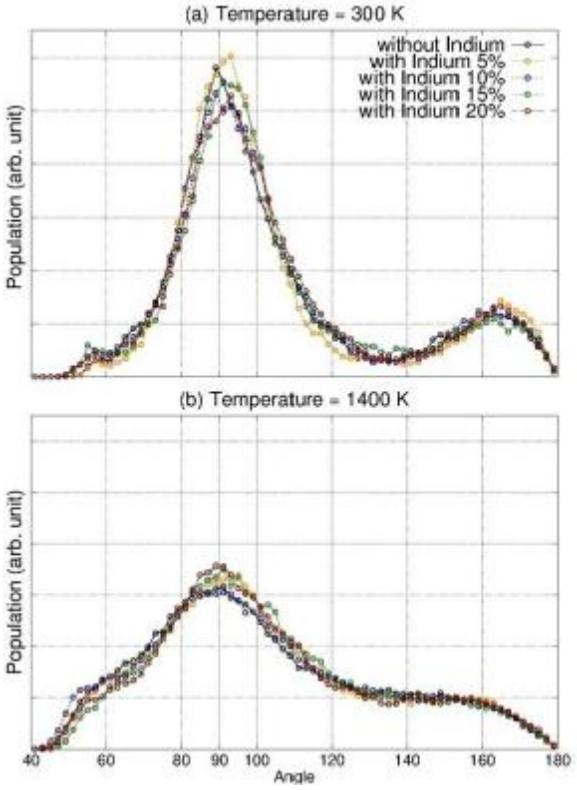

Figure 3. Band angle distribution of system $(GeTe_4)_{100-x}In_x$ (a) for temperature 300 K (amorphous) (b) for temperature 1400 K (liquid)

Bond angle distributions

Bond angle distribution between first neighbor atoms can give information about structural nature of system. As member of group IV chalcogenide we expect that $GeTe_4$ has tetrahedral nature as $GeSe_4$.

Bond angle distributions of Te-Ge-Te for amorphous and liquid $(GeTe_4)_{100-x}In_x$ in figure 3 gives us information that our systems have maximum at around 88°–100° and a contribution lower than 180° in amorphous state. These results indicate that tellurium atoms can lay either in equatorial plane (90°) of a Ge atom or at its vertices (180°). Surprisingly, this structure doesn't display a full tetrahedral character which should show by max at 109° like in system $GeSe_4$.

We anticipate that structure of our system with max angle distribution found between 88°and 109° should be made of 4-fold which is partially tetrahedral and higher coordinated species in octahedral nature.

Ring statistics

Topology analysis of Amorphous, liquid or crystalline systems is often based on part of structural information which can be represented in the graph theory using nodes for the atoms and links for the bonds. A series of nodes and links connected sequentially without overlap is called a path. Following this definition a ring is therefore simply a closed path.

The ring statistics which show connectivity between atoms is an important structural parameter to investigate crystal growth in amorphous-crystal transition. Ring calculation in present study using definition of ring which was proposed by Guttman [15], who defines a ring as the shortest path which comes back to a given node (or atom) from one of its nearest neighbors.

Result of ring statistics calculation with total cut-off 3.2 angstrom is shown in figure 4. Figure 4(a) shows that amorphous $(GeTe_4)_{100-x}In_x$ have a significant number of fourfold rings (four member square rings) which responsible to the rapid crystal growth in crystal-amorphous transition according Hegedus [16]. It is increase if compared to liquid

state as expected. These results show promising properties as candidates of phase change material.

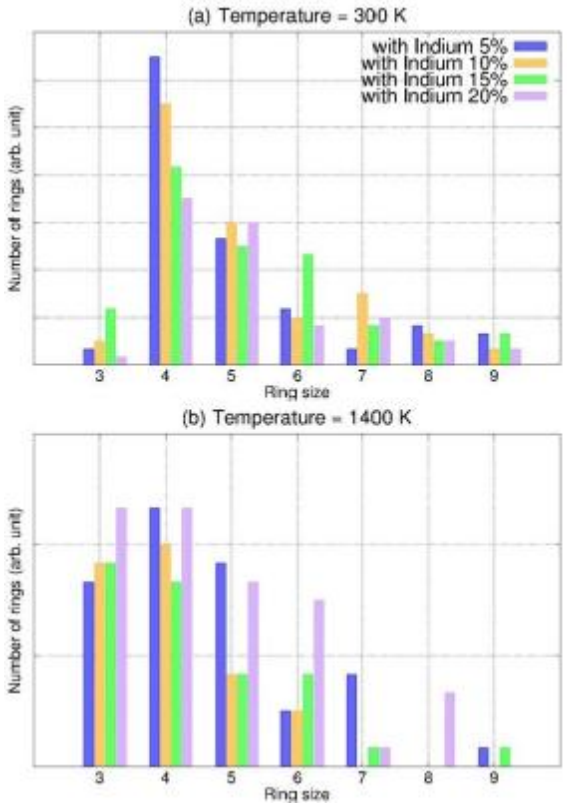

Figure 4. Ring statistics of system $(GeTe_4)_{100-x}In_x$ (a) for temperature 300 K (amorphous) (b) for temperature 1400 K (liquid)

IV. Conclusion

We made models of $(GeTe_4)_{100-x}In_x$ with x = 0, 5, 10, 15, 20 with melt quenching AIMD. Calculation result of bond angle distributions suggest that the structure of our system should be made of 4-fold which is partially tetrahedral and higher coordinated species in octahedral nature. We found that amorphous $(GeTe_4)_{100-x}In_x$ have a significant number of fourfold rings which responsible to the rapid crystal growth in crystal-amorphous transition. These results show promising properties as candidates of phase change material. With further development, we believe that Ge-Te-In system can be applied as new phase change materials.

V. References

1. M. Boniardi, D. Ielmini, T. Tortorelli, A. Redaelli, A. Pirovano, M. Allegra, M. Magistretti, C. Bresolin, D. Erbetta, A. Modelli, E. Varesi, F. Pellizzer, A.L. Lacaita, and R. Bez, Solid-State Electronics, 58 [1] (2011).
2. Véronique Sousa, Microelectronic Engineering, 88 [5] (2011.
3. S.A. Kozyukhin, A.I. Popov and E.N. Voronkov, Thin Solid Films, 518 [20] (2010.
4. A. Abrutis, V. Plausinaitiene, M. Skapas, C. Wiemer, O. Salicio, M. Longo, A. Pirovano, J. Siegel, W. Gawelda, S. Rushworth and C. Giesen, 85 [12] (2008).
5. K. Kolev, C. Popov, T. Petkova, P. Petkov, I.N. Mihailescu and J.P. Reithmaier, Sensors and Actuators B: Chemical, 143 [1] (2009).
6. V.S Vassilev and S.V Boycheva, Talanta, 67 [1] (2005) 20-27.
7. A. V. Rode, A. Zakery, M. Samoc, R.B. Charters, E.G. Gamaly, B. Luther-Davies, Applied Surface Science, 197-198 (2002).
8. Juejun Hu, Vladimir Tarasov, Nathan Carlie, Laeticia Petit, Anu Agarwal, Kathleen Richardson, Lionel Kimerling, Optical Materials, 30 [10] (2008).
9. C. Florea, J.S. Sanghera, I.D Aggarwal, Optical Materials, 30 [10] (2008).
10. S. Raoux, M. Wuttig (ed), "Phase change materials and applications", Springer, 2008.
11. D. Lencer, M. Salinga, B. Grabowski, T. Hickel, J. Neugenauer,M. Wuttig, Nature Mat. 7, 972 (2008)
12. A. Zaidan, A. Supardi, Vl. Ivanova and P. Petkov, Proceedings of 3rd International Conferences and Workshops on Basic and Applied Sciences Surabaya, Indonesia, 2011.
13. A. Zaidan, Vl. Ivanova and P. Petkov, Adv. In natural science: theory and applications. 1, 1 (2012).
14. E. Artacho, E. Anglada, O. Dieguez, J.D. Gale, A. García, J. Junquera, R.M. Martin, P. Ordejón, J.M. Pruneda, D. Sánchez-Portal and J.M. Soler, J. Phys.: Condens. Matter, 20 (2008).
15. L. Guttman. J. Non-Cryst. Solids., 116:145–147 (1990).
16. J. Hegedus, S.R. Elliot, Nature Mat. 7, 399 (2008).

Effect of Surface Structure and Constituent Atom toward O_2 Dissociative Adsorption

Cica Gustiani*,[1], Wilson A. Dinõ[2], Hideaki Kasai[2], and Hermawan K. Dipojono[1]

[1]Department of Engineering Physics, Institut Teknologi Bandung, Bandung 40132, Indonesia
[2]Department of Applied Physics, Osaka University, Suita, Osaka 565-0871, Japan

abstract

The O_2 dissociative adsorption on the metal surfaces Pt(001), Pt(111), Cu(001), and Cu(111) are investigated. In this study, effects of surface structure and constituent atom to the reactivity of O_2 dissociative adsorption are analyzed by using first principle calculations within density functional theory (DFT). Results show that the difference of O_2 dissociative adsorption on the different surface structure is given by the quasiatomic adsorption on (111) and dissociative adsorption on (001) surface. In addition, here, (001) surface is more reactive than (111) surface. On the other hand, the difference in constituent atoms is given mainly by adsorption-mediated by precursor states on Cu and dissociative adsorption on Pt.

Key words: *dissociation, adsorption, oxygen, metal, surface, platinum, copper*

**Corresponding author.*
E-mail address*: cica@students.tf.itb.ac.id*

I Introduction

In designing catalytic materials for certain reaction, it is important to understand the properties that can be used to control the surface reactivity and to steer reaction selectivity in the desired direction. One of the strategies to achieve those is identifying the key properties that can be used as control parameters. An advantage of a theoretical study is that an ideal model can be established wherein a single parameter of the property of the material can be varied to observe how that parameter affecting the characteristics of the material. Fuel cell is a newly emerging renewable energy source and it is promising to cut our dependence of fossil fuel. Lots of experiences has been performed, however, deeper understanding in fundamental phenomena is necessary in order to elucidate the results. The oxygen dissociative adsorption might be one of important steps that occurs on the cathode. Platinum (Pt) based catalyst is typically used for cathode of fuel cells nowadays, however it is rare and quite cumbersome to maintain. On the other side, ORR interestingly occurs on copper (Cu) which drives to the corrosion. However, some experimental of oxidation on Cu[20] shows that oxidation on Cu can be prevented or promoted depending on impinging kinetic energy.
In this study, effects of surface structure and constituent atom to the O_2 dissociative adsorption are analyzed by comparing the dissociation of O_2 on clean (001) and (111) surfaces of Cu and Pt using first principle calculations within the Density Functional Theory (DFT). Here, the reaction pathway of O_2 dissociative adsorption on these surfaces is determined by calculation the total energy of the O_2-substrate system while varying the bond length r and center of mass distance Z of oxygen from the surface. As shown in Fig.1, the center of mass (c.m) of oxygen is fixed at the bridge site of both surfaces (001) and (111) while here are considered both of O atoms dissociate towards the hollow sites. In order to provide a physical description of the reactive pathway, the potential energy surfaces (PESs) of O_2 on the (001) and (111) surfaces of Cu and Pt are presented.

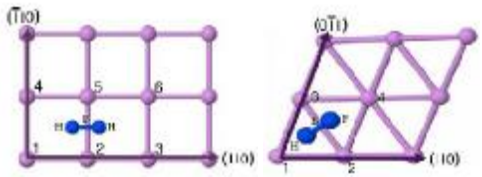

Figure 1: Top view of the model in calculation. The left figure is (001) surface, and the right figure is (111) surface. The blue balls denote oxygen and the pink balls denote Cu (or Pt). "H", "B", and "F"denote the hcp hollow site, bridge site, and fcc hollow site respectively.

II Method

Performing reliable calculation is important in order to get reasonable results. The parameters need to be determined carefully. Lattice parameters are determined by getting the energy minima of total energy of bulk system by varying the lattice parameter. The lattice constants are 3.64 Å for Cu and 3.97Å for Pt, which are in good agreement with experimental data 3.601Å for Cu[7] and 3.923Å for Pt.[16]. The isolated O_2 molecule stable gas phase bond length is 1.23Å and dissociation energy is 6.02 eV which has good agreement with experiment.[17] The cut-off energy for both systems (O_2 dissociative adsorption on Cu and O_2 dissociative adsorption on Pt) is 740 eV, which is determined based on convergence of total calculation for each component atom. The surface Brillouin

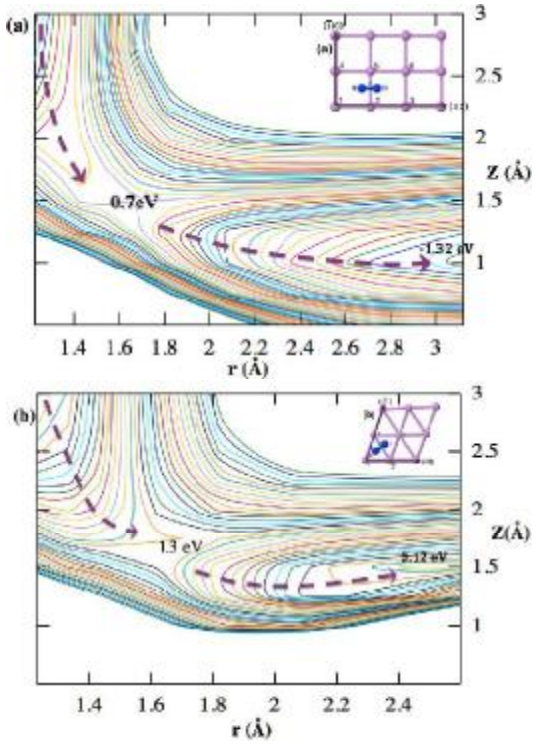

Figure 2: Contour plots of the potential-energy surfaces for O_2 dissociative adsorption o n Pt surfaces. The above figure indicates Pt(001) surface, the bottom figure indicates Pt(111) surface .

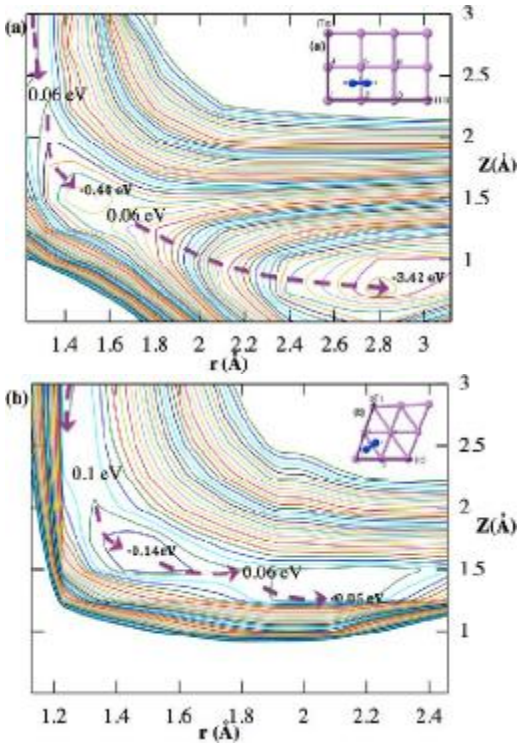

Figure 3: Contour plots of the potential-energy surfaces for O_2 dissociative adsorption on Cu surfaces. The above figure indicates Cu(001) surface, the bottom figure indicates Cu(111) surface.

zone integration is performed using the special-point sampling technique of Moknhrost-Pack kpoint with 8x8x1 meshes. Spin-polarized total energy calculations using Projector Augmented Wave (PAW) method[4,15] and plane-wave basis set are performed within DFT[8] framework by using Vienna ab initio simulation program (VASP).[11,12,13,14] The generalized gradient approximation (GGA) of Pedrew, Burke, and Ernzerhof (PBE) is used for the exchange-correlation functional.[21,22] To model the situation with O_2 and metal surfaces, five layers of fcc(001) surfaces and four layer of fcc(111) surfaces for both Cu and Pt are used. The number of layers are varied until the local density of states (LDOS) of the atom in the middle of the layers resemble that of the atom in the bulk system. Layers are separated by 17Å vacuum which is large enough to avoid the surface interaction along z axis.

As shown in figure 1, the symmetric O_2 dissociative adsorption sites on (001) and (111) surfaces are considered in this study. The H-B-F site shown in figure 1 (right) on the (111) surface corresponds to the case when the c.m. of O_2 molecule is fixed at the bridge (B) site. After dissociation, O atoms are positioned at the hcp (H) and fcc (F) hollow sites. These configurations are chosen among all the possibilities since they allow the maximum (nearest) approach of the O_2 c.m. to the corresponding surfaces. The orientation of the O-O bond is kept parallel to the surface. Energies are given in eV relative to the values of the energy surface and isolated O_2.

III Results and Discussion

The potential-energy surfaces (PESs) for O_2 dissociative adsorption on the surfaces are shown in figure 2 and figure 3 as a function of O-O bond length r and O-O c.m distance normal to the surface Z. The contour spacing is 0.1 eV in all figures. The dashed arrows indicate the reaction pathways for each case. The activation barriers indicated by small fonts and adsorption energies indicated by large fonts.

In comparison of PESs on figure 2 and figure 3, it shows drastically the difference between potential-energy surfaces of Cu and Pt. In the reaction pathways of O_2 dissociative adsorption on Cu, O_2 facing two small activation barriers and two minima. On the other hand, in the reaction pathways of O_2 dissociative adsorption on Pt, O_2 facing one activation barrier. By comparing the surface structure, (001) surface is more reactive than (111) surface in O_2 dissociative adsorption, indicated by lower activation barrier and smaller adsorption energy for both cases of Cu and Pt. The reactivity dependency on surface structure has been investigated[24,25] which concludes that reactivity on the surface can be enhanced by changing the surface structure from (001) to (111) surface.

As indicated in both figures (001) and (111), O_2 can approach (001) surface closer than on (111) surface which makes the adsorption energy of O_2 smaller on (001) rather than on (111) surface. And also this result of O_2 dissociation on Cu(001) is in good agreement with experimental studies of surface of measuring sticking coefficient of the incoming O_2 molecules [19,20]. The sticking coefficients have been found to be very low at small energies which imply that there is small dissociation barrier for the O_2 dissociation on clean Cu(001). This calculation has revealed this barrier which was not revealed by previously reported study[1]. In addition, These results are in good agreement with a series of experiments showing the oscillating behavior in oxidation of CO on Pt surface, which also shows that the reactivity of oxygen has improved by changing surface structure from hexagonal to the (001) surface. [5,6,23]

In both figures 2 and 3, show difference of dissociation by surface structure. In case of (001) surfaces, O_2 dissociates completely, indicated by separation of O more than twice of O_2 stable bond length. In case of Pt, O–O separated by 3.12 Å on (001) and 2.4 Å on (111). In case of Cu, O–O separation are 2.8 Å and 2.1 Å for (001) and (111) surfaces respectively. This is caused by local structure of surface, which allows O_2 to separated easily on (001) surfaces than on (111) surfaces. By referring to figure 1, on (001) surface, the oxygen can separated easily due to availability of space which allows O_2 to expands. On the other hand, in case of (111), the oxygen must encounter repulsion force from surface atom numbered "1"and "2"on the figure. Therefore, oxygen is not completely dissociated and tends to almost dissociate. Then, "quasi-atomic"adsorption happens on (111) surface, which means oxygen is not completely dissociate.

In comparison of reactivity of constituent atom effect, in this reaction pathway of O_2 dissociative adsorption, Cu is more reactive than Pt. If the adsorption sites compared, oxygen comes closer to the Cu surfaces rather than to Pt surfaces which allows more hybridization and transfer electron with surfaces. Adsorption site of (001) surface of Cu and Pt are $(r,Z)\sim(2.8,0.75)$ and $(r,Z)\sim(3.12,1.0)$ respectively with adsorption energy -3.42 eV for Cu and -1.32 eV for Pt. Transfer electrons at this site are $2.2e$ for Cu and $1.5e$ for Pt. It obviously shows that high transfer electron on Cu contrives very low adsorption energy. In addition, transfer electron from Cu comes not only from most top layer as happens to Pt, but also comes from lower layers. However, this high transfer electron can induce reconstruction of Cu surface and contrives higher adsorption energy. This is because of the atom size of Cu smaller than Pt which makes oxygen comes closer to Cu surface rather than to Pt surface, hybridization makes sense here as reason of high adsorption energy in case of Cu.

IV Conclusion

In summary, DFT-based total energy calculations have been invoked in order to investigate the difference in the dissociative adsorption of O_2 on two types of Cu and Pt surfaces, viz., Cu(001), Cu(111), Pt(001), and Pt(111). Of the several parameters that might govern to reactivity of O_2 dissociative adsorption, the focus here is the static effect of surface structure and constituent atoms. The reactive pathways are derived from the trace of energy minimum under the same conditions. Results show that the difference in O_2 dissociative adsorption on the different surface structures is given by the quasiatomic adsorption on (111) and dissociative adsorption on (001) surface. The quasiatomic adsorption on (111) surface is due to the local structure of the surface. Also, changing the surface structure affects the surface reactivity of O_2 dissociative adsorption. Here, (001) surface is more reactive than (111) surface indicated by the lower activation barrier and higher adsorption energy. The difference in O_2 dissociative adsorption for different constituent atoms is given mainly by adsorption which is mediated by precursor states on Cu and direct dissociation on Pt, and also Cu is more reactive than Pt due to Cu has smaller atom size than Pt.

References

1. M. Alatalo, S. Jaatinen, P. Salo, and K. Laasonen. *Phys. Rev. B*, 70:245417, 2004.
2. R. F. W. Bader. Oxford University Press, UK, 1990.
3. Richard F. W. Bader. In *Density functional theory*, volume 337 of *NATO ASI series. Series B, Physics*, pages 237–272. Plenum Press, 1995.
4. P. E. Blöchl. *Phys. Rev. B*, 50:17953–17979, Dec 1994.
5. M. P. Cox, G. Ertl, and R. Imbihl. *Phys. Rev. Lett.*, 54:1725–1728, Apr 1985.
6. M. Eiswirth, P. Ḿoller, K. Wetzl amd R. Imbihl, and G. Ertl. *Phys. J. Chem.*, 90:510–521, 1989.
7. Takaya Fujita, Yuji Okawa, Yuji Matsumoto, and Kenichi Tanaka. *Phys. Rev. B*, 54:2167–2174, Jul 1996.
8. P. Hohenberg and W. Kohn. *Phys. Rev.*, 136:"B864–B871", 1964.
9. Y.P. Kim, M. Fregonese, H. Mazille, D. Feron, and G. Santarini. *Corrosion Science*, 48(12):3945 – 3959, 2006.
10. Anusorn Kongkanand, Susumu Kuwabata, G. Girishkumar, and Prashant Kamat. *Langmuir*, 22(5):2392–2396, 2006.
11. G. Kresse and J. Furthmüller. *Comput. Mat. Sci.*, 6:15, 1996.
12. G. Kresse and J. Furthmüller. *Phy. Rev. B*, 54:11169, 1996.
13. G. Kresse and J. Hafner. *Phy. Rev. B*, 47:558, 1993.
14. G. Kresse and J. Hafner. *Phy. Rev. B*, 49:14251, 1994.

15. G. Kresse and D. Joubert. *Phys. Rev. B*, 59:1758–1775, Jan 1999.
16. G. W. R. Leibbrandt, R. van Wijk, and F. H. P. M. Habraken. *Phys. Rev. B*, 47:6630–6643, Mar 1993.
17. D.R. Lide. CRC Handbook of Chemistry and Physics, 86th Ed. CRC Press, 2005.
18. N. M. Markovic, T. J. Schmidt, V. Stamenkovic, and P. N. Ross. *Fuel Cells*, 1(2):105, 2001.
19. Michio Okada, Kousuke Moritani, Seishiro Goto, and Toshio Kasai. *Chemical Physics*, 119(14):6994, 2003.
20. Michio Okada, Kousuke Moritani, Akitaka Yoshigoe, Yuden Teraoka, Hiroshi Nakanishi, Wilson Agerico Di no, Hideaki Kasai, and Toshio Kasai. *Chemical Physics*, 301:315 – 320, 2004.
21. John P. Perdew, Kieron Burke, and Matthias Ernzerhof. *Phys. Rev. Lett.*, 77:3865–3868, 1996.
22. John P. Perdew, Kieron Burke, and Matthias Ernzerhof. *Phys. Rev. Lett.*, 78:1396–1396, Feb 1997.
23. H. H. Rotermund, W. Engel, M. Kordesch, and G. Ertl. *Nature*, 343(6256):355–357, jan 1990.
24. Satoshi Yotsuhashi, Yuka Yamada, Wilson Agerico Diño, Hiroshi Nakanishi, and Hideaki Kasai. *Phys. Rev. B*, 72:033415, Jul 2005.
25. Satoshi Yotsuhashi, Yuka Yamada, Wilson Agerico Diño, Hiroshi Nakanishi, and Hideaki Kasai. *Phys. Rev. B*, 77:115413, Mar 2008.

Analysis of Dielectric and Magneto-dielectric of Superparamagnetic Iron oxide Nanoparticles (SPIONs) Magnetite

Dini Zulia, Eni Astuti, Muflihatun, Felicitas Titan, and Edi Suharyadi
Department of Physics, Faculty of Mathematics and Natural Sciences, Gadjah Mada University
Sekip Utara PO BOX BLS.21 Yogyakarta Indonesia 55281

Abstract

Dielectric properties of Superparamagnetic Iron oxide Nanoparticles (SPIONs) Magnetite have been successfully investigated. SPIONs Magnetite have been fabricated using copresipitation method with temperature steering variation at (30, 60 and 90) ^{o}C and NH_4OH concentration variation at 10% and 6%. This method resulted nanoparticle Fe_3O_4 with sizes of 13.0 nm, 14.4 nm, 14.8 nm, 15.5 nm, and 16.5 nm. Dielectric properties of SPIONs Magnetite were investigated at range frequency start from 70 to 350 kHz. The results show that the value of real part and imaginary part of dielectric permittivity were changes with the change of particles sizes. The dielectric permittivity was dependent on frequency, however nanoparticles with the similar size has the similar trend. Magneto-dielectric of SPIONs Magnetite had been also investigated under external field from 100 G to 400 G. Dielectric properties were change by applying external field.

I. Introduction

In the last two decades, new terms with the prefix `nano' have rushed into the scientific vocabulary nanoparticle, nanostructure, nanotechnology, nanomaterial, nanocluster, nanochemistry, nanocolloids, nanoreactor and so on. The enhanced interest of the researchers in nanoobjects is due to the discovery of unusual physical and chemical properties of these objects, which is related to manifestation of so-called quantum size effects. These arise in the case where the size of the system is commensurable with the de-Brogli wavelengths of the electrons, phonons or excitons propagating in them. A key reason for the change in the physical and chemical properties of small particles as their size decreases is the increased fraction of the surface atoms, which occur under conditions (coordination number, symmetry of the local environment, etc.) differing from those of the bulk atoms. From the energy stand- point, a decrease in the particle size results in an increase in the fraction of the surface energy in its chemical potential [1].

The magnetic properties of nanoparticles are determined by many factors, the key of these including the chemical composition, the type and the degree of defectiveness of the crystal lattice, the particle size and shape, the morphology (for structurally inhomogeneous particles, the interaction of the particle with the surrounding matrix and the neighbouring particles. By changing the nanoparticle size, shape, composition and structure, one can control to an extent the magnetic characteristics of the material based on them. However, these factors cannot always be controlled during the synthesis of nanoparticles nearly equal in size and chemical composition; therefore, the properties of nanomaterials of the same type can be markedly different [1].

Nanoparticles with super-paramagnetic properties have great potential to achieve such desirable properties. Various methods have been developed to synthesize Fe_3O_4 (magnetite) particles in nanometer size range. However, the magnetic properties of magnetite based nanoparticles or films highly depend upon the synthesis procedure [2].

Many investigations with several types of Superparamagnetic Iron Oxides Nanoparticles (SPIONs) have been carried out in the field of nanosized magnetic particles (mostly, magnetite or maghemite (γ-Fe2O3) single domains of about 5∼20 nm in diameter). These iron oxide particles of nanometer size present superparamagnetic property and are ideal for magnetic resonance imaging (MRI) contrast agent by enhancement of proton relaxation in the tissue microenvironment. For the MRI application, these SPIONs must have high magnetization values, stability in physiological environment, and size smaller than 20 nm with overall narrow particle size distribution so that the particles have uniform physical and chemical properties [3].

Biosensors based on Surface Plasmon Resonance (SPR) spectroscopy have attracted tremendous interest in the past decade, both from a fundamental-physics perspective and as highly

sensitive devices for biological studies, health science research, drug discovery, clinical diagnosis, and environmental and agricultural monitoring. Although these SPR biosensors are selective and can detect large biomolecules, compared with the traditional means, there are still some shortcomings in testing costs, background interference and sensitivity, particularly for the detection of target with very low concentration in real samples. So far there has been little research reported on the SPR response of MNPs [4].

SPIONs magnetite as biosensor SPR for DNA (Deoxyribo Nucleic Acid) detection was also investigated. SPIONs magnetite has numerous advantages i.e. high dispersibility, quick binding with bio molecular, controlled by external field [5].

On the other hand, magnetic Hyperthermia is a method of cancer treatment using magnetic nanoparticles. In the process, magnetic particles were injected locally into cancer tissues that can be heated up to the required temperature of about 45°C with the help of an external alternating magnetic field. It was found that magnetic fluid based on superparamagnetic Fe_3O_4 nanoparticles coated by biocompatible layer is suitable for hyperthermia because the particles have a high magnetic moment, strong magnetic specific loss power (SLP) and non-toxicity [6].

The purpose of this research was preparing SPIONs magnetite with size differences and focus on investigating the dependent of permittivity dielectric and magneto-dielectric on the size differences at alternating magnetic field at frequency range (1-1000) kHz, and under external field (103-403) G. Here, we report an information of real permittivity for SPIONs magnetite as parameter to safe charge ability, and imaginary permittivity as parameter to describe loss power and release as energy. This investigation will help to optimize for choosing SPIONs with various sizes which is suitable for Hyperthermia and SPR application.

II. Experimental Methods

A. SPIONs magnetite synthesized.

SPIONs magnetite was synthesized by precipitation method with mixing of $FeCl_3.6H_2O$ and $FeSO_4.7H_2O$ and ammonia solution (NH_4OH). Concentration of ammonia solution, temperature and time steering are the factors that control the particle size in this process as shown in table 1. The precipitate thus obtained was filtered and left for drying at temperature 80 °C.

B. SPIONS magnetite Characterization.

X-ray diffractometer (XRD) was used to study structural phase and grain size identification. Coherently diffracting domain size (d_{xrd}) was calculated from the width of the XRD peak under the Scherer approximation. The morphology of the SPIONs magnetite was examined using Transmission Electron Microscopy (TEM).

C. Dielectric-permittivity and magneto-dielectric of SPIONs magnetite.

Frequency dependences of resistance R and capacity C were measured by the oscilloscopic method under condition that the equivalent scheme of sample is the parallel linked resistance and capacity. The frequency of the measuring signal was changing within the range (70-350) kHz. Based on the known R and C, ε' and ε'' were determined. For magneto-dielectric measurement a direct magnetic field was created by two magnets that were located on both sides of SPIONs magnetite which antiparallel with the direction of polarization field. Dielectric and magneto-dielectric properties of the samples were measured at the temperature 293 K

III. Result and Discussion

A. SPIONs magnetite Characterization

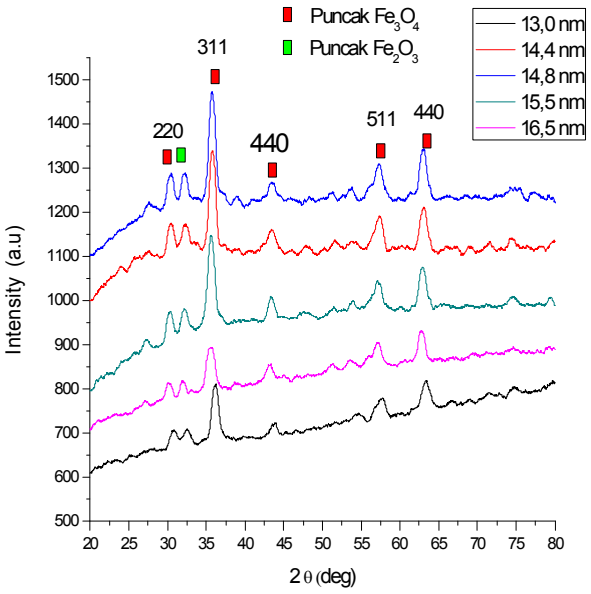

Fig. 1. XRD pattern of SPIONs magnetite in difference sizes

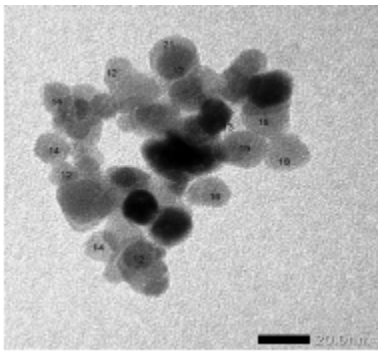

Fig. 2. TEM image of SPIONs magnetite sample 1

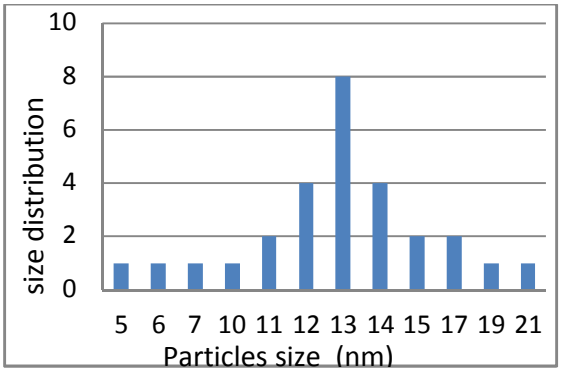

Fig. 3. Histogram of size distribution for spherical SPIONs magnetite sample 1.

Table 1. Variation preparation, particles size and lattice parameter of SPIONs magnetite

Sample	Variation			Particles size (nm)	Lattice parameter (nm)
	Temperature (^oC)	Concentration of NH_4OH solution (%)	Steering time (menit)		
1	30	10	90	13.0	0.824
2	60	10	90	14.4	0.832
3	90	10	90	14.8	0.833
4	60	6	150	15.5	0.835
5	30	6	90	16.5	0.837

Figure 1 shows a typical XRD pattern, which reveals the formation of Fe_3O_4 phase in all these samples. As expected, the particle size was change as the variation treatment of preparation (Table 1). Figure 2 is a representative image taken for the sample 1. TEM images indicate that the particles of all sizes are spherical in shape. Figure 3 shows that dominant grain size in sample 1 is in range 12-14 nm, with the most dominant size is 13 nm.

B. SPIONs Magnetite permittivity dielectric behave

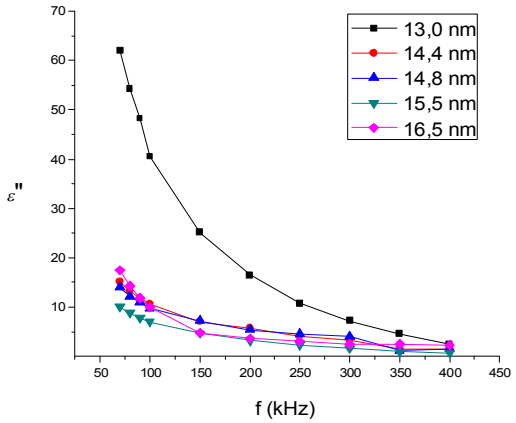

Fig. 4 Frequency dependences of ε" SPIONs magnetite samples with size differences (nm).

Figure 4 is shown the dependences of ε" SPIONs magnetite to frequency with various particles sizes. From the point of view dependences of ε" SPIONs magnetite to frequency was indicates that ε" decreased when frequency increased. From the point of view dependences ε" SPIONs magnetite to particles sizes, generally was imply that ε" decreased when particles sizes increased. Figure 5 shown the same phenomenon as figure 4, which ε' was decrease when frequency increased and ε' is decreased when particles sizes increased. Generally the frequency dependences of ε can easily explain by Debye equation as shown in eq. below.

$$\varepsilon' = \varepsilon_\infty + \frac{\varepsilon_s - \varepsilon_\infty}{1+\omega^2\tau^2}$$

$$\varepsilon'' = \frac{(\varepsilon_s - \varepsilon_\infty)\omega\tau}{1+\omega^2\tau^2}$$

$$\tan\delta = \frac{\varepsilon''}{\varepsilon'} = \frac{(\varepsilon_s - \varepsilon_\infty)\omega\tau}{\varepsilon_s + \varepsilon_\infty\omega^2\tau^2}$$

The eq. indicates that the real and imaginary dielectric constant is inversely proportional to the frequency.

Fig. 6 and 7 is shown the dependences of ε" and ε' SPIONs magnetite to particles sizes, which caused by the differences fraction of surface charge by the differences of particles sizes. The smaller particle size SPIONs magnetite the higher fraction of surface charge, so it will be result the increasing of ε, as the consequence of

polarization field increments by polarization raises. as we know, that the polarization is proportional to the number of dipole surface charge, while the polarization is proportional to the magnitude of the internal field, and the value of the dielectric constant is proportional to the magnitude of the internal field, so the larger the volume fraction, the larger the dielectric constant.

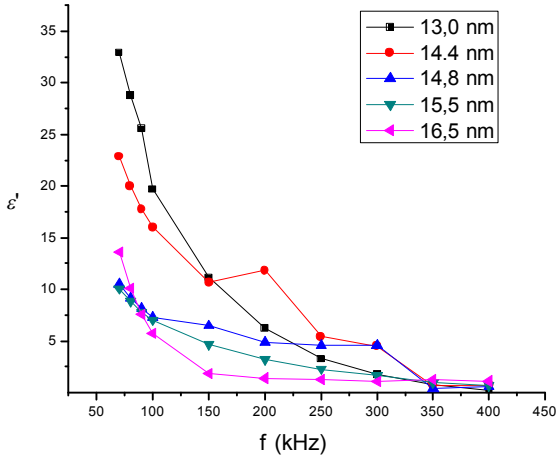

Fig. 5 Frequency dependences of ε' SPIONs magnetite samples with size differences

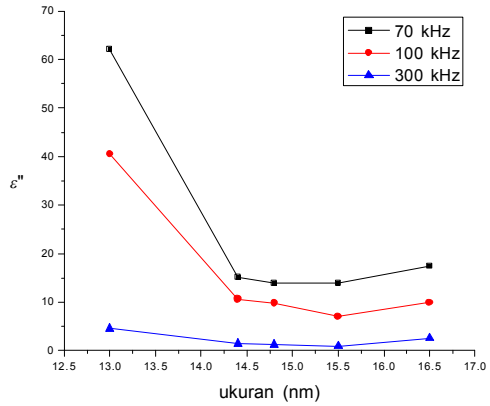

Fig. 6 Sizes dependences of ε" SPIONs magnetite at numerous frequencies.

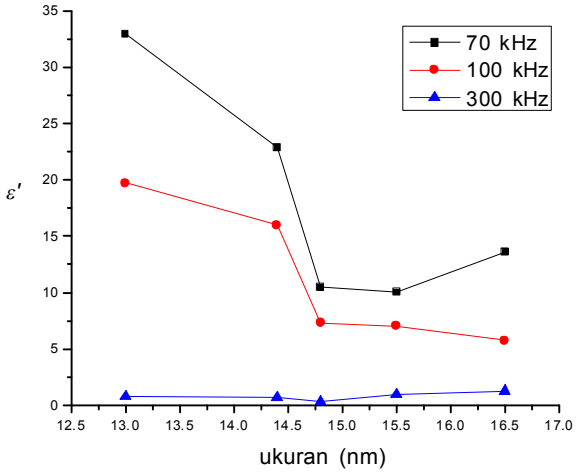

Fig. 7 Sizes dependences of ε' SPIONs magnetite at numerous frequencies.

C. SPIONs magnetite magneto-dielectric behave

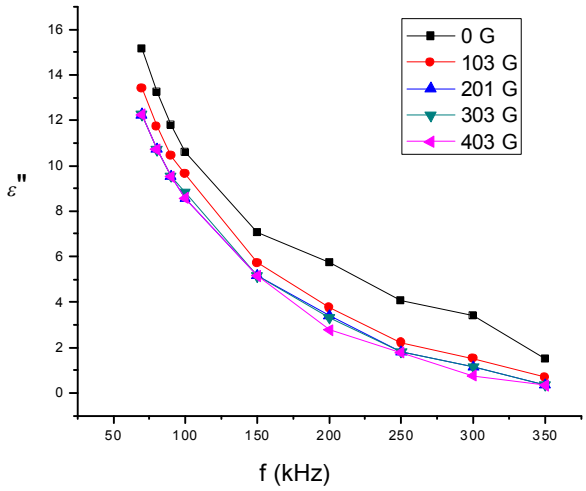

Fig. 8 Frequency dependences of ε" SPIONs magnetite samples with size differences under external field (magneto-dielectric investigated).

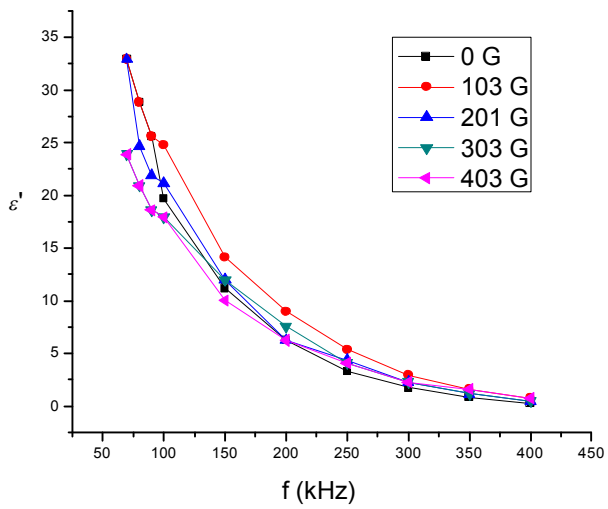

Fig. 9 Frequency dependences of ε' SPIONs magnetite samples with size differences under external field (magneto-dielectric investigated).

Figure 8 and figure 9 was shown the frequency dependences of ε" and ε' under influence of external field. It exposed that the ε" and ε' value was change by external magnetic field influence. It caused by the external magnetic field is against the polarization field of electrical material concerns reduced the ε" and ε' value. Figure 10 and 11 was shown ε" and ε' value dependences to magnitude of external field.

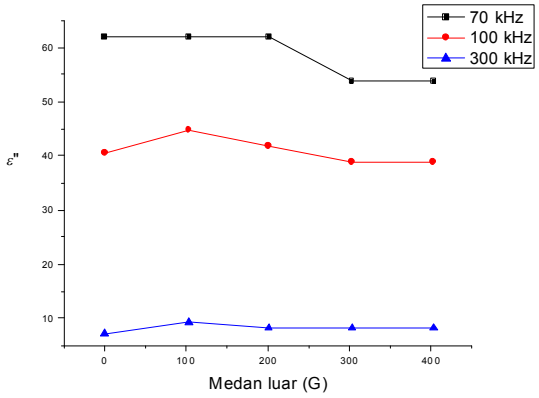

Fig. 10 dependences of ε" SPIONs magnetite to magnitude of external field at numerous frequency alternating potential.

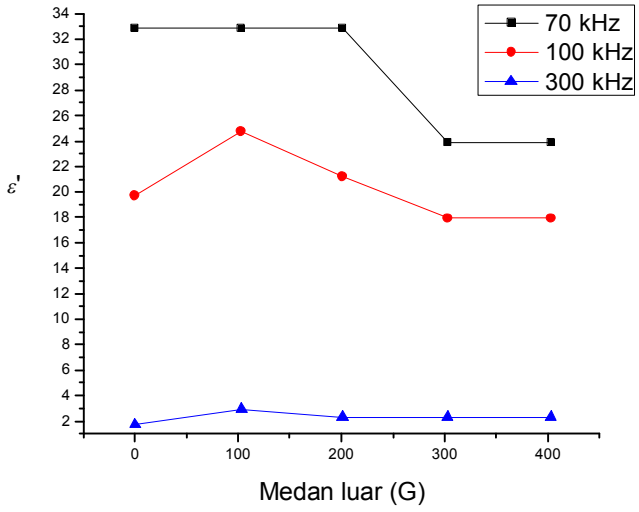

Fig. 10 dependences of ε" SPIONs magnetite to magnitude of external field at numerous frequency alternating potential.

IV. Conclusion

The copresipitation method is effective to fabricate SPIONs magnetite with particles sizes <20 nm. The first variation of preparation is the most effective variation of fabricated SPIONs magnetite because its result the smallest SPIONs magnetite sizes and cost lowest energy. The SPIONs magnetite dielectric permittivity is decreased with the frequency and particles sizes rising. Magneto-dielectric behave of SPIONs magnetite is has dependences to the magnitude of external field, antiparallel direction of external field caused the deceases the ε" and ε' value.

V. Acknowledgment

Authors would like to thank Prof. Kamsul Abraha, Dr, Kuwat Triyana, Dr. Rinto Anugraha for the guidance.

VI. Reference

[1] Gubin, S.P., Koksharov, Y.A., Khomutov, G. B., Yurkov, G. Y., 2005, Magnetic Nanoparticles: Preparation, Structure and Properties, *Russian Academy of Sciences and Turpion*.

[2] Linh, P.H., Thach, P.V., Tuan, N.A., Thuan, N.C., Manh, D.H., Phuc, N.X., Hong, L. V., 2009, Magnetic Fluid Based on Fe_3O_4 Nanoparticles: Preparation and Hyperthermia Application, *APCTP–ASEAN*

Workshop on Advanced Materials Science and Nanotechnology (AMSN08) IOP Publishing.

[3] Riyanto, A., 2012, Sintesis Nanopartikel Fe_3O_4 dan Potensinya sebagai Material Aktif pada Permukaan Sensing Biosensor Berbasis SPR, *Tesis,* Program Pascasarjana, Universitas Gadjah Mada, Yogyakarta.

[4] Thapa, D., Palkar V. R., Kurup M. B., Malik, S. K., 2005, Properties of Magnetite Nanoparticles Synthesized through a Novel Chemical Route, *Tata Institute of Fundamental Research, Mumbai 400 005, India*

[5] Yang, T., Brown, R.N.C., Kempel, L.C., Kofinas, P., 2008, Magneto-dielectric Properties of Polymer– Fe_3O_4 Nanocomposites, *Journal of Magnetism and Magnetic Materials.*

[6] Yoo, M.K., Kim, I.Y., Kim, E.M., Jeong H.J., Lee, C.M., Jeong, Y.Y., Akaike, T., Cho, C.S., 2007, Superparamagnetic Iron Oxide Nanoparticles Coated with Galactose-Carrying Polymer for Hepatocyte Targeting, *Hindawi Publishing Corporation Journal of Biomedicine and BiotechnologyVolume 2007.*

Wavelength Measurement of Soft-Mode Turbulence Pattern on Homeotropically Aligned Nematic Liquid Crystal

Dwiria Wahyuni[1,2*], Sri Hartini[1,3], Yusril Yusuf[1]
1 Department of Physics, Faculty of Mathematics and Natural Sciences, Gadjah Mada University
Sekip Utara PO BOX BLS.21 Yogyakarta Indonesia 55281
2 Department of Physics, Faculty of Mathematics and Natural Sciences, Tanjungpura University
Jl. Ahmad Yani Pontianak Kalimantan Barat Indonesia 78124
3 Department of Education of Natural Sciences, Faculty of Education, Lambung Mangkurat University
Jl. Brigjen H. Hasan Basri Kayutangi Banjarmasin Kalimantan Selatan Indonesia 70123

Abstract
We measured the wavelength of a typical convective pattern, Soft Mode Turbulence (SMT), in homeotropic nematic liquid crystal samples with 50μm and 100μm of thickness when external electric field on certain frequency applied into samples. A nematic liquid crystal, 4-methoxy-benziledene-4-n-buthyl-aniline (MBBA), is used. When applied voltage exceeds a typical threshold voltage V_{EHD}, an electrohydrodynamics (EHD) effect appears and shows SMT pattern. SMT pattern optically observed by a polarizing microscope integrated to CCD camera. Wavelength of SMT pattern for homeotropic samples has been measured using image processing with ImageJ software. The result showed that threshold voltage for SMT (V_{SMT}) increased nonlinearly to frequency and the wavelength of SMT was in the same order as sample's thickness and decreased linearly to applied frequency.
Keywords: *Homeotropic nematic liquid crystal, soft-mode turbulence, wavelength, image processing*

* Corresponding author.
E-mail address: hertieswhitelighter@yahoo.com

I. Introduction

Liquid crystal (LC) is a material that exhibits intermediate phases between crystalline and liquid ones. Liquid crystalline phases combine both the fluidity of the liquids and the anisotropy of crystals. Responses of nematic liquid crystal (NLC) observed by using a system consists of a thin layer of NLC which is sandwiched between two parallel electrodes. There are two alignments of LC's cells, namely homeotropic, where director **n** is perpendicular to the electrodes, and planar, where the director is parallel to the electrodes. The anisotropic properties of NLC allow it having response to induced external field, showing different patterns phenomenon such as stripes patterns that can be optically observed and give rise to certain novel instability mechanisms that are not encountered in the classical problem of hydrodynamic instability in ordinary liquids. This called electrohydrodynamics (EHD) of LC. The EHD mechanism, called the Carr-Helfrich mechanism, occurs when external field exceeds critical field. There are two different regimes in EHD mechanism: conductive regime and dielectric regime, respectively below and above a certain critical frequency f_c [1-3]. Electroconvection (EC) is known as an EHD system that gives similar approach to Rayleigh-Bénard thermal convection. In homeotropic, the EC pattern called *Soft-Mode Turbulence* (SMT) [4].

When the voltage is increased beyond critical voltage ($V > V_c$), the EC occurs in the homeotropic system. On this condition, a type of spatiotemporal chaos (STC) called the SMT occurs. The SMT is induced by nonlinear interaction between Goldstone mode and convective mode. The Goldstone mode comes from the spontaneous breaking of the continuous rotational symmetry [5]. The Goldstone mode leads to the unusual STC directly from the quiescent state [6]. There are two typical roll patterns in EC of nematics in the conductive regime, namely oblique rolls (OR) and normal rolls (NR). The NR pattern appears when sample is induced by frequency above Lifshitz point (LP), while OR one appears on frequency below LP [6-7]. The pattern in EC shows convection rolls due to a spatially periodic modulation of the director of nematics and the space charge distribution. Change of the convection rolls on the pattern depending on the experimental conditions were presented in the wide range of possible wavelength (λ) which scales with the thickness (d) of the nematic layer [7].

The subject of this work is to observe the SMT's wavelength on homeotropic NLC using

image processing. The work is also aimed to find dependency between frequency (f) and SMT voltage (V_{SMT}) and SMT's wavelength (λ_{SMT}) on homeotropic NLC samples.

II. Experimental Method

A nematic liquid crystal *4-methoxy-benzilidene-4-buthyl-aniline* (MBBA) was filled between two parallel glass plates whose surfaces were coated with transparent electrodes, indium tin oxide (ITO). The space between the glass plates was maintained with mylar spacers of 50µm and 100µm of thickness. In order to have a homeotropic alignment, the electrodes were coated with *n-n'-dimethyl-n-octadecyl-3-aminopropyl-trimethoxy silyl chloride* (DMOAP). Experimental setup is shown in Figure 1. The sample cell was placed in a hot stage and maintained at a constant temperature of (30 ± 0.01)ºC using a digital temperature-controller. Patterns were observed on the *xy*-plane by a CCD camera integrated to a polarizing microscope. An alternating voltage generated from function synthesizer-amplifier was applied perpendicularly to the electrodes. Frequency (f) was the AC frequency of the alternating voltage. The applied frequency on this research was set below critical frequency, f_c. The f_c is a frequency separating the conductive and dielectric regime. On each flat frequency variation, the threshold voltage of SMT was read on multimeter. Image analysis of the SMT pattern used *Pixel View* software to get a snapshot of pattern, while its wavelength analyzed by using *ImageJ* software. The wavelength value (in pixel) then conversed into micrometer, with 1 pixel equal to 2µm. The conversion obtained by comparing the image to objective micrometer.

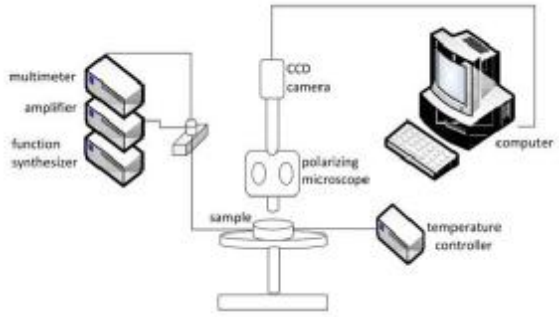

Figure 1. Experimental setup

III. Result and Discussion

The observation of the SMT convective pattern was initiated by applying external frequency-voltage into samples. The SMT pattern that appeared was a NR type. The threshold voltage of SMT (V_{SMT}) was obtained by setting the frequency (f) induced into the samples, and then the voltage was adjusted until the SMT pattern appeared.

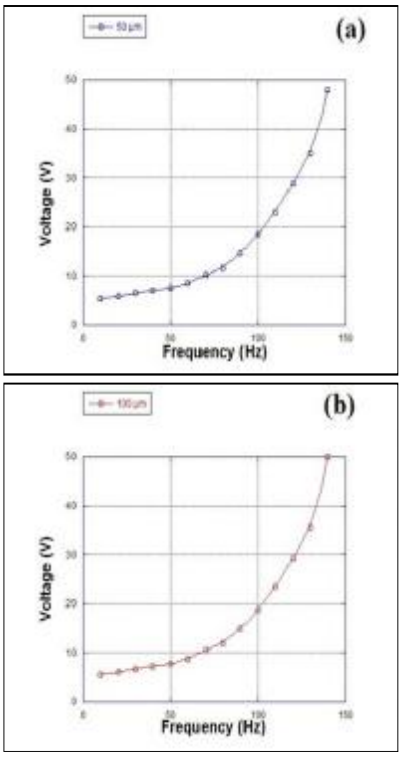

Figure 2. Phase diagram of V-f for sample of: (a) 50µm of thickness, (b) 100µm of thickness

Figure 2 shows a dependency between the threshold voltage and frequency when SMT pattern emerged. It can be concluded that the higher the frequency induced, the higher the threshold voltage as SMT patterns appears on the homeotropic MBBA sample. The threshold voltage increases along with the increasing of frequency, and become infinite when getting near to the critical frequency due to the sharp rise on the frequency. Thus, it formed a graph of the voltage-frequency relationship which is nonlinear. The threshold voltage for both samples, tend to be on a similar values. This indicates that the thickness of the samples does not affect the threshold voltage of SMT.

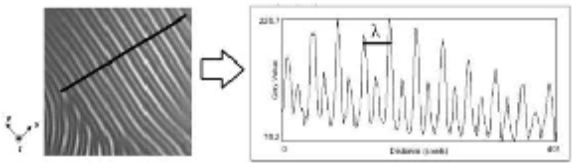

Figure 3. Plot profile application on SMT pattern (f = 130 Hz, d = 100µm)

The wavelength (λ) is the periodicity, i.e. the length of that part of the pattern which is

repeated. The pattern formation emerged on the samples showed a regular dark and bright lines. The wavelength can be defined as the distance between two intensive bright lines (holding one less intensive–weak bright line) that appears on the convective pattern, as shown in Figure 3. The wavelength of convective patterns in NLC can be observed by image processing.

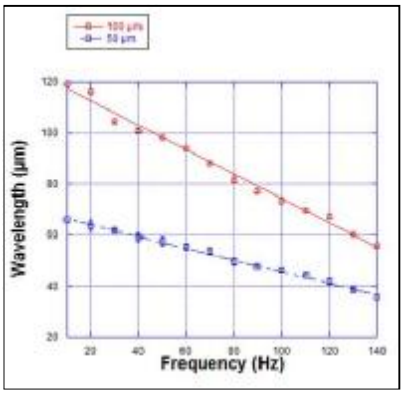

Figure 4. Dependency of SMT's wavelength as function of frequency

Using image processing with *ImageJ* software through plot profile draw tool, the wavelength of the SMT convective pattern (λ_{SMT}) at each frequency induced into the samples obtained. Figure 4 shows relationship between the frequency and the wavelength. It shows that the wavelength of SMT pattern on the sample 100μm of thickness is wider than the wavelength of the 50μm one. Hence, the SMT convective pattern has the wavelength which is proportional to the thickness of NLC layer. Both wavelengths were in the same order as sample's thickness. It also shows that the SMT's wavelength was decreased linearly to the applied frequency. The higher the frequency induced into samples, the smaller the wavelength of the SMT's patterns is.

IV. Conclusion

Convective patterns of soft-mode turbulence (SMT) with normal rolls (NR) type in MBBA homeotropic NLC sample is observed when the sample is induced the frequency and the electric field exceeds the threshold voltage, V_{SMT}. The higher the frequency-voltage applied into samples, the higher the threshold voltage which shown in the phase diagram of the voltage-frequency that is nonlinear. At the same frequency, the sample's thickness has no effect on threshold voltage. The relationship between the frequency and the SMT's wavelength is linear. It means that when the frequency induced is higher, the wavelength gets smaller and the wavelength is of the order of the cell thickness.

V. Acknowledgment

We would like to express our gratitude to Dr. Rinto Anugraha for his guidance on image processing process of pattern formation images and valuable discussions.

VI. References

1. Chandrasekhar, S., *Liquid Crystal,* Clarendon Press, Oxford, 1992.
2. de Gennes, P. G., and Prost, J., *The physics of Liquid Crystal*, Clarendon Press, Oxford, 1993.
3. Yusuf, Y., Prewavy Instabilities in Nematic Liquid Crystal, *Thesis*, Faculty of Engineering, Kyushu University, Fukuoka, 2002.
4. Huh, J-H., Hidaka Y., and Kai S., *Journal of the Physical Society of Japan*, 6, 67, 1948 (1998).
5. Hidaka, Y., and Kai, S., *Forma*, 24, 123 (2009).
6. Anugraha, R., New Type of Order-Disorder Transition in Soft-Mode Turbulence of Electroconvection in Nematics, *Dissertation*, Faculty of Engineering, Kyushu University, Fukuoka, 2008.
7. Buka, A., Eber, N., and Pesch, W., *Electronic-Liquid Crystal Communications*, (2005).

The Influence of Co-content on Coated Carbon Steel to Improve the Oxidation and Hardness Properties

Fredina Destyorini[1*], Eni Sugiarti[2], Kemas A. Zaini Thosin[3]
1,2,3 Research Center for Physics, Indonesian Institute of Sciences (LIPI)
Puspiptek Serpong Tangerang Banten – Indonesia 15418
Email : fredina_destyorini@yahoo.com [1]
eni_ayumi@yahoo.com [2]
zaini.th@gmail.com [3]

Abstract
Low carbon steel is one of the metal material which is widely used as construction material. However, this material has low corrosion resistance. Therefore, it is necessary to improve the corrosion resistance of material, one of which is to provide protection layer on the surface of low carbon steel by high corrosion resistance metal alloy. The study conducts a low carbon steel surface coated by NiCoCrAl material. NiCo layer is deposited on low carbon steel surface by using electroplating techniques, meanwhile Cr and Al use the pack-cementation. This study used variation on the concentration of Co, respectively 1% and 5% to observe the influence of the amount of Co on oxidation resistance at high temperature and hardness. The oxidation resistance was evaluated by weight gains during high temperature oxidation test at 800°C for 150 hours. Hardness was calculated by Vickers hardness test, whereas the microstructure before and after oxidation test was observed by SEM-EDX. The result indicated that FeNi(5%)CoCrAl sample show lower weight gain at 800°C than FeNi(1%)CoCrAl. Vickers hardness test result was known that the concentration of Co also affect the hardness of the layer system.
Keywords : *electroplating, pack-cementation, oxidation resistance, hardness.*

* Corresponding author.
E-mail address: fredina_destyorini@yahoo.com

I. Introduction

Carbon steels are the most commonly used materials in various industrial fields because of their availability, low cost, ease of fabrication, and high strength [1]. One example in the geothermal industry piping systems mostly uses pipes made of carbon steel material. The pipes distribute the high temperature gas to reach ± 200°C. pipes corroded easily, since the carbon steel material has limitation when it is applied in high temperature environments. Therefore it is necessary to protect the carbon steel at high temperature level, such as coating using MCrAlY alloy (M = Ni and / or Co). This alloy is a kind of material which has high corrosion and oxidation resistance [2]. NiCoCrAl alloys are extensively used as alloy compositions, e.g. for the manufacturing of corrosion-protective coatings to be applied on superalloy components [3].

Some research on MCrAl alloy coating technique is relatively complex and expensive. In general, this alloy is coated with thermal spray techniques, HVOF [4], VPS, etc. In this study, NiCoCrAl deposited onto the carbon steel surface using a simple technique, electroplating and pack cementation. The general objective of this study is to improve the oxidation resistance and the hardness of carbon steel with deposition of NiCoCrAl, while the particular aim is to study the effects of cobalt content on the oxidation resistance and the hardness of carbon steel alloy coated by NiCoCrAl.

II. Experimental Procedure

NiCo electroplating on carbon steels substrate was carried out by varying the concentration of Cobalt, they were 1% and 5%. Composition of the electrolyte solution bath were composed of: (5% NiCo) 313.5 g/L $NiSO_4.7H_2O$, 16.5 g/L $CoSO_4.6H_2O$, 45 g/L $NiCl_2.6H_2O$, 40 g/L H_3BO_3 and (1% NiCo) 326.7 g/L $NiSO_4.7H_2O$, 3.3 g/L $CoSO_4.6H_2O$, 45 g/L $NiCl_2.6H_2O$, 40 g/L H_3BO_3. All reagents dissolved in distilled water and adjusted the pH in the range 3.6 - 3.8. Experimental set-up for the electroplating process consists of an electrolyte in the beaker sea of glass, carbon steel substrate as a cathode and nickel as the anode. Anode was mounted on both sides of the glass beaker wall, while the cathode is located in between. Before the deposition process of Ni-Co, the cathode was coated with a solution of

Ni-strike for 30 seconds. Electrolyte temperature is maintained at a temperature of 50°C with a thermostatic bath, and the process is done with magnetic agitation stirrer. Ni-Co deposition time lasted for 120 minutes with a constant current density of 20 mA/cm^2. After the electroplating process, the cathode washed with distilled water, dried, and weighed. Ni-Co electroplating process is equipped with a stage of heat treatment at temperatures of 800^{o}C for 5 hours.

The chromizing pack mixture is composed of 30 wt % Cr powder, 10 wt % NH_4Cl and 60 wt % Al_2O_3 powder as an inert filler. Whereas, aluminizing pack mixture composed of 24 wt % Al powder, 5 wt % NH_4Cl and 71 wt % Al_2O_3 powder as an inert filler. The substrate sample was embedded in the pack mixture in an alumina crucible positioned in horizontal quartz reactor under an argon atmosphere to avoid the oxidation of the underlaying materials during the process. Pack chromizing and aluminizing was done in resistance heated tube at 800 °C for 10 h and 20 minute respectively.

The isothermal oxidation test were performed in an electrical resistance furnace at 800 °C in dry air with cyclic oxidation up to 150 h. After isothermal oxidation, the speciment is placed out of the furnace in room temperature, cleaned ultrasonically in distillated water to remove unexpected material then it is weighted. The hardness of the coated carbon steels was measured on a Vickers' microhardness instrument at an applied load of 200 gF for 10 seconds. Five measurements were conducted on each sample and the results were averaged. The morphologies of coatings were observed using a scanning electron microscope (JEOL JSM-6390A) and the chemical composition of coatings was determined using an energy dispersive spectrometer (EDS) coupled with the SEM.

III. Results and Discussion

Fig. 1 presented microhardness of Ni–Co alloys as a function of Co content in alloys that conducted by Wang et al [5]. It is clearly that microhardness of Ni–Co alloys increased initially with Co content varying from 0 to approximately 49 wt.%, and then gradually decreased as Co content increased further above 49 wt.%. The explanation to this gradual reduction of microhardness is the gradual increase of grain size with the increase of Co content in Co-rich alloys [5]. These results are the basis for the present study to obtain the optimum composition of NiCoCrAl alloy. In the present study would be further investigated to determine whether the small addition of Co concentration can improve the oxidation resistance and hardness on coated carbon steel.

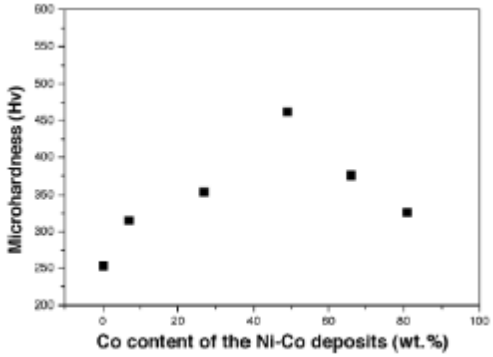

FIGURE 1. Microhardness as function of Co-content [5]

Fig.2 and **Fig.3** shows respectively the cross-sectional microstructure and elements concentration profile of FeNi(1%)CoCrAl and FeNi(5%)CoCrAl coatings on Fe substrat. As shown in **Fig 2**, the coating systems formed 4 zones: zone 1 is NiCo layer with a thickness of ±30µm containing (96-89 at%) Ni and (2.2 to 1.5 at%) Co, zone 2 with a thickness of ±19µm is an intermetallic zone. This zone has a concentration of Ni and Al elements are more stable in the amount (47-46 at%)Ni and (51-50 at%)Al, zone 3 that has a structure with dark spots scattered along the layers, this zone contains higher Al (66-54 at%)Al and (41-26 at%)Ni, zone 4 with a thickness of ± 22µm is an intermetallic zone of AlCr containing (73-74 at%)Al and (15-16 at%)Cr. While the microstructure of the coating system FeNi(5%)CoCrAl as shown in **Fig.3**, consists zone 1 (NiCo layer) containing (90-86 at%)Ni and (10-8 at%)Co, zone 2 (intermetallic zone) with the concentrations of Ni and Al elements are more stable in the amount (50-45 at%)Ni and (46-43 at%)Al, zone 3 which has a structure with dark spots scattered throughout most of the layer containing the higher amount of Al (53-49 at %) and (42-15 at%)Ni, zone 4 (AlCr intermetallic zone) contains (66-64 at %)Al and (20-18 at%)Cr. From these results shows that differences of Co content in the electroplating process affects the number of Co element in the coating systems. In the FeNi(1%)CoCrAl sample, Co element concentration was only detected at 2.2 to 1.5 at%, while in the FeNi(5%)CoCrAl sample Co element was detected reaching 10-8 at%.

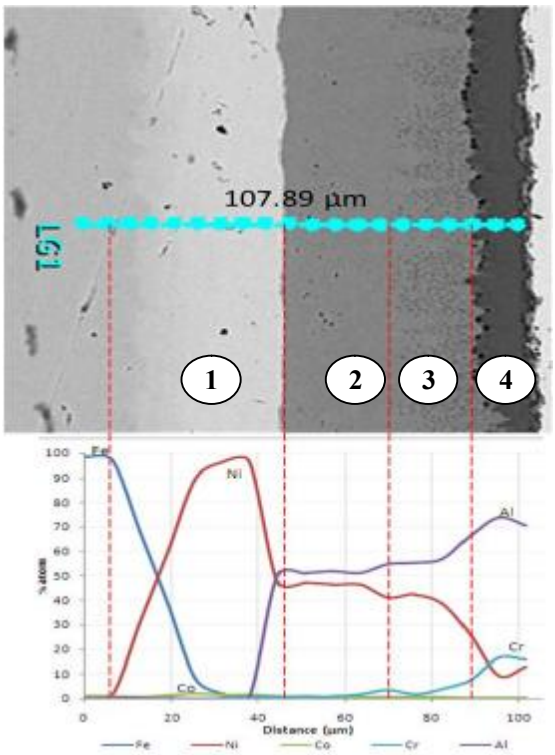

FIGURE 2. Cross-sectional microstructure and EDS concentration profile of FeNi-1%CoCrAl

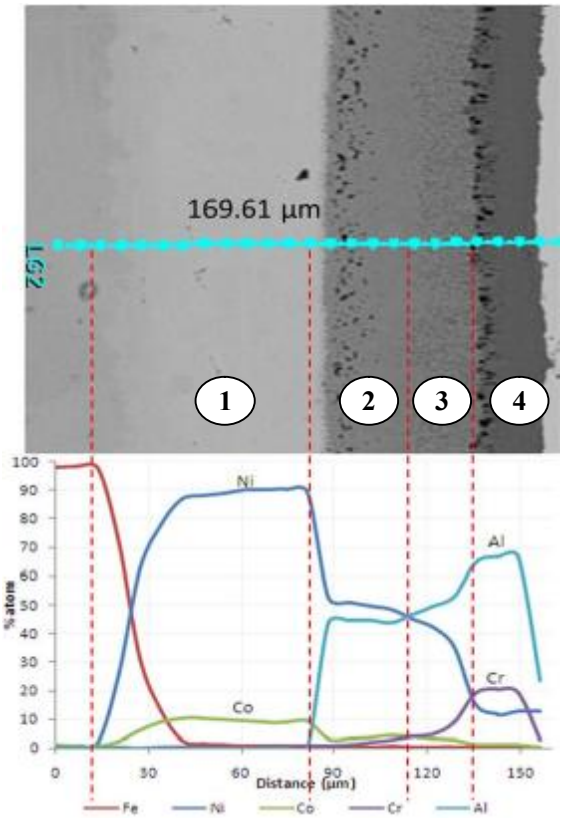

FIGURE 3. Cross-sectional microstructure and EDS concentration profile of FeNi-5%CoCrAl

Fig.4 shows the result of cyclic oxidation test (at 800°C in air) of FeNi(1%)CoCrAl and FeNi(5%)CoCrAl sample. As shown in this figure, FeNi(5%)CoCrAl sample has a better oxidation resistance compared to FeNi(1%)CoCrAl sample. This is evident from the rate of increase in mass gain of FeNi(5%)CoCrAl is lower than FeNi(1%)CoCrAl sample at 150 hours oxidation test at 800°C in air. From these results it can be concluded that the Co content have an influence on the increasing in oxidation resistance of NiCoCrAl coating system.

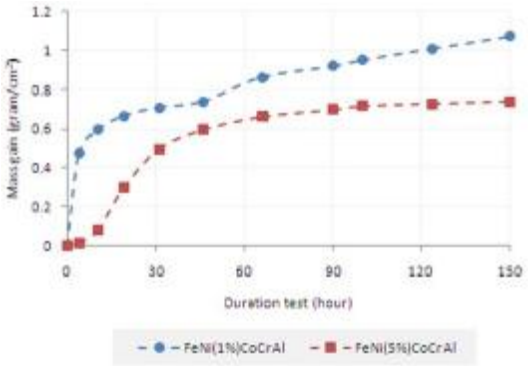

FIGURE 4. Oxidation kinetics of specimens in air at 800°C

Fig.5 and **Fig.6** shows respectively the cross-section micrograph and concentration profile after cyclic oxidation test at 800°C on FeNi(1%)CoCrAl and FeNi(5%)CoCrAl samples. From the concentration profile data on the FeNi(1%)CoCrAl sample shown that oxygen diffuse into the coating system and interact with the elements Al, Cr, and Ni to form oxide on the top layer. The depth of diffusion of oxygen into the NiCoCrAl coating system reach ± 36µm from the surface. While the diffusion of oxygen in the FeNi(5%)CoCrAl sample only reached a depth of ± 8µm from the surface and interacts with the elements Al, Cr, Ni, and Co to form oxides. Cobalt is also detected diffuse outward into the top layer. From the EDS data of the two samples shows that the top layer is expected only formed thermally growing oxide (TGO) Al_2O_3, but it also formed chromia oxide, nickel oxide and even cobalt oxide (need confirmation with XRD analysis).

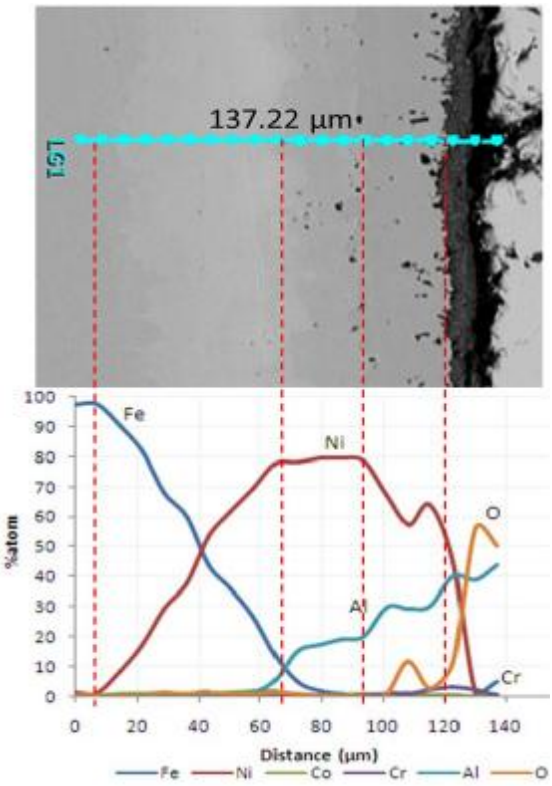

FIGURE 5. Cross-sectional microstructure and EDS concentration profile of Ni-1%CoCrAl after oxidation test 100h

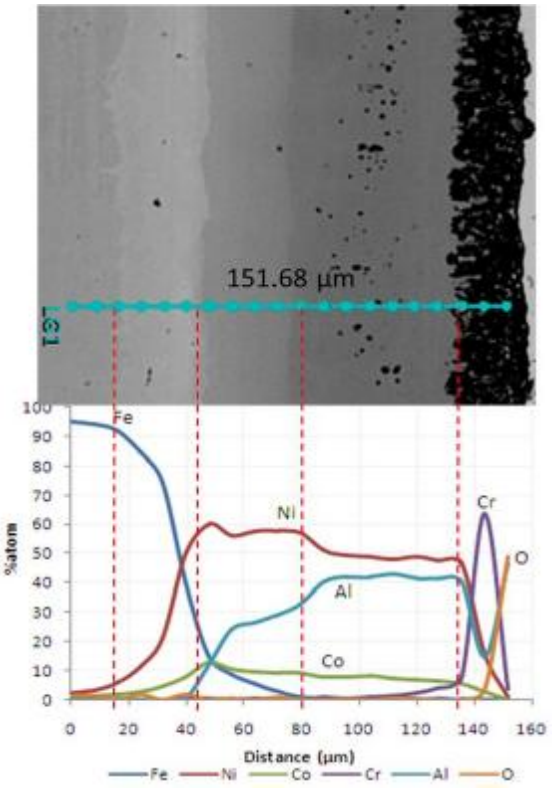

FIGURE 6. Cross-sectional microstructure and EDS concentration profile of Ni-5%CoCrAl after oxidation test 100h

Fig.7 shows the micohardness of Fe substrat, Ni(1%)CoCrAl and Ni(5%)CoCrAl samples. From these results shows that the addition of Co content from 1% to 5% in the NiCoCrAl coating systems can increase hardness value from 810,24 HVN to 1026,96 HVN. And the hardness values of these coated samples are higher 8 times and 10 times than the uncoated Fe substrate. It can be concluded that the Co content affect to increase hardness value of NiCoCrAl coating system.

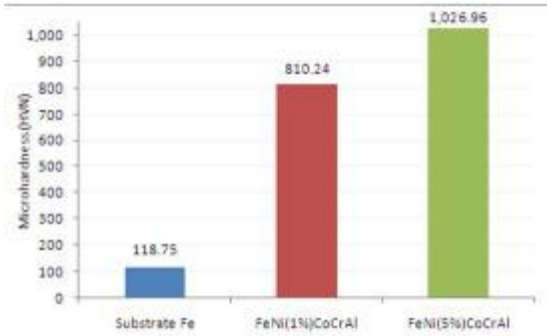

FIGURE 7. Microhardness of specimens

IV. Conclusion

From this study it can be concluded that:

1. NiCoCrAl-coatings can be obtained by the electroplating and pack-cementation process.
2. The addition of Co content in the NiCoCrAl coating system can improve the oxidation resistance of this coating system in air at 800°C.
3. Microhardness of NiCoCrAl coating system increased initially with Co content increasing from 1% to 5%.
4. Deposition of NiCoCrAl layer can improve oxidation resistance and hardness of carbon steel.

V. References

1. Osarolube, E., Owate, I. O. and Oforka, N. C., Scientific Research and Essay Vol.3 (6), pp. 224-228 (2008).
2. R. Streiff, Journal De Physique IV Colloque C9. Volume 3, Page 17-41 (1993).
3. K. Fritscher, Journal of Crystal Growth 250 (2003) 546–557.
4. A. Fossati, M. D. Ferdinando, A. Lavacchi, A. Scrivani, C. Giolli and U. Bardi, *Coatings*, *1*, 3-16 (2011).
5. L. Wanga, Y. Gaoa, Q. Xuea, H. Liua, T. Xu, Applied Surface Science 242 (2005) 326–332.

Ab initio Study of Surface Interaction Between Polypyrrole and Leucine in Water Environment

Hanifadinna[1], **Irma Syafitri, Nugraha, Hermawan K. Dipojono**
Laboratory of Computational Material Design and Quantum Engineering,
Engineering Physics Research Group, Faculty of Industrial Technology,
Institut Teknologi Bandung, Jl. Ganesha 10, Bandung 40132, Indonesia

Abstract

Adsorption based amino acids leucine on the surface of polypyrrole (Ppy) in water environment have been studied with B3LYP density functional method using 6-31G(d,p) basis set. This represents a simple model relevant to immobilization and transduction of bimolecule for biosensor application. The energy of the Ppy doped with amino acids is minimized with respect to the orientation and distance of the amino acids to the Ppy. Neutral leucine carboxyl in water environment has adsorption energy 0.25 eV at optimum distance of 2.87 *Å* from the surface of Ppy. This adsorption process for this amino acid shall proceed easily because the activation barier is either absent or very small. Hence amino acids leucine could easily be immobilized on Ppy surface in the water environment..

Keywords : *Adsorption, polypyrrole, leucine, density functional theory.*

1 Introduction

The development of fast and highly sensitive biosensors become a crusial step to recognize and control the global outbreaks of virus and infectious deseases in recent years. Conducting polymers have unique properties which make them getting attention for spesific materials currently applied for the fabrication of biosensors [1].

Polypyrrole based conducting polymers have very attractive characteristic due to its various special electrical properties which are highly recomended for the future generation of biomaterial transducer [2]. The special electrical properties of polypyrrole as a conducting polymers is originated from the fact that polypyrrole can be synthesized to have conductivity value up to 1000 S/cm which approaches the conductivity of metal[3]. Mainly because of the best of biocompatibility and the ease of immobilization, polypyrrole has been the most extensively investigated and widely used material for biosensors and immunosensors[4]

In the development of biosensors, the immobilization between surface interface of biomolecules and transducer material plays as a crucial factor to maintain the stabilization of biological system[5] thus enchanching the operational and storage ability of biosensor.

We focus our study on leucine as immobilized biomolecule into the polypyrrole surfaces. It is known that Leucine has a simple structure of essential amino acid and plays a role in muscles growth and body composition[6]. Therefore, study about leucine is a good starting point to learn deeper about biomolecules immobilization.

Recently, from our previous study of polypyrrole-leucine in gas phase, it shown that neutral leucine has greater adsorption energy (0.25 eV) with optimum distance 2.2 *Å* from the surface of polypyrrole.

However, in order to mimick a real biological system, water environment is more appropriate than gas phase condition. Hence further investigation on surface interaction between leucine and polypyrrole is an urgent issue for biosensor application.

2 Computational Detail

In this report, we considered neutral form of leucine as an immobilized biomolecule on the top of polypyrrole surface. As a first step we performed structural optimization of leucine and polypyrrole in water environment with the use of Osanger model[11] at B3LYP/6-31G(d,p)[10] level to place the solute in 15 *Å* dipole water. These optimized structure then used for single point energy calculation (SCF). The orientation and position of polypyrrole and leucine are shown in Figure 1

The immobilization process should occur in the presence of common functional groups, including amines, thiols, carboxylic acids, and alcohols [7]. Roman et al [8]observed that the carboxyl ends with its dipolar nature promoted the adsorption of the molecule to the amino acid by small charge transfer. We limited the calculations to the neutral leucine form with the distance 3.17 *Å* from the surface of polypyrole surface with the carboxyl groups (COOH) approach directly to the surface of polypyrrole.

[1] Corresponding author:
hanifadinna@gmail.com (Hanifadinna)
dipojono@tf.itb.ac.id (HK. Dipojono)

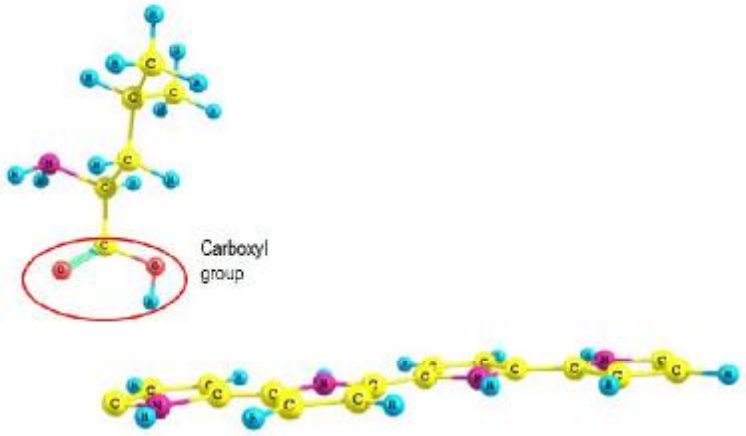

Figure 1: Computational model of neutral leucine-carboxyl side on top of Polypyrrole surface (in Hartee)

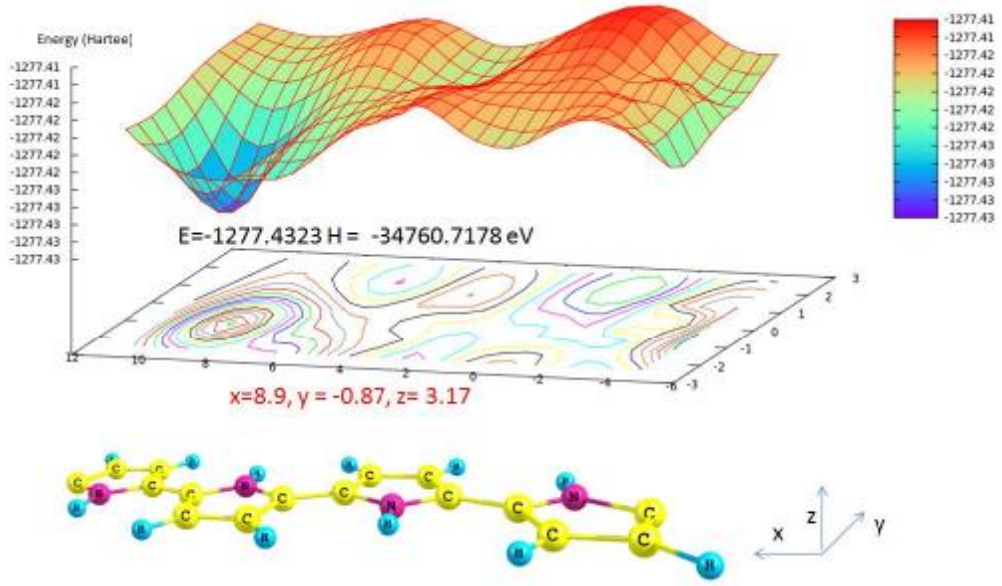

Figure 2: PES and Contour Map of leucine-carboxyl side on the top of Polypyrrole surface

To find the optimum adsorption site of polypyrrole, we scanned over the polypyrole surface with neutral leucine form to determine the minimum potential energy surface of polypyrrole. Figure 1 shows the observation area of PES evaluated with 0.1 $\AA$ resolution. Figure 2 shows the countour maps and PES correspond to polypyrrole surface. The minimum energy of this configuration was used to calculate the adsorption energy. All calculation in this work were carried out using GAUSSIAN 03 software package[9, 10].

3 Result and Discussion

The active site of polypyrrole is searched potential energy surface (PES) (see Figure 2). The PES is calculated by scanning the total energy over 15.5 $\AA$ x 5 $\AA$ on top of polypyrrole area with 0.1 $\AA$ at a heigh 3.17 $\AA$.

The adsorption energy $E_{ads} = E_{tot} - (E_{ppy} + E_{leu})$, where E_{tot} correspond to the energy of the total system from PES calculation , E_{ppy} is the total energy of the isolated polypyrrole, and E_{leu} is the total energy of the isolated leucine.

Leucine through the carboxyl group in water environment

is attracted to the polypyyrole surface with $E_{ads} = 0.47$ eV at optimum distance 2.87 $\AA$. On Comparing with our previous results [12] it is observed that neutral leucine in the gas phase is attracted to the polypyrole surfaces through the carboxyl group (E_{ad} = 0.25 eV at 2.2 eV optimum distance). In other word, leucine is more difficult to be immobilized in water environment than in gas one; leucine is unfavourably interacting with water. [13].

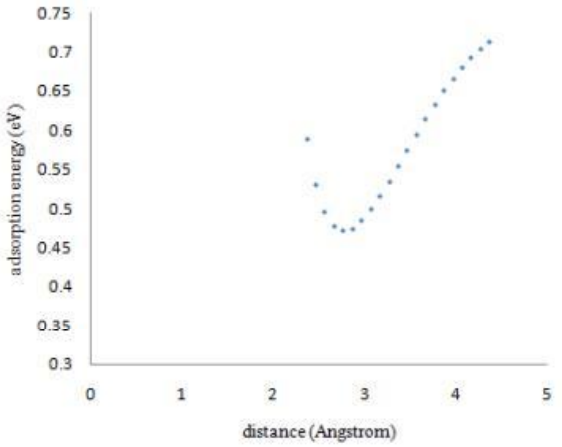

Figure 3: adsorption energy of neutral leucine trough the carboxyl end

It also observed that leucine in water environment is trying to find it's stable configuration in zwitterionic form. The observations are supported by the fact that most of conformational search gave to a tendency of zwitterionic form.

4 Conclusion

We have investigated the effect of water environment to the surface interaction between neutral amino acid leucine and polypyrrole surface. In water environment, neutral leucine have a tendency to shift it's configuration to the stable of zwitterionic with E_{ads}= 0.47 eV at optimum distance 2.87 $\AA$. The result indicates that in water environment zwiterionic of leucine is more favorable than it's neutral form. Hence leucine in zintterionic is more appropriate than in the neutral form for biosensor applications.

5 Acknowledgement

This work is partially supported by Asahi Glass Foundation. HKD would also like to acknowledge the financial support from the Ministry of Research and Technology through Incentive Research Grant.

References

[1] K. Arshak, V. Velusamy, O. Korostynska, K. Oliwa-Stasiak, and C. Adley. 2009. IEEE Sensor Journal Vol. 9, No. 12.

[2] D. D Ateh, H. A. Navsaria and P. Vadgama. 2006. J. R Soc. Interface 3, 741-752. (doi: 10.1098/rsif2006.0141).

[3] S. Sangawar, and N. A Moharil. 2012. . Chem Sci Trans 1(2), 447-455.

[4] A.Ramanavicius , A. Ramanaviciene and A. Malinauskas. .2006. Electrochim Acta 51:60256037.

[5] Lan Bui. 2009. Thesis. Division of Chemistry, Department of Physics, Chemistry and Biology Linkpings universitet, SE-581 83 Linkping, Sweden.

[6] Jacob Wilson .2006. Journal of HYPERPLASIA.

[7] Marco Mascini. 2004. Immobilization of Biomolecules. Grenoble.

[8] T. Roman, W.A. Dino, H. Nakanishi1 , and H. Kasai .2005. Eur. Phys. J. D 38, 117120. DOI: 10.1140/epjd/e2006-00043-1.

[9] P. Hohenberg and W. Kohn. 1964. Phys. Rev. 136. B864

[10] M. J. Frisch et al. 2004. Gaussian 03, Revision D.02. Gaussian, Inc.,Wallingford, CT.

[11] L. Onsager. 1936. J. Am. Chem. Soc., 58, 1486-93.

[12] Hermawan K. Dipojono, Irma Syafitri, Nugraha, Nuryanti, Adhitya G. Saputro .2011. ITB Journal of Science.

[13] Kyoko Kobayashi, Noriyuki Yonezawa, Ryoichi Katakai. .1995. 28(24), pp 8242-8246 DOI: 10.1021/ma00128A038

Effect of Ti-dopant and sinter temperature of $LiFe_{1-x}Ti_xPO_4$ as cathode material for lithium battery on its conductivity

Joko Triwibowo[1*], Desty Anggita Tunggadewi [2], Etty Martiwigayati [1], Kuwat Triyana [2]

1 Research Center for Physics – LIPI,
Kawasan PUSPIPTEK Serpong, Tangerang Selatan 15314
2 Department of Physics, Faculty of Mathematics and Natural Sciences, Gadjah Mada University,
Sekip Utara PO BOX BLS.21 Yogyakarta 55281

Abstract

LiFePO4 is widely used as cathode material for secondary lithium battery. This material is abundant, environmental friendly and theoretically has a high specific capacity as 170mAh/g. The only drawback of this material is its low electronic conductivity, i.e. ca. 10^{-9} S/cm. Low electronic and ionic conductivity limits the specific capacity of the cell practically. In order to reach the high specific capacity one should increase the electronic conductivity and ionic conductivity as well. In this research LiFePO4 powder is synthesized by means of sol-gel method. The sinter temperature is varied from 700, 800 to 900^oC. Certain sinter temperature will affect the microstructure which has an effect on the electronic conductivity. Varied wt% of Ti is added to form $LiFe_{1-x}Ti_xPO_4$. Element Ti is used as a dopant to create some defects in the crystal $LiFe_{1-x}Ti_xPO_4$, so that the ionic conductivity will increase. The obtained phase is observed through XRD-pattern. The morphology of the powder is observed by SEM. The electric conductivity of the sample is further determined by Electrochemical Impedance Spectroscopy (EIS) test. The result shows that the conductivity is decreased by increasing the sinter temperature or by increasing the Ti addition. The highest conductivity is obtained by the sample with the sinter temperature of 700 ^oC and 2wt% Ti addition, i.e. 8.5 10^{-8}S/cm.

Keywords: *Electronic conductivity, Ionic conductivity, Specific Capacity,*

* Corresponding author.
E-mail address: joko011@lipi.go.id

I. Introduction

Nowadays portable electric devices such as cellular phone, game consoles, laptops etc are widely used. Most of them use the secondary lithium battery as the electric source. Compared to the conventional secondary battery, lithium battery has a longer cycle life and lighter in weight. Olivine LiFePO4 is one of the cathode materials for secondary lithium battery. This material is abundant, environmental friendly and has a theoretical specific capacity as 170mAh/g. Unfortunately, this material has a poor rate capability which has been attributed to low electronic conductivity prevents its use in high-power application [1, 2]. Improvements in rate capability have been achieved and reported. It included the using of nano particle, application of carbon coating on cathode material, micro structure controlling and doping with a conducting metal ion [3, 4]. Synthesis of cathode material can be done by some methods, such as solid state [5], hydrothermal [6], co-precipitation [7] and sol-gel route [8, 9]. Due to the advantage of forming uniform distribution and porous structure, sol-gel route is taken to this experiment. The effect of varied sinter temperature and weight percentage of Ti-dopant on the conductivity of obtained cathode material is observed. X-ray diffraction (XRD) is used to characterize obtained phase. Microstructure and the morphology of the material are observed by SEM/EDS. The conductivity of the sample is tested by Electrochemical Impedance Spectroscopy (EIS).

II. Experimental

Sample synthesis

LiFePO4 was synthesized from a stoichiometric mixture of reagent grade Li2CO3 (Merck), FeC2O4.2H2O (Kanto), NH4.H2PO4 (Kanto), Citric acid (Aldrich) and distilled water by sol-gel

reaction method. As precursors, FeC2O4.2H2O and the mixture of Li2CO3 and NH4.H2PO4 were dissolved in the distilled water separately and then mixed together. Citric acid and PEG (molecular weight of 400) were added into the mixed solution slowly with moderate stirring and heated to 80°C until the gel was formed. The resulting gel precursor was dried in an air oven at 100°C for 24h. After grinding of this dry precursor, the precursor was decomposed at 320°C for 10h in flowing nitrogen gas. Obtained powder was added with TiO2 to get 0, 2 and 4 wt% Ti as a substitute element for Fe in $LiFe_{1-x}Ti_xPO_4$. This mixed powder was wet ball milled for 24h and sintered for 12h at 700, 800 and 900°C in flowing nitrogen gas. Samples with 2wt% Ti that were sintered at 700, 800 and 900°C were marked as sample (A), (B) and (C) respectively. Samples with 0 and 4wt% Ti that sintered at 700°C were marked as sample (D) and (E) respectively.

Characterization

X-ray powder diffraction (XRD) characterization was performed on Shimazu equipment to analyze obtained phase(s) after sinter process. Microstructure and the morphology of the samples were observed by SEM equipment from Zeiss Bruker. Conductivity of the samples was tested on HIOKI LCR Meter 3532-50. Sample was in the form of composite pellet. Sample contained active material as filler and PVdF as matrix with the composition of filler : matrix = 75:25. Electrochemical impedance spectroscopy measurement was carried out by applying alternating voltage in the frequency range of 1Hz to 100kHz with amplitude of 5mV.

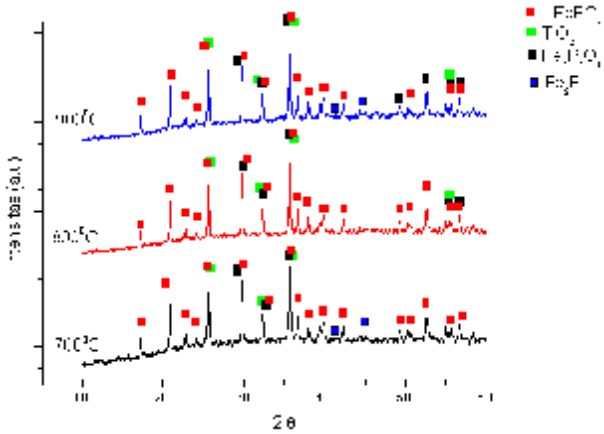

Fig. 1 XRD pattern of samples with 2wt% Ti, synthesized at varied sinter temperature 700 (A), 800 (B) and 900°C (C).

III. Results and discussion

XRD analysis

X-ray diffraction patterns of $LiFe_{1-x}Ti_xPO_4$ with addition of 2wt% Ti are shown in Fig. 1. Samples were synthesized by varied sinter temperatures, i.e. 700, 800 and 900°C, there were sample (A), (B) and (C) respectively. Some diffraction peaks can be attributed to $LiFePO_4$. It refers to JCPDS 40-1499 for ordered olivine structure indexed by orthorhombic. Other diffraction peaks are attributed to the following phases: TiO_2, Fe_2P and $Fe_2P_2O_7$. Through GSAS analysis of XRD-pattern, it was found that the obtained phases were $LiFe_{0,95}Ti_{0,05}PO_4$ (sample A) and $LiFe_{0,96}Ti_{0,04}PO_4$ (sample B and C).

Fig. 2 shows diffraction patterns sample (A) and (D). Sample (D) was also multi phases, similar with other mentioned samples. The grain size D was calculated using the Scherrer's equation: $\beta \cos(\theta) = \kappa\lambda/D$, where β is the full-width at half-maximum length of the diffraction peak on a 2θ scale and κ is a constant (0.9). From the Scherrer's equation, D values for sample (A), (B), (C), and (D) were 100.04, 109.17, 130.63, 96.53nm. These values implied that the grain size is bigger when the sample was added with Ti element or sintered at higher temperature.

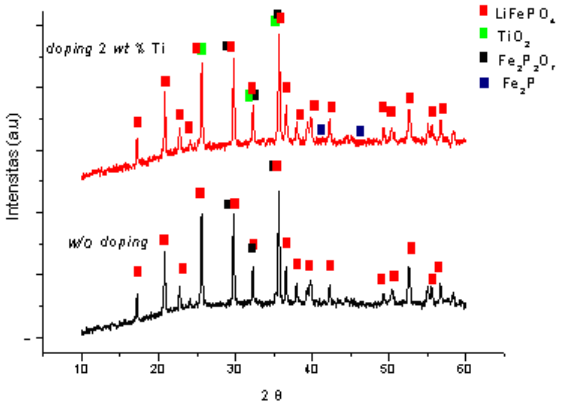

Fig. 2 XRD pattern of samples with 0 (D) and 4 wt% Ti (E), synthesized at 700°C

Morphology

SEM images of samples are putted in Fig. 3 and Fig. 4. Fig. 3 showed samples that had been synthesized at varied sinter temperatures. Sample (A) exhibited small and globular powders. Sample (B) and (C) both showed the agglomeration of the powders. Sample (A) and (B) showed more uniform structure than structure from sample (C).

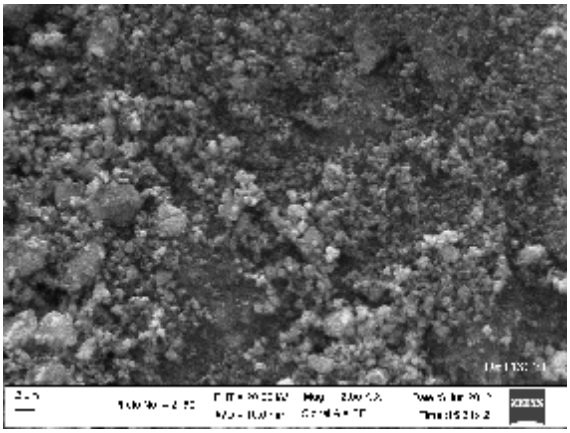

(A)

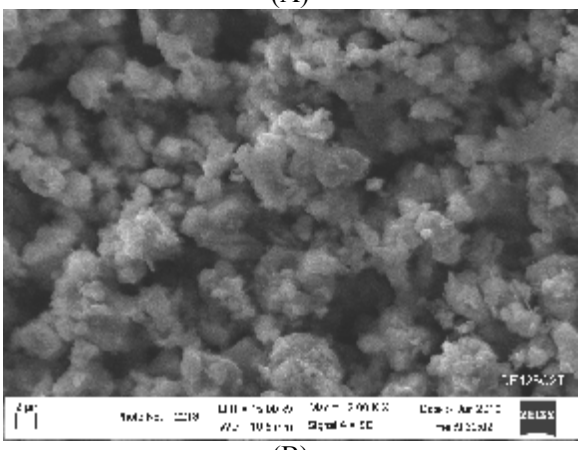

(B)

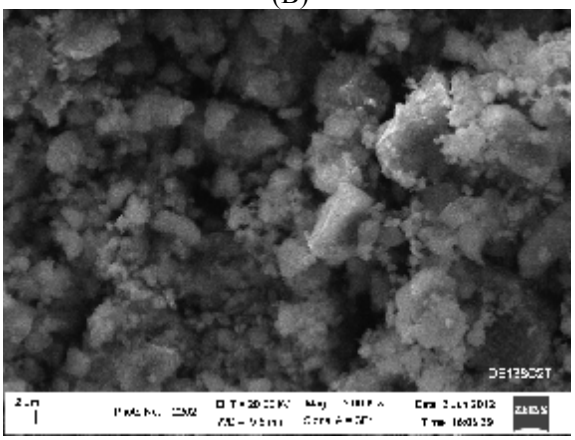

(C)

Fig. 3 SEM micrographs of samples with 2wt% Ti synthesized at varied sinter temperature 700 (A), 800 (B) and 900°C (C).

Compared to sample (B) and (C), sample (A) has the smallest particle size. It could create a better contact surface with the liquid electrolyte or the current collector. It could also reduce the diffusion path of lithium ion the bulk. Sample (B) exhibits more connected particles and regular microstructure than sample (C).

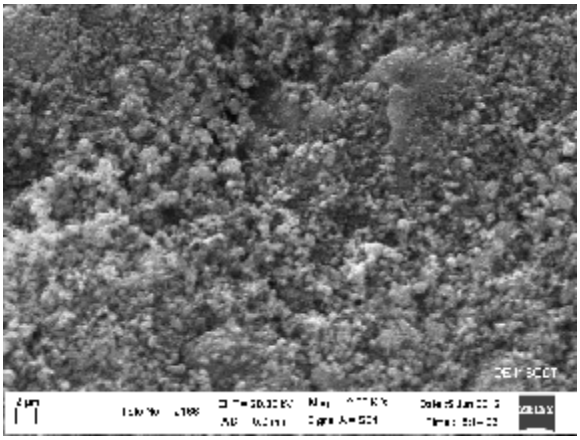

(D)

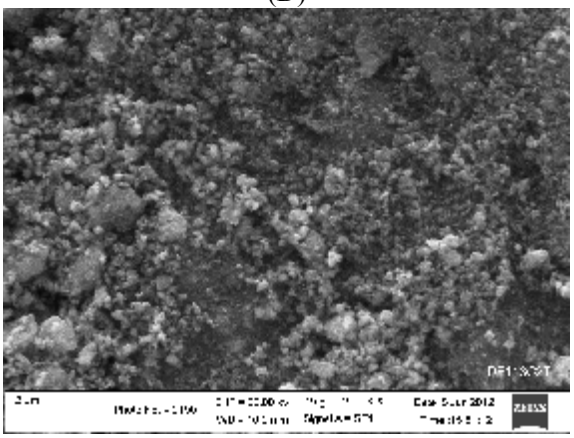

(A)

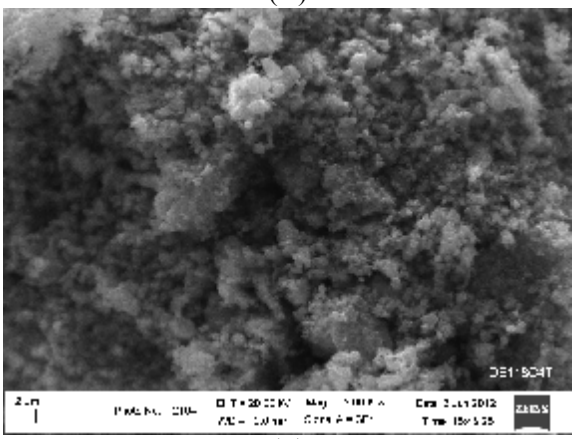

(E)

Fig. 4 SEM micrographs of samples with 0 (D), 2 (A) and 4 wt% Ti (E) synthesized at 700°C.

In Fig. 4 sample (D) showed smaller globular powders than that from sample (A) and (E). Sample (D) showed individual globular particle yet, while sample (A) and (E) seem to begin to agglomerate with the neighbor particles. But the globular form of the original individual particles is still recognized. In general the powder particle size increased with increasing the sinter temperature or the dopant content.

Conductivity analysis

The conductivity of the electrode material as a function of the sinter temperature is shown at Fig. 5. This figure exhibited the conductivity decrease with the increasing sinter temperature. It was caused probably by the grain growth of the particles. Higher temperature made consolidation among the small particles possible. Small particles tend to agglomerate each other and created a bigger particle. Electron that previously moved through the grain boundaries of the small grain size had to follow the new grain boundary of the bigger grain size. Due to the grain growth mechanism, the "electron path" is now longer. It decreased the conductivity of the material. Conductivity of sample (B) and (C) are practically similar, i.e. 3.45 and 3.81 10^{-9}S/cm respectively.

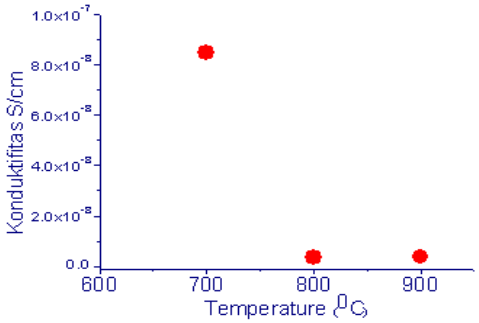

Fig. 5 Conductivity as a function of sinter temperature of the sample A, B and C

Fig. 6 showed the conductivity of the samples as a function of the dopant content. Addition of Ti-element increased the conductivity slightly, i.e. from 3.80 to 8.50 10^{-9}S/cm. It is caused probably by the defects forming in the crystal structure. It may keep the grain size small.

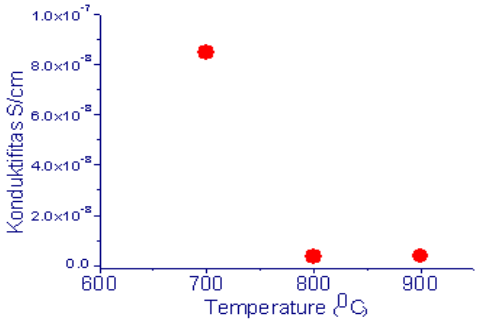

Fig. 5 Conductivity as a function of sinter temperature of the sample A, B and C

Continuing addition of Ti-element more than 2wt% decreased the conductivity abruptly. It indicated that the maximum Ti-addition that could be still adopted by LiFePO4 structure was 2wt% Ti. The rest of Ti-addition will probably create new phase that had a lower conductivity than that of the pure LiFePO4. It also could stimulate the small particles to agglomerate. Bigger size particle could decrease the conductivity. The summary of the sample conductivity is given in Table 1 and 2.

Table 1. Conductivity of the sample as a function of the sinter temperature.

Sample	σ (S/cm)
A (Ts= 700C/12h, 2wt%Ti)	8,50E-08
B (Ts= 800C/12h, 2wt%Ti)	3,45E-09
C (Ts= 900C/12h, 2wt%Ti)	3,81E-09

Table 2. Conductivity of the sample as a function of Ti-element content.

Sample	σ (S/cm
D (Ts= 700C/12h, 0wt% Ti)	3,80E-08
A (Ts= 700C/12h, 2wt%Ti)	8,50E-08
E (Ts= 700C/12h, 4wt%Ti)	1,95E-08

IV. Conclusion

The cathode material $LiFe_{1-x}Ti_xPO_4$ (x=0.05 and 0.06) is obtained by sinter process at 700, 800 and 900°C for 12h. Grain size is increased by increasing sinter temperature or dopant quantity. Grain growth and agglomeration mechanisms affected the conductivity. Big grain size and big particle size decreased the conductivity. Optimum conductivity was reached by heating sample with 2wt% Ti at 700°C for 12h, i.e. 8.5x10-8 S/cm.

V. Acknowledgement

This work is financially supported by the 2012 SINAS KEMENRISTEK Republic of Indonesia (Proposal No. RT-2012-124).

VI. References

1. J.-M. Chen, C.-H. Hsu, Y.-R. Lin, M.-H. Hsiao, G.T.-K. Fey, Journal of Power Sources 184, 498 (2008).
2. J.-K. Kim, G. Cheruvally, J.-H. Ahn, J. Solid State Electrochem., 12, 799 (2008).
3. S.Y. Chung, J.T. Bloking, Y.-M. Chiang, Nat. Mater. 1, 123 (2002).

4. G. Wang, Journal of Solid State Electrochemistry 9, (2006).
5. D.-K. Kim, H.-M. Park, S.-J. Jung, Y.-U. Yeong, J.-H. Lee, J.-J. Kim, J Power Sources 159, 237 (2006).
6. K. Dokko, S. Koizumi, K. Sharaishi, K. Kanamura, J Power Sources 165, 656 (2007).
7. C.-W. Ong, Y.-K. Lin, J.-S. Chen, J Electrochem Soc 154, A527 (2007).
8. X. Li, W. Wang, C. Shi, H. Wang, Y. Xing, J Solid State Electrochem 13, 921 (2009).
9. M.M. Doeff, Y.Q. Hu, F. McLarnon, R. Kostecki, Electrochem Solid-state Lett 6, A207 (2003).

The Effect of Various Immobilization Layer Materials to The Microcantilever Sensor Sensitivity

Ratno Nuryadi, Winda Rianti, Lia Aprilia
Center of Materials Technology, Agency for Assessment and Application of Technology
22nd BPPT Bulding, 22 floor, MH. Thamrin 8 Street, Jakarta 10340, Indonesia

Abstract

A microcantilever has become an attractive sensor, because it can be applied to many fields such as medicine, chemistry, environment and biology. In order to detect specific object, the microcantilever must be coated with functional (antigen/antibody) layer. Immobilization layer is required to provide a suitable place for functional layer on microcantilever surface. In this work, we investifate the effect of various materials which is coated on microcantilever surface to the sensor sensitivity and compare each other. The materials are gold, silver, platinum, aluminum and titanium. Our calculation results showed that the different materials of immobilization layer produce different sensor sensitivity. Therefore, the selection of sensitive material layer is important for designing the microcantilever sensor.

Keywords : *microcantilever (I-shaped), immobilization layer, sensitivity, resonance frequency.*

* Corresponding author.
E-mail address: ratnon@gmail.com

I. Introduction

Microcantilever-based sensors have been found in various applications, i.e, physical, chemical, biological, medical, and environmental fields in recent years. This is because the micromechanical cantilever show great potential as highly sensitive bio/chemical sensors [1]. The microcantilever-based sensor involves the transduction of a (bio) molecular interaction to a measurable mechanical change in the cantilever, resulting from induced surface stresses [2-3], the transfer of heat [4-7] or added mass [8-10].

When the microcantilever is used as a mass detector, the cantilever surface needs to be coated with a functionalization layer for absorption of specific organic materials. Absorbed molecules will add to the mass of the cantilever and thereby cause a change in the resonance frequency which can be detected. Moreover, immobilization layer is required to provide a suitable place for functional layer on microcantilever surface. The functionalization of the sensing surface can be accomplished by attachment of organic molecules (antigen/antibody). For the immobilization layer, metal materials and polymers are usually coated on the surface of cantilever .

Considering the fact that surface modification of the cantilever is vital to bio/chemical sensor performance, a study on effect of various immobilization layer materials on the microcantilever surface is needed. In this work, varieties of metal coatings on the surface of microcantilevers are simulated in order to investigate their effect on the sensitivity of the sensor.

II. Formulation of Microcantilever Sensitivity

Microcantilevers can work in two different modes of operation, i.e., static and dynamic. In the static mode, the binding of target molecules to the cantilever is detected as a result of the surface stress and cantilever bending [12,13]. In the dynamic mode, the cantilever is actuated and its resonant frequency is determined. The binding of the molecules is detected due to the mass change and resulting resonant frequency shift [14,15].

Microcantilever resonance frequency at dynamic mode is described in formula (1)

$$f = \frac{1}{2\pi}\sqrt{\frac{k}{m}} \qquad (1)$$

where m is cantilever mass, and k is spring constant of the cantilever beam. The resonance frequence changes (Δf) happened based on

molecular absorption on the microcantilver surface, resulting in mass changes, which can be calculated based on the following formula:

$$\Delta m = -2\frac{m}{f}\Delta f \quad (2)$$

From the formula (2), a mass sensitivity can be calculated as follow.

$$\frac{\Delta m}{\Delta f} = -2\frac{m}{f} \quad (3)$$

In this work, we consider the microcantilever structure in a rectangular type (I-shaped) as shown in Fig. 1. In this structure, the end of the I-beam is fixed, while the other end is free.

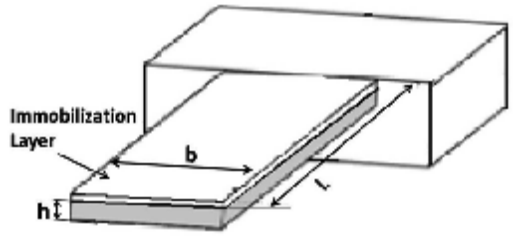

Figure 1. The microcantilever structure with immobilization layer in rectangular type

The moment of inertia for the rectangular microcantilever with width *b*, length *L*, thickness *h* can be calculated with the equation (4):

$$I = \frac{1}{12}bh^3 \quad (4)$$

From the formula (4), spring constant can be calculated with the formula (5).

$$k1 = \frac{3\hat{E}I}{L^3}$$

Effective modulus young $(\hat{E})$ is define as follow.

$$\hat{E} = \frac{E}{1-v^2} \quad (6)$$

where *E* is a microcantilever modulus young.

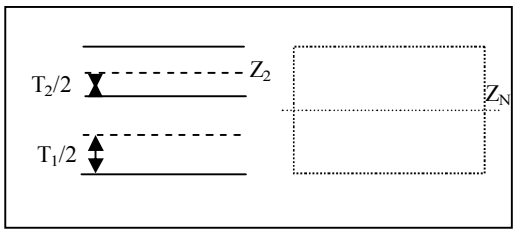

Figure 2. Neutral Axis microcantilever with immobilization layer in the cross-section view of microcantilever

For microcantilever with immobilization layer (Fig.1), the value of effective stiffness $(\hat{E}I)_{eff}$ can be calculated with this formula:

$$(\hat{\mathrm{E}}\mathrm{I})_{eff} = w\sum_i \hat{E}_i\left(\frac{t_i^3}{12} + t_i(Z_i - Z_N)^2\right) \quad (7)$$

where $(Z_i - Z_N)$ is the distance between the center of *i*-layer from neutral axis as shown in Fig. 2.

Because the spring constant equation (5) is the function of effective Modulus Young of materials microcantilever, the effective spring constant become:

$$k_{eff} = \frac{3(\hat{\mathrm{E}}\mathrm{I})_{eff}}{L^3} \quad (8)$$

From the formula (1), mass effective microcantilever I-shaped is obtained as follow

$$m_{cantilever} = \frac{k}{(2\pi f_n)^2} \quad (9)$$

where *n* is mode of vibration.

Next, resonance frequency for microcantilever can be known from the equation (10)

$$f_n = \frac{x}{2\pi}\left(\frac{\alpha_n}{L}\right)^2\sqrt{\frac{EI}{\rho A^2}} \quad (10)$$

Hence, the formula (9) become,

$$m_{cantilever} = \frac{\frac{3EI}{L^3}}{\left(2\pi\left[\frac{1}{2\pi}\left(\frac{a_n}{L}\right)^2\sqrt{\frac{EI}{\rho A}}\right]\right)^2}$$

$$m_{cantilever} = \frac{3\rho AL}{{\alpha_n}^4} \quad (11)$$

In this equation, *A* is a cross-sectional area of microcantilever, therefore *A=b*x*h*. Hence, mass effective microcantilever I-shaped is

$$m_{cantilever} = \frac{3\rho bhL}{{\alpha_n}^4} \quad (12)$$

α_n in the formula (10-12) is a dimensionless parameter which obtained from transcendental equation for microcantilever.

$$\cos\alpha_n \cosh\alpha_n + 1 = 0 \quad (13)$$

The solution of the formula (13), i.e., value of α_n, can be obtained by the calculation using Newton-Raphson method, as shown in Table 1.

Tabel 1. Values of α_n

n	α_n
1	1,87510407
2	4,69409113
3	7,85475744
4	10,99554073

Formulation for the microcantilever with any metal layer on the surface which has length and width as same as surface of microcantilever can be seen in equation (14), which consist of the

mass effective (12) cantilever added with mass of layer.

$$m_{eff} = \frac{3}{\alpha_n{}^4} m_{cantilever} + m_{add}$$
$$m_{eff} = \left(\frac{3Lw}{\beta^4} \sum_i \rho_i t_i\right) + m_{add} \quad (14)$$

III. Result and Analysis

Based on mathematic formulation which has been described above, the sensitivity and the resonance frequency of microcantilevers can be calculated. The detail parameters which are used in the calculation are shown in Table 2.

Table 2 Simulation Parameters

No.	Parameter	Value
1	Length Silicon microcantilever, *L(i)*	L min = 0 – L max= 1e-5 [m]
2	Width Silicon microcantilever, *w*	L(i)/2
3	Thickness Silicon microcantilever, *h*	100x10^{-9} [m]
4	Young's Modulus Silicon, E_1	1.94x10^{10} N/m²
5	Poisson Ratio Silicon, v_1	0.27
6	Mass Density Silicon, ρ_1	2330 gr/m^3
7	Thickness various materials layer, h_1	10x10^{-9}[m]
8	Young's Modulus Gold, E_2	7.65x10^9 N/m²
9	Poisson Ratio Gold, v_2	0.31
10	Mass Densisity Gold, ρ_2	19280 gr/m^3
11	Young's Modulus Silver, E_3	8.3e9 N/m²
12	Poisson Ratio Silver, v_3	0.37
13	Mass Density Silver, ρ_3	10500 gr/m^3
14	Young's Modulus Platinum, E_4	16.8x10^9 N/m²
15	Poisson Ratio Platinum, v_4	0.38
16	Mass Density Platinum, ρ_4	21450 gr/m^3
17	Young's Modulus Aluminum , E_5	7e9 N/m²
18	Poisson Ratio Aluminum, v_5	0.35
19	Mass Density Aluminum, ρ_5	2700 gr/m^3
20	Young's Modulus Titanium, E_6	11.6x10^9 N/m²
21	Poisson Ratio Titanium, v_6	0.32
22	Mass Density Titanium, ρ_6	4506 gr/m^3

The figure 3 shows the relationship between sensitivity with the various material immobilization layer and the microcantilever length.

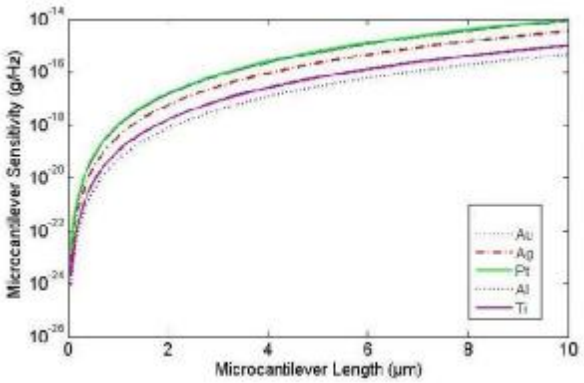

Figure 3. Sensitivity Microcantilever with different material

The highest sensitivity of microcantilever is resulted for aluminum material as immobilization material, whereas platinum and gold has the lowest sensitivity. The aluminum material has the highest of sensitivity because the mass density and Young's Modulus of the aluminum is lowest than those of the others. The aluminum is well known as light materials, so the addition of aluminum on the microcantilever surface results in a less mass changes on microcantilever. That is the reason why the sensitivity of microcantilever with aluminum immobilization layer reaches the highest one. However, despite aluminum has the highest sensitivity, aluminum has never been used as material for immobilization layer because lack in biocompatible properties.

The immobilization layer on the microcantilever surface is usually made from gold or silver [16]. This is because the surfaces of metals such as gold and silver easily react with organic thiol groups and spontaneously form self assembled monolayers. Titanium has a higher

sensitivity and better bicompatibility properties than gold, but the gold is more easy to obtain and to deposit it on the microcantilever surface.

Among the materials used as immobilization component in bio/chemical sensors, recently gold nanoparticle have received greatest interest as immobilization layer because they have several kinds of intriguing properties. The gold nanoparticle has high surface-to-volume ratio and high surface free energy to provide a stable immobilization of a large amount of biomolecules retaining their bioactivity. Morever, gold nanoparticle have excellent biocompatibility and catalytic properties. In addition, the high density and high molecular weight of gold nanoparticles increase the apparent mass of the analytes immobilized them [17].

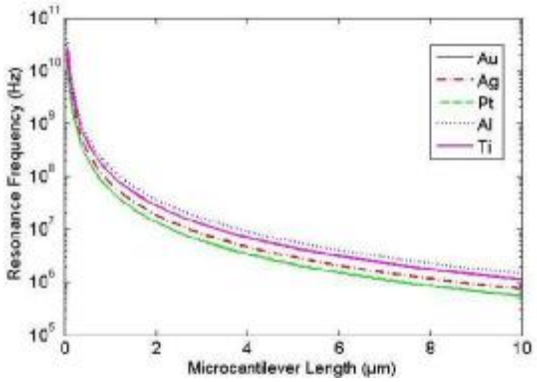

Figure 4. Resonance frequency as a function of the microcantilever lenght for different immobilization materials

Fugure 4 shows the resonance frequency as afunction of the microcantilever length for various immobilization materials. The resonance frequencues are found to be different for each others. This is because the difference of the microcantilever mass and the spring constant as shown in equation (1).

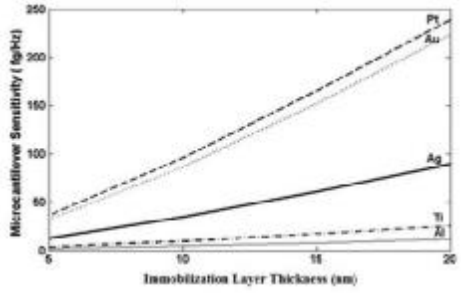

Figure 5. Microcantilever sensitivity with different thickness of various material immobilization layer.

Figure 5 shows microcantilever sensitivity as a function of immobilization layer thickness for various materials. The microcantilever sensitivity decrease with increasing the microcantilever layer thickness. The sensitivity of alumunium and titanium increase slightly with increasing gold coating thickness. On the other hand, for platinum and gold, the increasing gold coating thickness results in a significant increase of sensitivity. For gold, the increasing 5 nm thickness results in the changes of microcantilever sensitivity from about $3x10^{-14}$ g/Hz to about $8x10^{-14}$ g/Hz.

The increase of the coating aluminum thickness leads only to a small addition reduction of sensitivity because the low mass density. The added thickness is influenced by the added mass on the cantilever surface. For gold with high mass density, the added thickness leads a significant number of mass which causes a significant changes in microcantilever sensitivity.

IV. Conclusion

We have studied the effect of immobilization layer on the microcantilever surface on the sensor sensitivity. Our calculation results showed that the different materials of immobilization layer produce different sensor sensitivity. The highest sensitivity of microcantilever is microcantilever with immobilization layer of alumunium. Although the gold is less sensitivity than the other metals, the gold is widely used as material immobilization layer due to bicompatibility properties. Moreover, the increase of immobilization thickness decreases the sensitivity of microcantilever. These results indicate that the selection of immobilization layer both the type of material and the thickness is very important in the design of microcantilever sensor.

V. References

1. Michel Godin, Vincent Tabard Cossa, Yoichi Miyahara, Tanya Monga, PJ Williams, LY Beaulieu, R Bruce Lennox and Peter Grutter. *Nanotechnology* 21, 075501(2010)
2. Gimsewski JK, Gerber Ch, Meyer E and Schlittler RR. *Chem Phys. Lett*. 217, 589 (1994)

3. Berger R, Delamarche E, Elang HP, Gerber Ch, Gimzewski JK, Meyer E and Guntheridt H-J. *Science* . 176, 2021 (1997)
4. Barnes JR, Stephenson RJ, Welland ME, Gerber Ch and Gimzewki JK. *Nature*. 372, 79 (1994)
5. Thundat T, Sharp SL, Fischer WG, Warmack RJ and Watcher EA. *Appl. Phys. Lett*. 66, 1563 (1995)
6. Varesi J, Lai J, Shi Z, Perazzo T and Majumdar A. *Appl. Phys. Lett.* 71, 306 (1997)
7. Manalis SR, Minne SC, Quate CF, Yaralioglu GG and Atalar. *Appl. Phys Lett*. 70, 3311 (1997)
8. Berger R, Gerber Ch and Gimzewski JK. *Anal Methods Instrum* . special issues 74 (1996)
9. Ilic B, Craigead HG, Krylov S, Senaratne W, Ober C and Neuzil P. *J. Appl. Phys.* 95, 3694 (2004)
10. Nugaeva N, Gfeller KY, Backmann N, Lang HP, Duggelin M and Hegner M. *Bosens Bioelectron*. 21, 849 (2005)
11. Fritz J. *Analyst*. 133, 855 (2008)
12. J. Fritz, M.K Baller, H.P. Lang, H. Rothuizen, P. Vettiger, E. Meyer, H.-J. Guntherodt, C. Gerber, J.K. Gimzewski, Tr*, Science* 288, 316 (2000).
13. M.Alvarez, L.G. Carrascosa, M. Moreno, A. Calle, A. Zaballos, L.M. Lechuga, C. Martinez-A, J. Tamayo*, Langmuir* 20, 9663. (2004)
14. M. Su, S. Li, V.P. Dravid, *Appl. Phys. Lett.* 82 (2003).
15. B. Illic, D. Czaplewski, H.G. Craighead, P. Neuzil, C. Campagnolo, C. Batt,. *Appl. Phys. Lett*. 77 (2000).
16. A. Hirlekar Schmid, S.E. Stanca, M.S Thakur, K. Ravindranathan Thampi. C. Raman Suri. *Sensors and Actuators*. B 113, 297 (2006).
17. Yuanyuang Li, Hermann, J.Schluesener, Shunqing Xu.*Gold Bulletin*. Vol. 43 Nol1 (2010)

The Enhancement of Sensitivity of Graphene-Based Surface Plasmon Resonance (SPR) Biosensors

Rina Dewi Mayasari[1*], Moh. Adhib Ulil Absor[2], Kamsul Abraha[2]
[1] Department of Physics, Faculty of Mathematics and Natural Sciences, Gadjah Mada University
[2] Research Group of Advanced Materials and Surface Plasmon Resonance, Department of Physics, Faculty of Mathematics and Natural Sciences, Gadjah Mada University

Abstract
The study of surface plasmon resonance (SPR) phenomenon for SPR based biosensor using silver thin film with increcement graphene layer has been done. The aim of this research is to improve the sensing capability of the SPR biosensor. The model and calculation of the SPR biosensor has been performed by using the coupled prism method under modified Kretschmann configuration. The results of calculation show that the existence of graphene layer can shift the SPR angle and make it sharper to reach optimum point due to the dispersion relation curve together with the attenuated total refelection curve. The SPR angle for SPR biosensor before additional graphene is 53,6^o with constant wave surface plasmon being 13,78×10^6 m^{-1}, respectively. After the additional graphene material, the SPR angle become 54,3^o with constant wave surface plasmon being 13,88×10^6 m^{-1}, respectively. In conclusion, the graphene material can be used as material candidate to improve the sensing capability of SPR biosensor.
Keyword: *Graphene, SPR*

* Corresponding author.
E-mail address: rinadewi.mail@gmail.com

I. Introduction

Biosensor based surface plasmon resonance (SPR) is familiar as coupled prism method using metal thin film. The kind of metal thin films using in this biosensor is the metal supporting the surface plasmons (SPs) propagation at visible light frequencies, noble metal, such as gold, silver, etc. Silver is often used but it is easy oxidized by oxygen containing atmosphere. Hence, the new improvement with preventing oxidation is needed to work with SPR biosensor using silver thin film for long time.

In 2004, Geim and Novoselov introduced new material graphene gotten from carbon material. In 2010, Wu *et al* proposed to add graphene material on SPR biosensor using gold thin film. Graphene shows that it is capable to stably absorb bimolecules on gold thin film because of the hexagonal carbon structure [1]. In 2011, Choi *et al* presented SPR biosensor using silver thin film and adding graphene sheet to prevent oxidation because graphene sheet proven to be impermeable to gases as small as He. Choi *et al* use graphene material because in Bunch's research group discover that the electron density of hexagonal rings is substantial enough to prevent atoms and molecules from passing through the ring structure [2]. Therefore, graphene material promises to increase the capability of SPR biosensor.

II. Theory

Surface plasmons (SPs) are collective oscillations of free electrons that propagate along the interface between a thin metal film and dielectric material. SPR biosensor model generally uses Kretschmann configuration (Picture 1). This configuration bases on total internal reflection (TIR) phenomenon, the light will be reflected back into dense medium when the light propagates through a dense medium and reaches the interface abutting on a medium having lower optical density. However, evanescent wave of *p*-polarized light penetrates into a medium having lower optical density [3].

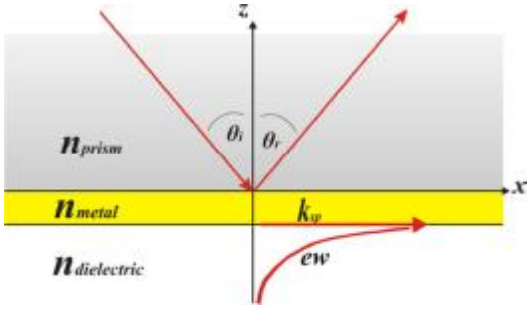

Picture 1. Kretschmann configuration

The wave vector of the evanescent field (K_{ev}) is given by

$$K_{ev} = \frac{\omega_0}{c} n_p \sin\theta_i \qquad (1)$$

where ω_0 is incident light frequency, n_d refractive index of dense medium, θ_i incident light angle, and c the speed of light in vacuum.

The wave vector of surface plasmon (K_{sp}) is given by

$$K_{sp} = \frac{\omega_0}{c}\sqrt{\frac{\varepsilon_m n_d^2}{\varepsilon_m + n_d}} \qquad (2)$$

Where ε_m is the dielectric constant of metal thin film and n_b is refractive index of dielectric material. Surface plasmon resonance occurs when $K_{ev} = K_{sp}$, evanescent wave of incident light is coupled by osilating free electrons on metal thin film. SPR phenomenon can be seen by decaying reflectance drastically at a certain angle coinciding with loosing energy [4].

The equation of reflectance for graphene-based SPR biosensor using modified Kretschmann configuration can be gotten by Fresnel's equation [5]

$$R = |r|^2, \qquad (3)$$

$$R = |r_{ijk}|^2 = \left|\frac{r_{ij} + r_{jk}e^{2ik_{jz}d_j}}{1 + r_{ij}r_{jk}e^{2ik_{jz}d_j}}\right|^2 \qquad (4)$$

where $r_{ij} = \frac{k_i\varepsilon_j - k_j\varepsilon_i}{k_i\varepsilon_j + k_j\varepsilon_i}$, $(i,j,k = 1,2,\ldots)$ (5)

r_{ij} is reflectance between interface i and j medium, k_{jz} wave vector component perpendicular to interface, k_x is vector component paralel to interface, then d_j and ε_i are the thickness of j layer and material dielectric constant of i layer.

III. The Model of Graphene-Based SPR Biosensor

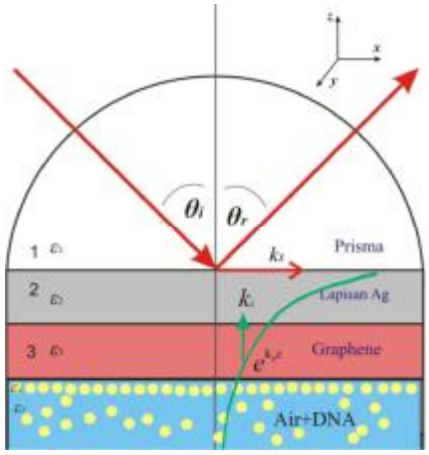

Picture 2. The model of graphene-based SPR biosensors

Picture 2 shows the proposed model of graphene-based SPR biosensors using coupling prism and modified Kretschmann configuration. For getting relation dispersion curve, this model uses the data of light wavelength from 330-1000 nm, refractive index of SF10 prism [6], refractive index of graphene for each light wavelength from 330-1000 nm [7], refractive index of mixture of water and DNA (n_5 = 1,330) and refractive index of DNA layer (n_4 = 1,335) [10]. For getting ATR curve, the using data is laser He-Ne (λ_o = 633 nm), SF10 prism (n_1 = 1,723), silver (n_2 = 0,13455+3,98651i), the thickness of silver (d_2 = 44 nm), graphene (n_3 = 2,5748+1,4935i), the thickness of one layer graphene (d_3 = 0,38 nm), and water (n_4 = 1,3).

IV. Result and Discussion

Using harmonic fields depending on x and z direction, the transverse magnetic (TM) mode can be resulted from Maxwell equations are

$$E_x = -i\frac{1}{\omega\varepsilon_0\varepsilon}\frac{\partial H_y}{\partial z}, \qquad (6.a)$$

$$E_z = -\frac{k_x}{\omega\varepsilon_0\varepsilon}H_y, \qquad (6.b)$$

$$\frac{\partial^2 H_y}{\partial z^2} + \left(k_0^2\varepsilon - k_x^{\,2}\right)H_y = 0. \qquad (6.c)$$

Using Helmhotz equation, E and H fields for multilayer system at n layer can be represented by [8]

$$F_j(z) = A_j e^{ik_{jz}\left(z - z_{j-1}\right)} + B_j e^{-ik_{jz}\left(z - z_{j-1}\right)}. \qquad (7)$$

Representing Eq. 6.a-6.c into Eq. 7, we find the equation of implicit dispersion relation for five systems [9]

$$e^{2ik_{4z}d_4} = -\frac{A + Ce^{2ik_{3z}d_3} + Ee^{2ik_{2z}d_2} + Ge^{2ik_{2z}d_2}e^{2ik_{3z}d_3}}{B + De^{2ik_{3z}d_3} + Fe^{2ik_{2z}d_2} + He^{2ik_{2z}d_2}e^{2ik_{3z}d_3}} \qquad (8)$$

where

$$A = \left(k_{2z}\varepsilon_1 - k_{1z}\varepsilon_2\right)\left(k_{3z}\varepsilon_2 + k_{2z}\varepsilon_3\right)\left(k_{4z}\varepsilon_3 + k_{3z}\varepsilon_4\right)\left(k_{5z}\varepsilon_4 + k_{4z}\varepsilon_5\right)$$
$$B = \left(k_{2z}\varepsilon_1 - k_{1z}\varepsilon_2\right)\left(k_{3z}\varepsilon_2 + k_{2z}\varepsilon_3\right)\left(k_{4z}\varepsilon_3 - k_{3z}\varepsilon_4\right)\left(k_{5z}\varepsilon_4 - k_{4z}\varepsilon_5\right)$$
$$C = \left(k_{2z}\varepsilon_1 - k_{1z}\varepsilon_2\right)\left(k_{3z}\varepsilon_2 - k_{2z}\varepsilon_3\right)\left(k_{4z}\varepsilon_3 - k_{3z}\varepsilon_4\right)\left(k_{5z}\varepsilon_4 + k_{4z}\varepsilon_5\right)$$
$$D = \left(k_{2z}\varepsilon_1 - k_{1z}\varepsilon_2\right)\left(k_{3z}\varepsilon_2 - k_{2z}\varepsilon_3\right)\left(k_{4z}\varepsilon_3 + k_{3z}\varepsilon_4\right)\left(k_{5z}\varepsilon_4 - k_{4z}\varepsilon_5\right)$$
$$E = \left(k_{2z}\varepsilon_1 + k_{1z}\varepsilon_2\right)\left(k_{3z}\varepsilon_2 - k_{2z}\varepsilon_3\right)\left(k_{4z}\varepsilon_3 + k_{3z}\varepsilon_4\right)\left(k_{5z}\varepsilon_4 + k_{4z}\varepsilon_5\right)$$
$$F = \left(k_{2z}\varepsilon_1 + k_{1z}\varepsilon_2\right)\left(k_{3z}\varepsilon_2 - k_{2z}\varepsilon_3\right)\left(k_{4z}\varepsilon_3 - k_{3z}\varepsilon_4\right)\left(k_{5z}\varepsilon_4 - k_{4z}\varepsilon_5\right)$$
$$G = \left(k_{2z}\varepsilon_1 + k_{1z}\varepsilon_2\right)\left(k_{3z}\varepsilon_2 + k_{2z}\varepsilon_3\right)\left(k_{4z}\varepsilon_3 - k_{3z}\varepsilon_4\right)\left(k_{5z}\varepsilon_4 + k_{4z}\varepsilon_5\right)$$
$$H = \left(k_{2z}\varepsilon_1 + k_{1z}\varepsilon_2\right)\left(k_{3z}\varepsilon_2 + k_{2z}\varepsilon_3\right)\left(k_{4z}\varepsilon_3 + k_{3z}\varepsilon_4\right)\left(k_{5z}\varepsilon_4 - k_{4z}\varepsilon_5\right)$$

First time reported theoretically the effect of graphene layer for SPR based biosensor considered by relation dispersion curve (Picture 3.a and 3.b) and ATR curve (Picture 4.a and 4.b).

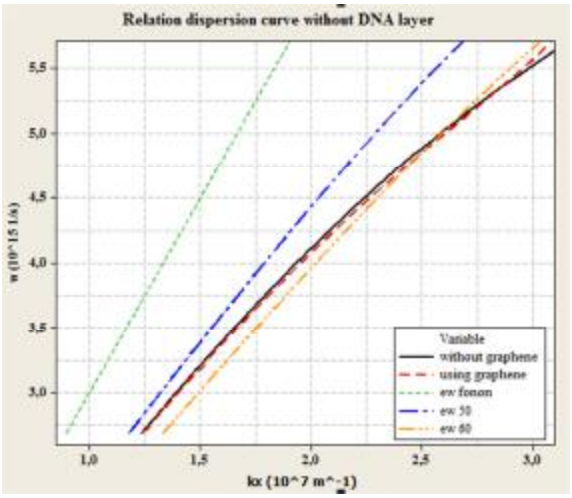

Picture 3.a. dispersion relation curve of SPR based biosensor before adding graphene

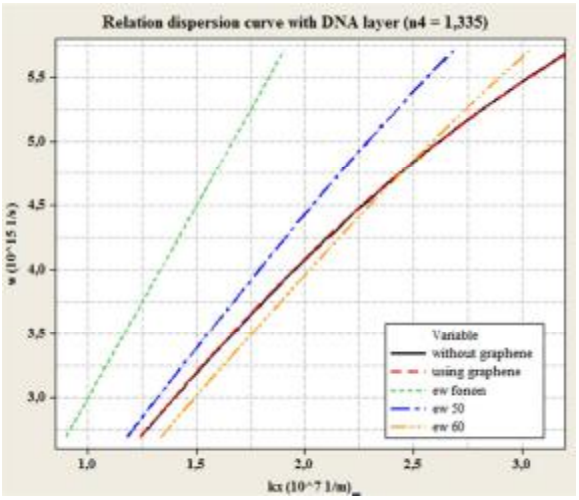

Picture 3.b. dispersion relation curve of SPR based biosensor after adding graphene

Relation dispersion is the relation between frequency (ω) of light wavelength and wave vector of x-direction (k_x). The surface plasmon resonance phenomenon is shown by intersecting curve between evanescent wave curve and surface plasmon curve. From the above curve, we found the data of the coupling evanescent wave and plasmon as follow

Table l. The data of dispersion relation at light wavelength 633 nm (He-Ne laser)

Δn_{DNA}	Without graphene		Using graphene	
	k_x (×10^6) m^{-1}	θ_{SPR}	k_x (×10^6) m^{-1}	θ_{SPR}
0	13.78	53.6^o	13.88	54.3^o
0.005	13.86	54.0^o	13.84	53.9^o

Now the surface plasmon resonance is simulated by ATR curve recognized as minimum in attenuated total reflection (Picture 4.a and 4.b). This simulation resulting the displacement of SPR angle data will be used to look for the change of sensitivity of graphene-based SPR biosensor. The sensitivity will be compared by before adding graphene and after adding graphene.

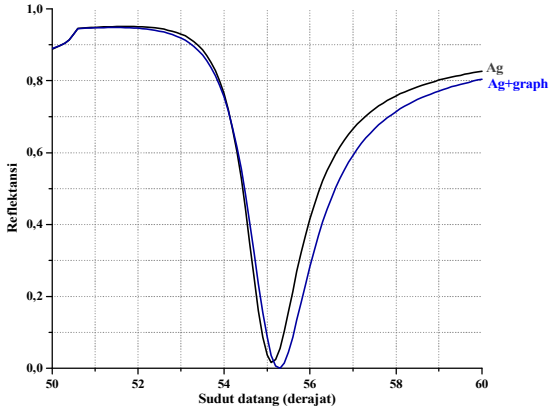

Picture 4.a. ATR curve without DNA layer

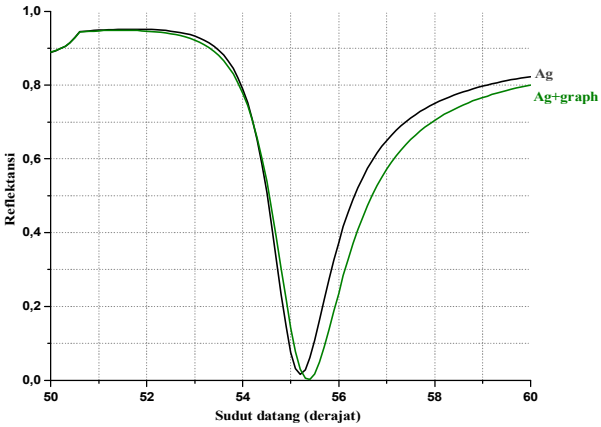

Picture 4.b. ATR curve with DNA layer (n_4 = 1,335)

Table 2. The data of ATR curve at light wavelength 633 nm (He-Ne laser)

Δn_{DNA}	Without graphene	Using graphene
	θ_{SPR}	θ_{SPR}
0	55.13^o	55.27^o
0.005	55.20^o	55.37^o

For getting the sensitivity of graphene-based SPR biosensor, Choi *et al* used Geim and Novoselov definition, the sensitivity of biosensor S is defined as the ratio of the change in sensor output P, e.g. the change of SPR angle $\Delta\theta_{SPR}$, to the change in measurement, e.g. the change of biomolecules moles, ΔM [10].

$$S = \frac{\Delta\theta_{SPR}}{\Delta M} = \frac{\Delta\theta_{SPR}}{\Delta n}\frac{\Delta n}{\Delta M} \qquad (8)$$

Using the data shown tabel 2, we found that the sensitivity of biosensor using graphene is 42,86%.

V. Conclusion

Proven theoretically, adding one layer of graphene material on silver layer of SPR biosensor can enhance the sensitivity of SPR biosensor. The sensitivity enhance 42,86%.

V. Acknowledgements

The authors would like to thank to DP2M Ditjen Dikti Depdikbud and LPPM UGM for financial support under the Fundamental Research's Grant program 2012.

VI. References

1. Lim Wu, H. S. Chu, W. S. Koh, and E. P. Li, America International Paper, Optics Express. 18, 14, 14395 (2010).
2. Seug Ho Choi, Young L. Kim, and Kyung Min Byun, America International Paper, Optics Express. 19, 2, 458 (2011).
3. Maier, SA., "Plasmonics: Fundamentals and Applications". Springer Science + Business Media LLC, New York, 2007.
4. Matsubara K, Kawata S, and Minami S., Applied Spectroscopy. 42, 1375-1379 (1988).
5. Raether, H., "Surface Plasmons on Smooth and Rough Surface on Gratings". Springer-Verlag, Berlin, 1988.
6. M. Polyanskiv,. Refractive index database of SF10 prism. Website: http://refractiveindex.info/?group=GLASSES&material=SF10, access February 6, 2012.
7. Gray, A., Balooch M., Allegert S., Gendt SD., and Wang WE. Journal of Applied Physics 104 (2008).
8. Maksimovic, M., Optical Resonance in Multilayer Structures, Ph.D dissertation. University of Twente, Netherlands, 2008.
9. Mayasari, R.D., Undergraduate Thesis, Yogyakarta. 2012.
10. Choi, S.H., Kim, Y.L., and Byun, K.M., Optics Express, 19, 2, 458 (2011).

Effect of Anchoring Groups on the Conduction Properties of Phenyl Based on Organic Molecules Connected to Copper Leads

***Setianto*[1,2*] *and Th. Niehaus*[2]**
[1] *Department of Physics, Faculty of Mathematics and Natural Sciences, Padjadjaran University*
Jl. Raya Bandung-Sumedang KM.21, Jatinangor 45363, Indonesia
[2] *Institute I – Theoretical Physics, University of Regensburg*
Universitätstraße 31, D-93053 Regensburg, Germany

Abstract

We report equilibrium and non-equilibrium conductance of terphenyl molecules with different anchoring groups including sulfur and nitrogen atom. The corresponding molecules are terphenyl-dithiols(TPDT) and diamino-terphenyl(DATP). The non-equilibrium Green's function (NEGF) technique has been implemented on the density functional tight-binding (DFTB) code to perform computations of the electronic transport properties of molecular devices. The NEGFs are used to compute the electronic density self-consistently with open boundary condition naturally encountered in transport problem which is imposed by the potentials at the contacts. As result, the value of the molecular conductance with amine groups is higher about ten times than the thiol anchored group.

Keywords : *Molecular conductance, Non-equilibrium transport, Green's functions*

* Corresponding author.
E-mail address: setianto@phys.unpad.ac.id

I. Introduction

A single molecule is attracting more attention both of experimental and theoretical study for its potential application of miniaturization from sub-micrometer conventional inorganic devices to the very small active component just in few nanometers. Electronic conduction through several molecules has been studied experimentally by many research groups [1-3]. However, the transport mechanism at the single molecule level still opened to scientific study in how the conductance of molecular junctions can be tuned by chemically modifying the molecules [4]. The role of anchoring groups in molecular junction is one of the main problems that remain to be understood.

Experiments [4,5] have shown that terminal groups that bind a molecule to the metal electrode can control the value of the conductance. Theoretically, it has been shown that the conductance of amine-anchored has better conductance value than thiolated molecules with connected to gold contacts [6-8]. The anchoring groups affect the energy level line up relative to the metal Fermi energy and consequently play important role the conductance plateaus.

In this study, we use terphenyl molecules with different anchoring groups including sulfur and nitrogen atom connected to copper leads. The corresponding molecules are terphenyl-dithiol(TPDT) and diamino-terphenyl(DATP). We present a systematic study that correlates the conductance values, binding energies and coupling strengths with different anchoring groups by using density functional tight-binding (DFTB)[9] with extended to the non-equilibrium Green's function (NEGF)[10,11] approach for computation of the charge density and electronic transport.

II. The Green's Function Formalism

The problem of quantum transport through a single molecule bridged to two contacting lead can be set by starting from the scattering states which propagate from one lead to the other. The waves scatter at the contact-molecule interface and partially reflected and transmitted across the molecule. Consider the retarded Green's functions of the α contact:

$$g_{\alpha}^{r} = \left[ES_{\alpha} - H_{\alpha} - i\delta\right]^{-1}$$

where $H\alpha$ is Hamiltonian of the contact, the overlap matrix, S is represented on non-orthogonal basis set. Assume that the contacts have no interaction in between, the Hamiltonian of the whole system can be written:

$$H = \begin{bmatrix} H_D & V_{D1} & V_{D2} \\ V_{D1}^{\dagger} & H_1 & 0 \\ V_{D2}^{\dagger} & 0 & H_2 \end{bmatrix}$$

where $V_{D1(2)}$ is the Hamiltonian of contact-molecule coupling. The complete Green's function of the system:

$$G_D^r = \left[ES_D - H_D - \Sigma^r \right]^{-1}$$

where Σ^r is the total self-energy of the two contacts,

$$\Sigma_\alpha^r = \left(ES_{D\alpha} - V_{D\alpha} \right) g_\alpha^r \left(ES_{D\alpha} - V_{D\alpha} \right)^\dagger$$

The tunneling current flowing through the molecule that naturally arises in coherent transport is given by the Landauer formula [11]:

$$I(V) = \frac{q}{h} \int dE\, T(E,V) \left[f(E,\mu_1) - f(E,\mu_2) \right]$$

where $T(E,V)$ = Tr $[\Gamma_L G^r \Gamma_R G^a]$ is transmission function and $\Gamma_{L/R}$ is the scattering rates related to the probability of injecting an electron into the molecule from left and right electrodes. These rates also describe the width that the molecular level acquires in virtue of the coupling to the metal leads and they can be used as measure of the strength of the metal-molecule coupling. Then $f(E,\mu)$ is the Fermi-Dirac function. In equilibrium and at zero temperature (T = 0 °K) case, the conductance can be expressed as :

$$G = \frac{2q^2}{h} T(E_F)$$

The advantages in using Green's function approach are that incoherent scattering and relaxations can be included within self-energies.

III. Result and Discussion

The types of systems under study can be represented as shown in figure 1. The contacts are semi-infinite leads and it is assumed that their properties coincide with those of bulk systems [12]. The device is a collection of atoms linking to the contacts, comprising a molecular bridge. The current flowing across the device when the contacts are kept at different electrochemical potentials.

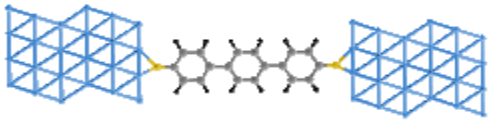

Fig.1 A model of single molecule device

We carried out calculations based on DFTB to determine the geometry and electronic structure of isolated molecules and the leads. The adsorption of all molecules on metal surface is optimized by ab-initio density functional theory (DFT) which uses a conjugated gradient technique. In these cases, we used the PBE exchange-correlation functional form of the generalized gradient approximation (GGA) [13]. We implemented basis sets with diffuse functions scheme for the Copper surface with longer cutoff and slower decay than the bulk DZP orbital [15]. The Cu[111] has (4x4) surface unit cell and repeated geometry consisting six-layers . The anchor groups (-SH and -NH_2) were optimized in the hollow site of Cu[111] surface and yields in a distance 1.87 and 1.45 angstrom respectively. Exploiting this computational scheme for the coherent transport properties, we assume that dithiol or diamine loses hydrogen atoms upon interaction with the copper leads [15]. Finally, single point calculations were performed on these systems and the transmission of the junctions was computed in the spirit of Landauer formalism using NEGF techniques which is implemented on DFTB code.

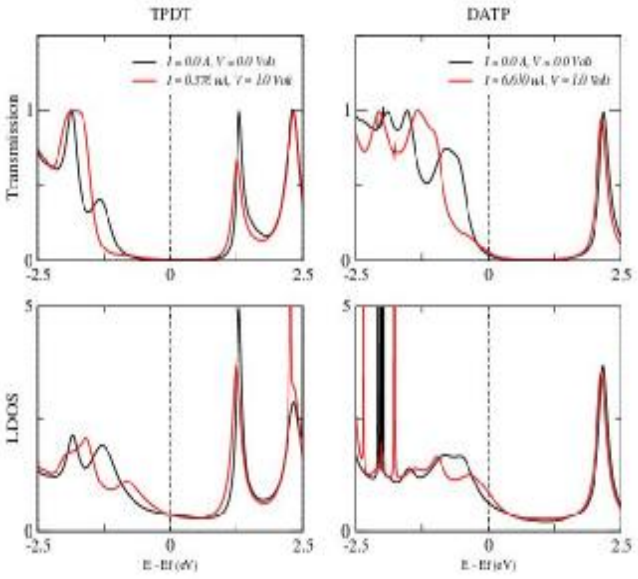

Fig. 2 Local density of states and Transmission of TPDT and DATP molecules in equilibrium and under applied bias.

In figure 2, we show the computed transmission as function of the energy for TPDT and DATP molecules in the same binding geometry. In zero-bias, concerning the thiol group, we find the Fermi energy is located in between the lowest unoccupied molecular orbitals (LUMO) energy and the highest occupied molecular orbitals (HOMO). In contrast result in Ref.15 for gold contacts case since the transport dominates on the HOMO. For the amine group, the conductance is

dominated by HOMO of the molecule and similar to earlier studies with the gold leads in Ref. 5. The HOMO and LUMO levels energy of both molecules broaden due to coupling of the molecules to the electrode. That also can be described by using appropriate anchoring groups to bind a molecule to the contacts and its effect on the molecular conductance. This is one of important factor in coherent transport through molecular junctions. The transport properties of each molecule are given in table 1 in detail.

Table l. Transport properties of the molecules

Properties	TPDT	DATP
HOMO - LUMO gap (eV)	2.88	3.04
Binding Energy (eV)	5.8	7.7
Conductance (Go)	0.0039	0.0388
Coupling strength (eV)		
- HOMO	0.0678	0.1234
- LUMO	0.0632	0.0840
Current at 1.0 Volt (mA)	0.5766	6.6102

In non-equilibrium condition, when the contacts have different chemical potential, i.e. one volt, the HOMO level of both molecules are shifted to the near Fermi energy. However, the current flowing through DATP molecule is higher about ten times than TPDT. That is clear since the transport of DATP is dominated of the HOMO.

IV. Conclusion

In summary, we have presented NEGF calculations for investigating quantum transport through terphenyl molecules with different anchoring groups and connected to copper leads. The broadening of the local density of states (LDOS) is related of the coupling strength or binding energy to the copper lead. There is direct relation between coupling strength, the metal-molecule binding energies for different anchoring groups and the conductance in this case.

V. Aknowlegments

We would like to thank A. Pecchia, B. Aradi and Prof. Thomas Frauenheim for short course of the DFTB+ code with NEGF extension. This work has been supported by Directorate of Higher Education (DIKTI) of the Republic of Indonesia and Stibet-DAAD Germany.

VI. References

1. M.A. Reed, J.Chen, A.M. Rawlett, D.W. Prince, J.M. Tour, *Appl. Phys. Lett.* 78, 3735 (2001).
2. C. Krezeminski, et al., *Phys. Rev. B* 64, 085405 (2001).
3. W. Tian, et al., *J. Chem. Phys*. 109, 2874 (1998).
4. L. Venkataraman, J.E. Klare, C. Nuckolls, M.S. Hybertsen, M.L. Steigerwalt, *Nature* 2006, 442, 904
5. A. Erbe et. al., *Small* 2010, 6, No. 14, 1529-1535
6. Z. Li. D.S. Kosov, *Phys. Rev. B*. 2007, 76, 035415.
7. S. Y. Queck, L. Venkataraman, H.J. Choi, S.G. Louie, M.S. Hybertsen, J.B. Neataon, *Nano Lett.* 2007, 7, 3477.
8. I.S. Kristensen, D.J. Mowbray, K.S. Thygesen, K.W. Jacobsen, *J. Phys.: Condens. Matter* 2008, 20, 374101.
9. Th. Frauenheim, G. Seifert, M. Eltsner, Z. Hajnal, G. Jungnickel, D. Porezag, S. Suhai, R. Scholz, *Phys. Stat. Sol (B)* 271 (2000) 41.
10. L.V. Keldysh, *Sov. Phys.* JEPT 20 (1965) 1018
11. S. Datta, *Electronic Transport in Mesoscopic System*, Cambridge University Press, Cambridge, 1995 (Chapter 3,8).
12. A. Pecchia and A. Di Carlo, *Rep. Prog. Phys*. 67 1497 (2004)
13. J.P. Perdew, K. Burke and M. Ernzerhof *Phys.Rev. Lett.* 77, 3865 (1996)
14. Garcia-Gil et al., Phys. Rev. B. 79, 754441(2009)
15. Cohen et. al., J. Phys. Chem. C, Vol. 111, No. 40, 2007

Wavelength Observation of Convective Pattern of Planar Nematic Liquid Crystal Using Image Processing

Sri Hartini [1,2*], ***Dwiria Wahyuni*** [1,3], ***Yusril Yusuf*** [1]
1 Department of Physics, Faculty of Mathematics and Natural Sciences, Gadjah Mada University
Sekip Utara PO BOX BLS.21 Yogyakarta Indonesia 55281
2 Department of Education of Natural Sciences, Faculty of Education, Lambung Mangkurat University
Jl.Brigjen H.Hasan Basri Kayutangi Banjarmasin Kalimantan Selatan Indonesia 70123
3 Department of Physics, Faculty of Mathematics and Natural Sciences, Tanjungpura University
Jl. Ahmad Yani Pontianak Kalimantan Barat Indonesia 78124

Abstract
Active response was given by planar nematic liquid crystal 4-methoxy-benziledene-4-n-buthyl-aniline (MBBA) when external electric field on certain frequency applied into samples. When applied voltage exceeds threshold voltage V_{EHD}, an electrohydrodynamics (EHD) effect appears and shows Williams Domain (WD) convective pattern. Observation of the convective pattern used a polarizing microscope integrated to CCD camera. Wavelength of WD pattern for planar samples with 50μm and 100μm of thickness has been measured using image processing with ImageJ software. The result showed that the wavelength of WD was in the same order as samples thickness and decreased linearly to frequency.
Keywords: *planar nematic liquid crystal, Williams Domain, image processing, wavelength*

* Corresponding author.
E-mail address: t2n_fis@yahoo.com

I. Introduction

Liquid crystals are also called as a mesophase material. The molecules in liquid crystals phase tend to align along a preferred direction as in crystal phase but they have fluidity of the liquids. One of liquid crystals types that used excessively in research is nematic liquid crystals, because its liquid crystal phase is at room temperature. The first type of nematic liquid crystals discovered was *4'-methoxy-benzylidene-4-butyl-aniline* (MBBA). At temperature 25°C, the MBBA has some physical properties such as dielectric anisotropy $\tilde{\varepsilon}_a = \tilde{\varepsilon}_{\parallel} - \tilde{\varepsilon}_{\perp} < 0$, electric conductivity anisotropy $\tilde{\sigma}_a = \tilde{\sigma}_{\parallel} - \tilde{\sigma}_{\perp} > 0$, and diamagnetic anisotropy $\tilde{\chi}_a = \tilde{\chi}_{\parallel} - \tilde{\chi}_{\perp} > 0$ [1].

In its equilibrium state, without influence of any external field, the molecules of nematic are homogeneously oriented. Its molecular orientation tends towards to one direction and called director (**n**). When an external field such as electric field applied into nematics, the molecules will give response [2]. In order to study the response of nematic liquid crystals to electric fields, the nematic liquid crystal is usually injected into a thin cell that consists of two parallel evaporated glass plates electrode (indium tin oxide; ITO). There are two typical alignments of the director **n** in nematic cell, namely planar alignment, where the director **n** = (n_x, n_y, n_z) has the initial state $\mathbf{n}_0 = (1, 0, 0)$, and the homeotropic alignment, where the director **n** has the initial state $\mathbf{n}_0 = (0, 0, 1)$ [3].

Many interesting phenomenon appear when an external electric field is applied on the nematic liquid crystal. One of the phenomenons is electrohydrodynamic (EHD) instability. EHD will appear when an electric voltage that induced into the nematic liquid crystal layer exceeds the threshold voltage (V_{EHD}). Mechanism of the EHD is described by Carr and Helfrich in Carr-Helfrich mechanism (CH) [3]. At onset EHD represents typically a regular array of convection rolls associated with a spatially periodic modulation of the director and the space charge distribution. Depending on the experimental conditions the nature of the roll patterns changes, which is reflected in particular in the wide range of possible wavelengths λ found. In many cases, λ scales with the thickness d of the nematic layer [4].

The frequency dependence of the EHD threshold was investigated theoretically in EHD mechanism [1]. There are two different regimes in EHD mechanism, respectively below and above a certain critical frequency f_c. At low frequency regime ($f<f_c$), the so called conductive regime, Williams Domain (WD) appears when a given

voltage is above the threshold voltage V_{EHD} [1-2]. At high frequency regime ($f>f_c$), the so called dielectric regime, a typical pattern called the dielectric chevron (DC) appears via defect turbulence [5].

The aim of this work is to observe the WD convective pattern on the conductive regime of planarly aligned nematic liquid crystal MBBA and measuring its wavelength by using image processing with *ImageJ* software.

II. Experimental Method

Nematic liquid crystal MBBA placed between parallel glass plates which are coated by ITO as electrodes. The thickness used for each sample was 50µm and 100µm according to the thickness of mylar spacer. Experiments were carried out at the initial planar alignment of director **n**. To provide uniform orientation of molecules to planar, the ITO glass of the Polyvinyl Alcohol (PVA) substrates were rubbed in one direction

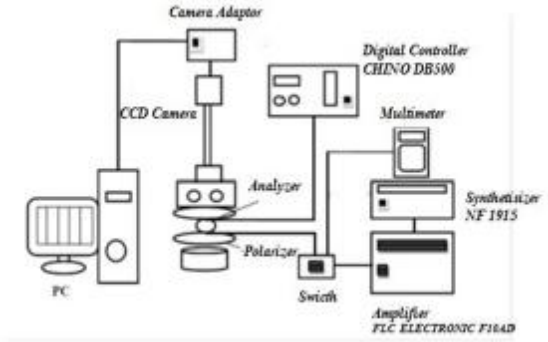

Figure 1. Experimental setup

The experimental setup is shown in Figure 1. The temperature of the samples was fixed at (30 ± 0.1) ° C. The sample was placed in a hot stage whose temperature is set by a digital temperature controller (Digital controller CHINO DB500). The electric field was generated by a function synthesizer (NF, 1915) and amplified by a voltage amplifier (FLC ELECTRONICS F10AD). The WD patterns were observed using a polarizing microscope (NIKON, OPTIPHOT2-POL) and captured by a charged couple devices (CCD) camera (Panasonic, WV-BD400) integrated to a personal computer (PC). *Pixel View* software was used to record the image into PC.

The wavelength of WD was observed by image processing with software ImageJ. The results of the analysis with ImageJ converted to micrometer scale of the micrometer objective. Hence, we had the wavelength of convective patterns in µm units.

III. Result and Discussion

Williams Domain (WD) convective patterns appear when the applied external field exceeds the threshold voltage V_{EHD} which is called WD voltage (V_{WD}).

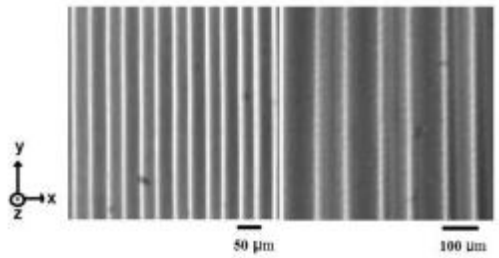

Figure 2. WD convective patterns at the frequency of 90 Hz with 50µm and 100µm of thickness.

Figure 2 shows the WD convective pattern emerged on samples of 50 µm and 100 µm of thickness at frequency of 90Hz. In Figure 2, the formation of convective patterns is in the form of a regular pattern of bright and dark lines parallel to the *y*-axis. This means that the director of WD convective pattern is perpendicular to the direction of the sample. According to de Gennes (1993), if dielectric anisotropy ($\tilde{\varepsilon}_a$) of the liquid crystal is negative (MBBA has negative $\tilde{\varepsilon}_a$) then the molecule will tend to take a direction perpendicular to a given field.

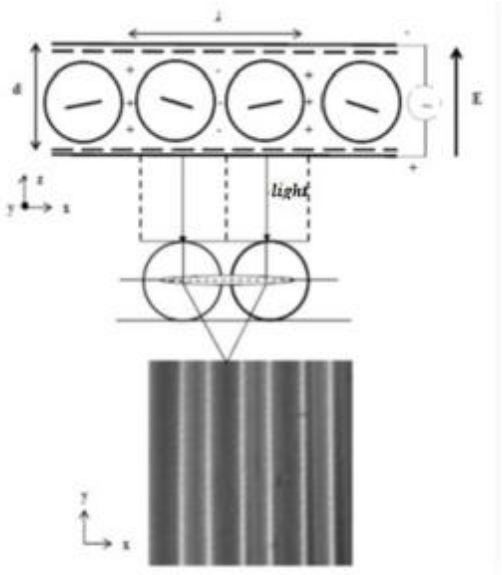

Figure 3. Wavelength of WD convective pattern

Definition of the wavelength of WD convective pattern is shown in Figure 3. It is defined as the length of three modulation of the convective pattern formed on the WD. In Figure 3, samples of the nematic liquid crystal MBBA with planar alignment assumed as optical lens. When light is transmitted through the liquid crystal

sample, due to its anisotropic, gives birefringence where one is perpendicular to the director and other is parallel to it. The dark lines caused by the refraction of light when passing through focus of the lens. Bright lines occur when light does not pass through the focus.

Wavelength of WD convective pattern obtained through the plot profile tool in units of pixels. For the conversion to μm unit, it was done by using a micrometer objective. After having the wavelength of the WD convective patterns, we plotted into a graph as in Figure 4 that showed a relationship between the wavelength and the frequency.

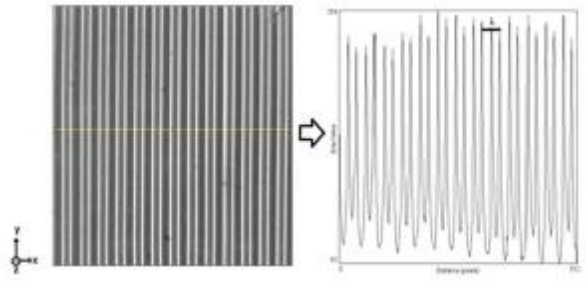

(a)

(b)

Figure 4. (a). WD convective pattern (b). Plot Profile ImageJ

Dependency between wavelength of WD convective pattern and frequency is shown in Figure 5. It gives a linear relation between wavelength and frequency up to 140 Hz of applied frequency. The frequency variation in this study is below the critical frequency.

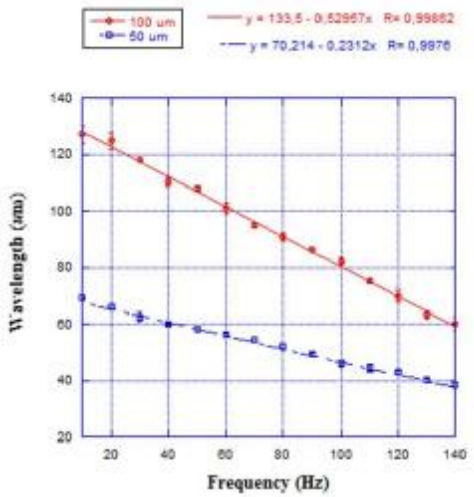

Figure 5. Dependency between wavelength of WD convective pattern and frequency.

Using image processing, differences of the wavelength (λ) of WD convective pattern's value of 50μm and 100μm of thickness can be observed. The wavelength is a distance of three bright lines. Figure 5 shows that the wavelength of WD convective pattern is decreased when the frequency is increased. It is also shows that the wavelength of WD of samples of 50μm of thickness is smaller than the 100μm one. This means that the WD convective pattern have a wavelength that is comparable to the layer thickness of nematic liquid crystal.

IV. Conclusion

The result showed that the wavelength of WD was in the same order as samples thickness and the wavelength of WD was decreased when the frequency was increased.

V. Acknowledgment

Authors wish to thank Dr. Rinto Anugraha for his guidance on image processing process on pattern formation images.

VI. References

1. de Gennes, P. G., and Prost, J., *The physics of Liquid Crystal*, 2nd edition, Clarendon Press, Oxford, 1993.
2. Chandrasekhar, S., *Liquid Crystal,* 2nd edition, Clarendon Press, Oxford, 1992.
3. Yusuf, Y., Prewavy Instabilities in Nematic Liquid Crystal, *Master Thesis*, Kyushu University, Japan, 2002.
4. Buka, A., Eber, N., and Pesch, W., *Electronic-Liquid Crystal Communication*, (2005)
5. Kai,S., Chizumi, N., and Kohno, M., *Physical Review A (General Physics),* 40, 11, 6554 (1989)

Doped TiO2 Anatase Photocatalyst Under Visible Light: A DFT-based Band Gap Analyses Study

Ganes Shukri, Wahyu Aji Eko Prabowo, Nugraha, Hermawan K Dipojono
Laboratory of Computational Material Design and Quantum Engineering
Engineering Physics Research Group, Faculty of Industrial Technology
Institut Teknologi Bandung, Jl. Ganesha 10, Bandung, 40132, Indonesia

Abstract

The photocatalytic reaction under visible light is considered as the most promising economically as well as environmental friendly for hydrogen production. TiO_2 doped with d-type metals is proposed as candidate for new functional catalyst materials in the photocatalytic processes. To uncover the physical phenomena responsible for the processes involved, the electronics structure of the proposed materials is investigated by using density functional theory (DFT). The presence of new states in the forbidden zone of doped TiO2 opens up the possibility of having a better catalytic properties than pure TiO_2. These findings are consistent with Standard Hydrogen Electrode (SHE) to carry out hydrogen reduction reaction (H^+/H_2) and oxidation reaction (H_2O/O_2). TiO_2 doped with (N, Fe) shall be a good alternative for photocatalyst materials.

Keywords : *Photocatalyst; N-doped TiO2; 3d transition metal; electronic structure; H_2O dissociation*

* Corresponding author.
E-mail address: ganesxv@gmail.com

I. Introduction

The increasing demand of world energy supply, which is mostly coming from fossil fuels, is unvoidable in order to support world economic growth [1]. Consequently the depletion rate of the world reserve of fossil fuels is continously increasing. In addition, the use of fossil energy has obvious serious damaging effects to global environment [2]. Hence the need of new and renewable energy sources is an urgent issue. Hydrogen based energy generation is one among a few other alternatives; Hydrogen may be used as fuels to generate electrical energy by using devices such as fuel cells. Hydrogen is the most abundant substance available on earth [3]. Nevertheless as the most active element hydrogen is always in the form of compounds, bonded with other chemical elements, such as with oxygen to form water molecule. Producing hydrogen from splitting water is environmental friendly process. However there is a huge obstacle to be resolved before such process become economically feasible. Splitting water into hydrogen and oxygen gases needs energy. To be economically feasible, the only reasonable energy sources to do so are those abundantly available without limit, at almost no cost, i.e. sun or visible light, wind, ocean wave, and etc. This paper will focus on exploiting sun or visible light for water splitting through photocatalytic phenomena by using photo activated substance, i.e. a photocatalyst [4].

There are varieties of materials that able to act as photocatalyst such as TiO2, SrTiO3, WO3, ZnO, BiWO6 and ZnS. TiO2 is the most investigated and developed because it has more advantages than the others [5]. However TiO2 in anatase phase has a wide band gap (Eg = 3.23 eV) which is serious drawback if one wants to use visible lights. TiO2 only reacts to UV light, a small fraction (about 5 %) of total sun irradiation on earth. In order to activate catalytic properties of TiO2 under visible light irradiation some works have been done in recent years such as: adding some impurities from transition metals [6-12], or non metal element [13-16], mixing with organic dye [17], adding some combination of transition metals with metal elements as impurities [18-20]. The presence of non metal in TiO2 structure may narrow the band gap; unfortunately narrowing the band gap will increase the rate of recombination and hence will decrease the photocatalytic activity. Meanwhile the presence of transition metals will create new states in the forbidden zone and can act as electron or hole traps. Consequently those transitions metals may avoid early recombinations. [21] This study will investigate the effect of the presence of both transition metals and non metals as impurities with the hope that the drawback of the one will be cancelled by the other and vice versa. As starting point, the focus will be directed toward the combination of nitrogen and iron (Fe) as impurities inside the anatase phase of TiO_2.

II. Computational Details

The calculations have been performed using density functional theory (DFT) [22-23] under the Kohn-Sham equation as implemented in the opEn Source Package for Research in Electronic Structure, Simulation, and Optimization (Quantum ESPRESSO) [24]. The ultra-soft pseudopotential method has been employed to describe the interaction between ion cores and electrons. The electron exchange correlation has been treated by a generalized gradient approximation (GGA) based on Perdew, Burke, and Ernzerhof (PBE) functional [25]. The planewave basis set with a cutoff energy of 300 eV is used for all calculations. For pure TiO_2 anatase model, we used a TiO_2 supercell (2 x 2 x 1) grid with 48 atoms, namely 16 atoms (Ti), 32 atoms (O), respectively. The Monkhorst-Pack method is used to sample k-points. By using a (3 x 3 x 3) k-point grid. Simulation model for the system with impurities is done by substituting one oxygen atom (O) with one nitrogen atom (N). Figures 1 and 2 show the structural models of TiO_2, TiO_2-N, and TiO_2-(N, Fe).

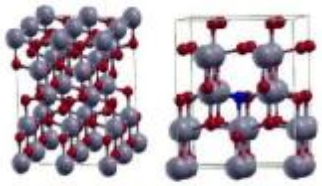

Figure 1: (left) Undoped TiO_2, (right) TiO_2-N. (red: oxygen; blue: nitrogen; grey: titanium)

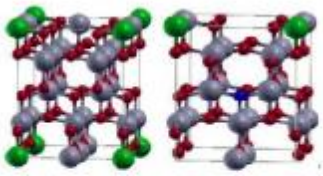

Figure 2: (left) TiO_2-TM, (right) TiO_2-(N, TM). where the green one is transition metals (TM), i.e Fe.

III. Results and Discussion

III. 1. Undoped TiO_2

Figure 3 shows an indirect gap about 2.3 eV for the undoped TiO_2 which is in a good agreement with previous theoretical studies by others [26-28]. However this result is not in agreement with the experimental result at about 3.23 eV. The discrepancy comes from excluding the presence of discontinuity in exchange correlation functional of DFT calculation method. Thus this study will only focus on electronic structure pattern variations for each type of doped TiO_2. In undoped TiO_2 the valence band edge is dominated by O 2p states and the conduction band edge is dominated by Ti *3d* states. These *3d* states break into two parts,i.e. t_{2g} (d_{xy}, d_{xz}, d_{yz}) and eg (d_{z2}, d_{x2-y2}). Consequently, the conduction band breaks into upper part (e_g > 3 eV) and lower part (t_{2g} <3 eV).

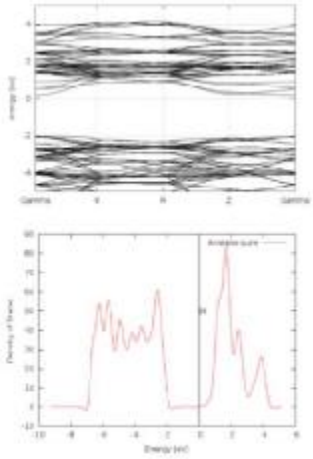

Figure 3: Undoped TiO_2. (left) band structure, (right) density of states

III. 2. Doped TiO_2: TiO_2-N

Figure 4 shows band gap at about 1.98 eV. Thus presence of N narrows the band gap of pure TiO_2 as much as 0.2 eV. It also show the creation of new states inside the forbidden zone, i.e. close to the valence band. The new states are dominated by N 2p state and forms shallow acceptors. The formation of the new states in turn activates the reactivity of TiO_2-N to visible lights.

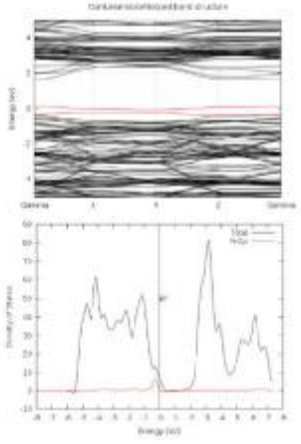

Figure 4: Doped TiO_2-N. (left) band structure (red: new states), and (right) density of states

III. 3. Doped TiO_2: TiO_2-Fe

Energy band structure calculation shows the creation of donor level in TiO_2-Fe. In other words, inside the forbidden zone, the new states are created far away from both maximum valence band and minimum conduction band. The new states are created very near to the Fermi level, i.e about 1.51 eV from the edge of the conduction band. It is crossing the Fermi level and obviously only some parts are occupied by electrons. Density of states analysis indicates that Fe *3d* state dominates the new energy level inside the forbidden zone. Some of unoccupied states are coinside with the conduction band of Ti *3d* and O *2p*. Electrons excitation process under UV and visible lights are predicted through several stages. First, electrons are excited from Fe *3d* states to conduction band. Second, electrons are excited from valence band to Fe *3d* states. However others are created very near, almost overlap with the conduction band and thus can act as electron traps. Figure 5 provides some additional insights.

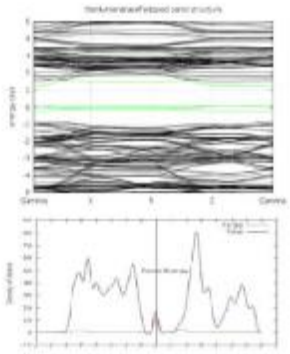

Figure 5: Energy band structure & density of state of TiO_2-Fe

III. 4. Doped TiO_2: TiO_2-Fe

Figure 6 shows the emergence of two states of impurities in TiO_2-(N, Fe). The energy level of impurities emerges because of hybridization of N *2p* and Fe *3d* states with a bit contribution from O *2p* states. Electron photoexcitation process under UV light occurs in several stages. Some Fe *3d* states behave as electron traps to reduce the rate of electron. The conduction bands consists of Fe *3d* and Ti *3d* energy levels while the valence bands are dominated by O *2p* and a few of occupied one. However, the higher the atomic number the more negative the potential of the impurity energy levels with the conduction and valence bands moving toward positive values.

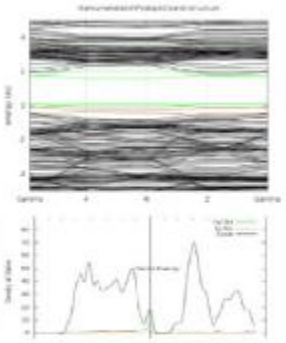

Figure 6: Energy band structure & density of state of TiO_2-(N, Fe)

IV. Conclusion

TiO_2-(N, Fe) may produce band structures that comply to SHE and thus may be able to conduct reduction reaction H^+/H_2 and oxidation H_2O/O_2. The presence of (N, Fe) impurities shifts the pure TiO_2 band structure to within the requirements for photocatalitic activities under visible lights.

V. Acknowledgement

The authors would like to express their gratitute to the Office of ITB's Vice Rector for Research and Innovation for generous financial support to this investigation. HKD would also to acknowledge the partial financial support from Directorate General of Higher Education of Republic of Indonesia through the Decentralization of Research Grant Project.

VI. References

1. IEA, *Key world energy statistics*, Paris: Stedi Media, 2008.
2. Liu P. I., *Energy, technology, and environment*, New York ASME Press, 2005.
3. Jain I. P., *Intl. J. Hydrogen Energy*, 34, 7368 - 7378, 2009.
4. Serponne N., and Pelizzetti E, Photocatalyst: *Fundamentals and Applications*, New York John Wiley and Sons, 1989.
5. Hashimoto K., Irie H., Fujishima A., *Japanese Journal of Applied Physics*, 44, 8269 - 8285, 2005.
6. Noor Shahina Begum, H.M. Farveez A., K.R. Gunashekar, *Bulletin of Material Science*, 31, 747-751,2008.

7. Cao K. N., Van K.N., Hoai A. N., Do T. N., Van M. N., *Advances in Natural Science: Nanoscience and Nanotechnology*, 2, 4, 2011.
8. Ha M. G., Jeong E. D.,Won M. S., Kim H. G., Pak H. K., Jung J. H., Shon B.H., Bae S.W., J. S. Lee, *Journal of the Korean Physical Society*, 49, S675 - S679, 2006.
9. Akihiko Kudo, *Catalyst Surveys from Asia*, 7, no. 1, 2003.
10. Ding Peng, Liu Fa-Min, Zhou Chuang-Cang, Zhong Wen-Wu, Zhang Huan, Cai Lu-Gang, Zeng Le-Gui, *China Physics B*, 19, 118 - 102, 2010.
11. M. Subramanian, S. Vijayalakshmi, S. Venkataraj, R. Jayavel, *Thin Solid Films*, 516, pp.3776 - 3782, 2008.
12. M. Iwasaki, M. Hara, H. Kawada, H. Tada, S. Ito, *Journal of Colloid and Interface Science*, 224, 202 - 204, 2000.
13. Mingce L., Weimin C., Zhengpeng W., Guangzeng L., *Chemical Physics Letter*, 420, 71 - 76, 2006.
14. Hongtao Gao, Jing Zhou, Dongmei Dai, Yadong Qu, *Chemical Engineering Technology*, 32, 867 - 872, 2009.
15. Kesong Yang, Ying Dai, Baibiao Huang, Shenghao Han, *Journal of Physics and Chemistry B*, 110, 24011- 24014, 2006.
16. D. J. Mowbray, J. I. Martinez, J. M. Garch Lastro, K. S. Thygesen, K.W. Jacobsen, *Journal of Physics and Chemistry C*, 113, 12301 - 12308, 2009.
17. Daimei Chen, Dong Yang, Jiaqin Geng, Juhong Zhu, Zhongyi Jiang, *Applied Surface Science*, 255, 2879 - 2884, 2008.
18. Wen-Xiu Liu, Jing Ma, Xiao-Guang Qu, Wen-Bin Cao, *Research on Chemical Intermediate*, 35, 321 - 328, 2009.
19. Zongyan Zhao, Qingju Liu, *Catalytic Letter*, 124, pp. 111 - 117, 2008.
20. Hu Yun, Xia Zhang, Chaohai Wei, *Material Science Forum*, 620-622, 683 - 686, 2009.
21. R. Dholam, N. Patel, M. Adami, A. Miotello, *International Journal of Hydrogen Energy*, 34, 5337 - 5346, 2009.
22. P. Hohenberg andW. Kohn, *Phys. Rev*, 136, B864, 1964.
23. W. Kohn and L. J. Sham, *Phys. Rev*, 140, A1133, 1965.
24. Paolo G. et al, *Journal of Physics: Condensed Matter*, 21, 39, 2009.
25. J. P. Perdew, K. Burke, M.Ernzerhof, *Phys. Rev. Lett*, 77, 3865, 1996.
26. Arny L. Linsebigler, Guangquan Lu, John T. Yates, Jr., *Chemical Reviews*, 95, 735 - 758, 1995.
27. Lichao Jia, Congcong Wu,Song Han, Nian Yao, Yuanyuan Li, Zongbao Li, Bo Chi, Jian Pu, Li Jian, *Journal of Alloy and Compounds*, 509, 6067 - 6071, 2011.
28. Zhahoui Z., Mingtao L., Liejin G., *Journal of Physics and Chemistry of Solids*, 71, 1707 - 1712, 2010.

The Effect of MnO_2 addition on The Electrical Characteristics of Fe_2TiO_5 Ceramics Sintered at 1200°C for NTC Thermistors

Wiendartun[a,b], *Risdiana*[c], *Fitrilawati*[c], *Dani Gustaman Syarif*[d], *R.E. Siregar*[c]

[a]*Program Doktor Ilmu Kimia Fisika, FMIPA, Padjadjaran University (UNPAD), Jl.Dipati Ukur No.35 Bandung, Indonesia.*
[b]*Department of Physics, Indonesia University of Education (UPI), Jl. Dr. Setiabudhi No.229 Bandung, Indonesia , Email: wien_upi@yahoo.com*
[c]*Department of Physics , Padjadjaran University (UNPAD), Jl.Raya Bandung-Sumedang km 21 Jatinangor Sumedang, Indonesia*
[d]*Physics of Materials Group, Physics Division, PTNBR BATAN, Jl. Tamansari No.71 Bandung , Indonesia*

Abstract.

The effect of MnO_2 addition on the characteristics of Fe_2TiO_5 ceramics for NTC thermistors has been studied in order to produce high performance thermistor. Powder of MnO_2 derived from commercial with various concentration of : 0, 0.5 and 1.0 mole % were mixed homogeneously in appropriate proportions to produce Fe_2TiO_5 based ceramics. The mixed powders were pressed with pressure of 4 ton/cm^2 to form pellets. The green pellets were sintered at 1200°C for 2 hours in furnace air. Electrical characterizations of the pellets were done by measuring electrical resistivity (ρ_{RT}) of the sintered ceramics at various temperatures from 55°C to 310°C. The pellets were also subjected to XRD and SEM analyses in order to know crystal structure and microstructure of the pellets. The XRD data showed that the dominant phase of the all ceramics was Fe_2TiO_5. According to the electrical data, it was found that adding MnO_2 to the Fe_2TiO_5 increased the thermistor constant (B) and the electrical resistance of the ceramics decreased with the increase of the MnO_2 concentration. Thermistor constant (B) of the ceramics was relatively big of 5146.4°K to 6612.4°K. The value of B indicated that adding MnO_2 to the Fe_2TiO_5 will increase performance of NTC thermistor..

Key words: *Ceramic, Thermistor, NTC, Fe_2TiO_5 , MnO_2,*

I. Introduction

It has been known that NTC thermistor could be applied in many applications such as temperature sensor, electric current limiter, and flow rate meter and pressure sensor [1]. The NTC thermistor is generally made of ceramic having structure of spinel of AB_2O_4 where A is the ion occupies tetrahedral position and B is the ion occupies octahedral position [2-6]. Although a report on NTC thermistor for higher temperature is available [5], however, the publication of the NTC thermistor with higher operation temperature made of Fe_2TiO_5 is not available so far. Compared to the traditional NTC thermistor material, Fe_2TiO_5 has higher bandgap so suitable for higher temperature operation. It is known that the traditional thermistor working temperature is up to 100°C [4]. In this work, the possibility of the application of the Fe_2TiO_5 ceramic for NTC thermistor with higher working temperature was studied.

Doping may be done to improve the performance of the NTC thermistor. The addition of dopant into the Fe_2TiO_5 ceramic may increase the thermistor constant which then improves the performance of the thermistor. Many efforts have been being performed in order to improve the characteristic of the spinel NTC thermistor. Fe_2TiO_5 ceramic is one of some ceramics that can be applied for NTC thermistor. The thermistor may be produced in the form of pellet, thick or thin film Here, the object of study is the pellet thermistor form. In this work, a study on the effect of MnO_2 addition on the electrical characteristics based on Fe_2TiO_5 ceramics for NTC thermistor was performed.

II. Methodology

Powders of Fe_2O_3, TiO_2, and MnO_2 were weighed in appropriate proportions to fabricate MnO_2 added-Fe_2TiO_5 ceramics and mechanically mixed. Powder of MnO_2 derived from commercial with various concentration of : 0, 0,5 and 1,0 mole % were mixed homogeneously in appropriate proportions to produce Fe_2TiO_5 based ceramics. The mixed powders were pressed with pressure of 4

ton/cm^2 to form pellets. The green pellets were sintered at 1200°C for 2 hours in furnace air.

The crystal structure of the sintered pellets was analyzed with x-ray diffraction (XRD) using Kα radiation at 40KV and 30mA. The microstructure of the pellets was investigated by scanning electron microscopy (SEM). Before electrical investigation, the pellets were polished and etched. The opposite-side surfaces of the sintered pellets were coated with Ag paste. After the paste was dried at room temperature, the Ag coated-pellets were heated at 700°C for 10 minutes.

Electrical characterizations of the pellets were done by measuring electrical resistivity (ρ_{RT}) of the sintered ceramics at various temperatures from 55°C to 310°C. using a digital multimeter and a laboratory made chamber equipped with a digital temperature controller. The pellets were also subjected to XRD and SEM analyses in order to know crystal structure and microstructure of the pellets.

Thermistor constant (B) was derived from Ln resistivity vs. $1/T$ curve where B is the gradient of the curve based on (1)[10]:

$$\rho = \rho_o . \exp (B/T) \quad (1)$$

Where, ρ is the electrical resistivity, ρ_o is a constant or the resistivity at T is infinite, B is the thermistor constant and T is the temperature in Kelvin.

Room temperature resistance (R_{RT}) was determined as the electrical resistance at room temperature and sensitivity (α) was calculated using (2) [6].

$$\alpha = B/T^2 \quad (2)$$

Where, α is the sensitivity, B is the thermistor constant and T is the temperature in Kelvin.

III. Results and Discussion

Fig. 1 shows the appearance a typical green pellets. The ceramics are visually good, it shown by smooth area surface.

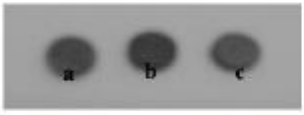

Fig.1. Visual appearance of typical MnO_2 Added-Fe_2TiO_5 ceramic. (a. 0,0, b. 0.5 and c. 1.0 mole % MnO_2)

XRD profiles of Fe_2TiO_5 green pellets ceramics sintered at 1200°C for 2 hour in the furnace air , respectively are shown in Fig.2, Fig.3 and Fig.4. As shown in the figure Fig. 2, Fig.3 and Fig.4 the profiles are generally similar. The XRD profiles show that the structure of the pellets ceramics is pseudobrookite after being compared to the XRD standard profile of Fe_2TiO_5 from JCPDS No.41-1432). The fabrication of the ceramics has been well done at 1200°C it shown in this data . Diffraction peaks from MnO_2 were not observed . It may be due to solid solution formation or the coincidence of peaks of MnO_2 and Fe_2TiO_5 or due to small concenration of doped MnO_2 . The absent of the additional peaks in the XRD patterns of MnO_2 added-samples may indicate that the main grain boundary material is the same structure with the matrix.

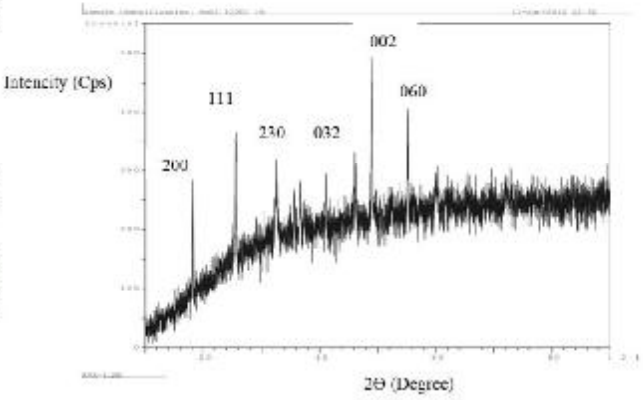

Fig. 2. XRD profile of Fe_2TiO_5 pellett ceramic without MnO2

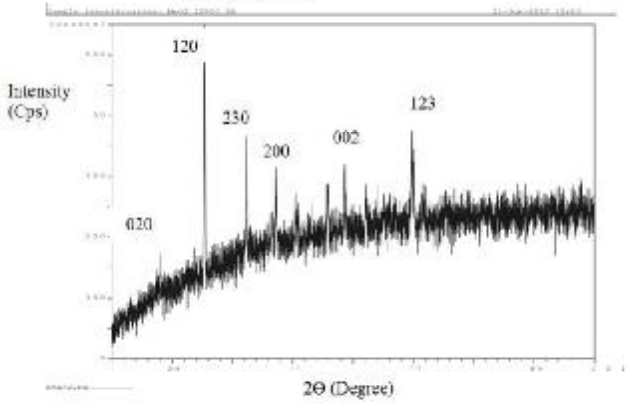

Fig.3 .XRD profile of 0.5 mole % MnO_2 added-Fe_2TiO_5 Ceramic

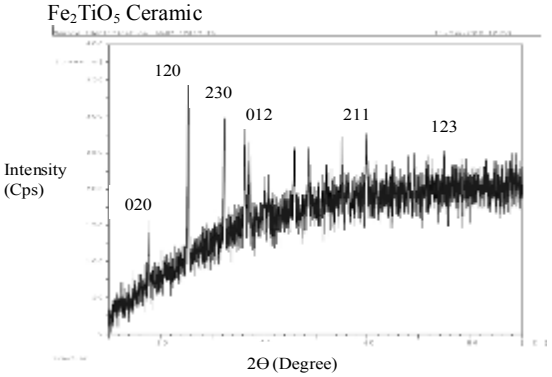

Fig.4 .XRD profile of 1,0 mole % MnO_2 added-Fe_2TiO_5 Ceramic

Fig.5, Fig.6 and Fig. 7 are microstructures of the Fe_2TiO_5 ceramics added with 0.0, 0.5.and 1.0 % mole MnO_2, respectively.

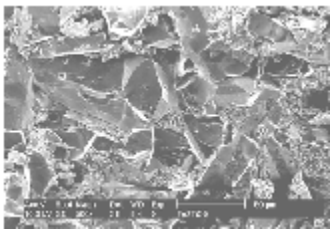

Fig. 4. Microstructure of the Fe_2TiO_5 ceramic without MnO_2

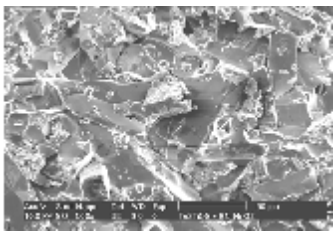

Fig. 5. Microstructure of the 0.5 mole % MnO_2 added- Fe_2TiO_5 ceramic.

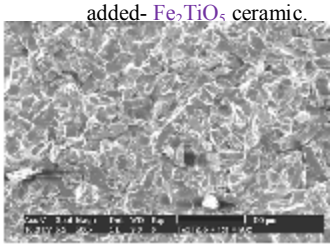

Fig. 6. Microstructure of the 1.0 mole % MnO_2 added- Fe_2TiO_5 ceramic.

From Fig. 5, Fig. 6 and Fig. 7 it can be seen that the Fe_2TiO_5 ceramics has small grains and addition of MnO_2 decreases the grain size. The grain size of of the Fe_2TiO_5 ceramics added with 0.0, 0.5.and 1.0 % mole MnO_2, respectively 6.73 µm, 5.16 µm, and 4.07 µm. The effect of the MnO_2, addition is not clearly seen, because the change is quite small. The absent of the additional peaks in the XRD patterns of MnO_2 added-samples may indicate that the main grain boundary material is the same structure with the matrix.

The electrical data of the MnO_2 added-Fe_2TiO_5 eramics is shown in Fig.7 and Table 1.

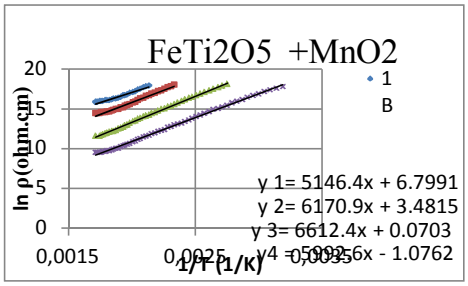

Fig. 7. Ln resistivity (ρ) vs. 1/T of MnO_2 added-- Fe_2TiO_5 ceramics.

Table 1. Electrical characteristics of the MnO_2 added-- Fe_2TiO_5 ceramics.

Additive of MnO_2 (mole %)	B (K)	E_a (eV)	α (%/K)	ρ_{RT} (Mohm.cm)
0.0	5146.4	0.71	1.51	25076.41
0.5	6170.9	0.85	1.81	23594.63
1.0	6612.4	0.91	1.94	3964.39

The electrical data of Fig. 7 shows that the electrical characteristics of the ceramics follow the NTC tendency expressed by eq. 1. As shown in Table 1, the addition of MnO_2 decreases the room temperature resistivity (ρ_{RT}) and increases the thermistor constant (B). Compared to those of Felts [5] the thermistor constant in Table 1 is larger Compared to the commercial thermistor constant provided by American Zetler [1] the thermistor constant value of Table 1 is also larger and compared to the (B) value for market requirement where $B \geq 2000^oK$, the value of B for our ceramics

is larger and it means that our ceramics are better and fitted these for market requirement.

IV. Conclusion

The XRD data showed that the dominant phase of the all ceramics was Fe_2TiO_5. According to the electrical data, it was found that adding MnO_2 to the Fe_2TiO_5 increased the thermistor constant (B) and the electrical resistance of the ceramics decreased with the increase of the MnO_2 concentration. Thermistor constant (B) of the ceramics was relatively big of 5146.4^{o}K to 6612.4^{o}K. The value of B indicated that adding MnO_2 to the Fe_2TiO_5 will increase performance of NTC thermistor..

Acknowledgment

It is a pleasure to acknowledge many helpful sugges-tions from Yamin, NiLuh, Eva and Sri (BATAN-Indonesia University of Education)

References

[1] Anonymous, NTC Thermistor, American Zetler, Inc., Available at www.azetler.com.

[2] R. Metz, Electrical properties of NTC thermistors made of manganite ceramics of general spinel structure;$Mn_{3-x-x'}M_xN_{x'}O_4$($0\leq x+x'\leq 1$;M and N being Ni,Co or Cu). Aging phenomena study, Journal of Materials Science 35 (2000) 4705-4711.

[3] M. Vakiv, O. Shpotyuk, O. Mrooz, I. Hadzaman, Controlled thermistor effect in the system $Cu_xNi_{1-x-y}Co_{2y}Mn_{2-y}O_4$, Journal of the European Ceramic Society 21 (2001) 1783-1785.

[4] Wiendartun, D.G. Syarif, Electrical characteristics of $CuFe_2O_4$ thick film ceramics with different glass concentrations fired at 1000^{o}C for negative thermal coefficient (NTC) thermistor, Journal of Materials Science Research, 1(3) (2012) 70-75.

[5] A. Feltz, W. Polzl, Spinel forming ceramics of the system $Fe_x Ni_y Mn_{3-y-x} O_4$ for high temperature NTC thermistor applications, Journal of the European Ceramics Society 20 (2000) 2352-2366.

[6] G. D. C. Csete de Gyorgyfalva, I. M. Reaney, Decomposition of $NiMn_2O_4$ spinel: an NTC thermistor material, Journal of the European Ceramics Society 21 (2001) 2145-2148.

The study on X-ray diffraction patterns of the cardanol compound of CNSL isolation from NTT Province

Zakarias Seba Ngara[1],
Igusti M. Budiana[2], Aliwarsito[3], Selviana Rambu Patti[4], Febi Nanggo[5]
1, 3, 4 and 5 Physics Department, Nusa cendana Univesity, Kupang
e-mail : Zakarias_vdm@yahoo.com
2. MIPA Department, Nusa Cendana University, Kupang

ABSTRACT

The study on X-ray diffraction patterns of cardanol compound that is isolated of CNSL from Alor district of NTT province has been done. These researching aims to find the crystal structure, crystallinity, and grain size of cardanol compound. It is obtained from isolation of CNSL. These sample is annealing on temperature of 400 ^{0}C, 500^{0}C, 600^{0}C and 700^{0}C. Then it is analyzed by X-ray diffraction method in order to obtain its X-ray diffraction patterns. Based on its X-ray diffraction patterns analysis, one can obtain a) the crystal structure of cardanol compound that is annealing on temperature of 400^{0}C is amorphus. While as the structure crystal of cardanol compound that is annealing on temperature of 500^{0}C is the same crystal structure of Tin Methylammonium Bromide ($CH_6Br_3NS_n$) with ID number is 32-1927. Furthermore, the crystal structure of cardanol compound that is annealing on temperature of 600^{0}C and 700^{0}C is the same Uranium Oxide Phosphate (U_3 O_5 P_2 O_7) with ID number : 34-148 . b) if annealing temperature is morethan 500^{0}C, cardanol compound has crystal structure, d) crystallinity of cardanol compound is high on annealing temperature more than 500^{0}C , c) the higher annealing temperature, the smaller grain size of cardanol compound .

Key words : *cardanol compound , X-ray diffraction patterns, Crystal structure, crystallinity, grain size*

INTRODUCTION

At present, The research on physics properties of organic materials as alternative active material on electronics device is developing very fast [1]. It is in consequence of the cost of Organic material is cheaper than anorganic material and the fabrification of electronics device based organic material using by spin coating and evaporator [2]. One of the organic material as local potential from Alor, NTT Province that is investigated in this researching is *Anacardium occidentale L*. One of compound that is containing the skin of Anacardium occidentale L is cardanol compound [3,4]. On june, 2009, Ngara, et.al, in competitive grant, have determined energy gap of cardanol compound and cardanol complex compound from province NTT. Based on their researching result, their energy gap are 2.58 eV and 2.48 eV, respectively [5]

In 2010, Ngara, et.al, have fabrificated prototype of organic solar cell based cardanol complex compound from Alor District, Province NTT. The efficiences of this prototype is 1.1 % [6]. One of parametre that is contribution on optic properties of material is its structure ordering. Therefore, These researching aim to study on X-ray diffraction patterns of cardanol compound that is isolated of CNSL from Alor district of Province NTT. Based on its X-ray diffraction patterns, one can find crystal structure, crystalinity and grain size of cardanol compound.

Cashew Nut Shell Liquid (CNSL) and cardanol compound

There are some districs in East Nusa Tenggara that is producing of *Anacardium occidentale L*, i.e Kupang, Belu, Alor, East Flores, Sikka, West Sumba, and East Sumba [5]. CNSL can be obtained from extraction result of *Anacardium occidentale L* skin . If CNSL is isolated, one can obtain cardanol compound. In classification systematic, *Anacardium occidentale L* has Divisio: Spermatofita, Subdivisio: Agiospermae, class: Dikotiledoneae, Ordo: Sapindales, Familia: Anacardiaceae, Genus: Anacardium, Spesis : *Anacardium occidentale L* [3].

The molecule structure of cardanol compound shown in Fig.1. There are some researchers that have studied physics properties of cardanol compound from NTT, i.e:

a. In 2008, Ngara & Budiana have find energy gap of CNSL [7].
b. In 2009, Lalus, at al have find mechanics and optic property of CNSL from Alor [8]
c. In, 2009, Laka has find viscousity and refraction index of CNSL from East Sumba [9]
d. In 2009, Ngara, et.al have find energy gap of cardanol compound and cardanol complex compound [5].
e. In 2010, Ngara, at al have find efficiences of solar cell prototype based cardanol complex compound [6]

f. In 2011, Rambu Patti has studied x-ray diffraction patterns of CNSL from East Sumba [10]

Crystalstructure

The patterns of X-ray diffraction from a material can be used for determination crystal structure, crystal plane, grain size, and crystallinity. X-ray diffraction method is based on bragg law, i.e [11]

$$2d \sin\theta = n\lambda \quad (1)$$

Where d, θ, n, λ is distance of crystal planes, diffraction angular, diffraction order, and wave length, respectively.

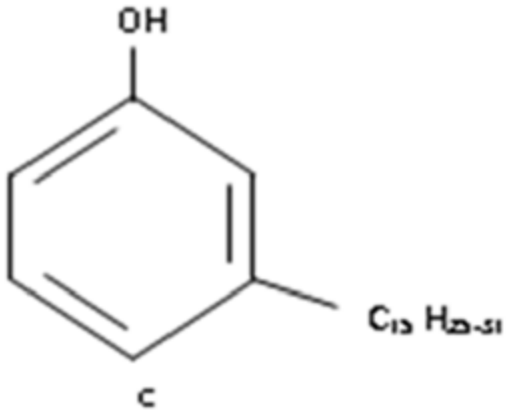

Figure 1. Molecule structure of cardanol compound

In order to find the crystal structure of a material, it is used Hanawalt card method. In this method, one can compare between crystal plane distance from three highst peaks of sample and standard material that have same value. The diffraction peaks of sample and standard meterail is obtained from its X-ray diffraction patterns and PCPDFWIN program, respectively. If the value of crystal plane distance of sample material is the same of material standard, the crystal structure of sample material is the same crystal structure of standard material.

Crystallinity of a material is comparation between five crystal planes distance of sample and standard that has highst intensity. Mathematically, crystallinity (C_r) can be wrote [12]

$$C_r = \frac{\sum_{i=1}^{5} d_{i\,SP}}{\sum_{i=1}^{5} d_{i\,ST}} \quad (2)$$

where d_{SP} and d_{ST} are crystal plane distance of sample and standard material that has highst intensity, respectively.

In order to find grain size of a material, it is used Scheerrer equation, i.e [11]

$$L = \frac{0,9\lambda}{FWHM \times \cos\theta} \quad (3)$$

Experimental

Preparation of cardanol compound sample

The preparation of sample include extraction, destilation, evaporation and isolation process of *CNSL*.

Analysis of sample by using X-ray diffraction method

cardanol compound is made four treatments, i.e sample is annealing on temperature of 400^0C, 500^0C, 600^0C, and 700^0C, respectively. Then, they are analyzed using X-ray diffraction method in chemistry department, UGM, Yogyakarta.

Results and Discussion

The study on X-ray diffraction patterns of cardanol compound that is annealing on temperature of 400^0C.

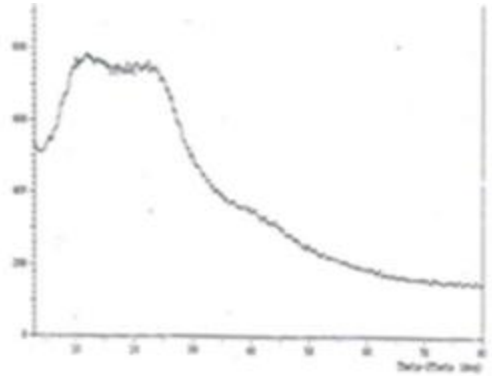

Figure 2. The patterns of X-ray diffraction of cardanol compound that is annealing on temperature of 400^0C

X-ray diffraction patterns of cardanol compound that is annealing on temperatuire of 400^0C shown in Fig.2. Based on Fig.2, the crystal structure of cardanol compound is amorphous. It is mean, annealing process on temperature of 400^0C can not make yet crystal structure of cardanol compound. Therefore, one can't find crystal structure, crystallinity, and grain size of cardanol compound

The study on X-ray diffraction patterns of cardanol that is annealing on temperature of 500^0C

X-ray diffraction patterns of cardanol compound that is annealing on temperature of 500^0C shown in Fig.3. Based on Fig.3, three peaks that have highst intensity is occurred on diffraction angular of $2\theta = 30.28^0$, $2\theta = 33.96^0$, and $2\theta = 41.36^0$. The distance of their crystal planes is 2.95 Å, 2.63 Å and 2.18 Å. Based on those crystal planes distance values and using Hanawalt card method with helping PCPDFWIN program, crystal structure of this cardanol compound is the same crystal structure of Tin Methylammonium Bromide ($CH_6Br_3NS_n$) with ID number in PCPDFWIN program is 32-1927. The highst diffraction peak is occurred on diffraction angular of

30.28^0. It is mean, on diffraction angular of 30.28^0, cardanol compound has periodic layer structure. The other mean, cardanol has many crystal planes that has same miller index.

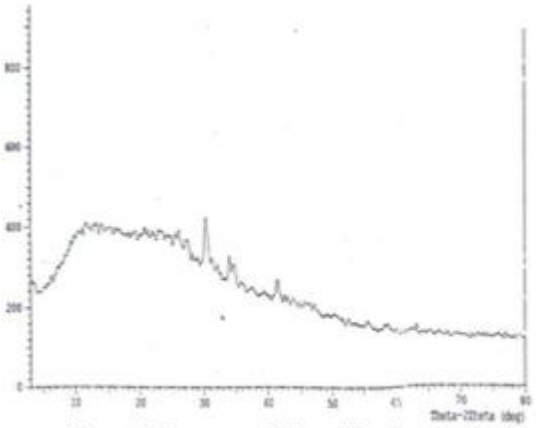

Figure 3. The patterns of X-ray diffraction of cardanol compound that is annealing on temperature of 500^0C

The grain size of cardanol compound on diffraction angular of $2\theta = 30.28^0$, $2\theta = 33.96^0$, and $2\theta = 41.36^0$ is 25.99 nm, 42.33 nm and 40.84 nm, respectively. The average size of its grain size is 36.38 nm. In this paper, it is given calculation example of grain size on $2\theta = 30{,}28^0$ with FWHM = 0,6333, is

$$d = \frac{0{,}9 \times 0{,}154nm}{\left(\frac{0{,}6333}{2} \times \frac{3{,}14}{180}\right) \times \cos\left(15{,}14^0\right)} = 25{,}99nm.$$

The annealing process on temperature of 500^0C can change cardanol structure, i.e from amorphous structure to crystal structure. It is mean cardanol compound has high crystallinity.

The study on X-ray diffraction patterns of cardanol that is annealing on temperature of 600^0C

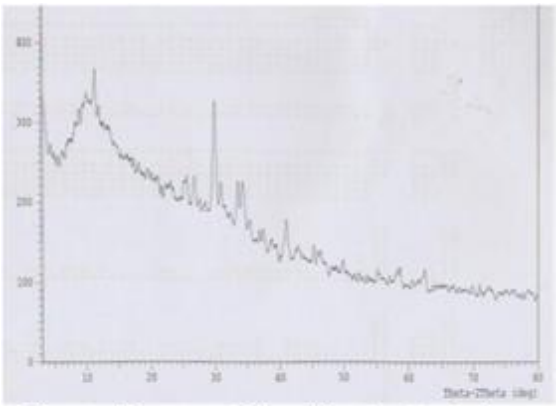

Figure 4. The patterns of X-ray diffraction of cardanol compound that is annealing on temperature of 600^0C

X-ray diffraction patterns of cardanol compound that is annealing on temperature of 600^0C shown in Fig.4. Based on Fig.4, three peaks that have highst intensity is occurred on diffraction angular of $2\theta = 29{,}79^0$, $2\theta = 11{,}22^0$, dan $2\theta = 34{,}24^0$. The distance of their crystal planes is $d = 2{,}9970$ Å, $d = 7{,}8508$ Å, and $d = 2{,}6165$ Å, respectively . Based on those values and using Hanawalt card method with helping PCPDFWIN program, crystal structure of this cardanol compound is the same crystal structure of Uranium Oxide Phosphate ($U_3\ O_5\ P_2\ O_7$) with ID : 34-1487. The highst diffraction peak is occurred on diffraction angular of 29.79^0.

Based on Fig.4, The grain size of this cardanol compound on diffraction angular of $2\theta = 29.79^0$, $2\theta = 11.22^0$, and $2\theta = 34.24^0$ is 30.01 nm, 33.03 nm, and 27.41nm, respectively. The average size of its grain size is 30.15 nm.

Based on Fig.3 and Fig.4, the number of diffraction peaks of cardanol compound that is annealing on temperature of 600^0C is more than cardanol compound that is annealing on temperature of 500^0C. It is mean the higher annealing temperature, the higher crystallinity of cardanol compound.

The study on X-ray diffraction patterns of cardanol that is annealing on temperature of 700^0C

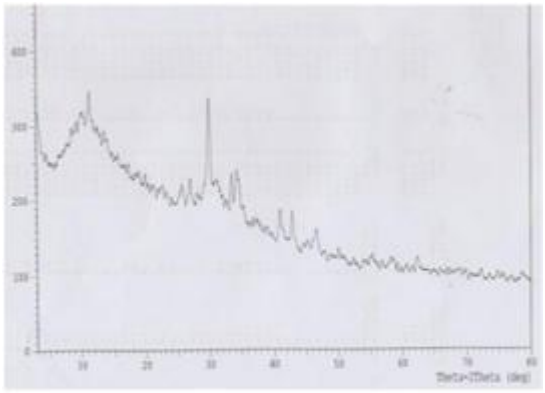

Figure 5. The patterns of X-ray diffraction of cardanol compound that is annealing on temperature of 700^0C

X-ray diffraction patterns of cardanol compound that is annealing on temperatutre of 700^0C shown in Fig.5. Based on Fig.5, three diffraction peaks that have highst intensity is occurred on diffraction angular of $2\theta = 29{,}860$, $2\theta = 11{,}300$, dan $2\theta = 34{,}180$ with their crystal planes distance are $d = 2{,}9898$ Å, $d = 7{,}8207$ Å, and $d = 2{,}6212$ Å, respectively . Based on those values and using Hanawalt card method with helping PCPDFWIN program, crystal structure of this cardanol compound is the same crystal structure of Uranium Oxide Phosphate ($U_3\ O_5\ P_2\ O_7$) with ID : 34-1487. The highst diffraction peak is occurred on diffraction angular of 29.86^0.

Based on Fig.5, The grain size of this cardanol on diffraction angular of $2\theta = 29.86^0$, $2\theta = 11.30^0$, and 2θ

= 34.18^0 is 31.02 nm, 33.07 nm, and 27.51 nm, respectively. The average size of its grain size is 30,41 nm. Based on Fig.4 and Fig.5, the patterns of their x-ray diffraction almost is the same.

There are some phenomena from diffraction patterns of cardanol compound, i.e

a) When annealing temperature is morethan 500^0C, Cardanol compound has crystal structure.
b) The higher annealing temperature, the higher crystallinity of cardanol compound. These statement is true if annealing temperature lie $500^0C \leq t^0C \leq 700^0C$.
c) Crystal structure of cardanol compound that is annealing on temperature of 500^0C is not the same crystal structure of cardanol that is annealing on temperature of 600^0C and 700^0C.
d) On diffraction angular of $2\theta = 29{,}8^0$, cardanol compound has highest diffraction peak. It is caused on $2\theta = 29{,}8^0$, cardanol has a number of peaks that has same miller index.

Conclusion

When annealing temperature is morethan or equal 500^0C, Cardanol compound has crystal structure. The structure crystal of cardanol compound that is annealing on temperature of 500^0C is the same crystal structure of Tin Methylammonium Bromide ($CH_6Br_3NS_n$) with ID number is 32-1927. While as crystal structure of cardanol compound that is annealing on temperature of 600^0C and 700^0C is the same Uranium Oxide Phosphate ($U_3\ O_5\ P_2\ O_7$) with ID number : 34-148, On diffraction angular of $2\theta = 29{,}8^0$, cardanol compound has highst diffraction peak. the higher of annealing temperature, the smaller of grain size of cardanol compound and the higher its crystallinity.

Suggestion

It is need to study X-ray diffraction patterns of cardanol compound for annealing temperature is more than 700^0C.

Acknowledgements

These researching obtains financial from DP2M in Jakarta. Therefore, In this case, The author thanks for DP2M that has given financial in national strategy grant.

Refference

1. Ngara, Z.S., Bunganaen, Y., Budiana, IG, M.N., Dule, M., Patty, R., Laetia, K., The study on X-Ray Diffraction Patterns of Flavonoid Compound of *Sterculia Urceolata Smith* Extraction Yield from Kupang district, NTT Province, *Proceeding international conference on X-ray Microscopy and smart materials*, ISBN: 987-602-99344-0-3 (2011)

2. Triyana, K., Yasuda, T., Fujita, K., and Tsutsui, T., Effects of Different Materials Used for Internal Floating Electrode on the Photovoltaic Properties of Tandem Type Organik Solar Cell, *Jpn. J. Appl. Phys.* 43, 2352 (2004)

3. Muljoharjo, Anacardium Occidental L. and Technology,, Liberty, Yogyakarta, (1990).

4. Budiana, I..M.N., Isolation and Identification of Cardanol Compound from East Flores, *Buletin of researching and developmental of IAEUP Alumna,* Undana, Vol. 7, ISSN : 1412-3703, (2005).

5. Ngara,Z.S., Aliwarsito, Budiana, I.M.N., Synthesis of Compound Derivative of CNSL as Alternative Active Material in Organic Solar Cell Prototype, final report in competitive grant researching, Undana, Kupang, (2009)

6. Ngara,Z.S., Aliwarsito, Budiana, I.M.N., Fabrication of Organic Solar Cell Prototype Based Cardanol Complex Ccompound from Alor, NTT Province. Final report in Vocher grant researching, Undana, Kupang, (2010)

7. Ngara,Z.S., & Budiana, I.M.N., The Study on Absorption Spectra and Determination Energy Gap of CNSL from NTT as Alternative Active Material in Electronics Device, final report of youth lecture researching, Undana, Kupang, (2008).

8. Lalus, H.F., Amitiran, I., Mala, H.U., *The study on mechanics and optic property of CNSL from NTT*, researching final report in student creativity program, Physics Department, Undana, Kupang, (2009)

9. Laka, A., 2009, *Determination viscousity and refraction index of CNSL from East Sumba*, Thesis S1, Physics Department, Undana, Kupang, (2009)

10. Patti, S.R, *The Study on X-ray Diffraction patterns of CNSL from East Sumba, Thesis S1,* Department Physics, Undana, Kupang, (2010)

11. Cullity, B.D., *Elements of X-Ray Diffraction*, second edition, Addison-Wesley Publishing Company, INC, California, (1978)

12. Ngara, Z.S, The Study on Optic property and Determination Crystal Structure of 3,4,9,10-Perylene Tetracarboxilic Diimide, Thesis S2, Department Physics, UGM, Yogyakarta, (2006)

Change in Microstructure of Kenaf Fiber due to Chemical and Steam Treatments

H. Sosiati[1,2]*, Harsojo[1,3], Soekrisno[1,4], R. Widyorini[5], D.A. Wijayanti[3], K. Triyana[1,3]
1Nanomaterials Research Group, LPPT, Gadjah Mada University, Indonesia
2The Graduate School, Gadjah Mada University, Indonesia
3Department of Physics, Faculty of Mathematics and Natural Sciences, Gadjah Mada University, Indonesia
4Mechanical Engineering Department, Faculty of Engineering, Gadjah Mada University, Indonesia
5Department of Forest Product Technology, Faculty of Forestry, Gadjah Mada University, Indonesia

Abstract

We have presently addressed our attention on changes in microstructure of kenaf fiber due to chemical and steam-chemical treatments. Better understanding of microstructural properties of kenaf fiber is necessary for developing kenaf fiber-reinforced composites. Raw kenaf fibers were firstly dried at 70ºC for 30 minutes. The chemical treatment was done by immersing dried kenaf fibers in 10 g/L NaOH (mercerization) at ~100ºC for 1 h and followed by bleaching in solution of X g/L NaOH and Y ml/L H_2O_2 under similar condition to mercerization. The ratio of the fiber and chemical solution was 1: 100. X and Y were 5 and 20, and 10 and 100. Two grams of Teepol were added in mercerization and bleaching solutions to reduce the surface tension of fiber surface. Steam pre-treatment was carried out with a pressure cooker under 1.8 Bar (~117ºC) for 20 minutes, followed by scouring and bleaching. Chemical and steam-chemical treated kenaf fibers were then mechanically treated with a ultrasonic cleaner for various durations to completely remove the non-cellulosic components and to decompose kenaf macrofibers to be micro and nano scales. Microstructural observations of kenaf fibers by scanning electron microscopy (SEM) have summarized the following results. Bleached fibers with lower amount of H_2O_2 showed pores-like damage on fiber surface, while higher amount of H_2O_2 tended to efficiently reduce the fiber size (diameter), increase in removing the non-cellulosic components and improve the brightness of fibers. Steam pre-treatment at ~117ºC for 20 minutes improved the decomposition of macrofiber to microfiber and increased the crystalline properties. A part of decomposition to be nanofiber revealed in chemical treated fibers followed with longer mechanical treatment. It has been suggested that decomposition to be nanofiber could be accelerated with prolong steam pre-treatment and mechanical treatment after bleaching. The present results are expected to provide useful information.

Keywords: kenaf fiber, chemical, steam, SEM, microstructure

* Corresponding author.
E-mail address: hsosiati@gmail.com

I. Introduction

Nowadays, increase of standard human life will correlate with material use and environmental effect. Natural fiber based composites as green material have been declared to be used in wide range of applications due to the advantage properties such as low cost, low density, non-toxicity, biodegradability, environmentally safe and lower level of skin irritation [1].

Presently, we have paid great attention on the natural fiber used in automotive application. It is known that some kinds of natural fibers such as kenaf, abaca, hemp, flax and jute are good in their high mechanical properties [2]. This makes good reinforcement of polymer composite for the automotive components. However, those fibers cannot be cultivated well in Indonesia except kenaf.

Studies on the properties of kenaf by various treatments have been previously reported. The properties of kenaf fiber were drastically degraded after immersing in the acid and base solutions for about 140 days. Degradation of the properties was explained due to ions and chemical degradation which formed the fiber damage [3]. Tensile strength of kenaf tended to increase with increasing volume fraction of fibers, while decrease with heat treatment higher than 150ºC [4]. Decomposition of kenaf macro fibers to be micro and nano fibers was carried out by pulping, bleaching, acetylation and mechanical refining [5]. A similar work has been reported without acetylation [6]. Efforts to improve the properties

of kenaf fibers by combining treatments, however, are still opened for discussion.

In our investigation, we have characterized microstructure of kenaf fibers after chemical and steam-chemical treatments in comparison to raw kenaf. Better understanding of microstructural properties of kenaf fiber is necessary for developing kenaf fiber-reinforcing composites.

II. Experimental

Specimen used in this investigation is Indonesian cultivated kenaf obtained from Balitass, Malang, Indonesia. Raw kenaf fibers were dried in an oven at 70ºC for 30 minutes. The chemical treatment was done by immersing dried kenaf fibers in alkaline (NaOH) as called mercerization and followed by bleaching solution of NaOH and H_2O_2 at similar condition (~100ºC, 1 hour) as shown in table 1. Ratio of the fiber and chemical solution was 1:100. Two grams of Teepol were added in mercerization and bleaching solutions to reduce the surface tension of fiber surface. Steam pre-treatment was carried out with a pressure cooker under 1.8 Bar (~117ºC) for 20 minutes, followed by scouring and bleaching. Duration of steam pre-treatment was started after reached the pressure of 1.8 Bar.

Table 1. Treatment condition of kenaf fibers

Specimen	Treatments		
	Scouring (~100ºC, 1 h)	Bleaching (~100ºC, 1 h)	Ultrasonic Cleaner (h)
S10-B52	10 g/L NaOH	5 g/L NaOH+ 20 ml H_2O_2	1
S10-B10	10 g/L NaOH	10 g/L NaOH+ 100 ml H_2O_2	1, 6
ST20-SB10	Steam (20`) +10 g/L NaOH	10 g/L NaOH+ 100 ml H_2O_2	1

Based on the differences in duration of mechanical treatment, specimens were designated as follows. S10-BS52(1), S10-B10(1), S10-B10(6) and ST20-SB10(1).

After scouring, the fibers were washed with distilled water and remaining NaOH was neutralized with CH_3COOH, then again washed with distilled water. Washing the fibers with run distilled water was also done after bleaching. In order to improve in removing the non-cellulosic components and decomposition of the fibers, mechanical treatment with a ultrasonic cleaner (Power Sonic, LUC-405) was carried out by immersing the fibers in ethanol. Mechanical treatment for 1 hour was conducted on all specimens for comparing their microstructural changes. Extension time of mechanical treatment for 6 hours on S10-B10 was to understand how far the ultrasonic cleaner can efficiently work to decompose the fibers.

Microstructure of untreated and treated kenaf fibers was examined by scanning electron microscopy (SEM, INSPEX S50-FEI). Crystalline properties of the fibers were qualitatively analyzed from x-ray diffraction results (XRD, X`Pert Pro, PAN Analytical).

III. Results and Discussion

Drying condition used in present work was an optimum condition. Drying at higher than 70ºC would break the fiber structure and maximum of moisture removal was attained in 30 minutes. Figure 1 shows SEM micrograph of dried raw kenaf fibers with high surface roughness. Average diameter of fiber is around 100 μm. In this case, a fiber is a bundle of crystalline micro or nano cellulose fibers covered with amorphous phases of non - cellulosic components [7].

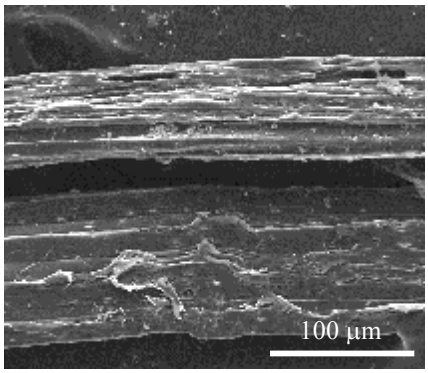

Figure 1. SEM micrograph of dried raw kenaf fibers

Microstructure of S10-B52(1) and S10-B10(1) in similar magnification is demonstrated in figure 2 (a) and (b), respectively. It is clearly exhibited that there are some different features between them. Fiber size (diameter) of S10-B52(1) appears larger than that of S10-B10(1), but individual microfiber in S10-B10(1) cannot be obviously recognized. They seem to tightly bind with each other, indicating that amorphous phase of non - cellulosic components still remain at around the fibers. In addition, pore-like damage as indicated by white arrows are distinctly shown on fiber surfaces in S10-B52(1), but not in S10-B10(1). However, surface roughness of fibers in S10-B10(1) seems to be higher compared with that in S10-B52(1). NaOH is well kown as a chemical solution that can partially remove the non-

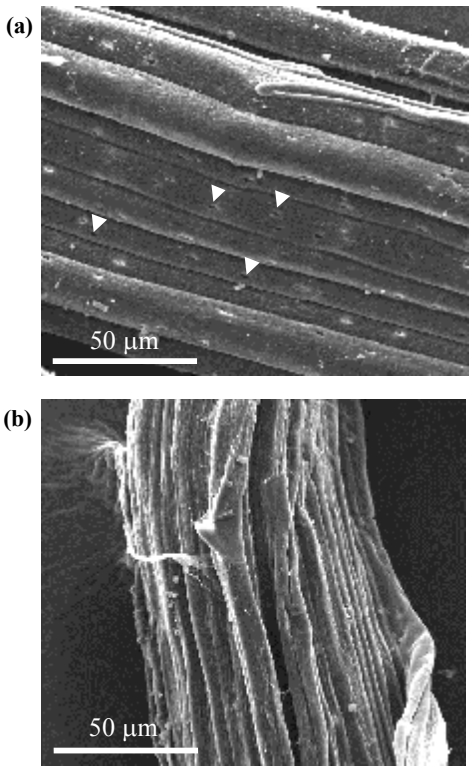

Figure 2. Microstructure of chemical treated kenaf fibers. (a) specimen S10-B52(1) and (b) specimen S10-B10(1).

cellulosic components and increase surface roughness. When NaOH was added on the fibers, the OH groups present in the fibers will react with NaOH as follows [8, 9],

$$\text{Fiber-OH} + \text{NaOH} \rightarrow \text{Fiber-ONa} + H_2O$$

Removing non-cellulosic components would be improved by bleaching in (NaOH and H_2O_2) and completed by mechanical treatment. It is considered that addition of H_2O_2 in bleaching solution played a significant role on microstructural changes of fiber. In this case, bleaching with higher amount of H_2O_2 does not only improve the brightness of fibers, but also tends to efficiently reduce the fiber size, increase in removing the non-cellulosic components. To high amount of H_2O_2, however, seemed to reduce bleaching efficiency.

In addition, with prolong the duration of mechanical treatment for 6 hours after bleaching, changes in microstructure of S10-B10(6) is presented in figure 3. Both microfiber (d: less than 5 μm) and nanofiber (d varies from about 100 nm to larger than 100 nm) are clearly seen in this figure. Microfibers in this specimen are separated from each other, indicating relatively free from covering the non-cellulosic components. It is also interestingly shown that a part of microfibers started to decompose to be nano-fibers even though the size distribution is still non-uniform. This suggests that as duration of the mechanical treatment after bleaching is longer, the formation of nanofibers will be gradually completed.

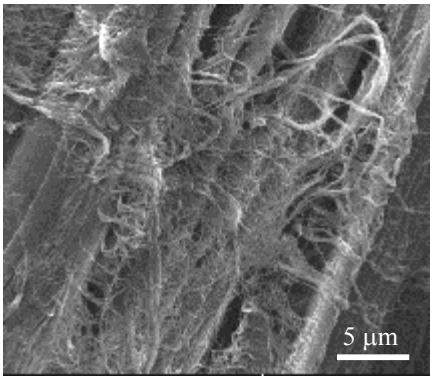

Figure 3. Microstructure of chemical treated kenaf fibers: specimen S10-B10(6)

On the other hand, steam pre-treatment for 20 minutes in ST20-SB10(1) reveals slightly changes in microstructure as illustrated in figure 4. Detail observation on this figure recognizes individual microfiber clearer than that in S10-B10(1). It is emphasized, therefore, that steam pre-treatment provides effect in improving the removal the non-cellulosic components. In other words, the decomposition of macrofibers to be microfibers could be accelerated with steam pre-treatment.

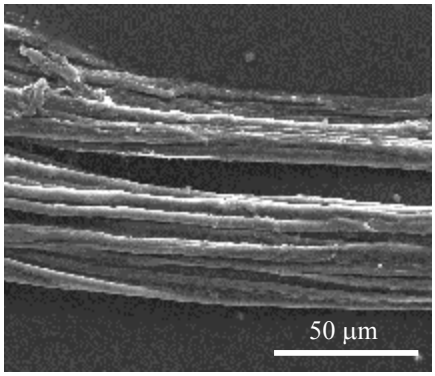

Figure 4. Microstructure of steam-chemical treated kenaf fibers: specimen ST20-SB10(1)

Steam pre-treatment by explosion technique for isolated cellulose has been reported by Ibrahim *et al*. [10]. High volume fraction of cellulose with high crystallinity is resulted from the treatment at longer explosion residence times.

In addition, steam explosion raises the crystallinity of the cellulose component [11]. Steam pre-treatment (not by explosion technique) in this work that was carried out at lower temperature and longer duration in comparing with the work in Ref. [10]. This treatment also increases the crystalline properties in ST20-SB10(1) meaning the steam pre-treatment promotes the cleavage of the non-cellulosic components and maintains the crystalline microfibers [11]. Higher crystalline properties in ST20-SB10(1) than that of in the S10-B10(1) is qualitatively indicated from the following XRD patterns. Figure 5 (a) and (b) depict XRD patterns of S10-B10(1) and ST20-SB10 (1), respectively. Both results show

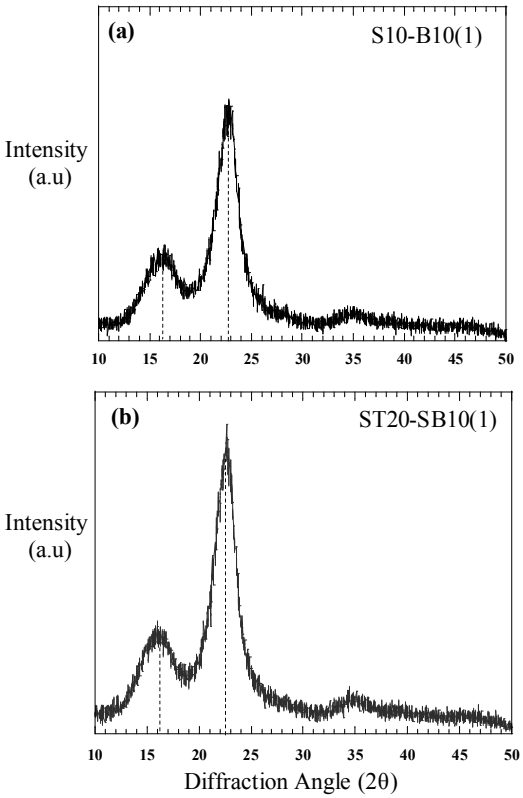

Figure 5. XRD patterns of treated kenaf fibers (a) Specimen S10-B10(1) and (b) specimen ST20-SB(10)(1).

maximum intensity at the position of 2θ close to 22.6º related to crystalline structure of native cellulose. These patterns also reveal that peaks in ST20-SB10(1) are slightly sharper than that in S10-SB10(1) attributed to full weight of half maximum (FWHM) for peak at 2θ = 22.6º in ST20-SB10(1) accompanied by a higher intensity. This smaller in FWHM states and the higher intensity indicates a larger in crystallite size and a better degree of crystallinity [12].

IV. Conclusions

Microstructural observations on raw and treated kenaf fibers by SEM have summarized the following results.

1. Raw kenaf fibers revealed as macrofibers whose average diameter is 100 μm.
2. Bleached fibers with lower amount of H_2O_2 showed pores-like damage on fiber surface, while higher amount of H_2O_2 tended to efficiently reduce the fiber size (diameter), to increase in removing the non-cellulosic components and to improve the brightness of fibers.
3. Steam pre-treatment at ~117ºC for 20 minutes improved the decomposition of macrofibers to microfibers and increased the crystalline properties.
4. A part of decomposition to be nanofibers in chemical treated had to be followed with longer mechanical treatment.
5. The decomposition to be nanofibers could be accelerated with prolong steam pre-treatment and mechanical treatment after bleaching.

V. References

1. M. Zampaloni, F. Pourboghrat, S.A. Yankovich *et al.*, *Composites: Part A*. 38, 1569 (2007).
2. D. Rouison, M. Sain, M. Couturier, *Compos. Sci. Technol*., 64, 629 (2004).
3. N. Nosbi, H. M. Akil, Z. A. M. Ishak and A. Abu Bakar, *BioResources*, 6, 950 (2011).
4. S. Ochi, *Machanics and Materials*, 40, 446 (2008).
5. M. Jonoobi, J. Harun, A. Shakeri, M. Misra and K. Oksman, *BioResources*, 4, 626 (2009).
6. M. Jonoobi, J. Harun, A. P. Mathew, M. Z. B. Hussein and K. Oksman, *Cellulose*, 17, 299 (2010).
7. C. Siqueira, J. Bras and A Dufresne, *Polymer*, 2, 728 (2010).
8. K. C. C. Carvalho, D. R. Mulinari, H. J. C. Voorwald and M. O. H. Cioffi, *BioResources*, 5, 1143 (2010).
9. H. M. Akil, M. F. Omar, A. A. M. Mazuki *et al*., *Materials and Design*, 32, 4107 (2011).
10. M. M. Ibrahim, F. A. Agblevor and W. K. El-Zawawy, *Bioresouces*, 5, 397 (2010).
11. W. G. Glasser and R. S. Wright, *Biomass Bioenergy*, 14, 219 (1998).
12. J. F. Revol, A. Dietrich and D. A. I. Goring, *Can. J. Chem*., from www.nrcresearchpress.com

Synthesis of Magnetite (Fe_3O_4) Nanoparticles and Their Potency as Active Materials for Surface Plasmone Resonance (SPR)-Based Biosensor Application

Agus Riyanto, Desi Listiawati, and Edi Suharyadi
Department of Physics, Faculty of Mathematics and Natural Sciences, Universitas Gadjah Mada
Sekip Utara PO BOX BLS.21 Yogyakarta 55281

Abstracts
Magnetite nanoparticles of different size ranging 11.9-14.9 nm have been synthesized chemically by co-precipitation method. It was synthesized by $FeSO_4.7H_2O$ and $FeCl_3.6H_2O$ with ratio 1:2. The spinel cubic structure was obtained and was identified by x-ray and transmission electron microscopy (TEM). The result of magnetic properties measurement using vibrating sample magnetometer (VSM) shows that the smaller grain size of magnetite nanoparticles has higher response to external magnetic field and has low coercivity. The potency analyses of magnetite nanoparticles as active materials on SPR-based biosensor application were done by making single layer on surface of magnetite nanoparticles using poly ethylene glycol (PEG-4000). After that, the target biomolecules, alpha-amylase, was added on magnetite nanoparticles which were modified by PEG-4000. According to image which was taken by microscope, surface modification of magnetite nanoparticles can improve their dispersibility in fluid. The analysis of infra-red spectroscopy (FTIR) shows that surface of magnetite nanoparticles can be modified with PEG-4000. The covalent bond Fe-O has been created by Fe atoms of magnetite and O atoms of PEG-4000. In addition, FTIR analysis shows that PEG-4000 layer can bind alpha-amylase (biomolecules) effectively. So, the smallet grain size of magnetite nanoparticles has great potency to improve immobilization of biomolecules on the sensing surface of SPR-based biosensor.

Keywords : magnetite nanoparticles, surface modification, biomolecules.

E-mail address: ariyanto165@yahoo.com

I. Introduction

Recently, SPR-based biosensor was developed as a biomolecules detection device. The SPR-based biosensor was developed by many researchers because it has a good sensitivity. However, in the practice, there is a problem in detection process, so it was not optimal. The problem was caused by immobilization of biomolecules on sensing surface was not maximal. To improve detection process is needed active materials which can immobilize target biomolecules on sensing surface, so the process of biomolecules detection becomes more effective and efficient.

Magnetite nanoparticles are magnetic materials which have a good potency as candidate of active materials to increase accumulation of target biomolecules on sensing surface of SPR-based biosensor. The potency of magnetite nanoparticles is responsive to external fields magnetic and dispersive on biology fluid [1]. Besides, the Iron atoms (Fe) on surface of magnetite nanoparticles have reactive properties to another material. For example, in the water medium, much Fe atoms on surface of magnetite nanoparticles will bind oxygen atoms (O) of water molecules. Hence, magnetite nanoparticles can be modified their surface by certain materials which have active site such as several polymers. Magnetite nanoparticles modified by polymers have a good potency to bind biomolecules [2].

In design of biomolecules immobilization using magnetite nanoparticles, the external magnetic field or permanent magnetic is needed to guide magnetite nanopaticles which have bound biomolecules in order to it can be immobilized on sensing surface of SPR-based biosensor. The design of biomolecules immobilization using magnetite nanoparticles was shown in Figure 1.

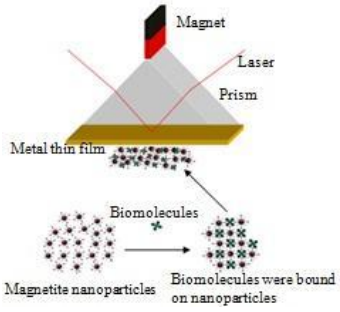

Figure 1. The model of magnetite nanoparticles utilization as active materials on SPR-based biosensor [3]

According to Figure 1, magnetite nanoparticles which have a good response to external magnetic fields are needed to immobilize biomolecules on sensing surface. So, the purpose of this research is to study relationship between grain size of magnetite nanoparticles and its responsibility to external magnetic fields. Furthermore, the purpose of this research is also to analyze the potency of magnetite nanoparticles to immobilize biomolecules. If, magnetite nanoparticles can be utilized as active materials in SPR-based biosensor application, the process of biomolecule detection will be done quickly, more effective, and efficient.

II. Materials and Method

Magnetite nanoparticles were prepared by co-precipitation method. 4,170 g of $FeSO_4.7H_2O$ and 8,109 g of $FeCl_3.6H_2O$ were dissolved into 30 ml of deionized water until were gotten precursor solution. The precursor was added 60 ml NH_4OH solution. After that, it was stirred by magnetic stirrer under certain temperature. The procedure will be continued with decantation process to get sample of Fe_3O_4 nanoparticles. The sample was washed until clean and then was dried on temperature 80^{o}C. After that, it was analyzed their crystal structure, grain size, and their magnetic properties by x-ray diffractometer (XRD), TEM, and VSM.

The sample of magnetite nanoparticles was prepared again to analyze their potency of which binding biomolecules. The process of preparation i.e.: 0.5 g of magnetite nanoparticles was mixed by 0.5 g of PEG-4000 which was melted on temperature 40^{o}C until homogeny. So, the surface of magnetite nanoparticles was coated by PEG-4000. Then, alpha-amylase molecules were added into magnetite nanoparticles which were modified by PEG-4000. Nanoparticles which have added by alpha-amylase were analyzed their dispersibility and chemical reaction using microscope and infra red spectroscopy (FTIR).

III. Result and Discussion

The Figure 2 shows XRD pattern of four samples which have different grain size. The grain size of samples was calculated by Scherrer equation. The arising of diffraction peaks which have Miller index (220), (311), (400), (511), and (440) shows that have been formed cubic spinel stucture of magnetite in all samples [4,5]. Estimation of lattice parameter shows that samples have lattice parameter close to reference (8,397Å) [5] like is showed in Table 1.

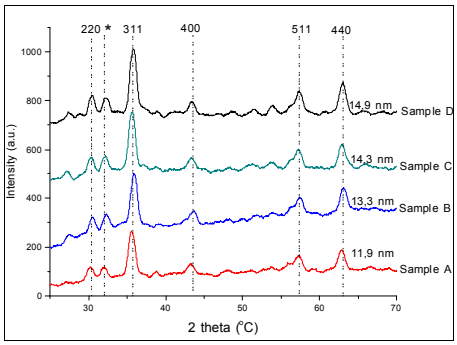

Figure 2. XRD patterns of magnetite nanoparticles (symbol * represent impurity)

Table 1. Grain size and lattice parameter of magnetite nanoparticles

No	Sample	Grain size (nm)	Lattice parameter
1	A	11,9	8,336
2	B	13,3	8,281
3	C	14,3	8,343
4	D	14,9	8,321

Figure 3 shows morphology and diffraction pattern of sample A. The diffraction pattern on Figure 3 shows rings pattern which related to Miller index of magnetite structure. The disscontinue pattern represents a good crystalinity in sample of magnetite. According to Figure 3, we can observe that grain size of magnetite under 20 nm. Besides, the shape of magnetite nanoparticles close to spherical geometry. The characteristic of magnetite which shows in Figure 3 gives information that it has a great potency for active materials in SPR-based biosensor application.

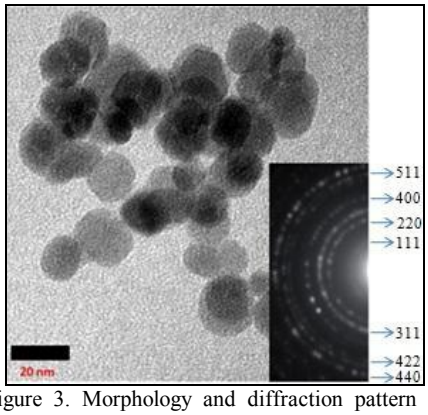

Figure 3. Morphology and diffraction pattern of magnetite nanoparticles

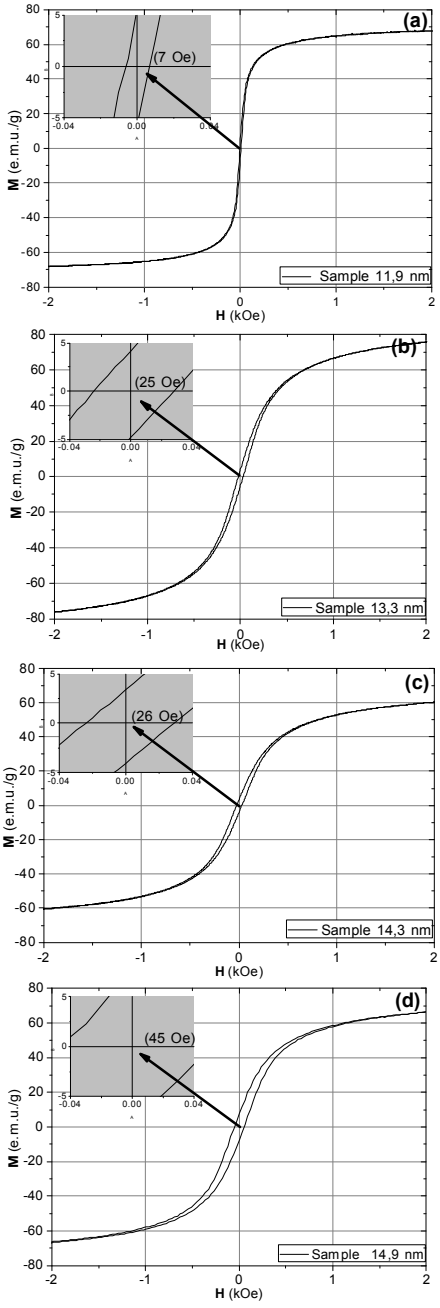

Figure 4. Hysteresis loop of magnetite nanoparticles

Figure 4 shows hysteresis loop of magnetite nanoparticles which have different grain size. These measurements show that the smallest grain size of magnetite nanoparticles so it has greatest response to external magnetic fields. It can be observed in Figure 4 (a) where the magnetization curve in this sample has the largest slope (gradient). The increasing of grain size causes gradient of hysteresis curve more decrease. It gives indicating that the response to external magnetic fields of magnetite nanoparticles is weaker. In addition, the increasing grain size of magnetite also leads to increase coercivity of samples. This phenomenon indicates that the energy barrier (anisotropy energy) of magnetite nanoparticles more increases if grain size of magnetite grows. Thus, it takes strong external magnetic fields to align magnetic moment on magnetite nanoparticles which has bigger grain size. From study of magnetic properties of magnetite nanoparticles, we get information that magnetite nanoparticles which have the smallest grain size have a great potency for active materials on SPR-based biosensor application.

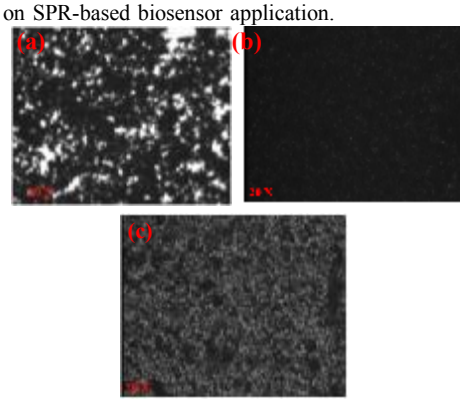

Figure 5. Modification of magnetite nanoparticles and complex reaction to biomolecules (a) magnetite nanoparticles, (b) magnetite nanoparticles have been modified by PEG-4000, and (c) the appearance of complex reaction between magnetite nanoparticles modified by PEG-4000 and alpha-amylase (biomolecules)

The utilization of magnetite nanoparticles as active materials not only depends on the magnetic properties and dispersibility of magnetite nanoparticles in biology fluid but also depends on being active of magnetite binds biomolecules. Therefore, nanoparticles which have been obtained by process synthesis were modified by PEG-4000. Actually, surface modification of magnetite nanoparticles can improve dispersibility of sample effectively as is shown in Figure 5 (b). In addition,

the layer of PEG-4000 can bind biomolecules (alpha-amylase) as shown in Figure 5 (c).

The FTIR analysis shows that the Fe atoms on surface of magnetite nanoparticles can be modified by PEG-4000. Magnetite nanoparticles were modified by PEG-4000 through Fe-O bond which was formed by Fe atoms on surface of magnetite and O atoms of PEG-4000 polymer chains. In spectrum 6 (c), the deep of Fe-O bond vibrations is located at wavenumber 563.21 cm^{-1}. If the deep compared by unmodified nanoparticles (spectrum 6 (a)), it has shifted. In unmodified nanoparticles, the Fe-O vibration is at wavenumber 578.60 cm^{-1}. The shifting of the deep indicates presence of PEG-4000 on surface of nanoparticles. It is also confirmed by the appearance of new absorbance deep at wavenumber 455.20 cm^{-1} and 401.19 cm^{-1} which associated by vibrations of Fe-O bound (spectrum 6 (c)) [6,7,8,9].

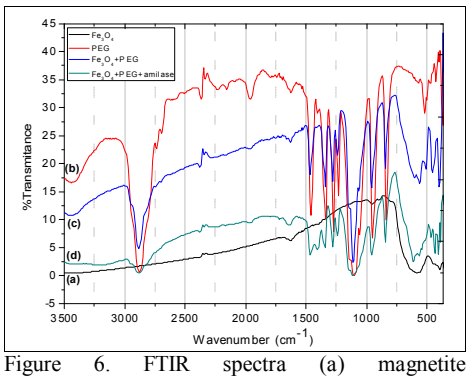

Figure 6. FTIR spectra (a) magnetite nanoparticles, (b) PEG-4000, (c) magnetite nanoparticles have modified by PEG-4000, and (d) magnetite+PEG-4000+alpha-amylase

Spectrum 6 (d) is spectrum of magnetite+PEG-4000+alpha-amylase system. The spectrum has pattern almost similar to the spectrum of magnetite+PEG-4000 system. It was caused by alpha-amylase has monomer chains which composed by identical molecules bond with PEG-4000. Besides, every bond which connects PEG-4000 and alpha-amylase is covalent C-O bond also, where the type of bond is also a constituent chain of PEG-4000. Nevertheless, the spectrum of magnetite+PEG-4000+alpha-amylase system has a new absorbance deep which is located at wavenumber 1404.61 cm^{-1}. The deep of 1404.61 cm^{-1} is a deep associated by C-O bond vibration [10]. The appearance of C-O vibrations at this wavenumber is predicted as a new bond between PEG-4000 and alpha-amylase. This phenomenon shows that apha-amylase can be bound by the PEG-4000 on surface of magnetite nanoparticles. Thus, magnetite nanoparticles which coated by PEG-4000 monolayer system could be applied to capture biomolecules on the sensing surface of SPR-based biosensor, especially alpha-amylase.

IV. Conclusion

Studying about magnetic properties of magnetite nanoparticles and potency of magnetite nanoparticles as active materials concludes that magnetite nanoparticles which have the smallest grain size have a greater potency as active materials for SPR-based biosensor application.

V. Acknowledgement

This research was supported by Hibah Unggulan Universitas Gadjah Mada 2011.

VI. References

1. Sahu, S.K., Chakrabarty, A., Bhattacharya, D., Ghosh, S.K., dan Pramanik, P., *J Nanopart Res*, 13, 837-841 (2011).
2. Loh, K., Lee, Y.K., Musa, A., Salmah, A.A., dan Zamri, I., *Sensor*, 8, 5775-5791 (2008).
3. Lee, K.S., Lee, M., Byun, K.M., dan Lee, I.S., *J. Mater. Chem*, 21, 5156 (2011).
4. Xu, C., Modification of Superparamagnetic Nanoparticles for Biomedical Applications, *Dissertation*, Brown University, 2009.
5. Coey, J.M.D., *Magnetism and Magnetic Materials*, United States of America, Cambridge University Press, 2009.
6. Sahu, S.K., Chakrabarty, A., Bhattacharya, D., Ghosh, S.K., dan Pramanik, P., *J Nanopart Res*, 13, 837-841 (2011).
7. Covaliu, C.I., Berger, D., Matei, C., Diamandescu, L., Vasile, E., Critea, C., Ionita, V., dan Iovu, H., *J Nanopart Res* (2011).
8. Hoa, L.T.M., Dung, T.T., Danh, T.M., Duc, N.H., dan Chien, D.M., *Journal of Physic: Conference Science*, 187, 012048 (2009).
9. Zang, F., Su, Z., Wen, F., dan Li, F., *Colloid Polym*, 286, 837-841 (2008).
10. Dhanalakshmi, C.P., Vijayalakshmi, L., dan Narayanan, V., 7, 13, 2093 – 2101 (2012).

Study of spin models with polyhedral symmetry on square lattice

Tasrief Surungan[1]* and Yutaka Okabe[2]†
[1]*Department of Physics, Hasanuddin University, Makassar, South Sulawesi 90245, Indonesia*
[2]*Department of Physics, Tokyo Metropolitan University, Hachioji, Tokyo 192-0397, Japan*
(Dated: 19 September 2012)

Anisotropy is important for the existence of true long range order in two dimensional (2D) systems. This is firmly exemplified by the q-state clock models in which discreteness drives the quasi-long range order into a true long range order at low temperature for $q > 4$. Previously we studied 2D edge-cubic spin model, which is one of the discrete counterpart of the continuous Heisenberg model, and observed two finite temperature phase transitions, each corresponds to the breakdown of octahedral (O_h) symmetry and C_{3h} symmetry, which finally freezes into ground state configuration. The present study investigates discret models with polyhedral symmetry, obtained by e equally partioning the 4π of the solid angle of a sphere. There are five types of models if spins are only allowed to point to the vertices of the polyhedral structures such as Tetrahedron, Octahedron, Hexahedron, Icosahedron and Dodecahedron. By using Monte Carlo simulation with cluster algorithm we calculate order parameters and estimate the critical temperatures exponents of each model. We found a systematic decrease in critical temperatures as the number of spin states increases (from the Tetrahedral to Dodecahedral spin model).

PACS numbers:

I. INTRODUCTION

Phase transitions are ubiquitious phenomena in nature, firmly exemplified by the melting of ice, spontaneous magnetization of ferromagnetic material and transformation from normal conductor of metal into a superconductivity at very low temperatures. In general, a phase transition is related to the breakdown of symmetry of a system[1]. For a thermal-driven phase transition, systems are in high degree of symmetry at high temperature because all configurational spaces are accessible. The decrease in temperature will reduce thermal fluctuation and the system stays in some favorable states. If the phase transition occurs with no latent heat, the system experiences continuous transition, also known as second order phase transition, which is a transition between the ordered and the disordered state.

According to Mermin-Wagner-Hohenberg theorem, spin models with continuous symmetry and short-range interaction can not have a true long range order (TLRO) for two dimensional (2D) lattices, thus no finite temperature transition[2]. However, a unique type transition called Kosterlitz-Thouless (KT) transition can exist in the XY model (O(2) symmetry)[3]. It is a transition between a high temperature paramagnetic phase and a low-temperature quasi-long range order (QLRO), known as KT phase. If the 2π planar angle of the XY model is discretized into q equal angles, we obtain a q-state Clock model. This model, apart from inheriting the KT phase, possesses a lower-temperature TLRO driven by the discretness[4, 5].

It is of interest to systematically study the role played by the discrete symmetry for 3D case. In analogy with the Clock models for 2D symmetry, we discretize the continuous orientation of Heisenberg spin (O(3) symmetry) for obtaining spin models with polyhedral symmetry. This is done by equally partioning the 4π solid angle of a sphere, resulting in five regular polyhedrons, also known as Platonic solids, i.e., Tetrahedron, Octahedron, Cube, Icosahedron and Dodecahedron[6]. Table I tabulates the characteristics of each structure, to which we define a model with spin orientations restricted to point to the vertices of the corresponding structure. Previously we study the edge-cubic spin model with underlying symmetry, the Octahedral symmetry (O_h), similar to that of Hexahedron and Octahedron (cubic) model[7]. However, spin orientation of the model is only allowed to point to the middle point of cubic's edges, therefore there are 12 possible states. We observed two finite temperature phase transitions which comes from the fact that this model partitions the solid angle unequally.

The present paper studies models with polyhedral symmetry. We expect to observe finite temperature second order phase transitions due to the discreteness. The re-

TABLE I: Characteristics of regular polyhedrons.

Name	Vertices (q-state)	Faces	Edges	Group Symmetry
Tetrahedron	4	4	6	S_4
Octahedron	6	8	12	$O_h = S_4 \times C_2$
Hexahedron (cube)	8	6	12	O_h
icosahedron	12	20	30	$A_5 \times C_2$
dodecahedron	20	12	30	$A_5 \times C_2$

*Electronic address: tasrief@unhas.ac.id
†Electronic address: okabe@phys.metro-u.ac.jp

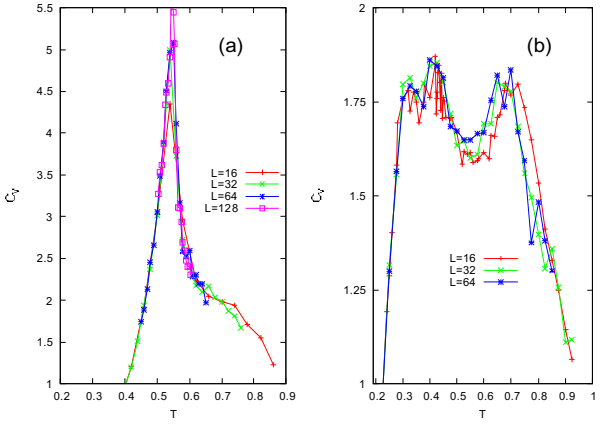

FIG. 1: The temperature dependence of the specific heat for various system sizes of (a) Dodecahedron and Icosahedron models. As shown, there exists a clear peak for Icosahedron while two peaks for dodecahedron. The peaks may signify the existence of phase transitions. The error bar, in average, is in the order of symbol size.

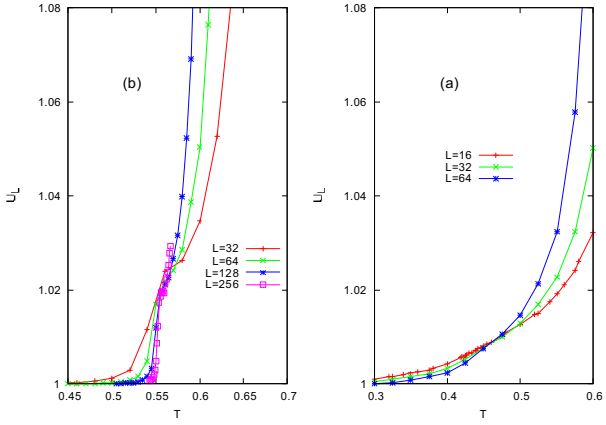

FIG. 2: Temperature dependence of moment ratios for several system sizes of (a) Icosahedron and (b) Dodecahedron models. The crossing points indicates a phase transition between the disordered and the intermediate phase. Error bar is in the order smaller than the symbol size.

maining part of the paper is organized as follows: Section II describe the model and the method. The result is discussed in Section III. Section IV is devoted to the summary and concluding remark.

II. MODEL AND SIMULATION METHOD

The polyhedral spin models are the discrete version of the Heisenberg model with spins are only allowed to point to the vertices of the structures listed in Table I. The Hamiltonian of the model is written as follows

$$H = -J \sum_{\langle ij \rangle} \vec{s}_i \cdot \vec{s}_j \qquad (1)$$

where $\vec{s}_i$ is the spin on site i-th. Summation is performed over all the nearest-neighbor pairs of spins on a square lattice with ferromagnetic interaction ($J > 0$) and with periodic boundary condition. The energy of the ground state configuration, i.e., when all spins having a common orientation, is $-2NJ$ with N is the number of spins.

We use the canonical Monte Carlo (MC) method with single cluster spin updates introduced by Wolff [8] and adopt Wolff's idea of embedded scheme in constructing a cluster for the 3D vector spins. Spins are projected into a randomly generated plane so that they are divided into two Ising-like spin groups. This scheme is essential for carrying out cluster algorithm applied to such spins as 2D and 3D continuous spins.

After the projection, the usual steps of the cluster algorithm is performed [9], i.e., by connecting bonds from the randomly chosen spin to its nearest neighbors of similar group, with suitable probability. This procedure is repeated for neighboring spins connected to a chosen spin until no more spins to include. One Monte Carlo step (MCS) is defined as visiting once the whole spins randomly and perform cluster spin update in each visit. It is to be noticed that for each step a spin may be updated many times, in average, in particular near the critical point.

Measurement is performed after enough equilibration MCS's (10^4 MCS's). Each data point is obtained from the average over several parallel runs, each run is of 4×10^4 MCS's. To evaluate the statistical error each run is treated as a single measurement. For the accuracy in the estimate of critical exponents and temperatures, data are collected upto more than 100 measurements for each system size.

III. RESULTS AND DISCUSSION

A. Specific heat and magnetization

The first step in the search for any possible phase transition is to measure the specific heat defined as follows

$$C_v(T) = \frac{1}{Nk_BT^2}(\langle E^2 \rangle - \langle E \rangle^2) \qquad (2)$$

where E is the energy in unit of J while $\langle \cdots \rangle$ represents the ensemble average of the corresponding quantity. All temperatures are expressed in unit of J/k_B where k_B is the Boltzmann constant.

The specific heats of Dodecahedron and Icosahedron models are ploted in Fig. 1. Although peaks in a specific heat are more directly related to energy fluctuation, they may signify the existence of phase transitions. More quantitative analysis in searching for phase transition is performed through the evaluation of the order parameters from which critical temperatures and exponents may be extracted using finite size scaling (FSS) procedure. In this paper we present the analysis of obtaining exponents only for Dodecahedron and Icosahedron models as other models are equivalent to the commonly known models. The Tetrahedron model is equivalent to the 4-state Potts model while the Hexahedron (corner-cubic model) is equivalent to the Ising model. The Octahedron model which is face-cubic model has been studied by Yasuda and Okabe[11].

As the probed system is ferromagnetic we consider magnetization $M = |\sum \vec{s}_i|$ as the order parameter. By defining M^k as the k-th order moment of magnetization and $g(R) = \sum \vec{s}(r) \cdot \vec{s}(r+R)$ as correlation function, the moment and correlation ratios are respectively written as follows

$$U_L = \frac{\langle M^4 \rangle}{\langle M^2 \rangle^2} \quad (3)$$

$$Q_L = \frac{\langle g(L/2) \rangle}{\langle g(L/4) \rangle} \quad (4)$$

Precisely, the distance R for the correlation function $g(R)$ is a vector quantity. Here we take the simple and more convenient distances, i.e., $L/2$ and $L/4$, both in x- and y-directions.

The existence of a phase transition can be observed from the temperature dependence of U_L and Q_L. At very low temperature where system is approaching the ground state, both moment and correlation ratio are trivial. Due to the absence of fluctuation, the distribution of M is a delta-like function, giving moment ratio equals to unity. Correlation ratio also goes to unity as correlation function for small and large distance is the same due to highly correlated state. In excited states, the moment and the correlation ratios are not trivial, they depend on temperature. The plot of moment ratio for various system sizes of Icosahedron and Dodecahedron models shown in Fig. 2, exhibits crossing points indicating phase transitions. The crossing point for the Icosahedron model is slightly mild compared to the that of Dodecahedron which is related to the performance of moment ratio. Crossing points for both models are strongly indicated by the plot of correlation ratio shown in Fig. 3. The procedure for estimating critical temperatures using FSS will be presented in the next subsection.

B. Finite Size Scaling

FSS analysis for obtaining critical temperature and exponents are shown in Fig. 4, where we plot correlation ratio of the models. In general, moment ratio has larger correction to scaling than the correlation ratio [12], which happens to be the case here, shown for example by the mild crossing point of moment ratio for Icosahedron models (Fig. 2a), while sharp crossing for correlation ratio (Fig. 2b). However, if the variables of the two correlation functions are not local quantity, the correlation ratio may have larger correction to scaling. Our estimate of T_c is based on result obtained from the correlation ratio.

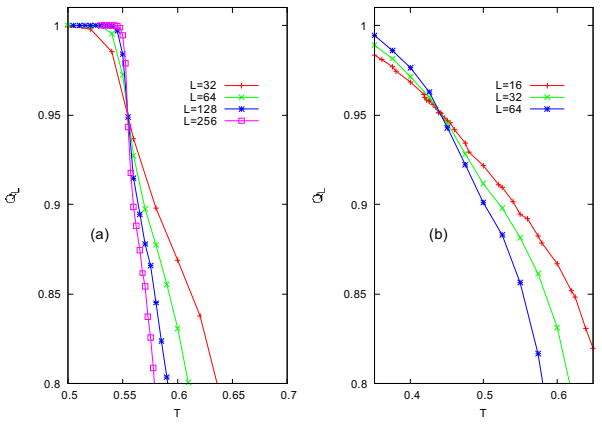

FIG. 3: Temperature dependence of correlation ratios for several system sizes of (a) Icosahedron and (b) Dodecahedron models. The absis of the crossing points are the critical temperatures of the corresponding models, comparable to the numerical values given by the moment ratio of Fig. 2. Error bar is in the order smaller than the symbol size.

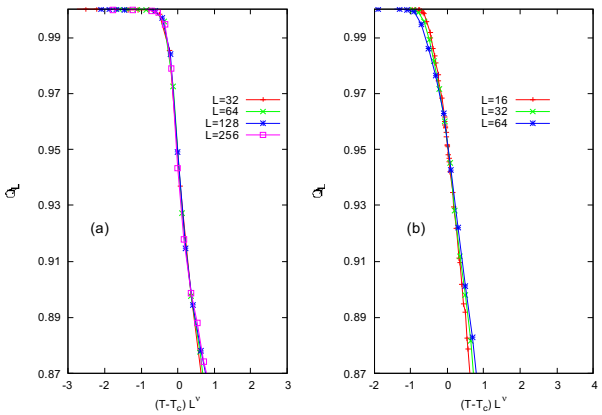

FIG. 4: The FSS plot of correlation ratio for (a) Icosahedorn and (b) Dodecahedron models. The estimates of critical temperature and the exponent of correlation length ν are obtained.

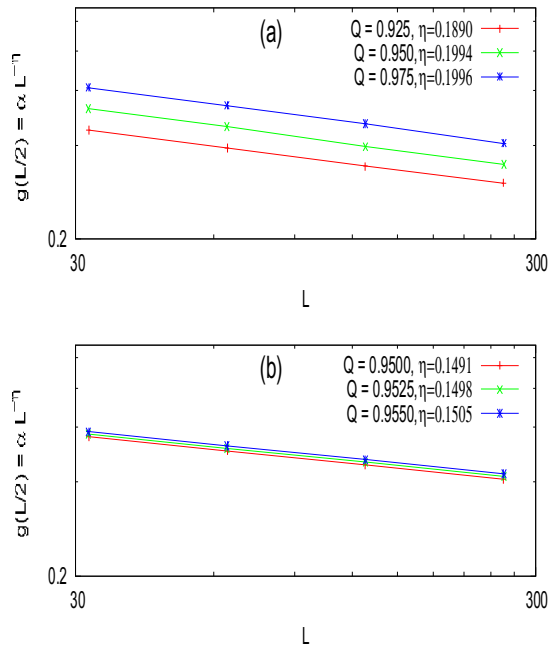

FIG. 5: Double logarithmic plot of $\bar{g}(L/2)$ vs L. The gradient of the fitted line associated with $Q = 0.82$ for Icosahedron and $Q = 0.92$ for Dodecahedron model. The best estimate for η are respectively 0.149(1) and 0.199(1).

For Icosahedron model, the estimated values of T_c and ν are respectively 0.555(1) and 1.30(1), while for Dedecahedron, $T_c = 0.438(1)$ and $\nu = 2.01(1)$. The number in bracket is the uncertainty in the last digit.

Using the correlation ratio we can also extract the decay exponent η of the correlation function. This is done by looking at the constant value of correlation ratio Q for different sizes and then find the corresponding correlation function $g(L/2)$. The correlation function is in power-law dependence on the system size, $g(L/2) \sim L^{-\eta}$ [12]. Therefore, if we plot $g(L/2)$ versus L for various Q's in logarithmic scale, as in Fig. 5, the value of η will correspond to the gradient of the best-fitted line for each constant of correlation ratio. There are several lines plotted in Fig. 5. Since the critical temperature is associated with the value of $Q \sim 0.95$ for Icosahedron model (Fig. 3(a)), we assign $\eta = 0.199(1)$ as the best estimate. For the Dodecahedron model (Fig. 5b) the estimate in $\eta = 0.149(1)$.

After obtaining the critical exponents, we can now discuss the universality classes of the existing phase transitions. The expectation that models with the same underlying symmetry has to belong to the same universality class seems to be too good to apply. As indicated, although the underlying symmetry of the Icosahedorn and the Dodecahedron is the same, both models have different universality class. It is of interest to investigata whether this finding also holds for 3D systems.

TABLE II: Critical temperatures and exponents of phase transitions of 2D Polyhedral spin models.

Model (q-state)	T_c	ν	η
4	$(4/3) * (1/\ln(3)) = 1.214$	2/3	1/4
6	0.9085(2)	0.685(2)	0.23(1)
8	$(1/3) * (2/\ln(2.42)) = 0.756$	1	1/4
12	0.555(2)	1.31(1)	0.199(1)
20	0.438(1)	2.0(1)	0.149(1)
12* [7]	0.602(1)	1.50(1)	0.260(1)

IV. SUMMARY AND CONCLUDING REMARKS

In summary, we have studied critical properties of spin models with polyhedral symmetry on a square lattice. They are the discrete version of the Heisenberg model. If the 4π solid angle is equally partitioned, then there exist five regular octahedrons, as listed in Table II. We only consider the Icosahedron and the Dodecahedron models as the Tetrahdron and the octahedron are equivalent to the common models, i.e., the Ising and the 4-state Potts model, respectively while the Hexahedron model has been studied by Yasuda and Okabe. We observed a second order phase transition for each correspoding model studied and estimated the critical temperature and exponents by using FSS of correlation ratio. Our results are tabulated in Table II, including results from previous studies. We found a systematic decrease in critical temperatures as the number of spin states increases ($T_c \to 0$ as $q \to \infty$). This implies that $T_c = 0$ for the model with continuous symmetry, which emphasizes the importance of discretness in 2D systems.

Acknowledgments

The authors wish to thank J. Kusuma and Bansawang BJ for valuable discussions. The extensive computation was performed using the supercomputer facilities of the Institute of Solid State Physics, University of Tokyo, Japan and Parallel computers at the Department of Physics, Hasanuddin University. The present work is financially supported by the Incentive Research Grant No. 246/M/Kp/XI/2010 of Indonesian Ministry of Research and Technology.

[1] L. D. Landau, *On the theory of phase transition*, in *Collected Paper of L. D. Landau*, edited by D. T. Haar (Pergamon Press, 1965).
[2] N. D. Mermin and H. Wagner, Phys. Rev. Lett. **17** 1133, (1966) ; P. C. Hohenberg, Phys. Rev. **158**, 383 (1967).
[3] J. M. Kosterlitz and D. Thouless, J. Phys. C **6**, 1181 (1973); J. M. Kosterlitz, J. Phys. C **7**, 1046 (1974).
[4] J. V. José, L. P. Kadanoff, S. Kirkpatrick, and D. R. Nelson, Phys. Rev. B **16**, 1217 (1977).
[5] T. Surungan, Y. Okabe, and Y. Tomita, J. Phys. A **37**, 4219 (2004).
[6] K. J. M. MacLean, *A Geometric Analysis of the Platonic Solids and Other Semi-Regular Polyhedra* , (The Big Pictures. Press, Oxford, 2002).
[7] Tasrief Surungan, Naoki Kawashima and Yutaka Okabe, Phys. Rev. B77, 214401 (2008).
[8] U. Wolff, Phys. Rev. Lett. **62**, 361 (1989).
[9] P. W. Kasteleyn and C. M. Fortuin, J. Phys. Soc. Jpn, Suppl. **26**, 11 (1969); C. M. Fortuin and P. W. Kasteleyn, Physica (Amsterdam) **57**, 536, (1972).
[10] F. Y. Wu, Rev. Mod. Phys. **54**, 235, (1982).
[11] T. Yasuda and Y. Okabe, *in preparation.*
[12] Y. Tomita and Y. Okabe, Phys. Rev. B **66**, 180401(R) (2002).

PHASE DIFFERENT AT SUPERCONDUCTOR WITH AN ARRAY OF HOLE UNDER AC ELECTRIC CURRENT

Harsojo[1,2]

[1] *Department of Physics, Faculty of Mathematics and Natural Sciences, Garuda University Sekip Utara PO BOX BLS.21 Yogyakarta 55281*
[2]*Nanomaterials Research Group, LPPT, Gadjah Mada University, Indonesia*

Abstract

It has been studied the V-I properties of the type II superconductor having an array of hole under AC electric current having value smaller than the critical current. The study was done numerically using time dependent Ginzburg-Landau equation which solved explicitly using a gauge link. Various de Gennes extrapolation length was also investigated in the study to explore the role of the boundary in the AC properties of the superconductor. The result reveals the existence of the phase difference in V-I due to the hole and the boundary although the electric current is still in the critical state. The role of the holes and the boundary in contributing the phenomenon were discussed.

Keywords : *V-I, Superconductor, Hole, AC Magnetic field*

*corresponding author; Harsojo
E-mail address: harsojougm@ugm.ac.id

I. Introduction

Voltage versus current or *V-I* characteristic had been long studied experimentally[1,2] or numerically using time dependent Ginzburg-Landau equation [3,4,5]. Most of the studied using time dependent Ginzburg-Landau concentrated on the DC transport phenomena [5,6] and the vortices dynamics since due to its role in producing a higher current density [7,8]. In this last decade, the use of the superconductor having a micro and nano structure to manipulate the vortices motion has become widely spread. Some have used asymmetric microstructure to guide vortices [9], and rectify them[10] to produce an interesting phenomena with might promise a novel application. On the other side, when superconductor under AC magnetic field, the guarantee of the stopping the vortices using pinning vortices mechanism could be limited since the AC field might make the vortices moving and power may dissipate in the superconductor. However, a very limited studied were done related to this issue. Only a few studies were done to investigate the AC properties of the superconductor without holes [10]. In this contribution, we will address our study for this issue.

II. The Model

a. Time Dependent Ginzburg-Landau Equation

In our calculation, we use the simplest time dependent Ginzburg-Landau equation, abbreviated as TDGLE, with scalar order parameter Ψ. We assume that the complex scalar order parameter is sufficient to describe the vortex dynamics of the system. The external magnetic field is expressed in the form of vector field $\mathbf{A}$ couple with the scalar order parameter through TDGLE. In reaching the steady state, both vector and scalar field develop simultaneously. After scaling the TDGLE in dimensionless unit, we arrive the expression of the TDGLE in the following form [11,12]

$$(\partial_t + i\Phi)\Psi = \tfrac{1}{\eta}(-i\nabla - \mathbf{A})^2\Psi + (1-T)(|\Psi|^2 - 1)\Psi \quad (1)$$

$$(\partial_t \mathbf{A} + \nabla\Phi) = -\kappa^2 \nabla\times\nabla\times\mathbf{A} + (1-T)\mathrm{Re}\Psi^*(-i\nabla - A)\Psi \quad (2)$$

The length unit is expressed in coherence length at 0 K, $\xi(0)$, assuming $\xi(T) = \xi(0)(1-T_c)^{-1/2}$. The current density is expressed in unit $H_{c2}(0)/\xi(0)$ where $H_{c2}(0) = \Phi_0 / 2\pi\xi(0)^2$ is the second critical filed and Φ_0 is the unit flux quantization. The scalar order parameter Ψ is expressed in unit $\Psi_0 = \sqrt{\alpha/\beta}$ where are related to critical magnetic field as $H_c = 4\pi\Psi_T{}^2\alpha^2$ while β is one of the Ginzburg-Landau constants. Having done this, Eq. (1) and (2) can be formed as

$$\partial_t\Psi = (-i\nabla - \mathbf{A})^2\Psi + (1-T)(|\Psi|^2 - 1)\Psi, \quad (3)$$

$$\partial_t \mathbf{A} = -\kappa^2 \nabla\times\nabla\times\mathbf{A} + \mathbf{J}_s . \quad (4)$$

Using the gauge transformation $(\Psi, \Phi, \mathbf{A}) \rightarrow (\Psi e^{i\theta/\kappa}, \Phi - \theta_t/\kappa, \mathbf{A} + \nabla\theta)$, and choosing electricpotential $\Phi = 0$. Eq.(5) and Eq. (6) are implemented with boundary condition. On the surface of the superconductor , the external magnetic field is linked to its induction as $B_z = (\nabla \times A) \bullet \hat{z} = H$. The density current flows on the x-direction such that $\hat{x}.(i\nabla - A)\Psi = -J_t$, while $\hat{y}.(i\nabla - A)\Psi = 0$ where $\hat{x}$ and $\hat{y}$ is unit normal vectors. When de Gennes boundary condition is used at superconductor edges, we apply $(i\nabla - A)\Psi = -i\Psi / b$. This means that $b = \infty$ at superconductor-vacuum boundary, $b > 0$ at superconductor-metals. The value of $b < 0$ indicates the boundary between superconductor with other superconductor having higher T_c. This boundary is used in the outer edges of superconductor. In the hole, we assume that this boundary $(i\nabla - A)\Psi = -i\Psi / b$ is valid to present the possibility the hole in contact with other material beside the vacuum.

b. Calculation

The configuration of the model is shown at Fig.1

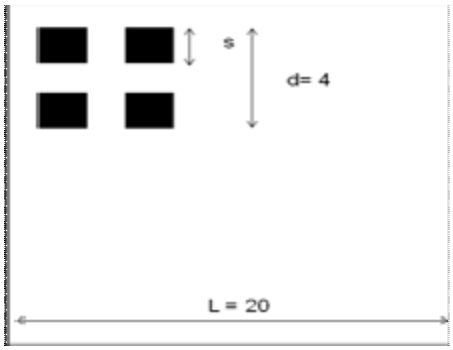

Fig.1 The configuration of the superconductor . The AC current is exposed at *x*-direxion while magnetic field is the *z*-direction perpendicular to the paper.

The calculation was done using explicit algorithm. Having an external current added to the sample, some extra boundary shall be managed such that the first derivative of the normal scalar field zero and the local magnetic field will contain the sum of external magnetic field and the current induced magnetic field. This boundary condition is taken by assuming that the superconductor material is bounded by other materials at side edges where the electric current flows. The external current density J_t is inserted via the local magnetic field. In the upper part the induced magnetic field will be added by $-Lj_t/2$ while on the lower part it will be added by $Lj_t/2$ where L is the width of the sample. We calculate directly the voltage from $V = L^{-1}\int < \partial_t A_x > dy$. Holes are introduced using boundary condition that normal density current is zero at the sides of the holes. The magnetic field inside the hole is the same with the one at outside. The induced magnetic field is updated using the proper magnetic boundary condition. The boundary condition on *N* holes is done similarly as the boundary condition for *N* single hole. On the calculation, we use the type II superconductor having $\kappa = 2$. The mesh size of the sample was $0.5\xi(0)$, so that the calculation was done in $N_1 \times N_2$ meshes array while N_1 and N_2 are the number of meshes related to the size of superconductor. The time difference 0.015τ is used in the calculation. The number of steps taken will be judged accordingly after obtaining the stable result of the voltage calculation, with is around 100,000. In producing AC magnetic field, we used the form of $H(t) = H_{dc} + H_{ac}\sin(\omega t)$ in all cases we use $H_{dc} >> H_{ac}$. The AC current density in the form of $I_{ac}(t) = I_m \sin(\omega t)$ is also implemented to see the similar effect accordingly. Using this condition, the phase different between the current and the voltage generated below the critical condition will be $\pi/2$ since the voltage is a derivative of the vector magnetic field. However, to show the changes from this condition, in the calculation, we assumed that the signal is pure sinusoidal such that we can use the average AC power formula which is

$$\cos Q = \frac{\frac{1}{2\pi}\int V(t)I(t)d\omega t}{V_m I_m}, \quad (4)$$

where Q is the phase difference, the subscript m is used to indicate maximum value of the voltage V and current I.

III. Result and Discussion

When AC current is implemented, it produces AC magnetic fields in which at a low magnetic field, the magnetization $M(t)$ showing difference phase with $H(t)$. The investigation of AC susceptibility due this effect was already investigated by other author[11]. Here we are interested in looking the phase different between electric current *I* and the electric voltage *V*.

Below the critical condition, the voltage and the current will be out of phase $\pi/2$ since the voltage here is generated through the related vector potential. Typical result under for the superconductor without an array of hole exposed under AC current without magnetic field at a certain frequency is shown in Fig. 1. It is shown clearly that the at below the critical electric current there is a phase different $\pi/2$. This phase different guarantee that there is no power dissipation caused by the electric voltage and the electric current. If there is a phase different deviating from $\pi/2$, it indicates that there is a power dissipation. In this case, we can calculate the phase different using Eq. (4).

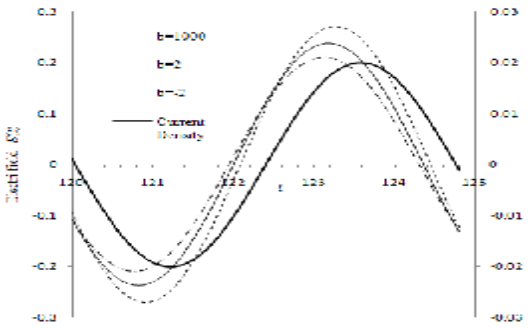

Fig.2 The relation between electric field and the current density at frequency $\omega = 0.02$ and for the superconductor without holes with de Gennes Boundary having extrapolation length $b = 1000$, reflecting superconductor-vacuum boundary, $b = 2$ representing superconductor-metal, and $b = -2$ representing superconductor and another-superconductor having a higher critical temperature. The amplitude of the AC current density is $j = 0{,}02$ and the DC magnetic field is $H = 0{,}2$. The superconductor is exposed under a zero external magnetic field. The right side ordinate is scaled for the current density.

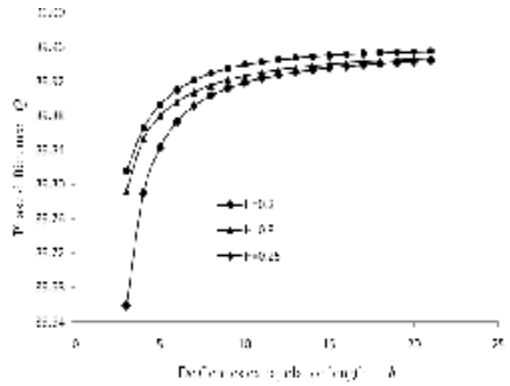

Fig. 3 The influence of the de Gennes extrapolation length b toward phase difference Q taken at $\omega = 0{,}02$ when superconductor is exposed under vertical DC magnetic fields H .

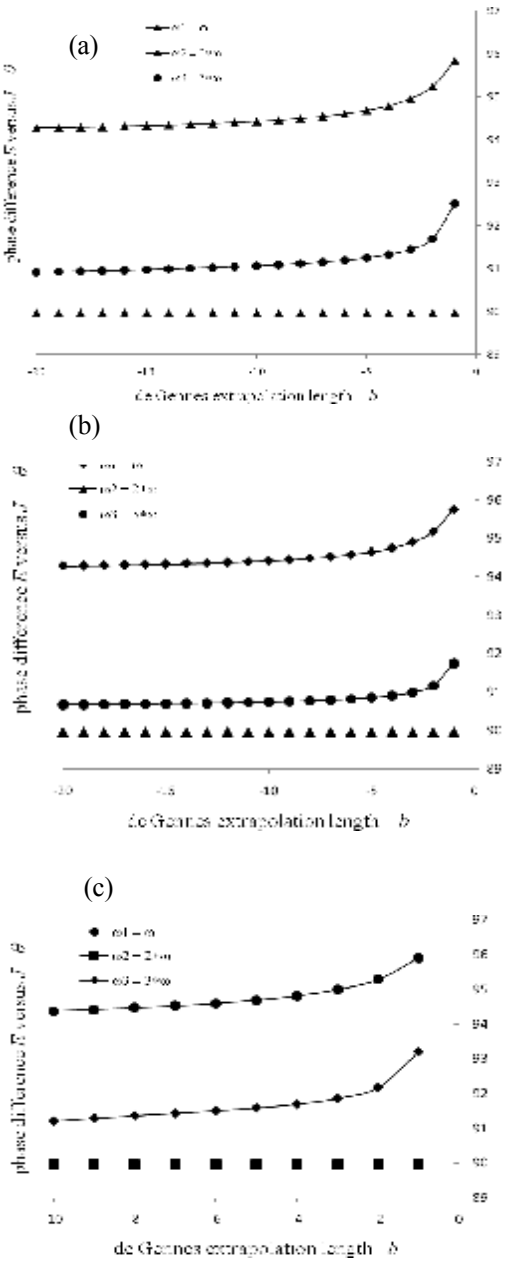

Fig. 4 The influence of frequency ω on the phase different of the superconductor having an array of holes at DC magnetic fields (a) $H = 0{,}25$, (b) $H = 0{,}275$, and (c) $H = 0{,}3$. The configuration of (j, H) is still under the critical condition of the superconductor.

As the boundary to be more metallic material , $b > 0$, the magnetic field generated from the AC current can penetrate the superconductor in the order of London penetration length producing the phase difference smaller than

$\pi/2$ through skin dept mechanism, meaning the dissipation energy starts to appear although superconductor is still under the critical state. The calculation result of the phase difference between the voltage and the electric current for $b = 1000$, $b = 2$, $b = -2$ gives $Q = 89{,}890$ $Q = 89{,}885$ and $Q = 89{,}893$ respectively. This result indicate that the phase different is influenced by the superconductor boundary. When the same superconductor is fabricated with an array of holes accompanied by de Genes boundary in every holes, the influence of the extrapolation length toward the phase difference is clearly more pronounced. It is because the oscillating penetrating magnetic due to the AC current can now covers a deeper distant. It is shown clearly at Fig.3. Some notes have to be mentioned here that the smaller b also means the easier AC magnetic fields penetrating the superconductor. The result in Fig.4 indicates that when the boundary is replaced with the materials having $b < 0$, instead of decreasing from $\pi/2$, the phase different are now bigger than $\pi/2$. This means that the magnetic field produced by the AC current is more difficult to penetrate to the superconductor. However, due to the existence of the greater surface barrier effect, this barrier decreases the phase different from $\pi/2$ and therefore still produces an AC power dissipation. At $\omega = \omega_2$ there is a condition where the phase different is uninfluenced by the boundary and the applied DC magnetic field. We predict that this is a resonance frequency due to the hole geometrical configuration. However, the detail of it still need a further investigation. In the last work, Ref.[7], we found that the critical current of the superconductor can be enhanced using the negative boundary and an array of hole. However, when such an enhancement is implemented in AC fields, it advices should consider this situation.

IV. Conclusion

When AC electric current is involved in the superconductor having de Gennes boundary, one should consider the effect of the hole and the boundary because there is a possibility that the configuration affecting the phase different between the electric voltage and the current producing an AC power dissipation. Both factors become more pronounce when the boundary is in contact with with material having lower absolute b and the maximum AC current is still under the critical current of the superconductor.

V. References

1. L.F. Goodrich, S.L. BrayT. Kobayashi, H. Yoneyama, and H. Tamura, J., 1990,*Cryogenics*, *30 667-677*.
2. L.F. Goodrich, 1991*, Cryogenics*, *Volume 31, 720-727*.
3. Masahiko Machida and Hideo Kaburaki, , Phys. Rev. Lett. **71**, 3206 (1993).
4. R. Kato, Y. Enomoto, and S. Maekawa, , Phys. Rev. B **47**, 8016 (1993).
5. T. Winiecki and C. S. Adams, , J. Comput. Phys. **179**, 127 (2002).
6. Harsojo, AIP Conf. Proc. 1454, 207 (2012)
7. Harsojo, , Advance Mechanical Material, 10-26, 862(2011).
8. J. Berger, J. Math. Phys. **46**, 095106 (2005)
9. A V Kapra, V R Misko, D Y Vodolazov and F M Peeters, *Supercond. Sci. Technol.* 24 024014(2011).
10. J. Van de Vondel, C. C. de Souza Silva, B. Y. Zhu, M. Morelle, and V. V. Moshchalkov, Phys. Rev. Lett. 94, 057003 (2005)
11. Alexander D. Hernández and Daniel Domínguez, Phys. Rev. B **72**, 020505(2005)
12. C. Bolech, G. C. Buscaglia, and A. López, Phys. Rev. B **52**, R15719 (1995)

URANS Application for Simulating Mixing Cross Flow between Sub channels of Tight-lattice Nuclear Fuel Pin Bundles

Azizul Khakim[1*], Hisashi Ninokata[2]

[1]Badan Pengawas Tenaga Nuklir (BAPETEN) Jl. Gadjah Mada No. 8 Jakarta 10120
[2]Nuclear Engineering Dept., Tokyo Institute of Tech.: N1-5, 2-12-1 O-okayama, Meguro-Ku, Tokyo 152-8550, Japan

Abstract

The tight lattice bundle is characterized by small gap connecting one sub channel to the neighboring ones. Due to its geometrical features, it produces global flow pulsation inducing flow mixing between one sub channels to the neighboring ones. The inter sub channel mixing is significantly enhanced by transport due to large scale, quasi periodic pulsation which form across the gap. Unsteady Reynolds Averaged Navier Stokes (URANS) is applied to simulate the phenomena of flow pulsation inducing mixing between sub channels.

Keywords: Pulsation, tight-lattice, mixing, URANS
* Corresponding author.
E-mail address: a.khakim@bapeten.go.id

I. Background

A lot of researchers have been pursuing a reactor concept having a long life core. Among the options of pursuing high burn-up core is the use of a high enriched fissile material, high density fuel material and/or high fuel volume fraction. This study is closely related to the high fuel volume fraction leading to a tight-lattice fuel pin array. The cylindrical pin in tight-lattice array raises a thermal hydraulic challenge. The array leads to a narrow coolant gap between two adjacent pins, leading to a poor heat transfer performance around the gap. Due to the presence of the narrow gap connecting two sub channels, a global flow pulsation might occur inducing mixing in a sub channels with its three neighboring ones [1].

The global flow pulsation in a tight lattice array is driven by the flow anisotropy of turbulence. This phenomenon will be less dominant at high *P/D* and at high *Re* numbers because the turbulence would be more isotropic. Therefore for high *Re* numbers, the roles of flow pulsation do not significantly enhance the heat transfer performance around the gap of tight-lattice array [2].

The flow characteristics of low *Re* numbers at tight-lattice bundle is expected to be unsteady, even in the absence of buoyancy. It has been found that secondary flow is very small and secondary flow vortices are expected to move within the elementary domain of the sub-channels. Therefore, they do not contribute significantly to the mixing between two adjacent sub-channels. Experimental investigations have found that the cross sub-channel mixing is significantly enhanced by transport due to large-scale, quasi-periodic pulsations which form across the gap [3].

There are a lot of experiments on turbulent mixing behavior between one sub channel to the neighboring ones of square and triangular arrays involving air or water [4]. But there are very few similar experiments involving liquid metal fluid.

This calculation is intended to investigate the flow mixing behavior undergoing global flow pulsation in tight lattice bundle at low *Re* numbers of *Liquid Metal Fast Reactor* (LMFR).

II. Governing Equations

CFD code of STAR-CD is used. The basis of CFD codes is Navier-Stokes equations comprising of mass continuity (Eq.1) and momentum equations (Eq.2),

$$\frac{\partial \rho}{\partial t} + \frac{\partial}{\partial x_j}\left(\rho u_j\right) = 0 \tag{1}$$

$$\frac{\partial \rho u_i}{\partial t} + \frac{\partial}{\partial x_j}\left(\rho u_j u_i - \tau_{ij}\right) = -\frac{\partial P}{\partial x_i} \tag{2}$$

Where, τ_{ij} is stress tensor components, defined as:

$$\tau_{ij} = 2\mu s_{ij} - \frac{2}{3}\mu \frac{\partial u_k}{\partial x_k}\delta_{ij} \tag{3}$$

For turbulent flow,

$$\tau_{ij} = 2\mu s_{ij} - \frac{2}{3}\mu \frac{\partial u_k}{\partial x_k}\delta_{ij} - \overline{-\rho u_i' u_j'} \tag{4}$$

The last term of Eq.4 is often referred to as Reynolds stress. The s_{ij} is strain tensor, defined as:

$$s_{ij} = \frac{1}{2}\left(\frac{\partial u_i}{\partial x_j} + \frac{\partial u_i}{\partial x_i}\right) \tag{5}$$

Where, x_j : Cartesian coordinate ($j=1,2,3$)
P : piezometric pressure $=P_s-\rho_0 g_m x_m$
δ_{ij} : Kronecker delta, which is unity when $i=j$ and zero otherwise
u_i : velocity component in direction x_i

III. Calculation Model

The geometrical domain composed of two sub-channels without grid-spacer, as shown in Fig.1, is selected for the calculations with 600 mm of axial length. The flow simulation of *Re*=5000, 10000 and 16000 have been performed. The two sub-channels are assumed being picked up from an infinite triangular pin array representing average behavior of the sub-channels. It comes up with around 1.08 million of grid cells. Liquid sodium of 400 °C is passing through the sub-channels. Cyclic boundary conditions are imposed in the four connecting channels; where surface *2′* is matched with surface *2‴* and surface *2″* with surface *2⁗*. In addition, partial cyclic boundary conditions are also applied in the main stream flow direction, one as inflow boundary condition where mass flow rate is imposed as driving force, and the other as outflow. The fluid surfaces attaching to the fuel pin are applied with wall boundaries. The effect of gravity is neglected. In order *k-ε* standard low *Re* number turbulence model is applied correctly, the y^+ is kept within 1.

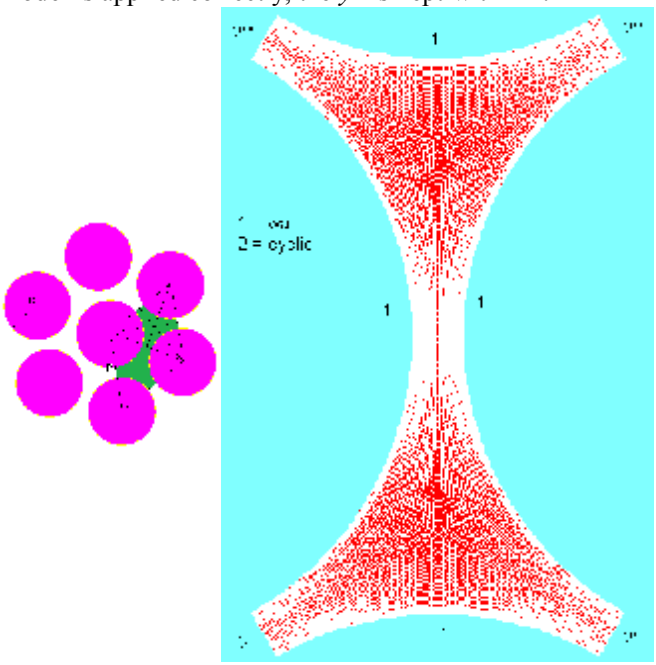

Fig.1. Geometrical domain of infinite array with *P/D*=1.08

As flow pulsation is naturally unsteady, the URANS (*Unsteady Reynolds Averaged Navier-Stokes*) method is performed. Steady RANS calculation was performed first which would be used for initial guess for URANS simulation, through restart mode. The simulation employs implicit temporal discretization scheme, with 20 maximum number of correction stages. In principle, the fully-implicit formulation allows any magnitude of time step to be used, but for transient problems, must be small enough to limit the temporal approximation errors to acceptable levels. In this case, time step of 10^{-4} s is sufficiently acceptable. In addition, third order spatial discretization scheme of QUICK (*Quadratic Upstream Interpolation of Convective Kinematics*) is applied. It fits a parabola two points upstream and one point downstream to get an interpolated value.

IV. Results and Discussions

Fig.2 shows how the axial velocity component (*W*) fluctuates. The data are taken in the middle of axial channel (*z=0.5H*) of the narrow gap center. For the *Re* numbers being calculated, we find three different peak values as a result of in-surge and out-surge flow from the neighboring three sub channels. The walking time from one high peak to the next one, i.e. wave period, of *Re*=5000 shows longer than that of *Re*=10000 and 16000. Therefore, the peak values are proportional to the *Re* numbers.

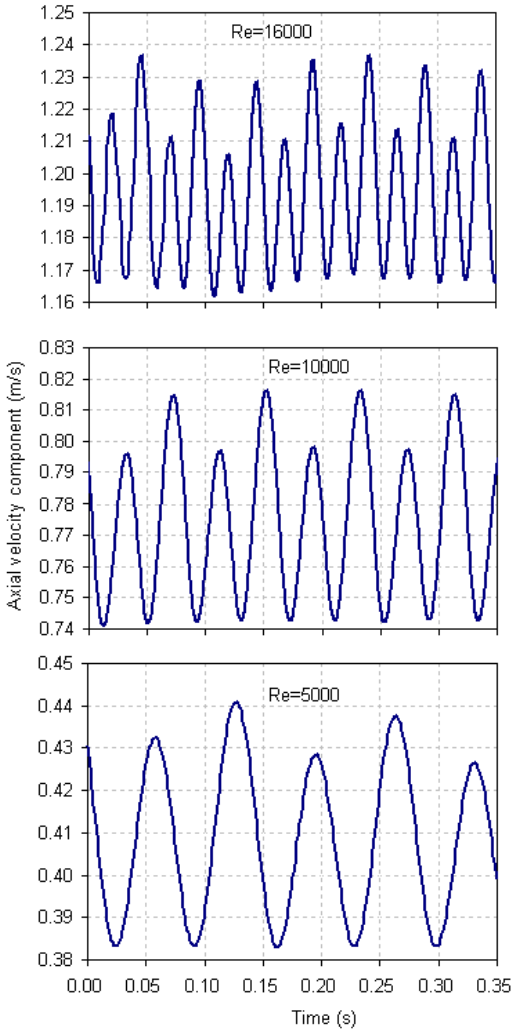

Fig.2. Axial velocity in the middle of connecting sub-channels

The fluctuation of cross flow velocity, measured in the center of narrow gap is shown in Fig.3. It indicates that the cross flow fluctuates with a single amplitude *A* and period *T*. The cross flow velocity in the middle of axial channel (*z=0.5H*) of the narrow gap center of *Re*=5000,

10000 and 16000 can be represented by traveling sinusoidal wave equation $V(t)=A.sin2\,\pi\,(t/T)$. The root mean square (*rms*) of velocity V is

$$V_{rms} = \sqrt{\frac{1}{T_2 - T_1}\int\left[A.\sin 2\pi\left(\frac{t}{T}\right)\right]^2 dt} = \frac{A}{\sqrt{2}} \qquad (6)$$

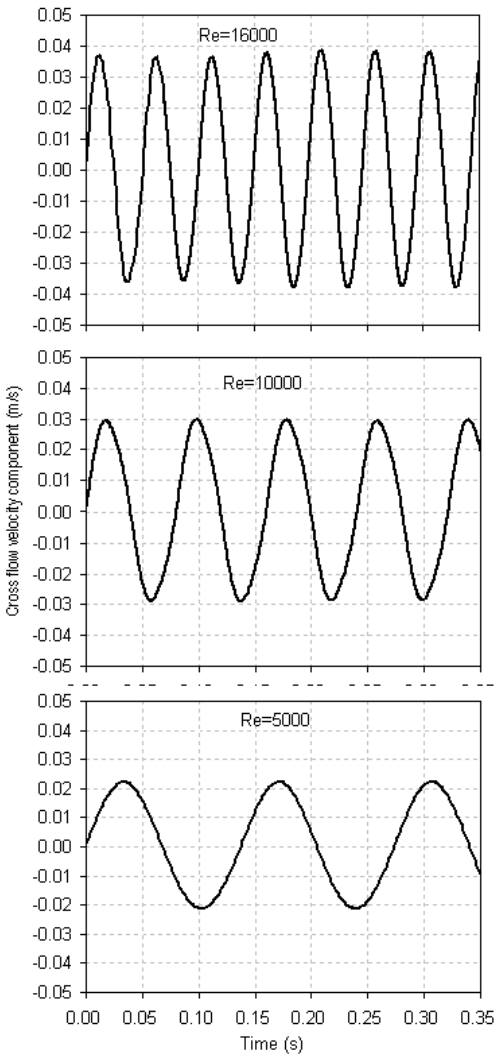

Fig.3. Cross flow velocity in the middle of connecting sub-channels

For *Re*=5000, the amplitude of cross flow velocity exhibits 0.022 m/s, 5.4 % of axial bulk velocity (0.412 m/s). The V_{rms} in the monitoring point is 0.0157 m/s (3.8 % of bulk velocity), calculated by Eq.6. The cross flow velocity oscillates every 0.14 s, leading to a frequency (*f*) of 7.1 Hz. There are 11 waves along the axial length of 600 mm; therefore the wave length is 54.55 mm. The time-averaged of axial velocity ($\overline{W_g}$) in the monitored point is 0.405 m/s as implied from Fig.2. *Strouhal* number (S_r) appears to be 0.24, evaluated by Eq.7. *Strouhal* number characterizes a vibration of a body passed by fluid flowing. It is equal to a characteristic dimension of the body times the frequency of vibrations divided by the fluid velocity relative to the body.

$$S_r = \frac{fD}{\overline{W_g}} \qquad (7)$$

where D is diameter of the fuel pin, 14 mm in this case.

For *Re*=10000, the amplitude of the cross flow velocity is 0.0295 m/s, which is about 3.6 % of axial bulk velocity (0.824 m/s). The V_{rms} is 0.021 m/s (2.5 % of bulk velocity). The wave travels periodically every 0.08 s; therefore the frequency is 12.5 Hz. Since the time-averaged axial velocity component in the measured point is 0.77 m/s, the S_r number is to be equal to 0.23.

For *Re*=16000, the amplitude of cross flow velocity exhibits 0.0385 m/s, approximately 2.9 % of axial bulk velocity (1.318 m/s). The period of traveling wave is 0.049 s (*f*= 20.4 Hz). There are 10 waves along 600 mm channel and therefore the wave length is 60 mm. As the time-averaged axial velocity component in the monitored point is 1.19 m/s, then the S_r number is 0.24. The V_{rms} is therefore 0.0272 m/s (2.1 % of bulk velocity). Relative to the bulk velocity, the cross flow velocities at low *Re* numbers show even stronger than that of high *Re* numbers.

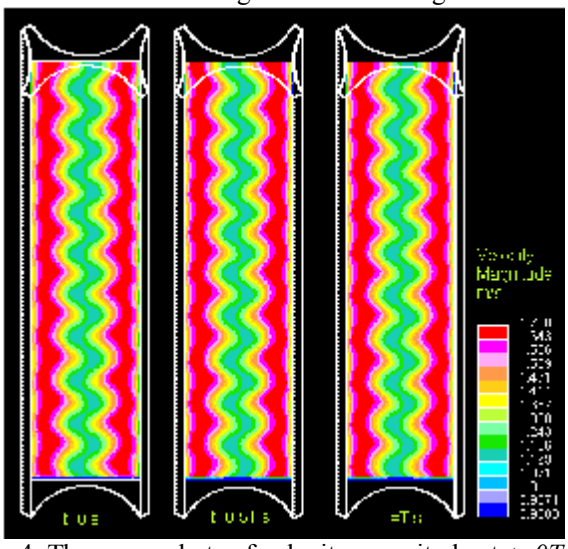

Fig.4. Three snapshots of velocity magnitude at $t=0T\ s$; $t=0.5T\ s$ and $t=1T\ s$, where T is period

Fig.4 describes three snapshots of velocity magnitude during one period. Global flow pulsation takes place along the coolant channel.

The mixing flow sub-channel is also clearly shown by the cross flow velocity component in the narrow gap, as shown in Fig.5. The figure presents both the scalar and vector of cross flow velocity component. The vector type of cross flow velocity component is monitored in cell grids bounded by black rectangular line. The negative sign in the color scale of the figure indicates the opposite direction of the cross flow.

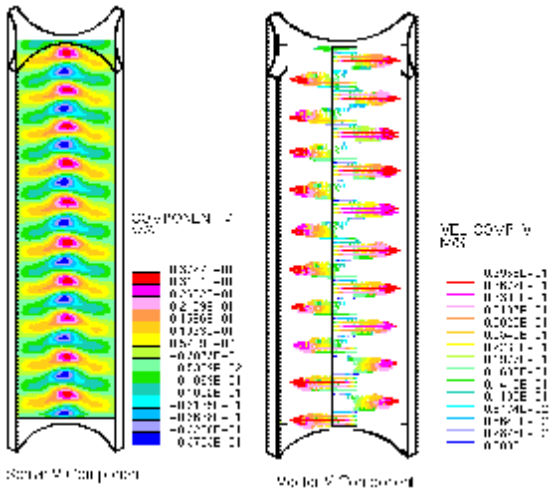

Fig.5. Cross flow velocity along the connecting sub channels in the form of scalar and vector

Fig.6 shows the dynamics of mixing flows in five connecting sub channels during one wave period for *Re*=16000. The data are snapshot at horizontal plane of the middle axial level (*z=0.5H*). It describes four steps of changes in cross flow directions every 0.25 *T* s. The figure shows the time sequence of in-surge and out-surge flow of one sub channel with its three adjacent sub channels.

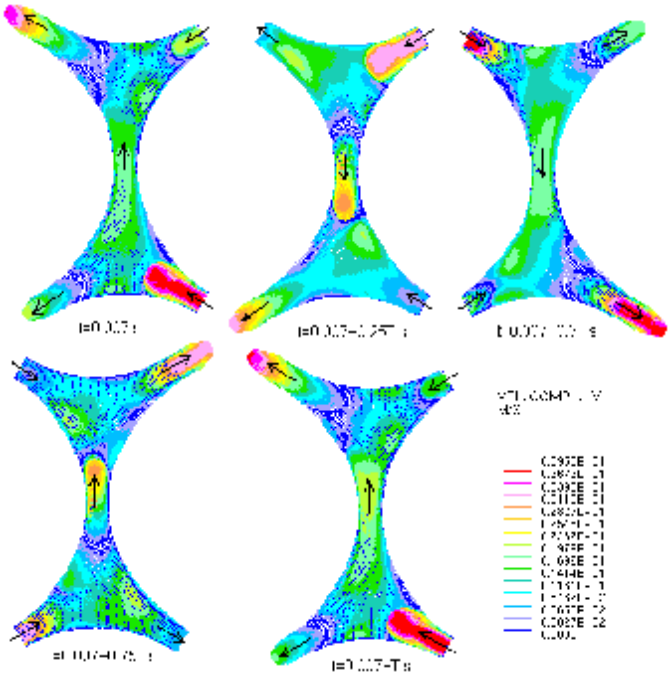

Fig.6. The dynamics of mixing flows in five connecting sub-channels

It is also of great interest to evaluate the wall friction factor in the presence of global flow pulsation and compare it with steady RANS calculation and the existing correlations. In order to achieve convergence for steady RANS calculation of naturally unsteady flow, the length of geometrical domain in the axial direction should be small enough to speed up convergence. Steady RANS calculation approach is time and space averaged flow behavior. The average wall friction factor is calculated by:

$$f = \frac{8\bar{\tau}_w}{\rho V_{bulk}^2} \tag{8}$$

where $\bar{\tau}_w$ is area-averaged wall shear stress, in which in each wall cell is calculated by:

$$\tau_w = -\mu \frac{\partial w}{\partial r} \tag{9}$$

Table 1. Friction factors with URANS and comparison with RANS calculation and Cheng-Todreas correlation

Re	Cheng-Todreas	Steady RANS		URANS-Pulsation	
		f	Deviation	*f*	Deviation
5000	0.0324	0.0317	2.33%	0.0320	1.32%
10000	0.0286	0.0263	8.06%	0.0269	6.16%
16000	0.0263	0.0239	9.25%	0.0245	6.75%

Table 1 summarizes the friction factors calculated in the presence of global flow pulsation. They show better agreement with Cheng-Todreas correlation. These results encourage the need to simulate the tight-lattice bundle at low *Re* number with unsteady calculation.

4.1. Transverse Mass Flow and Mixing Parameter

As transverse mass flow from one sub channel to the three neighboring ones plays an important role on the coolant mixing, it is of great interest to quantify the mixing parameter. Two principal dimensionless parameters have been introduced to characterize transverse mass flux, i.e., the mixing *Stanton (St)* number M_{ij} and mixing parameter β.

$$Mixing\ Parameter = \frac{transverse\ mass\ flux}{axial\ mass\ flux} \tag{10}$$

The M_{ij} employs that of sub channel *i*, whereas mixing parameter β employs that of interacting sub channels.

$$M_{ij} = \frac{w'_{ij}}{\delta_{ij} G_i} \tag{11}$$

$$\text{and} \quad \beta = \frac{w'_{ij}}{\delta_{ij} \bar{G}} \tag{12}$$

$$\text{where} \quad \bar{G} = \frac{G_i A_i + G_j A_j}{A_i + A_j} \tag{13}$$

G_i and $\bar{G}$ are mass flux of sub channel *i* and average mass flux, respectively, in kg/m^{2}s. The w'_{ij} is transverse mass flow rate per unit length from sub channel *i* to sub channel *j*, in kg/m.s. And, δ_{ij} is the connecting sub channel gap width (in m), which is equal to *P-D*.

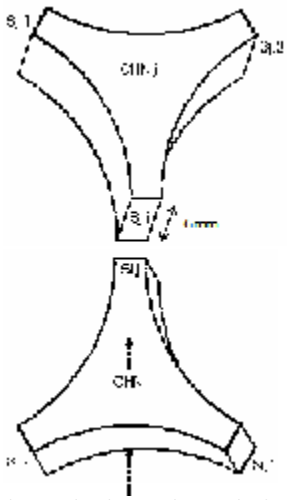

Fig.7. Interacting sub channel *i* and *j* in the mid plane

Fig.7 describes two connecting sub channel *i* and *j* of 6 mm axial thickness sliced in the middle of axial level. One sub channel comprises of three surfaces connecting to adjacent sub channels, and inward surface and outward surface. Surface S_{ji} interfaces sub channel *j* and *i*.

Fig.8 exhibits mass flow exchange of sub channel *j* for *Re*=16000 during one period. The axial mass flow rate, as shown in Fig.8a, fluctuates quasi-periodically with three different peaks as a result of in-surge and out-surge flow from adjacent sub channels. As axial mass flux is proportional to bulk velocity (at constant density), this type of fluctuation justifies the similar shape of axial velocity fluctuation in the narrow gap center of Fig.2. The mass flow rate crossing surface $S_{j,1}$, $S_{j,2}$ and $S_{j,i}$ of sub channel *j* are plotted in Fig.8b. The cross mass flow rates fluctuate following sinusoidal wave with single amplitude that is similar to cross flow velocity of one-point observation as shown in Fig.3. The net cross mass flow rate is a superposition of the three cross flow components, see Fig.8c. Due to in-surge and out-surge flow from three connecting sub channels, they produce three peaks of net cross flow during one period. The mixing parameter of *St* Number is observed between sub channel *i* and *j*. As the transverse mass flux fluctuates like sinusoidal traveling wave, it produces *St* Number in the same pattern, as seen in Fig.8d.

The transverse mass flow rates from sub channel *j* to *i* are proportional to the *Re* numbers, where high *Re* numbers produce higher transverse mass flow rates. However, the mixing parameter of *St* Number shows other wise, indicating that at low *Re* numbers the flow produces better mixing with neighboring sub channels than that of high *Re* numbers. The maximum *St* Number of *Re*=5000, 10000 and 16000 are 0.0415, 0.032 and 0.026, respectively. On the other hand the *rms* of *St* Numbers are 0.029, 0.023 and 0.018, respectively.

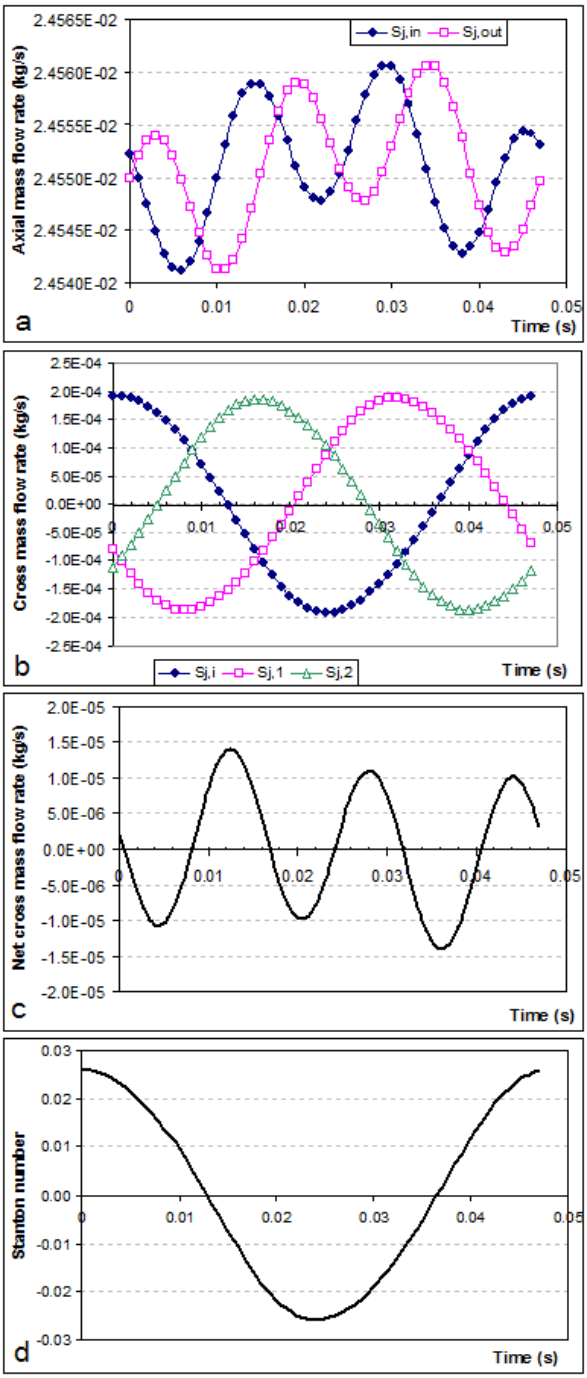

Fig.8. Mass flow exchange of sub channel *j* with neighboring sub channel of *Re*=16000

4.2. Comparison on the Mixing Parameter

Experimental data about the turbulent mixing for liquid metal flows in rod bundles are very rare. Russian researchers, Zhukov et al., could be the only ones having published a correlation on gap *St* Number, based on the experimental data for triangular array rod bundles. The following is the correlation of Zhukov et al.[5]:

$$St_g = 10^{-2}\left[\left\{\frac{138}{Pe}+\frac{1-e^{1-e^{-6.2x10^{-5}\,\mathrm{Re}\,\mathrm{Pr}^{1/3}}}}{8\sqrt{P/D-1}}\right\}^{D_H/D}_{P/D}+\frac{0.15\,\mathrm{Re}^{-0.1}}{P/D-1}\right]\times\left[1-e^{-80(P/D-1)}\right]$$
$$\left(1<{}^{P}\!/_{D}<1.32;\ 0.005<\mathrm{Pr}<0.03;\ 40<Pe<1500\right) \quad (14)$$

Since the current calculation domain is triangular array with P/D=1.08, Pr=0.005 and Pe=80, it is well-argued to compare the calculated gap St number with the Zhukov correlation.

Fig.9 shows the comparison between *rms* of CFD calculations with Zhukov correlation (Eq.14) on gap St Number. The CFD calculations exhibit higher values than that of Zhukov correlation by 47.9%.

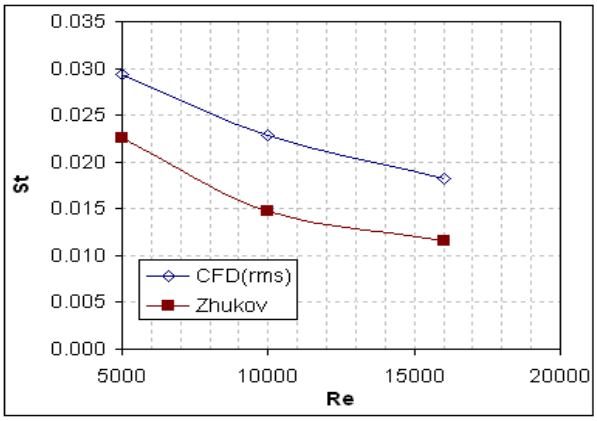

Fig.9. Comparison of CFD calculations and Zhukov correlation on gap St Number

V. Conclusion

With URANS method, the global flow pulsation has been observed in tight lattice bundle at low Re numbers, resulting in quasi-periodic axial flow. The cross flow between two adjacent sub channels produced sinusoidal wave. At low Re numbers, the flow produces better mixing than high Re. The wall friction factors calculated in the presence of global flow pulsation exhibit better agreement with Cheng-Todreas correlation.

V. References

1. Elia Merzari, Azizul Khakim, Hisashi Ninokata and Emilio Baglietto, *Unsteady Reynolds-averaged Navier-Stokes: toward accurate prediction of turbulent mixing phenomena*, Int'l Journal Systems Eng., Vol.1, 2009.
2. H. Ninokata, E. Merzari and A. Khakim, *Analysis of low Reynolds number turbulent flow phenomena in nuclear fuel pin subassemblies of tight lattice configuration*, Nuclear Eng. & Design, Vol.239, 2009.
3. D. Home, G. Arvanitis, M.F. Lightstone, M.S. Hamed, *Simulation of Flow Pulsation in a Twin Rectangular Sub-channel Geometry Using Unsteady Reynolds Averaged Navier-Stokes Modeling*, Nuclear Eng. and Design, Vol.239, Dec. 2009.
4. Silin, N., and Juanico, L.E., *Experimental study on the Reynolds number dependence of turbulent mixing in a rod bundle*, Nuclear Eng. and Design, Vol.236, 2006.
5. S. Kim and B.-J. Chung, *A scale analysis of the turbulent mixing rate for various Prandtl number flow field in rod bundles*, Nuclear Eng. and Design, Vol.205, 2001.

Quantum Mechanic for Financial Market

Dwi Satya Palupi[1*], Arief Hermanto[1*], MF.Rosyid[1*]
1 Department of Physics, Faculty of Mathematics and Natural Sciences, Universitas Gadjah Mada Sekip Utara PO BOX BLS.21 Yogyakarta 55281

Abstract

Some models have done to present financial market. In this paper quantum mechanic method was applied to present financial market. In Quantum mechanic, we used operators and Hamiltonian to describe the physical sistem. In this paper we used operators to describe financial market behavior. These operators were anihilation and creation operator for securities , cash operator which raise the amount of cash held by investor and price operator which modify price of the securities. Hamiltonians for financial market was formed from that operators. The time evolution of operators can be described in Heisenberg picture with this Hamiltonian and this implication to stock market will be analyzed.

Keywords :operator,finance market

* Corresponding author.
E-mail address: dwi_sp@ugm.ac.id

I.Introduction

Some physicists use quantum physics to learn about financial market. Dragulescu [1] constructed an Scrodinger like equation for Fokker Plank equation that present probability log return of stock and solved this equation with path integral. Srodinger equation and path integral were familiar for physicts. Baaquie [2] constructed Schrodinger like equation for Black Scole and Merton Garman equatio that presented option price.

Dragulescu and Baaquie [1,2] basiclly used differensial stochastic equation and then applicated quntum mechanic method to solve it. In other side Scaden [3] and Bagarello [4] have presented state-state on financial market on Hilbert Space. Evolution temporal the states is controlled by Hamiltonian sistem so we must develop the Hamiltonian. Observable is prensented by operator in quantum mechanic, in financel market we can propose some operators that present financial market observable like stock price, number stock and number of money that investor held.

In this paper , we will represent probabbility log return stock price and option from stochastik diferensial equation in quantum mechanic. However, we can not see the movement of stock and cash among investor by this method . So we will prepare another quantum mechanic method to represent the stock and cash movement each investor in simple model. Althoug this model is very simple, we can extend this model as a more realistic model.

II.Transisitian Probability for stock and option price

The Stocks movement follows stochastic diferensial equation as

$$dS(t) = \phi S(t)dt + \sigma(t)S(t)dW_S \qquad (1)$$

S is stock price, σ is volatility or deviation of stock price, and R was Gaussian white noise Wienner Standart proses. In this paper we assumed ϕ was constan,however some outhors [5] assumed that ϕ followed stochastik diferensial equation. Schole and black assumed Volatility was contant, [6] but here we assumed that volatility followed stochastic differensial equation as [7]

$$d\sigma = -\gamma\left(\sigma - \theta\right)dt + \kappa dW_v\left(t\right) \qquad (2)$$

With $v = \sigma^2$. Eq (2) well known as Ornstein Uhlenbeck proses. Hull and White, baaqui assumed volatiliy followed sde as [2,8]

$$dv = \mu v dt + \xi v dWt$$

We can make eq (1) more simpler by change variabel *S* as ln retur $l_r = \ln \frac{S(t)}{S(0)}$ and $z = l_r - \phi t$. Now we get

$$dz = -\frac{v}{2}dt + \sqrt{v}dW_S \qquad (3)$$

Probability transition to get log return z and volatility v at time t from initial log return z =0 and volatility v_i that followed eq(1) and (2) is

$$\frac{\partial P}{\partial t} = -\gamma \frac{\partial}{\partial v}\left[\left(v-\theta\right)P\right] + \frac{1}{2}\frac{\partial}{\partial z}\left(vP\right) + \rho\kappa \frac{\partial^2}{\partial z \partial v}\left(vP\right) + \frac{1}{2}\frac{\partial^2}{\partial z^2}\left(vP\right) + \frac{\kappa}{2}\frac{\partial^2}{\partial z^2}\left(vP\right) \qquad (4)$$

Eq(4) is well known as Fokker-Plank equation in two dimension for sde (1) and (2). We can make eq.(4) more simple with Fourier transformation as

$$P\left(z, v \mid v_i\right) = \frac{1}{2\pi}\int_{-\infty}^{\infty} dp_z e^{ip_z z}\tilde{P}\left(v \mid v_i\right)$$

So eq(4) become

$$\frac{\partial \tilde{P}}{\partial t} = \gamma \frac{\partial}{\partial v}\left[\left(v-\theta\right)\tilde{P}\right] - \left[\frac{p_z^2 - ip_z}{2}v - i\rho\kappa p_z \frac{\partial}{\partial v}v - \frac{\kappa^2}{2}\frac{\partial^2}{\partial v^2}v\right]\tilde{P} \qquad (5)$$

Now we will use quantum mechanic methode to solve eq.(5). In Quantum mechanic we know Scrodinger equation. Eq. (5) can be modified become Scrodinger like equation as

$$\frac{\partial \tilde{P}\left(v \mid v_i\right)}{\partial t} = -\hat{H}\tilde{P}\left(v \mid v_i\right) \qquad (6)$$

with

$$\hat{H} = \frac{\kappa^2}{2}\hat{p}_v^2\hat{v} - i\gamma\hat{p}_v\left(\hat{v}-\theta\right) + \frac{p_z^2 - ip_z}{2}\hat{v} + i\rho\kappa p_z\hat{p}_v\hat{v}$$

$\hat{H}$ is Hamiltonian operator. Solve eq.(6) will give solution for Transition Probability to have ln return z with transition volatility from v_i to v. $\tilde{P}$ is matrik elemen of the evolution operator $\exp(-\hat{H}t)$. probability transition. $\hat{p}_v$ and $\hat{v}$ is treated as canonically conjugate operator with the commutation relation $\left[\hat{v}, \hat{p}_v\right] = i$.

Now, we will try to find probability transition for Europe call option. Option is an derivative that it's price dependent on stock underlying. The simpler model is Black Schole model with constant volatility. The well known Black Schole equation for Europe call option is

$$\frac{\partial C}{\partial t} + rS\frac{\partial C}{\partial S} + \frac{1}{2}\sigma^2 S^2\frac{d^2C}{dS^2} = rC \qquad (7)$$

Shcrodinger like equation for option price can be found with the change of variabel $S = e^y$, $-\infty \le y \le \infty$ so we get Black Scholes Scrodinger equation

$$\frac{dC}{dt} = \hat{H}_{BS}C$$

with

$$\hat{H}_{BS} = -\frac{\sigma^2}{2}\frac{\partial^2 C}{\partial y^2} + \left(\frac{1}{2}\sigma^2 - r\right)\frac{\partial}{\partial y} + r \qquad (8)$$

was Black Schole Hamiltonian operator.

The price of option at $t < T$ is [2]

$$C\left(\tau, y\right) = \int_{-\infty}^{\infty} dy' \, p\left(y, \tau, y'\right)g\left(y'\right) \qquad (9)$$

$p\left(z, \tau, z'\right)$ was transition probability from y' to y on interval $\tau = T - t$. T was time option mature. At option mature time $\tau = 0$ or $T = t$ the price was $C\left(0, y\right) = g\left(y\right)$

The solution of eq.(8) have form $C\left(t, y\right) = e^{tH}C\left(0, y\right)$. Rewrite eq,(8) in Dirac notation , we have

$$\left\langle y\left|\frac{\partial}{\partial t}\right|C, t\right\rangle = \left\langle y\left|\hat{H}\right|C, t\right\rangle$$

and $\left|C, t\right\rangle = e^{tH}\left|C, 0\right\rangle$

so

$$C\left(t, y\right) = \left\langle y\left|C, t\right.\right\rangle = \left\langle z\left|e^{-\tau H}\right|g\right\rangle \qquad (10)$$

Wave function must complete in quantum mechanic. So we can insert completly boundary in eq.(10) and we get

$$C(t,y) = \int_{-\infty}^{\infty} y' \left\langle y \left| e^{-\tau H} \right| y \right\rangle \left\langle y' \middle| g \right\rangle$$

$$= \int_{-\infty}^{\infty} dy' \left\langle y \left| e^{-\tau H} \right| y' \right\rangle g(y') \qquad (11)$$

Eq.(9) and (11) give transition pobability for option price as

$$p(y,\tau,y') = \left\langle y \left| e^{-\tau H} \right| y' \right\rangle \qquad (12)$$

with $\hat{H}$ was Hamiltonian operator in eq.(8)

III. Evolution for fortofolio an investor

In chapter II, we use quantum mechanic methode to compute probability stock price and option price at instantantion time. But with this method we don't know the movement portofolio in each investor and we didn't know how the stock and it's price move. Scaden[3], Bagarelo [4] use quantum mechanic to know how stock moved among investor.

III.a State and opertor of financial market

State for market can be reprenseted by state-state in Hilbert space and the movement is expresed by operator as in Quantum mechanic. Financial market consist j=1,...., J investor and i=1,...,I security. This Financial market is develop by J investors with their and securities. So we can make basis for financial market as

$$\mathbf{B} := \left\{ \left| \left\{ x^j, n_j^i(s) \geq 0, \right\} \right\rangle, i = 1,...I, j = 1,....J \right\} \qquad (13)$$

This Basic state coresspond to possible event in financial markets.The market is represented by state M which is a linear superposition of basic state α with $\alpha \in \mathbf{B}$

Caches and number of security each investor can move, so we need operator to present this movement. The movement of cash is represented by operator $\hat{x}^j$, and the movement number security represented by annihilation a_j and creation operator $a_j^\dagger$. Cash operator can be writed as

$$\hat{c}^{\dagger j}(s) = \exp\left(-is\hat{p}_j\right) = \exp\left(-s\frac{\partial}{\partial x^j}\right) \qquad (14)$$

$s \geq 0$ dan $\hat{p}_j = -i\frac{\partial}{dx^j}$

$$\hat{c}^{\dagger j}(s) \left| \left\{ x^1, x^2, .., x^j, .., x^J \right\} \right\rangle = \left| \left\{ x^1, x^2, ..., x^j + s, ...x^J \right\} \right\rangle .$$

Creation operator add a security on portofolio investor j and annihilation operator move an security in portofolio investor j.

III.b. Hamiltonian for cash and fortofolio an investor.

Scaden (2002) proposed Hamiltonion for cash motion in investor j as

$$\hat{H}_c(t) = \sum_{j=1}^{J} H_c^j(t) \qquad (15)$$

with

$$H_c^j(t) = \frac{r^j(t)}{2}\left(\hat{x}^j \hat{p}_j + \hat{p}_j \hat{x}^j\right) = r^j(t)\left(\hat{p}_j \hat{x}^j + \frac{i}{2}\mathbf{1}\right) \qquad (16)$$

r^j is interest rate at time t.

(17)

The real financial market contain much investor and much security. For simple, We will take the simple case with assumtion (1) market only trade one kind of stock and the total number stock constant. No stock issued when calculating was done.(2) every investor interact each other as two body interaction. (3) the price every stock was not different, on other words shell price was same with price. buy , and the price can change with discrit value in curency unit. (4). Every investor have enough money so can buy stock every intantanous time, but the number cash the have was not presented in in the protofolio.

With these asumtion so basis for market was

$$\mathrm{B} := \left\{ \left| \left\{ n_j \geq 0, j = 1,....J \right\} \right\rangle \right\} \qquad (18)$$

Bagarello [4] proposed Hamiltonian for fortofolio an investor as

$$H = H_0 + H_{\text{harga}} \qquad (19)$$

$$H_0 = \sum_{i=1}^{L} \alpha_i a_i^\dagger a_i + \sum_{i,j=1}^{L} p_{ij} a_i a_j^\dagger$$

$$H_{\text{harga}} = \in p^\dagger p$$

$$\left[a_i, a_j^{\dagger}\right] = \delta_{ij} I \,, \left[p, p^{\dagger}\right] = I$$

the first part of H_0 contained number operator $\hat{n}_j = a_j^{\dagger} a_j$. This operator just to show number stock of investor *j*. Operator $a_i a_j^{\dagger}$ in second part of H_0 represent interaction between investor *i* and *j*. This operator increase one stock in portofolio investor *j* and at the same time decrease one stock in protofolio investor *i*. p_{ij} is 0 if there was no interaction betwen investor *i* and investor *j* , and if there is interaction betwen investor *i* and *j* .

The second part of *H* is $\hat{P} = \in p^{\dagger} p$ that appeared the stock price in $\in$, where $\in$ is the monetary unit.

Evolution of an operator *X* can represented in Heisenberg picture as

$$\frac{dX(t)}{dt} = i\left[H, X(T)\right] \qquad (20)$$

The time evolution of $\hat{n}_j$ operator will represent number stock of investor *j* at instantanous time. We can do the same for another operator toknow time evolution portofolio each investor.

IV.Conclusion

In these paper we show 2 kind of application of quantum mechanic in finance market. The first applicatian is use quantum method to compute condition probability of stock and option from stochastik diferensial equation. From the probability we can know the motion of stock price and option price but we don't the motion of stock in each investor. The second application find the motion of stock in each investor . The motion is represented by time evolution operators in Heisenberg picture as in quantum physics.

References

[1]. Dragulescu, A., Application of Physics to Economic and finance: money,income ,wealth, and the stock market, ArXiv:cond-mat/0307341v1,2003.

[2]. Baaqui BE.,Quantum Finance , Path Integral and Hamiltonian for Options and Interest Rates, Cambridge University Press, 2004

[3].Schaden, M., *Quantum Finance,* arXiv:physics/0202006v2, 2002

[4]. Bagarello,F., An Operatorial approach to stock markets, J.Phys.A,39,6823 (2006)

[5].Singh,JP and Prabakaran,S., Black Scoles Option Pricing with Pricing with Stochastic Returns on Hedge Portfolio, Electronis Journal of Theoritical Physics,EJTP 3,No.13 (2006) 19 – 28.

[6]Black. F, Scholes .M., Pricing of Option and Corporate Labilities , Journal of Political Economy ,Vol 81 No.3,1973

[7]. Heston,S.L,.Closed form solution for Option with stochastic volatility with Application to Bond and Currency Options,Review of Financial Studies,Vol 6,No.2,1993.

[8] Hull,J and White,A., Pricing of Option on Assets with Stochastic Volatiliies,The Journal of finance, vol XLII,no.2 Juni 1987.

Surface Interaction Between Doped TiO_2 and Water Under Visible Light: A Density Functional Theory Study

Dypta Rizky R. [1]***, Fajar F. , Nugraha, and Hermawan K. Dipojono***
Laboratory of Computational Material Design and Quantum Engineering
Engineering Physics Research Group, Faculty of Industrial Technology
Institut Teknologi Bandung, Jl. Ganesha 10, Bandung, 40132, Indonesia

Abstract

Hydrogen production using photocatalytic reaction under visible light is one plausible alternative for harversting cheap and environtmentally friendly energy sources. Doped TiO_2 can be used as photocatalic surface for breaking water molecule and producing Hydrogen. The adsorption processes between doped TiO_2 anatase (101) surface as a photocatalyst and water molecule is investigated. The addition of N and Fe impurities are expected to enhance the photocatalytic ability of pure TiO_2 under visible light. The dissociative adsorption process of water molecule on TiO_2 is computationally investigated using Density Functional Theory. The results show that the lowest adsorption energy of water molecule is -0.43 eV at the optimum distance of 2.70Å from the surface of TiO_2.

Keyword : Hydrogen production, photocatalyst,TiO_2, visible light , impurities, Density Functional Theory

1 Introduction

Currently, modern civilization heavily reliant on fossil fuels for energy needs. However in the last two decades or so, the issues of insustainability and climate change have come to the alarming level. It is becoming increasingly obvious that alternative energy sources must be developed to support future energy needs. A future energy source must be sustainable, environmentally friendly, and cheap.

Many prior studies have focused on alternative energy solutions such as high density batteries, solar cells, wind energy, ocean wave technology, and fuel cells. Fuell cells are considered the best alternative in terms of energy efficiency. Hydrogen is the main source of fuel for fuel cells[1], though other hydrocarbons such as natural gas ot methanol are sometimes used[2]. The advantage of using hydrogen is that it is the most abundant element in the known universe, though hydrogen in its pure state is not found in nature. Water is potentially the best indirect source of hydrogen, as its processing is environmentally friendly and it is abundant on earth.

The separation of hydrogen from water utilising photocatalytic material is a relatively recent development. Known photocatalytic materials include $SrTiO_3$, WO_3, ZnO, Bi_2WO_6, ZnS, and TiO_2. TiO2, however, is the standard against which the others are measured for its low cost, chemical stability, and relatively harmless [3]. Having wide band gap is the only known weakness of TiO2 as photocatalyst, i.e it reacts only under UV light. Fortunately, recent study indicates that introducing transition metal [4] and non metal impurities [5] may overcome the shorcoming. Experiments show a resultant widening of the reactivity spectrum after such a modification is implemented. Considering the largest amount of radiation the sun produces is in the visible spectrum, this is a large advantage. The anatase phase chosen because it known to be more reactive than both the rutile and brookite phases[6]. Anatase (101) surfaces, thought not as reactive as anatase (001) [7], is a candidate for mass production. The combination of metal impurities and nitrogen is used to lower the water splitting energy barrier. A theoretical study to examine the water splitting mechanism must be conducted, to establish a standard and reference for future experiments.

This paper reports on our investigation to the adsorption and dissociation mechanisms during water splitting through photocatalytic processess. Hopefully this result will some how open a new impetus for further breakthrough in photocatalytic technology.

2 Computational Methods

The calculations were conducted with the Density Funcional Theory on QUANTUM ESPRESSO software, with the plane wave basis set, Perdew-Burke-Ernzerhof exchange-correlation function, at 408 eV cutoff energy and gamma k-point mesh.

The TiO2 surface is modelled as a supercell of 44 atoms. The slab is made 5 layers highs with a thickness of 5.0 Å and a vacuum space of 13.52 Å (refer to figure 1a) to ensure that the surface will not interact with the z-axis periodic image. Relaxation conducted to improve geometry from the anatase (101) surface

[1] email : dypta.mathemusic@gmail.com

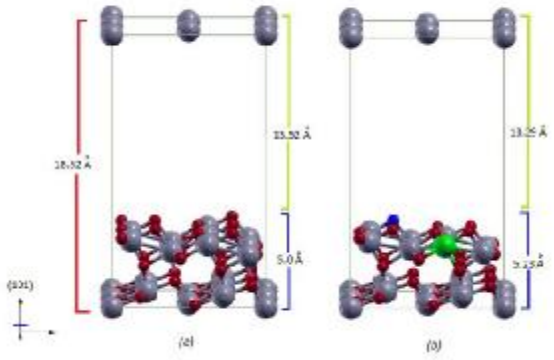

Figure 1(a) and (b), The relax surface without and with impurities. Grey, red, green, and blue balls represent Ti, O, Fe, and N atoms

The initial surface then modified by replacing a 5-fold-coordinate Ti atom (Ti_{5c}) with an Fe atom and replacing a 2-fold-coordinate O atom (O_{2c}) with a Nitrogen atom, hence obtaining a doped anatase (101) surface with Fe-N impurities, as seen in figure 1b. After relaxation, the geometrical configuration became assymetrical with a slab width of 5.23 Å and vacuum height of 13.29 Å

Energy adsorption of the system can be modelled in the following equation: $E_{ads} = E_{DA-H_2O} - (E_{DA} + E_{H_2O})$ with E_{DA-H_2O}, E_{DA}, and E_{H_2O} denoting, respectively, the energy of the entire system (doped anatase + H2O), the clean doped anatase surface, and the water molecule. To determine the specific site of water adsorption, the entire anatase surface is scanned with a water molecule at a particular height. The adsorption energy at each position is monitored and compiled into the Potential Energy Surface (PES).

A combination of scanning and geometry relaxation methods are used to determine the reaction path. The potential energy profile will be obtained after performing the necessary calculations.

3 Results and Discusions

3.1 Molecularly versus dissociattively adsorbed water

A number of potential adsorption and dissociation sites, shown in figure 2, are obtained after scanning for PES. As can be seen, sites are obtained on the top Ti_{5C} atom, also acting as the global minimum, and the top Fe atom. The top Ti_{5C} site is chosen in this study as it has, by far, the lower potential energy compared to the top Fe atom site.

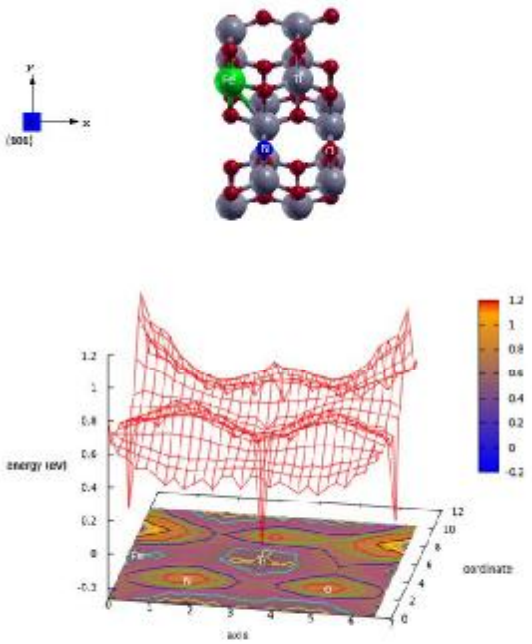

Figure 2. Potential Energy Surface of doped Anatase(101)

The orientation of the adsorbed H_2O molecule is determined through orientation prediction and geometric relaxation. By choosing the orientation shown in figure 3, an adsoprtion energy of -0.43 eV with an optimal distance of 2.70 Å from the top Ti_{5C} atom is obtained. On this surface the water is adsorbed as a molecule. After relaxation, the bonding distance between the oxygen and hydrogen atoms within the molecule is relatively unchanged (0.98 Å). Calculations show that the water molecule is more attracted to the Nitrogen atom. This is due to the extra space available on the Nitrogen atom's outer shell.

The reaction pathway is obtained through PES; a better alternative would be to use the Nudged Elastic Band (NEB). Results show a non-spontaneous break in the hydrogen-hydroxcyl bond. Watersplitting is obtained through the testing of a pathway in its initial state. Scanning results show that water adsorption occurs molecularly rather than dissociatively. The molecular adsorption energy of the system is -0.43 eV, whereas the dissociation adsorption energy is 1.15 eV. This gap in energy levels shows that the system is more stable in a molecularly adsorbed state.

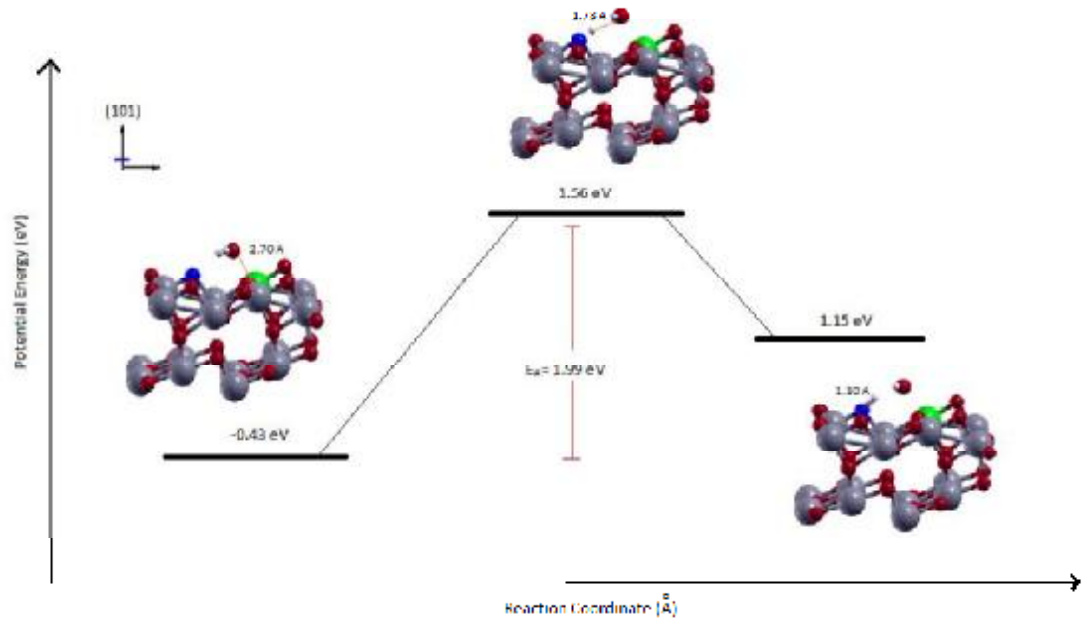

Figure 3. Potential energy of hydogen-hydroxcyl bond breaking

3.2 Dissociation pathway and barrier

The reaction pathway model is essential for establishing our simulation. The following is the chosen reaction pathway:

$$TiO_2 + hv \rightarrow h^+ + e^- + TiO_2 \quad (1)$$

$$H_2O \rightarrow H^+ + OH^- \quad (2)$$

$$OH^- \rightarrow H^+ + O^{2-} \quad (3)$$

$$O^{2-} + 2h^+ \rightarrow 0.5O_2 \quad (4)$$

$$2H^+ + 2e^- \rightarrow H_2 \quad (5)$$

The overall reaction is thus:

$$H_2O + 2hv \rightarrow H_2 + 0.5O_2 \quad (6)$$

Reaction pathways number 2, 3, and 4 are ordinary oxydation reactions of water with TiO2, whereas pathway 5 is a reduction reaction upon a Pt, as conducted in a study by Fujishima and Honda in 1972[8]. Pathways 2, 3, 4 are derived from the following reaction:

$$H_2O + 2h^+ \rightarrow 0.5O_2 + 2H^+ \quad (7)$$

The simulation carried out by scanning the potential energy in the x, y, and z axes between hydrogen and a stationary hydroxcyl group, as shown in figure 3. Results show an increase in energy with distance up to a certain point, after which it again drops. The highest energy recorded is then defined as the energy barrier. The transition state, as of writing, is unobtainable due to the lack of charge transfer and charge density data.

In the initial state, at the point water is adsorbed molecularly, the adsorption energy of the system -0.43 eV. This show chemisorb occured on the water molecule. Through various relaxation configuration it is clear that hydrogen and hydroxcyl easily create bonds. After being broken, relaxed hydrogen and hydroxcyl will again bond, releasing H_2O. With the scanning method, an energy barrier of 1.99 eV and adsorption energy of 1.15 eV obtained. This pathway shows that the energy barrier is surmountable by visible light. From the higher energy of product, we may assume that the reaction is endothermic, as is photosynthesis, the foundation of the waterspliting reaction. The barrier occurs at a distance of 1.72 Å between the hydrogen-hydroxyl bond, almost that of the H-OH bond in water (0.98 Å) with a potential energy of 1.56 eV (figure 3). The extra unbonded hydrogen atom will then become adsorbed at the site the top N atom at a distance of 1.10 Å from the N atom. Figure 3 elaborates the separation of the bond in the initial state, namely pathway 2.

4 Conclusions

The water molecule adsorption and the reaction of hydrogen bond breaking with hydroxcyl groups have been studied by using Density Functional Theory calculations. The adsorption of H_2O and H on doped TiO_2 surface are separately considered. We observe that the H_2O and H preferentially adsorb at the Ti_{5C} and N_{2C} sites. According to the potential energy calculations, the endothermic reaction $H_2O \rightarrow H^+ + OH^-$ is possible and indicates that external energy is expected in the form of light photon energy

5 Acknowledgment

Calculations are all performed on an AMD Phenom X6 1090T at the Laboratory of Computational Material Design and Quantum Engineering at Institut Teknologi Bandung, Indonesia. The authors would like to express their gratitude to the Ministry of Research and Technology for the generous financial support through Research Incentive Grant Project.

References

[1] H. K. Dipojono, A. A. B. Padama, H. N.-i. N. Ozawa, and H. Kasai *Jpn. J. Appl. Phys.*, vol. 49, p. 115702, 2010.

[2] M. K. Agusta, M. Y. David, H. Nakanishi, and H. Kasai. *Surf Sci.*, vol. 604, p. 245, 2010.

[3] S. M. Aspera, M. David, and H. Kasai *Jpn. J. Appl. Phys.*, vol. 49, p. 115703, 2010.

[4] Hanaor, D. A. H., Sorrell, and C. C. *J. Phys. Chem. B.*, vol. 110, pp. 6804–6809, 2006.

[5] W. Zhao, W. Ma, C. Chen, J. Zhao, and Z. Shuai *Am. Chem Soc.*, vol. 126, p. 4782, 2004.

[6] Hanaor, D. A. H., Sorrell, and C. C. *J. Mat. Sci.*, vol. 46, pp. 855–874, 2011.

[7] A. Vittadini, A. Selloni, and M. Grtzel *Phys. Rev Lett.*, vol. 81, p. 2954, 1998.

[8] A. Fujishima and K. Honda *Nature.*, vol. 238, p. 37, 1972.

The Effect of Contact Load on Plastic Deformation of a Rough Surface Using Finite Element Analysis

F. Fatah*, R. Ismail, E. Saputra, J.Jamari
Laboratory for Engineering Design and Tribology.
Department of Mechanical Engineering, Faculty of Engineering, Diponegoro University
Tembalang, Semarang50275

Abstract

Gear is a mechanical part that widely produces around the world. Most of gear's surface contacting each other makes surface study essential to understand its endurance and characteristic. An analysis on surface contact between gear by simplified the contact in asperity level is interest study to better understand the micro level phenomena of gear. This paper makes investigation on determining critical load on the real surface of gear using finite element analysis. The method of investigation used computational numeric under finite element analysis. The critical load is verified with equation from previous research as well as is compared with the result of flat surface in FEM. The result is covering on contact area, contact pressure, von Misses stress contour distribution and plot of surface topography

Keywords: *Surface, Critical Load, FEM*

* Corresponding author.
E-mail address: vanfattah@gmail.com

I. Introduction

Speaking about the most widely used mechanical component in the earth. A gear is the component that widely applied in many engineering device due to its capability to transform power and torque. In the past, many research tried to describe contact between gear's surface. Moreover, contact between surfaces occurs almost in the whole surface of gears. Now days, researchers investigate contact between surface in micro level observation. It give us information that surface is not flat but has rough profile with random height distribution. Thus, the topography of the surface is great interest and should be included in finite element simulations for understanding asperity-scale phenomena of surfaces [Fig. 1].In order to simplify contact between rough surface, many research modeled contact between rough surface as contact between hemisphere against rough surface.

An artificial surface usually made to represent the condition of real rough surface. Bryan *et al* [2] lately analyzed elastic-plastic finite element of line contact between cylinder and rigid plane using ABAQUS. They generated rough surface from measured real surface which imported to FEA using a Phyton script. Meanwhile, Sellgren [3] made FEM model to investigate contact between rough surface. The model were discretized with linear isoparametric elements using the commercial code ANSYS.

Modeling three dimensional surfaces has been an apparent passion of many researchers from the past. A computer model of real rough surface which uses data recorded directly from stylus measuring instrument [4-5] has already done in the past. However, their model was not accurately representing the model of interest due to the lack of computational ability at that time.

There have been many advances in technology in the past seventy years, especially in surface metrology and numerical analysis techniques. It is now possible to optically measure micro and macro scale surfaces features and record the surface data digitally. Thompson [6] similar with this paper, presents methods for generating, using, and operating on no uniform variants for the incorporation of probabilistic rough surfaces in ANSYS. David ET, al [7] demonstrated RF MEMS simulation. He used either an optical profilometer (VEECO) or an atomic force microscope (AFM) to capture three dimensional data points of contact surfaces.

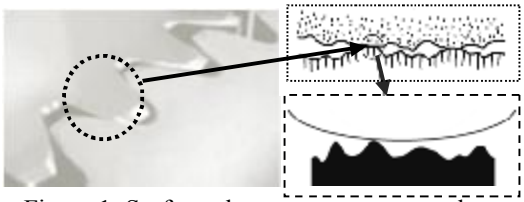

Figure 1. Surface phenomena on contact between gears [1].

This paper makes investigation on determining critical load of gears on the real surface using finite element analysis on static contact model of hemisphere against rough surface. The method of

investigation used computational numeric under finite element analysis. Numerical and finite element modeling, allow multi contact simulations, with complex geometry, boundary conditions, material properties, and material models to create more accurate models of surface phenomena.

II. Methodology

The method of measuring real surface is followed the experiment conducted by Jamari [8]. Transformation process of measured real surface undergo with the help of Profilometer and CAD software. The complete procedures are portrayed in figure 2. The measured data of surface from experiment were transformed into several forms of digital data from "txt", "xyz", "iges/sat", until "cae". In the generating process, it is known that the number of point measured, software capability, and computer specification are very determining the quality of surface. Higher those things in generating process will lead to better surface with similar dimension with experimental surface. This transformation process is widely known as reverse engineering.

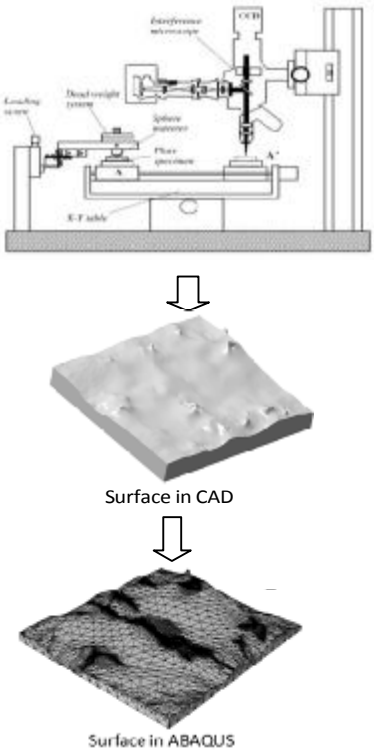

Figure 2.Transformation method from real surface into digital rough surface.

A hard and smooth curved surface in contact with a deformable nominally flat rough surface was used in Jamari experiment (Fig 2). A hardened steel sphere (H=7.5 GPa, E=210 GPa and v=0.3) with diameter of 10 mm and the average roughness Ra = 0.01 μm was used as hard smooth surface and aluminum (H=0.24GPa, E=75.2GPa, and v=0.34) plate were used as deformable flat surfaces. The topography of real surface is developed in CAD that obtained from experimental research. The load applied in surface sets as repeated loading to analyze surface deformation and von Misses stress distribution for each load cycle (Fig. 3).The critical load is verified with equation from previous research as well as is compared with the result of flat surface contact model in FEM.

The software package Abaqus was used to analyze the three models created in this study. In these cases the material properties were corresponding to experimental procedures with the corresponding material model of elastic–perfectly plastic behavior. Tangential behavior was specified as being frictionless while the normal behavior was specified to hard contact constraint in order to exploit the more advanced contact control options of the software. Convergence of the numerical solution was controlled by setting an absolute penetration tolerance of 10^{-15} m.

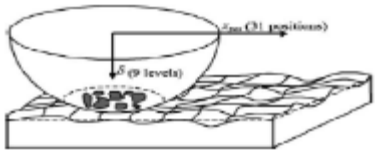

Figure 3. Contact modeling on deterministic real surface against rigid ball [3].

III. Result & Discussion

Jackson and Green [9] introduced load that eventually cause the material within the hemisphere to yield in contact between hemispheres against rigid flat. The load at the initial point of yielding is known as the critical load, *Pc*. Their work derives this critical load analytically using the von Mises yield criterion (VM).

$$P_c = \frac{4}{3}\left(\frac{R}{E'}\right)^2 \left(\frac{C}{2}\pi . S_y\right)^3 \qquad (1)$$

These critical values predict analytically the onset of plasticity. These values are, therefore, chosen to normalize the results of all the models. The normalized parameters are

$$P^* = {}^{P}/_{P_c} \qquad (2)$$

Applying Jackson and Green Equation with current work's properties will give us information that critical load of surface (P_c) is 0.0518 N. Putting those

properties parameter in finite element also provide same results as shown in figure 4. More detail about yield development of verified model is explained in figure 5.

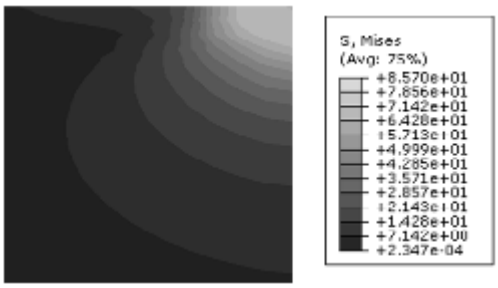

Figure 4. Critical load on smooth surface in finite element model.

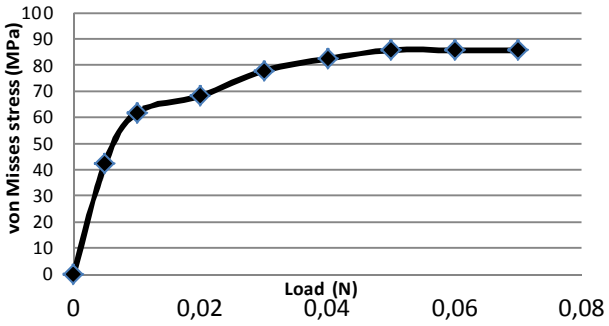

Figure 5. Stress development until reach yield stress.

Observation from top of surface by applying 20 P* shows von Misses stress distribution as in figure 6. It shown that real surface has greater and larger stress area than smooth surface.

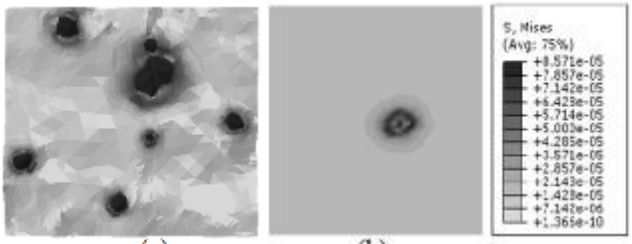

(a) (b)

Figure 6. Distribution of von Misses stress comparison (a) real surface (b) smooth surface.

Table 1. Critical load multiplied by certain constant

$P^* = P/P_c$	Load (N)
*1P**	0.0518 N
*5P**	0.256
*10P**	0.5177
*20P**	1,034

Deformation after unloading which make surface not deform back to the original shape is one of parameters indicate surface already reachingelastic plastic regime. Figure 7 is surface topography deformation in one cycle contact under load variation in table 1. On first contact after unloading, the surface will deform from the original shape. In this state, the increasing of load will increase the distance of deformed surface from the original one.In surface which load is small (a) the deformation almost invisible while in large contact (d) the deformation is clearly observed. In further contact, the deformation still occurs but smaller than the first contact. The trend of deformation in each load concludes that surface will deform gradually until it reach steady deformation. This phenomenon is called running-in.

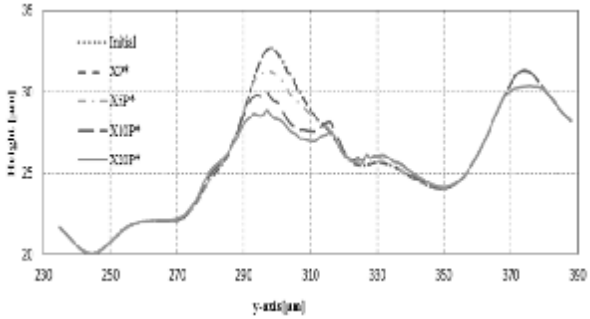

(a) Surface topography during first loading.

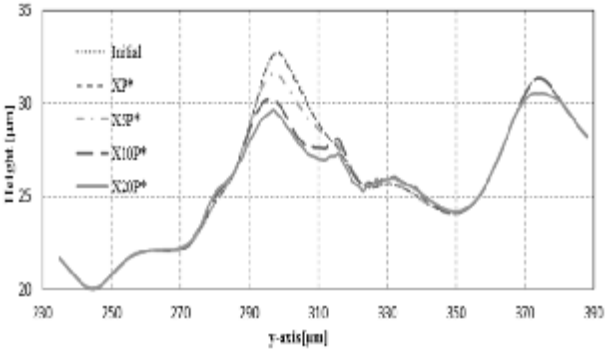

(b) Surface topography during first unloading.

Figure 7. Surface topography deformation at first contact cycle.

The surface will be permanently deformed even the load is increased as we see the deformation comparison in. It implies that the yield stress is increased after unloading from a yield state due to residual stresses. Furthermore, the deeper penetration of indenter will affect to contact neighbor asperity. The detail of stress on each surface during first unloading is portrayed in figure 9 consecutively from 1P*, 5P*, 10P*, and 20P*.

Observation on contact area by applying load equal with 20 P* shows different contact area between rough and smooth surface (Figure 8). Rough surface has scatter contact area with high pressure on

each high asperity and smooth surface contact area occur in whole of surface with small pressure and increasing in center of surface.

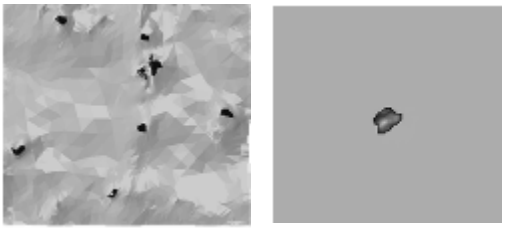

(a) (b)

Figure 8. Contact area comparison between (a) rough surface (b) smooth surface.

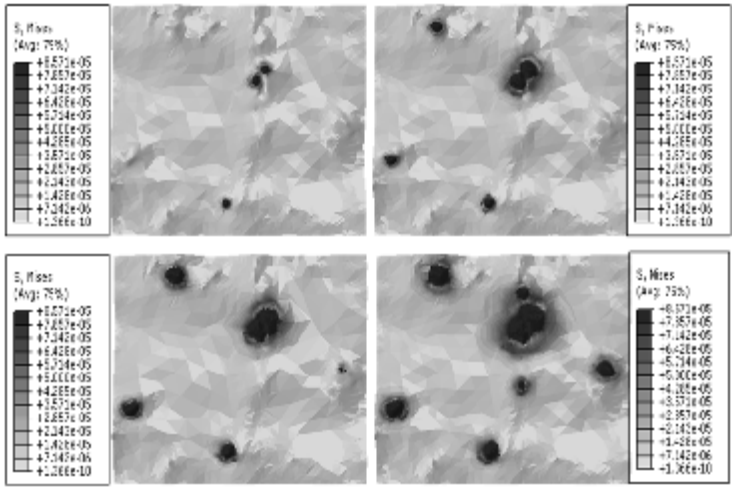

Figure 9. The evolution of von Misses stress distribution during first unloading.

It explains that in real surface contact existing only in surface which have high asperity relative to others. There are some areas of surface which not affected during contact. This indicates that model has different and random height of asperities on its surface. Surface with high asperities will have greater pressure than surface with low asperities. Meanwhile, in smooth surface contact area is distributed to the whole area penetrated by indenter. The highest pressure is located in the middle of surface where pressure from indenter is concentrated.

IV. Conclusion

The paper presents a method to generate real surface based on finite element method to investigate critical load of gear in real surface condition. The model is simplified as contact between balls against rough surface. Three dimensional model of surface allow user to give numerous condition of simulation than two dimensional models. The results show that verification of finite element approach is well suited with past research. Investigation on surface topography also shown that deformation is not occurs in whole area of contact but limited in asperities whose height is higher relative to others. Contact area of real surface is scatter and not concentrated on the location of indenter penetrating the surface. The elastic recovery surface will lower as the load increasing. Moreover, authors encourage others investigation using this method.

V. References

1. B. N. J. Persson, *Contact Mechanics for Randomly Rough Surface*, Surface Science Reports, 61: 201-227 (2006).
2. M. J. Bryant, H. P. Evans, R.W. Snidel, *Plastic Deformation in Rough Surface Line Contacts-a Finite Element Study*. Journal of Tribology International 46, pp. 269-278 (2011).
3. U. Sellgren, S. Bjorklund, S. Andersson, *A Finite Element-Based Model of Normal Contact Between Rough Surfaces*. Wear 254, 1180-1188 (2003)
4. F. Bucher, K. Knothe, A. Theiler, *Normal and Tangential Contact Problem of Surfaces with Measured Roughness*. Wear 253(1–2), pp.204–218. (2002).
5. T. Telliskivi, U. Olofsson, *Contact Mechanics Analysis of Measured Wheel–Rail Profiles Using The Finite Element Method*. Proc Inst Mech Eng 215 (Part F), pp. 65–72. (2001).
6. Thompson, M. K., "A Multi-scale Iterative Approach for Finite Element Modeling of Thermal Contact Resistance." Ph.D. Thesis, MIT, (2007).
7. P. David, et al, *A New Methodology for RF MEMS Simulation*. In Tech, ISBN 978-3-902613-25-7. Pp. 433-452. 2008.
8. J. Jamari, "Running-in of Rolling Contacts", Ph.D. Thesis, Twente, (2006).
9. R. L. Jackson, I. Green, *Finite Element Study of Elasto-Plastic Hemispherical Contact Against Rough Surface*, ASME 127, 343-354 (2005).

The Parallel Computation for *Multigroup* Diffusion Model using *Modified LU-Decomposition* and *Modified Gauss-Seidel Algorithm*

Mike Susmikanti[1], Khairina Ns[1], Winter Dewayatna[2]

[1]Center for Development of Nuclear Informatics–National Nuclear Energy Agency of Indonesia
PUSPIPTEK, Serpong, Tangerang, Indonesia
[2] Center for Nuclear Fuel Technology, National Nuclear Energy Agency of Indonesia
PUSPIPTEK, Serpong, Tangerang, Indonesia

Abstract

Neutron transport applications in nuclear reactors requires completion of multigroup diffusion model. The model of diffusion multigroup has the sparse matrix system. Several algorithms have been developed for the parallel solution of the sparse matrix. The multigroup model has complex computation. To determine the distribution of neutrons in the reactor we must investigate the process of neutron transport, which is the motion of the neutrons as the stream about the reactor core, frequently scattering off of atomic nuclei and eventually either being absorbed or leaking out of the reactor. The ratio of the number of neutron in one generation and the number of neutrons in preceding generation is called by multiplication factor k. We refer to a system characterized as being critical. Parallel computing can be help for fast computation and efficiently shared memory of integrated computer. These papers present the use of efficiency method for k-effective and temperature distribution in multigroup model using parallel computing. This paper compare Modified Gauss Seidel to Modified LU-decomposition. Most of the operation can be done in parallel. The parallel computing to solve the multigroup diffusion model are implemented by integrating C program and Message Passing Interface (MPI) on LINUX Open Source System in multicore computer environment.

Keywords*: Parallel, Modified Gauss Seidel, Modified LU-decomposition, Diffusion, Multigroup*

E-mail address: ***mike@batan.go.id***

I. Introduction

The base of neutron diffusion solution is temperatur distribution and criticality. The neutron distribution in the reactor core should be determined accurately, because it will affect both the reactor and environment safety. Some of neutron transport applications of nuclear reactor requires to solve multigroup diffusion model. The diffusion multigroup model has sparse and big diffusion matrix system.

Several algorithms have been developed for efficiency solution of the sparse and the big matrix. The multigroup model has complex computation. To determine the distribution of neutrons in the reactor, we must investigate the process of neutron transport, which is the motion of the neutrons in the reactor core, frequently scattering-off of atomic nuclei and eventually either being absorbed or leaking out of the reactor. The ratio of the number of neutron in one generation and the number of neutrons in preceding generation is called by multiplication factor *k* (*k-effective*) or the system characterized as being critical.

Parallel computing can be help for fast computation and efficiently shared memory of integrated computer. Parallel program for solving fixed source problem of the multigroup neutron diffusion have developed to solve multigroup neutron diffusion equation system.

This paper describe the algorithm of parallel method for neutron distribution solution based on the difussion theory. The parallel algorithm was applied to present the use of efficiency parallel method for *k-effective* and temperature distribution computation. *Modified Gauss Seidel* algorithm is compare to *Modified LU-decomposition* algorithm in two-dimensional (*2-D*) multigroup model. Most of the operation can be done in parallel. This application involves the case of four energy groups from the higher energy to the lowest energy.

The parallel computing for solving the multigroup diffusion model are implemented by integrating *C* program and *Message Passing Interface (MPI*) on *LINUX Open Source System* in *quard-core* computer system environment [1].

II. Numerical Solution of The Multigroup Diffussion Equations

The first step is to built the coefficient matrix of diffusion multigroup *M*. After then, we compute the solution of temperature distribution based on the equation system in equation (1),

$$M\phi = S \quad (1)$$

where ϕ is temperature distribution and S is fission source. The matrix structure of multi-group as follow,

$$\begin{pmatrix} m_{11} & m_{12} & & m_{14} & & & & \\ m_{21} & m_{22} & m_{23} & & m_{25} & & & \\ & m_{32} & m_{33} & m_{34} & & m_{36} & & \\ & & m_{43} & m_{44} & m_{45} & & m_{47} & \\ m_{51} & & & & \cdot & & & m_{58} \\ & m_{62} & & & & \cdot & & \\ & & & & & m_{n-1n-1} & \cdot & m_{n-1n} \\ & & & m_{n4} & & & m_{nn-1} & m_{nn} \end{pmatrix} \begin{pmatrix} \phi_{11} \\ \phi_{21} \\ \phi_{31} \\ \phi_{41} \\ \\ \\ \phi_{41} \\ \phi_{n1} \end{pmatrix} = \begin{pmatrix} S_{11} \\ S_{11} \\ S_{11} \\ S_{11} \\ \cdot \\ \cdot \\ S_{11} \\ S_{11} \end{pmatrix}$$

The multigroup diffusion equations are describe in equation (2) [2],

$$\begin{aligned} -\nabla D_1 \nabla \phi_1 + \sum\nolimits_{R_1} \phi_1 &= \frac{1}{k} x_1 S \\ -\nabla D_2 \nabla \phi_2 + \sum\nolimits_{R_2} \phi_2 &= \frac{1}{k} x_{21} S + \sum\nolimits_{S_{12}} \phi_1 \\ -\nabla D_2 \nabla \phi_2 + \sum\nolimits_{R_2} \phi_2 &= \frac{1}{k} x_{21} S + \sum\nolimits_{S_{12}} \phi_1 + \sum\nolimits_{S_{23}} \phi_2 \\ &\vdots \\ -\nabla D_2 \nabla \phi_2 + \sum\nolimits_{R_2} \phi_2 &= \frac{1}{k} x_{21} S + \sum\nolimits_{S_{12}} \phi_1 + \ldots + \sum\nolimits_{S_{G-1,G}} \phi_{G-1} \end{aligned} \quad (2)$$

Assume that there is no upscattering and also defined the fission source in equation (3)

$$S(r) \equiv \sum_{g=1}^{G} \nu_g \sum\nolimits_{f_g} \phi_g(r) \quad (3)$$

The spatial dence of the fission source is identical in each group diffusion equations.

For general to built matrix coefficient diffusion multigroup describe in equation (4),

$$(-\sum\nolimits_{s_i}^{i\to g}) \; (-\frac{D^g_{i,i-k}}{(\Delta_{i,i-k})^2}) \; (-\frac{D^g_{i,i-1}}{(\Delta_{i,i-1})^2}) \; (-\sum\nolimits_{s_i}^{g} + \frac{D^g_{i,i-k}}{(\Delta_{i,i-k})^2} + \frac{D^g_{i,j-1}}{(\Delta_{i,i-k})^2} + \frac{D^g_{i,i+1}}{(\Delta_{i,i-k})^2} + \frac{D^g_{i,i+k}}{(\Delta_{i,j-k})^2}) (-\frac{D^g_{i,i+1}}{(\Delta_{i,i-k})^2}) \; (-\frac{D^g_{i,i+k}}{(\Delta_{i,i-1})^2}) \quad (4)$$

The procedures of power iteration to compute the k-*effective* (*k*) and temperature distribution, is simply [2, 3],

(1) Initial guess for $k_0 = k^{(0)}$, $S^{(0)}$ and $\phi^{(0)}$

(2) Solve for $M\ \phi^{(n+1)} = \frac{1}{k^{(n)}} S^{(n)}$, for the next flux iterate, $\phi^{(n+1)}$. This solution involves the number of substeps:

(2-1) One solve the inhomogeneous diffusion equation characterizing each of the energy group *g*. And then using $\phi_1^{(n+1)}$ to solve $\phi_2^{(n+1)}$,and so on, solving successively down the groups.

(2-2) Solving even the inhomogeneous diffusion, such inner iteration to the outer iteration to convergence.

(3) $M\ \phi^{(n+1)} = \frac{1}{k^{(n)}} F\phi^{(n)}$,

and then using

$M\ \phi^{(n+1)} = \frac{1}{k^{(n+1)}} F\phi^{(n+1)}$,

to find

$$k^{(n+1)} = k^{(n)} \frac{F\phi^{(n+1)} F\phi^{(n+1)}}{F\phi^{(n)} F\phi^{(n)}}$$

(4) Repeat (1)-(3) until both $k^{(n+1)}$ and $\phi^{(n+1)}$ convergent.

III. Parallel Algorithm of *Modified LU-Decomposition* and *Modified Gauss-Seidel*

The efficient parallel implementation of decomposing a nonsingular matrix A into its *LU* factorization requires that how to split the matrix *A* among the processors and how to organize the triple loop so that efficient multiplication matrix can be employed and distributed to memory computers. The parts of the matrix A are stored in each processors. The obvious ways to split the matrix A are by rows or by column, but it may also be beneficial to split in blocks. The one of six ways of permutating the indices (*ijk*), just as in the matrix multiplication. This will depend on the specific way out the matrix A to also maximize parallel efficiency. Assume matrix A is accessed by rows as in the k_{ij}-*loop* [4],

for k = 1, n-1
for i = k+1,n
$l_{ik} = a_{ik}/a_{kk}$
for j= k+1,n
$a_{ij} = a_{ij} - l_{ik} * a_{kj}$

end for
end for
end for

Assumes also that the first processors P_1 holds the first row a_1^T, Processor P_2 holds a_2^T and so on. During the first elimination stage, the processor P_1 needs to send its rows to all other processor so that prosessors P_2, ..., P_n will simultaneously update. The operations,

$l_{i1} = a_{i1}/a_{11}$, $j = 2, ..., n,$
$a_{ij} = a_{ij} - l_{i1}*a_{1j}$, $P_2, ..., P_n$

can be performed in parallel. During this first state, processor P_1 remain essentially idle after it communicates with the rest of processors.

The second state, also starts with a communication step as P_2 needs to broadcast its new row to all other processors P_3, ..., P_n. It too remains idle after that, while P_3, ...,P_n update their rows in parallel and so on for the remaining stages. The computation of the multiplications as well as the updates are done in parallel, but after the k-th stage, *n-processors* (P_1, ...,P_n) remain idle. This approach significantly reduce the parallel efficiency [4, 5].

The algorithm for parallel back substitution step $\boldsymbol{Ux = y}$, which is also a triangular system, can be performed in parallel. This algorithm assumes that U is stored by rows, which accessed in the innermost loop *j* [4, 5],

for $j = i+1, n$
$b_i = b_i - u_{ij}*x_j$
end for
$x_i = b_i/u_{ii}$
end for

The parallel algorithm of *Modified Gauss Seidel* assumes given N processor, assign each processor the job of computing iterates for n/N components of the vector *x*. At the end of each iteration all processors must be synchronized before starting the next iteration. *Modifyed Gauss Seidel algorithm is* as follows [6],

Step 1 :
for i = 1 to n do
(i) $old_i = x_i^0$
(ii) $new_i = x_i^0$
Create Process i
end for
Step 2 : ***Process i***
(2.1) ***repeat***
(i) $old = new_i$
(ii) $new_i =$

$$(b_i - \sum_{k=1}^{i-1}(a_{ik} x\ old_k) - \sum_{k=i+1}^{n}(a_{ik} x\ old_k))/a_{ii}$$

until $\sum_{i=1}^{n} abs(new_i - old_i) < c$

(2.2) $x_i = new_i$

IV. Result and Discussion

The parallel algorithm of *Modified LU Decomposition* and *Modified Gauss-Seidel* were compared for diffusion of multigroup system solution in *Quard Core computer*. The process of *k-effective* and temperature distribution calculation use *MPI (Message Passing Interface)* concept in *LINUX Open Source system.*

Calculation of flux distribution in linear equations system used parallel algorithms of *Modified LU decomposition* and *Modified Gauss Seidel* has implemented in a multicore computer. Hepta-diagonal system is obtained from the process of formation of diffusion coefficient matrix *M*. Stated value of the source vector *S* is expressed on the right side of system equations. Stated value of the flux vector calculated in the following matrix form,

$$M\phi = S$$

The geometry material input was taken in two dimension with axial direction is 50 (unit length) and radial direction is 45 (unit radial). That geometry divided into 10 partitions and 9 partitions. The multigroup takes four groups from highest energy to lowest energy. The order of matrix is *360 x 360.*

Input material have the same contain with sigma absorbs cross section, diffusion constant and the productivity per fission. The initial guesses temperature or flux distribution is 10.0, the limit of convergenitas *epsilon* is 0.0000001 and *k-effective* is 1.0. At first, all elements of a diffusion coefficient matrix *M*, was calculated such as *eq.* (4). The form of matrix is *hepta-diagonal* matrix. The size of matrix is *360 x 360*.

The constanta target *four-group* data for one of irradiation position with Uranium 6.1866 g (x 10^6 b) are follows as in Table 1 [7];

Table l. The constanta target four-group with Uranium 6.1866 g (x 10^{-6} b) for IP1

Group	D_g	$\sum_{gabs}$	$\nu\sum_g$	$\sum_{gscat}$
1	1481	1820	58	-
2	976	391	84	3312
3	1278	1467	993	226
4	1079	1982	18677	222

Note: IP1 is the first irradiation position

Sigma absorbtion ($\sum_{gabs}$) for group-1 to group-4 are 0.001820, 0.000391, 0.001467 and 0.019822. Sigma scattering ($\sum_{gscat}$) for group-1 to group-2, group-2 to group-3 and group-3 to group-4 are respectively 0.003312, 0.000226 and 0.000222. Diffussion coeficient (D_g) for each group are 0.001481, 0.000976, 0.001278 and 0.001079. Cross-section for each group ($\nu \sum_g$) are 0.000058, 0.000084, 0.000993 and 0.018677.

The criticality values expressed by *k-eff*, with *Modified Gauss Seidel* is obtained 1.009094. Flux distribution values describe by xpsi(1) to xpsi(360) were calculated using the *Modified LU decomposition. The result* obtained respectively from 0.028197; 0.029009; 0.029032; 0.029032; 0.029032; 0.029845; 0.029892; 0.029894; 0.029894;0.029894; …… ; 0.931042. Using *Modified LU Decomposition, the c*riticality values *k-eff* is obtained 1.000000 and flux distribution values are 0.001699; 0.006378; 0.010648; 0.027054; 0.082748; 0.109899; 0.378308; 0.711553; 0.785872;.....; 0.931766 ; 0. 955165.

The computation time comparison between parallel computing criticality and flux distribution in the Quard-Core computer system using *Modified Gauss Seidel* parallel algorithm and *Modified LU Decomposition* to the settlement system of linear equations with *hepta-diagonal* matrix of size *360 x 360 are* expressed in Table 2.

Tabel 2 : Computation Time Comparison

Number of node	Parallel Time *Modified Gauss Seidel* (sec.)	Parallel Time *Modified LU Decomposition* (sec.)
1	0.1947	0.3695
2	0.1465	0.3685
3	0.1421	0.3557
4	0.1363	0.3326

The graphics of performance of parallel flux and criticality calculations using a modified LU decomposition method compare to Gauss Seidel shown in Figure 1.

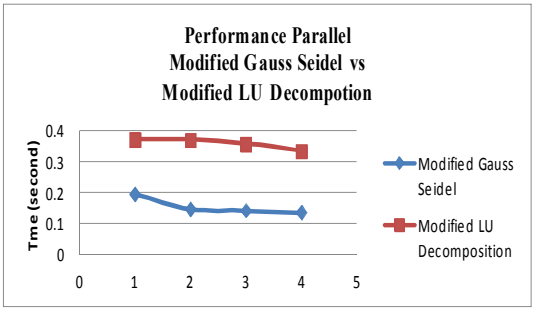

Figure 1. Performance of parallel Modified Gauss Seidel with LU Decomposition

V. Conclusion

Parallel algorithm of *Modified LU Decomposition* can be applied to get computing criticality and flux distribution in multigroup solution with large and sparse matrix in a short time as well as the *Modified Gauss Seidel*. Parallel computational simulations performed on Quard-Core Local Area Network (LAN). The computation time using *Modified Gauss-Seidel* is little faster than *Modified LU Decomposition*.

VI. References

1. M. D Grammatikakis; D. Frank Hsu and M. Kraetzl, *Parallel System Interconnections and Communications*, CRC Press LLC, New York. (2001)
2. J. J. Duderstadt; L. J. Hamilton, *Nuclear Reactor Analysis,* John Wiley & Sons, Inc. (1976)
3. J.R. Lamarsh, A.J. Baratta, *Introduction to Nuclear Enginerring*, Prentice-hall, ISBN 0-201-82498 (2001)
4. G.E. Karniadakis, Kirby ll, Robert M., *Parallel Scientific Computing in C++ and MPI,* Cambridge University Press, First Published. (2003)
5. T.H. Michael, *Parallel Numeric Algorithm, LU Factorization*. www.cse.illinois.edu/courses/cs554/notes/06_lu (2011)
6. S. G. Akl, *The Design and Analysis of Parallel Algorithms*, Prentice Hall, Inc., New Jersey (1989)
7. *W. Dewayatna, Irradiation Safety Analysis, FPM Target in Reactor Terace RSG-GAS (1995)*

Performance of Cluster Computing System in Molecular Dynamics Simulation

Mike Susmikanti[1], Dinan Andiwijayakusuma[1], Alan Maulana[2]
1 Center for Development of Nuclear Informatics, National Nuclear Energy Agency of Indonesia
PUSPIPTEK, South Tangerang, Indonesia
2 Center for Technology of Nuclear Industrial Materials - National Nuclear Energy Agency of Indonesia
PUSPIPTEK, South Tangerang, Indonesia

Abstract

There are so many applications of molecular dynamics simulations, one of them is moldy. Moldy is an open source program used for molecular dynamics simulation of liquid or solid material. This application can be used for monatomic or polyatomic simulation system, one to study properties of Pb-Bi as a coolant in fast reactors candidate and breeder reactors. The accuracy of the simulation results can be obtained by conditioning the simulation close to the real situation. This will give the consequences of simulation time is long enough, to solve this problem, and then builds a cluster computing system. This tool is utilized to execute or run computational simulation calculation that needs ability of high performance computing machine. In this paper, the author will describe the development of cluster computing systems for molecular dynamics simulations and discuss its performance with Moldy parallel Open Source. The results of this work show that the performance of cluster systems can accelerate the process of molecular dynamics simulations are quite significant. The performance of clusters has started on the optimal use of 4 processors and tends to stagnate in over 4 processors. The number of processors into consideration optimization for each case, this is because more and more processors does not always speed up simulation time. Also the length of simulation time is not only influenced by the number of atoms but also the number of chain and water blocks . The occurrence of this is made possible by the existence of bottlenecks in the network of cluster computing system, and it is a consideration for further improvement.

Keywords: *Cluster Computing, Molecular Dynamics, Moldy*

E-mail address: mike@batan.go.id

I. Introduction

Molecular Dynamics (MD) simulation is a simulation technique to observe the movement of molecules that interact with each other [1]. This technique is built to simulate the behavior of molecules that attract each other, pushing and hitting a single molecule with other molecules. Simulation provides both static and dynamic information such as position, velocity and forces acting on an atomic scale. This information is then processed to look at physical characteristics such as temperature, pressure and energy on a macroscopic scale.

The numbers of atom that can be simulated are generally still around hundreds or thousands. Thus when compared with the number of atoms/molecules on a macroscopic scale which has a very large number of molecules (Avogadro's number of order 10^{23}), Molecular Dynamics Simulation still has many limitations. A constraint in Molecular Dynamics Simulation during this requires large computational capabilities due to the number of simulated molecules are quite numerous and involve complex algorithms. Since the development of computer technology is rapidly increasing, one proposed solution is to use parallelism in the calculations using a high-performance computing cluster system so that the computing time needed will be shorter.

From research conducted by A. Maulana et al (2006), who performed molecular dynamics simulations for characterizations of material properties of Fe, Pb, Bi and nuclear reactor coolant Pb-Bi using moldy but the research is not conducted on a scale parallel to that could improve the efficiency of simulation time. In this paper, the authors will in parallel performance on study phenomena interaction stainless steel and coolant material in diverse the number of steps on some proccesor. The development of cluster computing systems from design to implementation for molecular dynamics simulations with *Moldy* parallel Open Source.

II. Design and Analysis

Development of cluster computing system is intended as a computing infrastructure in the process of design and research of nuclear materials-based computing using molecular dynamics simulations. However, the development of molecular dynamics simulations can also be used for drug design or bio-molecular research so

that the infrastructure is also developed that require computing infrastructure for molecular dynamics simulations in general. The availability of some applications which can be installed on cluster computing systems is a major challenge for the development of computational design of other studies using molecular dynamics simulations.

Cluster Computing System infrastructure design needs to be made to meet the goodness of computing services without neglecting the aspects of security. From the previous introduction, MD Simulations will require high performance computing resources. In addition, users also need a simple interface for ease of use computing resources and they are accessible anywhere. Many applications of molecular dynamics simulations are available, but in this development we have to select some of them having popular application and based on open source software. The main purpose of this MD Simulations Cluster Computing System is providing a practical but real working place for related users to perform MD Simulations on parallel environment without having the hardwares at all.

Needs of users can be accommodated by providing a simple interface that can be used to send the input data and run applications that meet their individual needs in computational resources to build. As providers of computing resources, we want the using computational resources remain safe from those who are not responsible. Only already registered people as users who are eligible to use the resources. Any usage is also well documented to allow the inspection activities occuring in the future. Moreover, MD Simulations Cluster Computing System is not designed as a multi purpose public cluster, but embedded with particular applications for MD simulations, in this case is Moldy.

Moldy is a program for performing molecular dynamics simulations to study the statistical mechanics of condensed phases composed of small molecules [2], atoms or ions. It imposes periodic boundary conditions and treats molecules in the rigid approximation by solving the Newton–Euler equations of rotational dynamics. The program is sufficiently general to be able to treat most model systems within these limitations. Therefore it can handle any assembly of rigid polyatomic molecules, atoms or ions and any mixture thereof. As the MD cell need not be cubic, the program is equally suitable for simulations of solids and liquids.

III. Infrastructure Design

MD Simulations Computing Cluster System Development will adopt the infrastructure-based Rocks Cluster [3]. The machines provider of computing resources will be collected and form a cluster. This cluster consists of one unit of the front-end machine as a head-node and 2 unit machines as computing-nodes. Head Node is a machine used as an initialization process or its processes to Compute Node machines. Compute nodes are the machines that are used to perform a computational process given by the head node. The design of the hardware cluster infrastructure is shown in Figure 1.

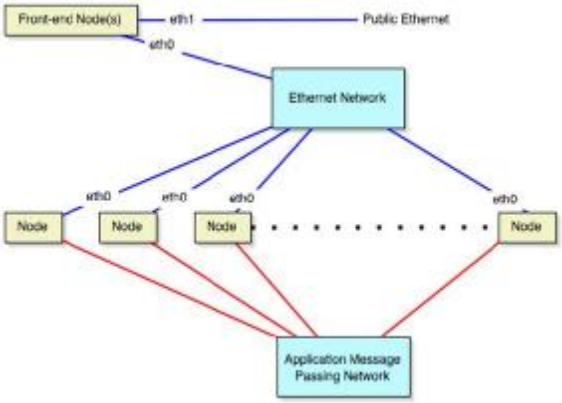

Figure 1. Hardware Cluster Infrastructure Design

Cluster computing system network topology is star-shaped. Front-end node has two NICs (Network Interface Card), one NIC connected to the network through a switch cluster with a local IP address and the other NIC connected to the web-server as a gateway to connects to the Internet and can be accessed by users via internet web-based. Each compute node only has single NIC that only connects to the network cluster. The hardware specification which is developed for cluster computing systems, consist of Processor : Intel® Core-i5 650 (Multicore 3.20 GHz, 4MB), Memory : 2 GB DDR3-1333 SDRAM PC-10600, Video : ATI Radon HD 5450 512 MB, Hard Drive : 500GB, Serial ATA 7200RPM, Networking : Gigabit LAN Card. To implement MD Computing Cluster System, it needs a Dedicated Private Network. In the private network any services that integrate existing machines in network to run the system are needed. The services are GTK, SGE, NFS, NIS, SSH.

IV. RESULTS

As already mentioned earlier that the cluster system adopt Rocks Cluster Operating System that centos-based. This option is selected with consideration of the simplicity of the Rocks cluster. They are easier in the management of cluster systems and capable of running on heterogeneous standard high volume components computing machines. Red Hat, Roll on the Application is an application package that is installed on the HPC as well as moldy package.

Rocks Cluster uses installation mechanism for the management of cluster systems. Installation is done on three important conditions, i.e. when the initialization of cluster system starts, when replacement of dead nodes, and when a new node is added. Installation mechanism is also used to manage the consistency of the software on cluster systems. On the development of this cluster system, web-interface has been developed as a web-portal to access computing resources, as shown in Figure 2.

Figure 2. Web-Interface Cluster System

On this web portal also has sections that are used to monitor the status of cluster computing systems, as shown in Figure 3. The package for molecular dynamics simulations will be installed in this cluster system. It is an open source-based applications. Through this application, users can perform molecular dynamics simulations on a cluster machine. Simply, by providing input files and parameters required in accordance with the needs of the simulation and the phenomenon cases being observed.

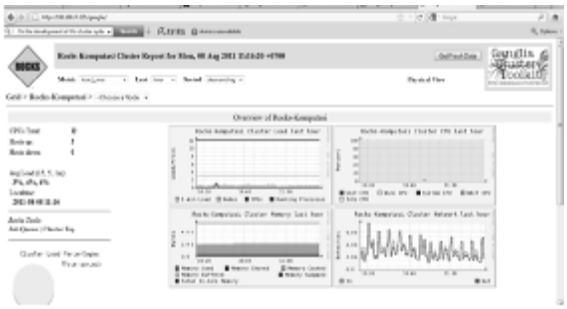

Figure 3. Cluster Status Monitoring via ganglia

Use of cluster computing systems for molecular dynamics simulations, is performed with the following steps:

1. User registration, it is required to register online to get authorization from the administrator.
2. Login, users log into the cluster system to use computing resources.
3. Preparation of input files, input files can be uploaded to the /home directory of users on a computer cluster or a user can edit input file by online text editor.
4. Simulation, after the preparation phase is completed, the next is to perform molecular dynamics simulations.
5. Visualization and analysis, after the simulation, if no errors and done, the job status will be obtained in the output file in the directory /home user, then download to retrieve the image file to be stored on your local computer for analysis and visualization.

In this test, the simulation of materials Fe, Pb, Bi and Pb-Bi using Moldy code. Stainless steel with a composition composed of Fe (74%), Cr (16%) and Ni (10%) and BP-Bi coolant composition comprising Pb (55%) and Bi (45%). Simulations performed at the same temperature but the number of different n step to see the consistency of the performance of cluster computing from 2000, 40000, 60000. 80000 and 100000. The results of the simulation can be seen in Table 1,

Table 1. Results of the simulations

No	nstep	Time of Simulations (s)							
		1CPU	**2CPU**	**3CPU**	**4CPU**	**5CPU**	**6CPU**	**7CPU**	**8CPU**
1	20000	1250,72	695,3	783,07	603,8	579,48	561,63	517,6	531,05
2	40000	2535,87	1390,62	1067,7	889,37	1157,92	1140,85	1036,78	1067,38
3	60000	3761,77	2087,92	1597,35	1331,15	1727,6	1706,73	1552,53	1598,08
4	80000	5010,88	2783,5	2143,12	1776,72	2312,62	2271,78	2242,22	2142,62
5	100000	6272	3463,08	2669,47	2227,4	2875,28	2852,35	2583,37	2655,77

From the test results, obtained graphs of system performance for use moldy as follows in Figure 4,

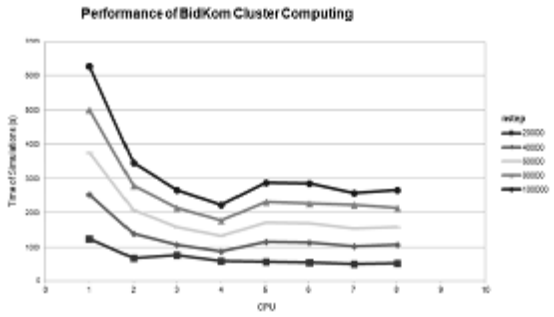

Figure 4**.** Performance of BidKom Cluster on Moldy application

From Figure 4 the graph shown that simulation acceleration time obtained is significant. Simulations with moldy applications in parallel to increase the simulation time is faster, so that by conditioning the number of atoms close to real conditions can be done with a relatively short time compared to serial.

V. Conclusion

A cluster computing system for molecular dynamics simulations has been developed. Performance cluster computing systems is sufficient to provide a significant acceleration of simulation time. The number of processors into consideration optimization for each case, this is because more and more processors does not always speed up simulation time. The occurrence of this is made possible by the existence of bottlenecks in the network. Some improvements are still needed and much to do, it is becoming a challenge in the future. This system for a while, in the testing phase, cluster systems can only be used for internal, but the future will be opened to public access. As the infrastructure of computing resources, the system is expected to contribute to accelerate molecular dynamics simulations.

VI. Acknowledgments

The Author would like to thank the Ministry of Research and Technology Republic of Indonesia that has funded this research through funding Incentive Program 2011.

VII. References

1. Michael P. Allen, *Introduction to Molecular Dynamics Simulation,* Computational Soft Matter: From Synthetic Polymers to Proteins, NIC Series, Vol. 23, ISBN 3-00-012641-4, pp. 1-28 (2004).
2. Keith Refson, *Moldy: a portable molecular dynamics simulation program for serial and parallel computers*, Computer Physics Communications, 126 (310–329) (2000).
3. Philip M. Papadopoulos,Mason J. Katz, and Greg Bruno, *NPACI Rocks: Tools and Techniques for Easily Deploying Manageable Linux Clusters* , Submitted: June (2002)
4. Moldy : http://www.ccp5.ac.uk/moldy/moldy.html
5. Rocks Clusters: *http:// www.rocksclusters.org*.
6. Sun Grid Engine: http:// gridengine. sunsource. net
7. OpenMPI: *http:// www. open-mpi. org/*
8. Sun Grid Engine Roll Users Guide: *http://www.rocksclusters.org/roll-documentation/ sge/ 4. 3/*

Vortex-Antivortex Assisted Magnetization Dynamics in Permalloy Nano Particle Studied by Micromagnetic Simulation

Shibghatullah Muhammady, Suharyana, Budi Purnama*
Department of Physics, Faculty of Mathematics and Natural Sciences, Sebelas Maret University
Jl Ir. Sutami 36A Kentingan Surakarta 57126

Abstract

Micromagnetic simulations are used to investigate a process of vortex-antivortex magnetization reversal in a Permalloy nano particle with uniform polarity of magnetization. A short field pulse is applied in a film plane anti parallel to magnetization direction. Sequence of simulation of reversals mechanism is evaluated for thickness of nano particle. In case thickness of 20 nm thin layer, magnetization reversal realized through a creation-annihilation of Neel-Bloch wall pair. Contrast for thickness of 60 nm thin layer, reversal mechanism via a creation-annihilation process of vortex-antivortex pair. By analyzing barrier energy of the sample we find that a maximum barrier energy reaches a threshold value (e.g., ~ 2.6×10^6 erg/cm^3 for Permalloy in this simulation).

Keywords : *Magnetization Reversal, Magnetic Vortex, Micromagnetic Simulation*

* Corresponding author.
E-mail address: bpurnama@gmail.com

I. Introduction

Nanometer-order size of magnetic devices is desired to be realized a high density hard disk drive (HDD), i.e. exceed to 10 Tbit/in^2 in the near future. The effort resulted of available magnetic material which is not lose their magnetic property when a magnetic material scale down to nanometer-order because thermal effect. Generally, read-write mechanism of magnetic device employs magnetization reversal. In conventional, magnetization reversal even occurs at infinite large medium such as continues films or bulk materials. There are two type of switching i.e. spontaneous magnetization via coherent rotation and magnetization reversal via domain nucleation following wall propagation to single domain configuration. Furthermore configuration of domain wall should be Néel wall and Bloch wall. In convinced condition, magnetization reversals occur via vortex-antivortex formation [1-6].

In this paper, micromagentic simulation is used to study magnetization reversal on nanometer pattern permalloy by solved Landau-Lifshitz-Gilbert (LLG) equation. Thickness dependence of magnetic field required for switching is detailed investigation via visual of step-step micrograph magnetization to confirm existence of vortex-antivortex. It should be attention that CGS unit is used for whole this manuscript.

II. Experiment Method

Generally, magnetisation under the influence of H_{eff} is given as Landau-Lifshitz-Gilbert (LLG) equation

$$\frac{\mathrm{d}\boldsymbol{M}^i}{\mathrm{d}t} = -|\gamma|\boldsymbol{M}^i \times \boldsymbol{H}^i_{eff} + \frac{\alpha}{M_\mathrm{s}}\boldsymbol{M}^i \times \frac{\mathrm{d}\boldsymbol{M}^i}{\mathrm{d}t}$$

with M_s is saturation magnetisation, $|\gamma|$ is gyromagnetic ratio ($|\gamma|$ = 1,76 × 107 Oe-1s-1 for free electron in metal) and α is Gilbert attentuation parameter. Magnetic energy consists of components, i.e. exchange energy, anisotropy energy, demagnetisation energy, and Zeeman energy. Without Zeeman energy, magnetic energy can be written as

$$E_{tot} = \int_V \left(A \sum_{i=x,y,z} (\nabla \boldsymbol{m}_i)^2 + \epsilon_{anis} - \frac{1}{2}\boldsymbol{M}\cdot\boldsymbol{H}_d \right) \mathrm{d}V$$

with $\boldsymbol{H}_d$ is demagnetisation vector, $\epsilon_{anis} = K[1 - \boldsymbol{m}\cdot\boldsymbol{k}]$, $\boldsymbol{m} = \boldsymbol{M} / M_s$ and $\boldsymbol{k}$ is unit vector directed to in-plane. In this simulation, 50 nm × 100 nm sized nanoparticel permalloy was subdivided into rectangular elements of 15 × 15. The nanosize permalloy was assumed as uniaxial anisotropy structured in-plane nanoparticle with anisotropy constant K = 5000 erg/cm^3, exchange

constant A = 1,3 × 10^{-6} erg/cm, saturation magnetisation $4\pi M_s$ = 1,0 × 10^4 gauss, α = 0,3 and step time integration (dt) = 2,5 × 10^{-13} s [4-5]. Finally, magnetic field linearly increased and obtained maximum at given maximum duration time.

III. Results and Discussion

In this paper, energy needed to cause magnetisation reversal process is defined as activation energy (E_a) i.e. minimum energy that magnetic moment need to change from initial minimum condition into another minimum condition as shown at Figure 1. A left region of peak curve is initial condition and a right region of peak curve is other local minimum which obtain after magnetization reversal. In this simulation, initial condition is set to be uniformly magnetization M = 1 when zero field is applied. Then field with disagree orientation to initial magnetization is used to reverse the initial magnetization. So that magnetization gradually along to field direction. When magnetization reduced to zero (M = 0) and start to reversed direction, magnetization reversal occur. The field is required for the magnetization reversal even define as switching field (H_{sw}).

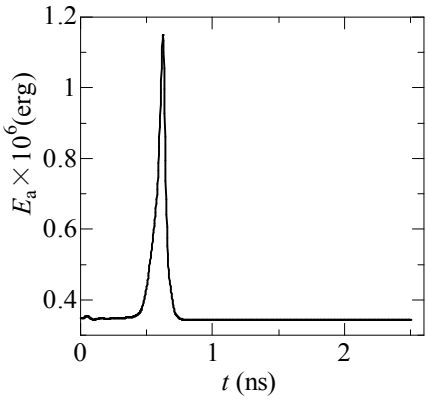

Figure 1. Activation Energy Curve (E_a) as function of time (t).

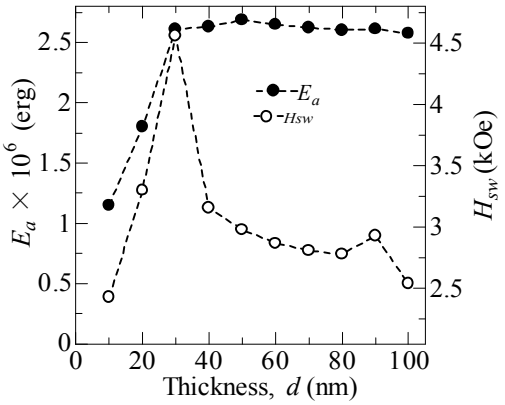

Figure 2. Thickness (d) dependence of the activation energy E_a and the switching field

Figure 2 show the E_a and the H_{sw} evaluated for variation of the thickness (d) under short pulse for 2.5 ns magnetic field of H_{eff} = 5 kOe. Clearly observed that the E_a go up with the increase of the thickness, d and then become constant at value 2.6 × 10^6 erg after critical thickness, d is obtained i.e. 30 nm. In this case the maximum of the E_a is attained. Contrast for the H_{sw} at the beginning linearly increase with the raise of the d, after d = 30 nm exceeded the H_{sw} decrease with the increasing thickness. From the fact experiment result that it should any addition mechanism for lowering the H_{sw} after critical thickness is attained. When the d is equal 30 nm, the field required for switching H_{sw} is about 4.56 kOe. And the H_{sw} is only 2.54 kOe at d = 100 nm. Here the lowering factor is about 44.3% (=((4.56-2.54)/4.56)×100%). The obtained result is well-suited to previous report by Zhang and Liu [7].

In order to detail be understand with the phenomena, step-step magnetization reversal appear on micro-magnetic graph is analyzed as depicted at Figure 3. Three sequence of magnetization reversal for thickness d of 20 nm (after that call **X**), 30 nm (**Y**) and 60 nm (**Z**) is compared their type of nucleation mode. For X case, formation mode is most simple than for both Y and Z cases. Here, a very fast creation and domain wall propagation is appeared. And then the domain wall is quickly disappeared. There are 3 domains separated by Néel walls with typical S-state during in about 0.09 ns (90 ps). Contrast for the Y and the Z cases. A pairing vortex-antivortex is observed during magnetization reversal. For the Y case, the first vortex-antivortex appear at t = 1.11 ns then make an interaction with the other and finally disappeared become single domain configuration at t = 1.21 ns. Duration time of the pairing vortex-antivortex available is about 0.1 ns (100 ps). For the Z case, very fast creation type of the vortex-antivortex is turned up at t = 0.68 ns and make interaction for t = 0.13 ns (130 ps) with other configuration to be a single domain formation via annihilation of domain wall. Clearly here that, time to first nucleation type of vortex-antivortex much effectively influence assisted magnetization reversal. For the Y case, time required for firstly nucleation is much longer than the Z case because

magnetic energy compensation of Bloch wall creation decrease with the increase of thickness. So that, field required for switching (H_{sw}) decrease with enlarges of the thickness (d) although the energy activation (E_a) is not so much different.

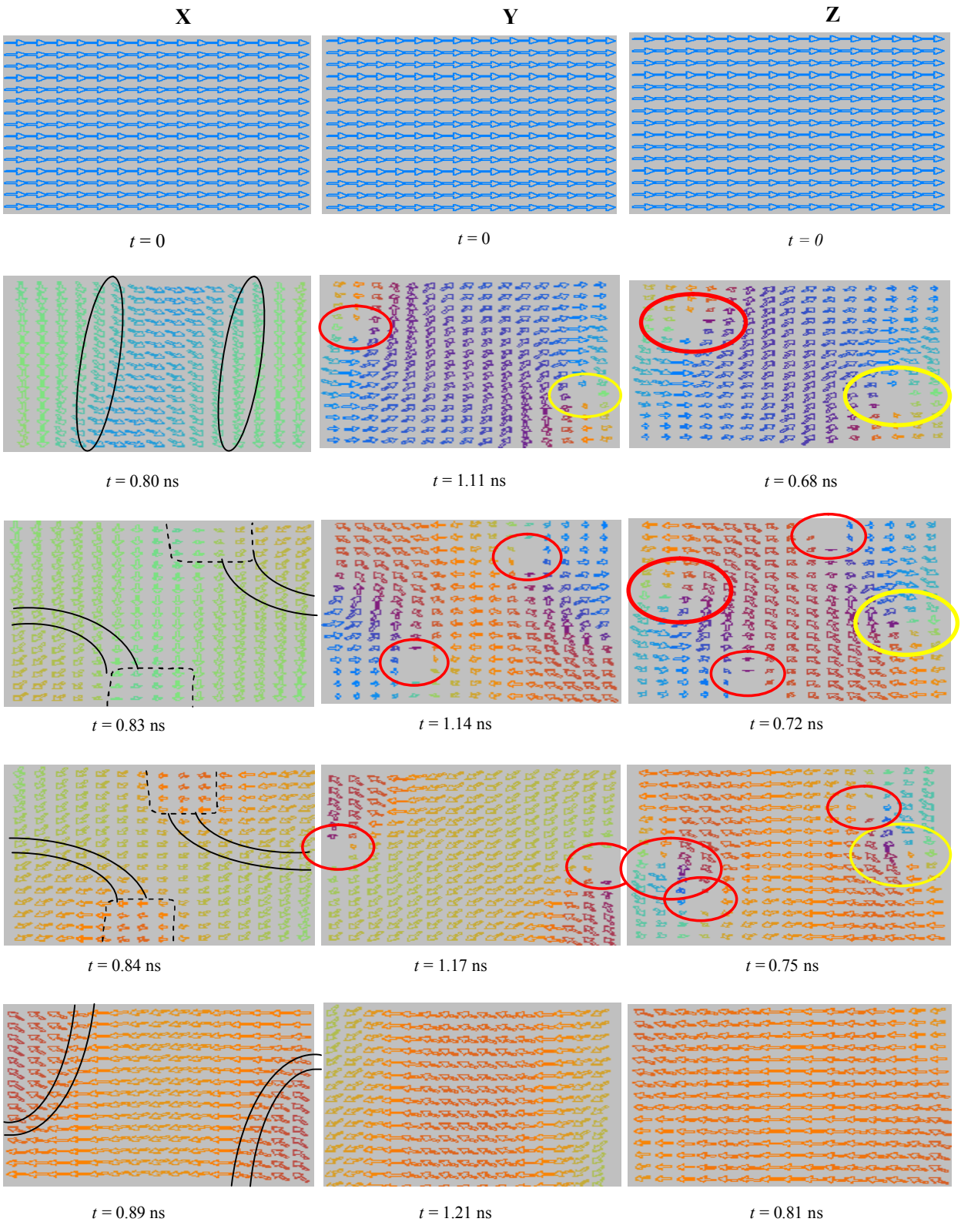

IV. Conclusion

We have studied a process of vortex-antivortex magnetization reversal in a Permalloy nano particle with uniform polarity of magnetization by Micromagnetic simulations. A short field pulse is applied in a film plane anti parallel to initial magnetization direction. Sequence of simulation of reversals mechanism is evaluated for thickness of nanometer order particle. In case thickness of 20 nm thin layer, magnetization reversal realized through a creation-annihilation of Neel-Bloch wall pair. Contrast for thickness of 60 nm thin layer, reversal mechanism via a creation-annihilation process of vortex-antivortex pair. By analyzing barrier energy of the sample we find that a maximum barrier energy reaches a threshold value (e.g., ~ 2.6×10^{6} erg/cm^{3} for Permalloy in this simulation).

V. References

1. Z. Yaying. *Magnetic Simulation on Advanced Recording Media*. Thesis. Department of Electrical and Computer Engineering, National University of Singapore (2003)
2. T. Schrefl, G. Hrkac, A. Goncharov, J. Dean, S. Bance, M. A. Bashir. *Finite Element/Boundary Element Simulation of Future Hard Disk Recording*. Applied Computing Conference, Istanbul, Turkey, May 27-30 (2008).
3. Jian-Gang, Z. *New Weights for Hard Disk Drives*. Materials Today July/August. Department of Electrical and Computer Engineering and Data Storage Systems Center, Carnegie Mellon University, Pittsburgh, PA (2003)
4. R. Gupta, M. Gupta, and T. Gutberlet. Magnetization in Permalloy Thin Films. *J. Phys*., 71, 1123-1127. (2008)
5. CA. Ross. Patterned Magnetic Recording Media. *Annu. Rev. Mater. Res.*, 31, 203-235 (2001).
6. M. B. W. Bolte, D. P. F. Möller, G. D. Meier, A. Thieme. *Simulation of Micromagnetic Phenomena*. Proceedings 18th European Simulation Multiconference Graham Horton (c) SCS Europe (2004)
7. H. Zhang and Y. Liu. Spin-Polarized current driven vortex-pair switching in a magnetic ellipse. *Journal of Nanoscience and nanotechnology*. Vol. 12. 1063-1066 (2012)

The Computation Study of Bayesian Approach on Confidence Intervals for Binomial Population in Astronomy: Stellar Population and AGN Fraction

Asih Melati [1*]
Department of Physics, Faculty of Science and Technology, Islamic State University
Jl Maksda Adi Sucipto No 1 Yogyakarta 55281

Abstract

Data analytical methods on the estimation of Confidence Intervals (CI) having important role in statistic astronomical studies. Population proportions arise frequently as quantities of interest in astronomical research; for instance, in studies aiming to constrain the bar fraction, AGN fraction, SMBH fraction, merger fraction, or red sequence fraction from counts of galaxies exhibiting distinct morphological features or stellar population. This research focusing on stellar population and AGN Fraction. In the Bayesian paradigm (the 'normal approximation' and the Clopper & Pearson approach.), the underlying population proportion is treated as an unknown model parameter and the binomial CI defined as an intervals. And then Bayesian binomial confidence intervals with more satisfactory behaviour estimated from the quantiles of the beta distribution using modern mathematical software packages. In this research using Matlab R2009 software.

Keywords : *data analysis methods, stellar population, astronomy*

* Corresponding author.
E-mail address: asih.melati@gmail.com

I. Introduction

One problem frequently encountered in astronomical research is that of estimating a confidence interval (CI) on the value of an unknown population proportion based on the observed number of success counts in a given sample. The unknown population proportion may be, for instance, the intrinsic fraction of barred disk galaxies at a specific epoch to be inferred from the observed number of barred disks in a volume-limited sample (e.g. Elmegreen et al. 1990; van den Bergh 2002; Cameron et al. 2010; Nair & Abraham 2010).

There is a fundamental difference between the 'classical' and 'Bayesian' definitions of the term '*confidence interval'*. In classical statistical theory a binomial CI is defined as a pair of random variables, P_l and P_u, (with each random variable necessarily a finite, real-valued, measurable function, (Rao & Swift 2006) operating on the set of all possible experimental outcomes. In the Bayesian paradigm, on the other hand, the underlying population proportion is treated as an unknown model parameter and the binomial CI defined as an interval (*Pl, Pu*) to which the experimenter believes may be assigned a probability (c), of containing the true value of p, based upon consideration of the likelihood function for p given the experimental data and the strength of any a priori beliefs (expectations) regarding the system under study. (Indeed, acknowledging the significant conceptual differences between these alternative approachs to the binomial CI.

The two most commonly used methods for estimating CIs on binomial population proportions is the 'normal approximation' and the Clopper & Pearson (1934) approach. Although exhibit significant flaws under routine sampling conditions (cf.Vollset 1993; Santner 1998; Brown et al. 2001, 2002). In particular, the 'normal approximation' (also called the 'Poisson error') may systematically under-estimate the CI width necessary to provide coverage at the desired level, especially for small samples.

Fortunately, there exist a multitude of alternative methods for generating CIs on binomial population proportions, many of which exhibit far more satisfactory behaviour than either the 'normal approximation' or the Clopper & Pearson (1934) approach. Here I review both the theory and application of one of these methods by using beta distribution quantiles that deriving from a simple Bayesian analysis in which a uniform ('noninformative') prior is adopted for the true population proportion (e.g. Gelman et al. 2003). As I will demonstrate, the beta distribution generator for binomial CIs is both theoretically well-motivated and easily applied in practice using widely available mathematical matlab R20009 software packages.

II. AGN Fraction and Stellar Population

The term AGN (Active Galactic Nuclei) now refers to galaxy nuclei that exhibit anomalous energy output when compared to the expected energy output of a "normal" mixture of stars and gas (Shlosman et al., 1990). In addition to their distinct spectrum, the host galaxy is sometimes overwhelmed by the violent activity in the nucleus, which can outshine the entire galaxy. This causes the AGN to appear as a point source in images. Occasionally, jets are observed coming out of the nucleus. It is unlikely that such a high level of energy output could be sustained for long periods of time, which is why it appears that AGN are one stage of evolution for normal galaxies (Karttunen et al., 2003).

Galaxy mergers are a fundamental component hierarchical paradigm. A statistical analysis could be done on these sources to find an upper limit on the AGN fraction by assuming that they are all group members and determining how many of those sources would exceed our luminosity cutoff. It is likely that the sources furthest from the center of the group would not be part of the group. The sources concentrated near the center of the field could either be associated with galaxies in the group or with the intragroup medium.

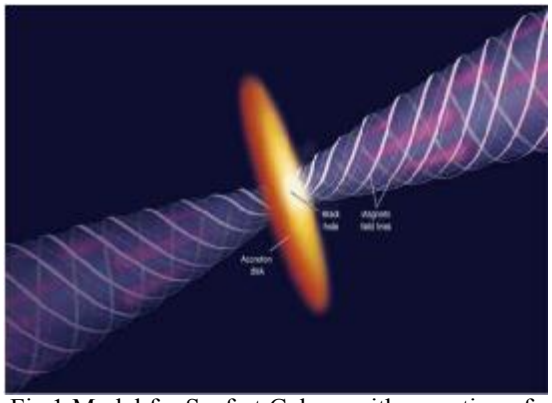

Fig 1:Model for Seyfert Galaxy with accretion of matter onto a supermassive black hole

III. The Binomial Distribution

There are two result in probability theory; succes and failure, if The probability ,P, particular number of sucesses k, in a series n independent Bernoulli succes to be signed with *k,* probability *P,* failure *q,*

$$P(k,n,p) = \binom{n}{k} p^k q^{n-k} \quad (1)$$

Where $0 \leq k \leq n, k \in \mathbb{Z}$ and

$$\binom{n}{k} = \frac{n!}{k!(n-k)!} \quad (2)$$

Probability given by *n+1* possible value of k correspond to the *n+1* terms of the binomial expansion of $(p+q)^n$. The number of barred systems counted in a given sample of disk galaxies is a classic example of binomially-distributed variable in astronomy. The coresponding expectation the value for the number of succes is $\sum_{k=0}^{n} k \times P(k,n,p) = np$ with a variance of $\sum_{k=0}^{n} k^2 \times P(k,n,p) = npq$. Moreover, the expectation value for the fraction k/n of successes is equal tho Bernoulli trial succes probablity and underlaying population proportion p and its variance is pq/n.

III. The Beta Distribution Generator for Binomial CIs

In astronomical data analysis it is standard practice to adopt the measured success fraction (also referred to as the 'observed population proportion'), $\hat{p} = k/n$ as one 'best guess' of the underlying population proportion. In statistical terms, $\hat{p}$ is employed as a point estimator for *p*. The likelihood of observing the result, $\hat{p} = k/n$ for a given value of p is. Proportional to Normalisation of this likelihood function over $0 < p < 1$ defines a beta distribution with integer parameters $a = k + 1$ and $b = n - k + 1$, $q = 1 - p$ (Gelman et al, 2003; Ross,2003)

$$B(a,b) = \frac{(a+b-1)!}{(a-1)!(b-1)!} p^{a-1} q^{b-1} \quad (3)$$

Differentiation of this likelihood function reveals that our best guess $\hat{p}$ is in fact the maximum likelihood estimator of p ilustrated in Figure 2 at a variety measured succes fraction for samples of sizes $n = 6$ (left panel) and $n = 36$ (right panel). A small *n,* the likelihood function for p is markedly asymmetric (ecxept where $\hat{p} = 1/2$) but at intermediate n it is visibly converging towards a narrow, symmetric or we can call (pseudo) normal distribution.

This condition is characterized using the Bayes-Laplace uniform prior, for which $P_{prior}(p) = 1$. Application of Bayes theorem under this assumption allows allows one to treat the normalised likelihood function for p as a posterior probability distribution.Thus, the quantiles of the beta distribution from Equation 3 may be used directly to estimate Bayesian confidence intervals on the underlying population proportion given the observed data. Specifically, the lower and upper bounds, p_l and p_u, defining an equal-tailed (central) interval for p at a nominal

confidence level of $c = 1 - \alpha$ are given by the quantiles formula:

$$\int_0^{pl} B(a,b)dp = {}^{\alpha}/_{2} \text{ and } \int_{pu}^{1} B(a,b)dp = {}^{\alpha}/_{2} \quad (4)$$

IV. Result and Discussion

The differences between binomial distribution and beta distribution using differences of number of examples. Its given five measured success fraction $\hat{p} = {}^{k}/_{n}$.

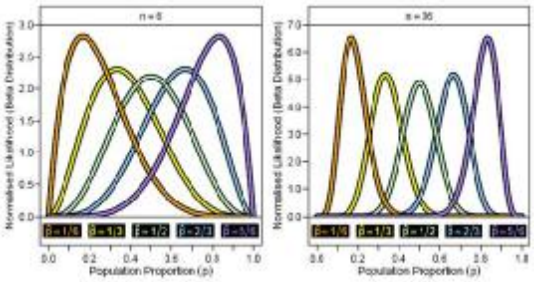

Fig.2 Example likelihood functions for samples of sizes n=6 (left panel) and n =36 (right panel).

In each case the shape of the curve is given by the beta distribution with shape parameters as specified by Equation 3. The asymmetric nature of this likelihood function in the small sample size regime is clearly evident amongst the n = 6 examples, as is its convergence in the intermediate to large sample size regime towards a narrower, more symmetric with normal distribution amongst the n = 36 examples. The probability of p greater than $p_u$equal to that p less than p_l. Its will be necessary asymetric about the maximum likelihood value $\hat{p}$ (except at $\hat{p} = 1/2$ owing the asymetric nature of the beta distribution likelihood in function p.

In the upper panel of Figure 2 I examine first the effective coverage, ce, of 'equal-tailed' binomial CIs defined using the beta distribution for a range of population proportions and sample sizes $0.025 \leq p \leq 0{,}975$ and sample sizes $1 \leq n \leq 100$ and at a nominal level of $c_n \approx 0{,}683\ (1\sigma)$ with the effective coverage defined as the fraction of samples drawn from the binomial probability function with given p and n for which the corresponding realisation of the CI under investigation encompasses the true population proportion. Thus, the effective coverage fractions c_e presented here are computed as the sum of all binomial probabilities $P(k,n,p)$ over $\{k: 0 \leq k \leq n, k \in \mathbb{Z}\}$ for which the triad $\{k,n,p\}$ produces a confidence interval (p_l, p_u)containing p.

One of the most striking features of this plot is the remarkable sensitivity of the effective coverage to the true underlying population proportion and sample size. This so-called 'oscillation signature' is an inherent property of all deterministic (non-randomising) generators for binomial CIs, arising from the discreteness of the binomial distribution (Brown, et al, 2001). Despite these oscillations it is clear that the beta distribution CIs do achieve an effective coverage close to (or slightly greater than) the desired confidence level over the vast majority of the parameter space explored here.

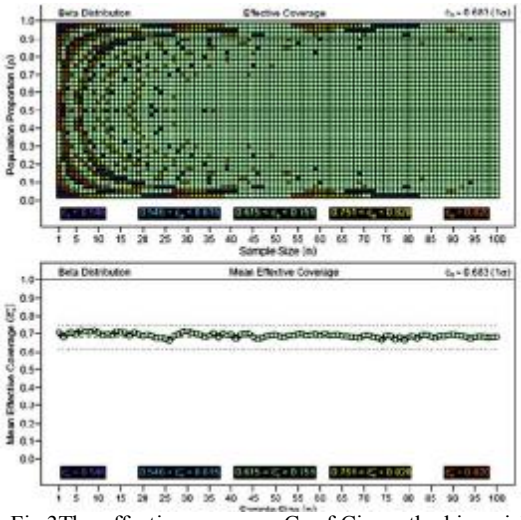

Fig.3The effective coverage C_e of Cis on the binomial population proportion generated from quantiles of beta distribution at a nominal level of $c_n \approx 0{,}683\ (1\sigma)$.

Indeed, even at the extremes of $p \leq {}^{1}/_{6}$ and $p \geq {}^{5}/_{6}$ where the oscillations are initially rather large, there is evidently a rapid increase in coverage stability with increasing sample size, such that the oscillation signaturemis vastly suppressed by $n \geq 40$, and effectively eliminated (at least for $0.025 \leq p \leq 0{,}975$) by $n \geq 80$. In the lower panel of Figure 3 examine the corresponding mean effective coverage (averaged uniformly over $0.025 \leq p \leq 0{,}975$) as a function of sample size. Whereas the effective coverage at given p and n shown the upper panel is consistent with the classical motion of confidence interval performance, the mean effective coverage may be considered a Bayesian CI performance diagnostic. if one really does hold all p values equally 'probable' a priori then one's favoured CI generator should be at least expected to provide coverage consistent with the nominal level in the longterm average of all equivalent experiments. Inspection of the lower panel of Figure 3 confirms a very close agreement between the mean effective

coverage of the beta distribution CI generator and the nominal confidence level, independent of n.

Most modern mathematical software packages providerobust, easy-to-use library functions for computing beta distribution quantiles. In this research i using matlab R2009 in command the betaincinv function.

In Tables 1 and 2 present compilations of equal-tailed CIs generated in this manner at nominal confidence levels of 1σ and 3σ, (in the appendix) respectively, for all possible observed success counts in sample sizes up to n =20. These tables are intended both as a convenient reference for use directly in studies involving samples of 20 objects or less, and as a benchmark against which to confirm the correct implementation of the beta distribution CI generator for users newly adopting this technique.

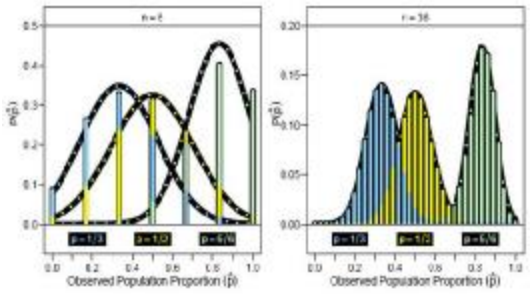

Fig.4 Comparison between the true binomial distribution of the $\hat{p}$ statistic assumed by the normal approximation

V. Conclusion

The (Bayesian) beta distribution quantile technique, is revealed to be a well-motivated alternative, consistently providing a mean level of coverage close to the nominal level, even for small-to-intermediate sample sizes. Given that the beta distribution generator for binomial CIs may be easily implemented using modern mathematical software packages. This technique be adopted in future studies aiming to constrain the true values of astronomical AGN fraction and stellar population .

VI. Acknowledgments

I would like to thank Department of Physics Sains and Technology Faculty Islamic State University Sunan Kalijaga Yogyakarta for funding this research and Hisab Rukyah Research Center Islamic State University Sunan Kalijaga for support and helpfull discussions on the role astronomy sains.

VII. References

1. Brown, L. D., Cai, T. T., DasGupta, A, Statistical Science, 16, 2, 101 (2001)
2. Cameron, E. et al. MNRAS, 409, 1, 346 (2010)
3. Elmegreen, D. M., Elmegreen, B. G., Bellin, A. D, *ApJ*, 364, 415(1990).
4. Gelman, A., Carlin, J. B., Stern, H. S., Rubin, D.B, *Bayesian Data Analysis*, Chapman & Hall, New York (2003)
5. Karttunen, P. Kroeger, H. Oja, M. Poutanen, and K. J. Donner, *Fundamental astronomy* (Fundamental astronomy, by Hannu Karttunen, P. Kroeger, H. Oja, M. Poutanen, and K.J. Donner, 4th ed., Berlin: *Springer*, 2003., (2003).
6. Nair, P. B., Abraham, R. G., *ApJL*, 714, 2, L260 (2010)
7. Rao, M. M., Swift, R. J., Mathematics and Its Applications, 582 (2006)
8. Shlosman, M. C. Begelman, and J. Frank, *Nature* 345, 679 (1990).
9. Van den Bergh, S. AJ, 124, 782 (2002)

ANALISIS TIPE RESERVOIR DAN SUHU LAPANGAN PANASBUMI TIRIS PROBOLINGGO JAWA TIMUR

A. Suprianto[1, 2], Wahyudi[2], W. Utama.[3], Suharno[4] dan W. Suryanto[2]
1. Universitas Jember,
2. Universitas Gadjah Mada,
3. Istitut Teknologi Sepuluh Nopember,
4. Universitas Lampung

Email: agus.suprianto@gmail.com

ABSTRAK

Lapangan panasbumi tiris terletak di wilayah Kabupaten Purbolinggo tepatnya di bagian timur Gunung Lamongan. Data geokimia diambil dari 15 lokasi. Dua lokasi Sungai Tancak dan Air Sumur Tiris dianalisis geokimia berdasarkan metode, geotermometer, geoindikator, dalam rangka menentukan karakteristik reservoir dan keadaan suhu sistem panasbumi Tiris Kabupaten Probolinggo Jawa Timur. Hasil sementara menunjukkan bahwa karakteristik reservoir bersifat basa dengan suhu reservoir lebih dari 280^{o} C.

THE ANALISYS OF THE RESERVOIR TYPE AND TEMPERATURE OF THE TIRIS GEOTHERMAL PROSPECT PROBOLINGGO JAWA TIMUR

A. Suprianto[1, 2], Wahyudi[2], W. Utama.[3], Suharno[4] dan W. Suryanto[2]

1. University of Jember,
2. Gadjah Mada University,
3. Sepuluh Nopember Institute of Technology,
4. University of Lampung

Email: agus.suprianto@gmail.com

ABSTRACT

The Tiris geothermal prospect situated within the Purbolinggo District, Jawa Timur Province, eastern the Gunung Lamongan. Geochemical data collected from fiveteen location. Two location were analised using geochemical methods of the geothermometer and geoindikator, doe to determine the reservoir characteristic and temperature conditions of the Tiris geothermal system, Probolinggo District, Jawa Timur Province. The tentaive result indicated that the the characteristic of the reservoir sould be sodium with temperature more than 280^{o} C.

1. INTRODUCTION

The Tiris geothermal field is located on one of the major volcanic areas spread throughout the country. Therefore, the country has many hot springs with a variety of temperatures ranging between 38 ^{o}C and 50^{o}C. The hot springs are located mainly on major active fractures and old crater lake volcanic areas one of which is air panas Tancak di Desa Segaran Kecamatan Tiris and Danau vulkanik Ranu Bedali, Ranu Klakah, Ranu Segaran.

The air panas Tancak is one of the prospective areas in Probolinggo District Jawa Timur Province. The map location is shown in Figure 1.

The Tiris geothermal field is located near the Pandak, Argopuro and Old Tengger volcanic rocks, which is Quarter in age. The Leprak Formation composed sedimentary unit, intrusive of the granite. The geothermal area covered by Tertiary sedimentary units assumed to be cap rock. The rocks of the Tiris geothermal field are divided into ten zones that are characterized in Figure 2.

The geothermal manifestation spreads throughout an area including travertine and swampy areas formed by hot water emergence and leakage, boiling hot springs, lake of carbonate water. The results of chemical analysis of hot and cold water samples have been evaluated for fluid using Giggenbach diagrams.

2. CHEMICAL COMPOSITIONS OF THE WATERS

The geochemical study is based on discharge water samples collected from the discharge of two hot water springs. These samples were collected in June 2010. Samples were untreated and included acidified water. Chemical analyses of Na, K, Mg, SO4, SiO2 pH, Cl, HCO3.

The average chemical compositions of the geothermal water from the Sungai Tancak and Sumur Desa Tiris are presented in Table 1. The discharge water from Tancak hot water are of the chlorate type with alkaline pH (6-7) and with total dissolved solids in range the of 400-700 mg/kg. The samples form Sungai Tancak, a HCO3 are predominate cations with concentration more than 1500 mg/l, SiO2 and Cl respectively 116 and 458 mg/kg, SO4 is less, about 1 mg/kg. The anion Na, K and Mg respectively 306, 306 and 238. In contrast, waters discharged from Sumur Tiris are neutral (pH-6-7) composite of the Na, K, Mg, SO4, HCO3, SiO2 and Cl respectively 8, 11, 18, 1, 186, 53, 27in mg/kg.

The chemical compositions of the waters were classified on the basis of major ions using the Cl-SO4-HCO3 triangular diagram of Giggenbach (Figure 3). All samples plot to area of mature waters and can be classified as Cl-rich geothermal water which formed by the interaction of geothermal fluids with the host rock and dilution with low salinity water at depth (White and Muffler, 1971).

The Tiris possesses great potentiality for the utilization of geothermal energy. The region has been centre of attraction to a number of visiting national scientists, encouraging them

to collect and analyze geothermal water samples at different localities on a sporadic basis. One of such studies has determined the temperature and reservoir characteristic.

3. ESTIMATION OF THE RESERVOIR

Even though the above table suggests that none of the springs have a huge mass flow rate, a number of springs emerging in the vicinity could have lowered the flow rate. Water containing chloride concentration more than 450 mg/kg. No high concentration of silica is observed relative to discharge temperature in all spring waters. The waters at sumur Tiris lying in this region have relatively high chloride, suggesting that the waters are fairly mature as indicated by the Giggenbach's diagram of concentrations of the major anions, Cl, SO4 and HCO3. This is illustrated in Figure 3. Figure 3 suggest that the reservoir is carbonat with high consentration of HCO3.

Table 1. Geochemical data from the Sungai Tancak and Air Sumur Tiris geothermal field.

Sampel	Na	K	Mg	SO4	HCO3	SiO2	Cl
Sungai Tancak	306	63	238	1	1585	116	458
Sumur Desa Tiris	8	11	18	1	186	53	27

4. SUBSURFACE TEMPERATURE ESTIMATION

Chemical geothermometers are used in order to estimate the reservoir temperature. The important criteria for chemical geothermometer application to thermal spring are the pH, temperature and discharge rate of the spring. Some of them give unreliable results such as either lower than spring temperature or extremely high temperature. These equations are based on geothermometers for chalcedony and quartz, which assume hat these minerals used in geothermometers, are not in equilibrium with rock – water interaction in reservoir.

The silica and cation geothermometers were used for the evaluation of subsurface temperature for discharges (Table 1). The Source of temperature equations: T–measured temperature, T: Na-K– Fournier and Truesdell (1973), T: Na-K – Giggenbach (1988), T-Fournier (1977) were used. The sample form Sungai Tancak suggest that the reservoir temperatures is about 287^{o}C. The Na-K geothermometer of Giggenbach (1988) suggested reservoir temperature temperatures is about 297^{o}C.

The Na-K-Mg triangular diagram shows the equilibrium between the geothermal fluids and rock and reservoir temperature (Figure 4). By considering the diagram presented in Figure 4, the Kozakli hot springs plot in the immature water part, so using the chemical geothermometers is not reliable according to the theory used to establish the diagram. In

this Na-K-Mg diagram all the samples have not gained equilibrium with rock, presumably due to fast circulation of luid through the rock fractures. This causes the water to be mature, considering the ion exchange processes that, equilibrium has not been reached yet with rock minerals because of circulation flow. Figure 4 shows that samples from studied geothermal fall on the full equilibrium line, suggested attainment of the (Sungai Tancak) has temperature between 287 - 297^{o}C.

3. CONCLUSION

The geothermal waters discharged from Sungai Tancak geothermal field and Sumur Tiris within the Sub-Disrict of Tiris, Probolinggo District, jawa Timur Province are of carbonate type with a high concentration of HCO3 and moderately Cl. The chemical compositions of reservoir waters indicate that the reservoir is located in the liquid dominant zone and geothermal waters come from an old geothermal system. The water composition from Sumur Tiris is carbonate and chloride water. Thermal fluid is in equilibrium with reservoir rocks, which can be the product of water-rock interaction at high temperature. Common geothermometers have been used for estimating the subsurface temperature. The results from Na-K geothermometers and Na-K-Mg geoindikcator, indicate that the reservoir temperature. The calculated temperatures using Na-K geothermometers and Na-K-Mg geoindikcator is more than 280^{o}C. However, the fact or temperature may confirm with the measurement well temperature arter drilling.

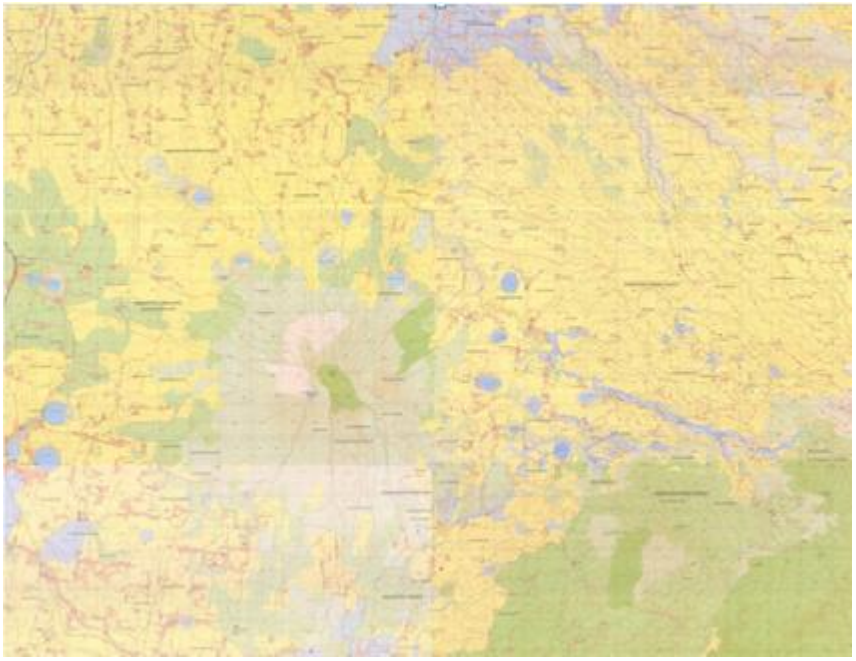

Figure 1. The topography map location of the Sungai Tancak and Air Sumur Tiris geothermal field.

Figure 2. The geological map of the Sungai Tancak and Air Sumur Tiris geothermal field.

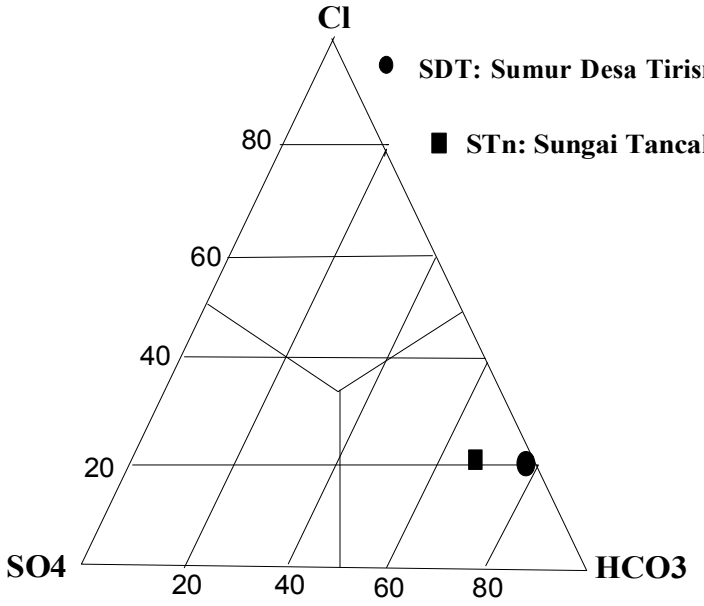

Figur 3. The diagram of the Sungai Tancak and Air Sumur Tiris reservoir characteristic.

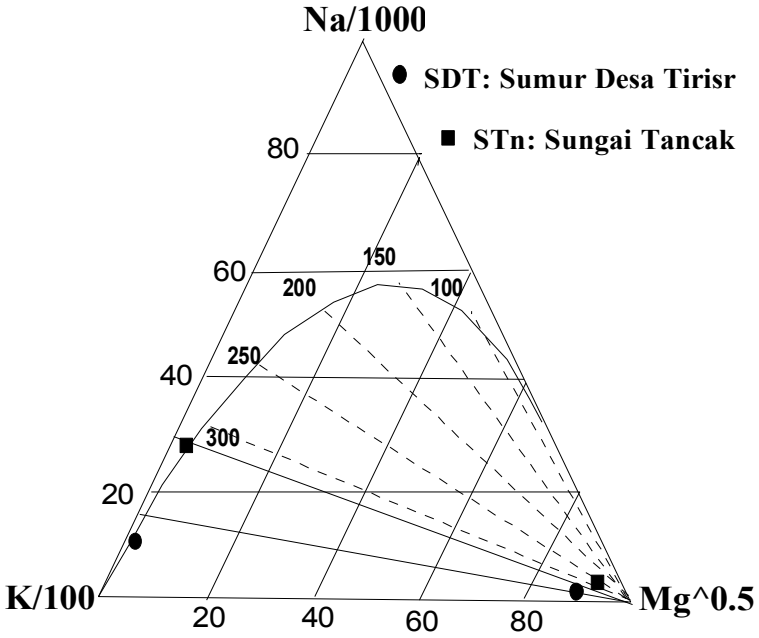

Figur 4. The diagram of the temperatures of the Sungai Tancak and Air Sumur Tiris geothermal reservoir.

4. REFERENCES

Fournier, R.O.: and White, D. E. and Truesdell, A. H. Chemical Geothermometers and Mixing Models for Geothermal System, *Geothermics*, **5**, (1977), 41-50.

Fournier, R., and Truesdell A.: An Empirical Na-K-Ca Geoindicators, *Geochim. Cosmochim. Acta*, **37**, (1973), 1255-1275. Giggenbach, W.: Geothermal Solute Equilibria. Derivation of Na-K-Mg-Ca Geoindicators, *Geochim. Cosmochim. Acta,* **52**, (1988), 2749-2765.

Geocemical indicators of subsurface temperature. U.S. Geol. Survey J. R. 2, (1974), 259-262.

Giggenbach, W. F. Geothermal Gas Equilibria. Geochemica Cosmochemica Acta 31, (1988).

Giggenbach, W.F.: Chemical Techniques in Geothermal Exploration. In: D'Amore, F(coordinator), *Application of geochemistry in geothermal reservoir development*. UNITAR/UNDP publication, Rome, (1991), 119-142.

White, D.E., and Muffler, L.G: Vapour-dominated Hydrothermal System Compared with Hot Water System. *Economic Geology*, **66**, (1971), 75-97.

GEOCHEMICAL RESERVOIR ANALYSIS OF THE GUNUNG UNGARAN GEOTHERMAL PROSPECT, SEMARANG DISTRICT, CENTRAL JAVA PROVINCE

Karyanto[1, 2], Wahyudi[2], Suharno[1], Ari Setiawan[2] dan W. Suryanto[2]

1. Geophysics Engineering, Lampung University,
2. Geophysics, Gadjah Mada University
Email: karyantodjon@yahoo.com

ABSTRACT

The Gunung Ungaran geothermal prospect situated within the Semarang District, Central Java Province. Geochemical data collected from sixteen location. The geochemical analysis using the ions balance, geothermometer and geoindikator analysis, doe to determine the reservoir characteristic and temperature conditions of the Gunung Ungaran geothermal prospect, Semarang District, Jawa Tengah Province. The tentative result, although the ions balance indicate that not good balance, but the geoindictor and geothermometer indicated that the characteristic of the reservoir should be acid with temperature more than 200^{o} C.

The discharge test measurements show that chemical composition of the reservoir water was analyzed by standard methods and subsequently classified using Cl-SO4, HCO3 and Cl-Li-B triangular diagram. A Na-K-Mg triangular diagram was used to classify waters according to the state of equilibrium at given temperatures. The geothermal waters are of sodium-acid type and from a relatively old hydrothermal system. Thermal fluid is in equilibrium with reservoir rocks. The calculated temperatures using Na-K geothermometers suggested the subsurface temperature is more than 325^{o}C and Na-K-Mg geoindicator suggested the subsurface temperature is more than 300^{o}C.

Key word: geochemical, geothermometer, geoindicator, geothermal Ungaran

1. INTRODUCTION

The Ungaran geothermal field is located on one of the major tectonic belts of the central Java. In addition to this, there are volcanic areas spread throughout northward from Mt.Merapai, Mt. Merbabu, Mt. Ungaran and Mt. Gunungpati. Therefore, the Ungaran has many hot springs with a variety of temperatures ranging up to 95^{o}C. The hot springs are located mainly on major active fractures and volcanic areas one of which is called Gedongsongo and others.

The Ungaran geothermal field is located near the Gunung Ungaran Massive, which is Paleozoic in age. This Massive is mainly composed of metamorphic schists, marble and granite, and forms the basement of the geothermal area covered by Tertiary volcanic-sedimentary units assumed to be cap rock. The geothermal manifestation spreads throughout an area including boiling hot springs, travertine and swampy areas formed by hot water emergence and leakage. The results of chemical analysis of hot and cold water samples have been evaluated for fluid using Giggenbach diagrams.

2. CHEMICAL COMPOSITIONS OF THE WATERS

The geochemical study is based on discharge water samples collected from the discharge of six hot water springs. Samples were untreated and included acidified water. Chemical analyses of Na, K, Ca, Mg, B, Li, and SO4, and the SiO2 pH, Cl, HCO3.

Table 1. Geochemical data from Ungaran geothermal feild

No	LOKASI	SiO2	Ca	HCO3	SO4	Cl	Li	B	Na	K
1	**Gedongsongo 1**	78	18	61	96	35	7	11	4	8
2	**Gedongsongo 2**	106	6	0	372	164	0	0	5	9
3	**Gedongsongo 3**	74	16	36	146	59	0	1	3	8
4	**Gedongsongo 4**	129	22	0	1681	176	0	0	5	14
5	**Gedangan**	38	10	73	5	6	0	0	1	2
6	**Diwak 1**	67	182	1416	7	112	3	3	105	29

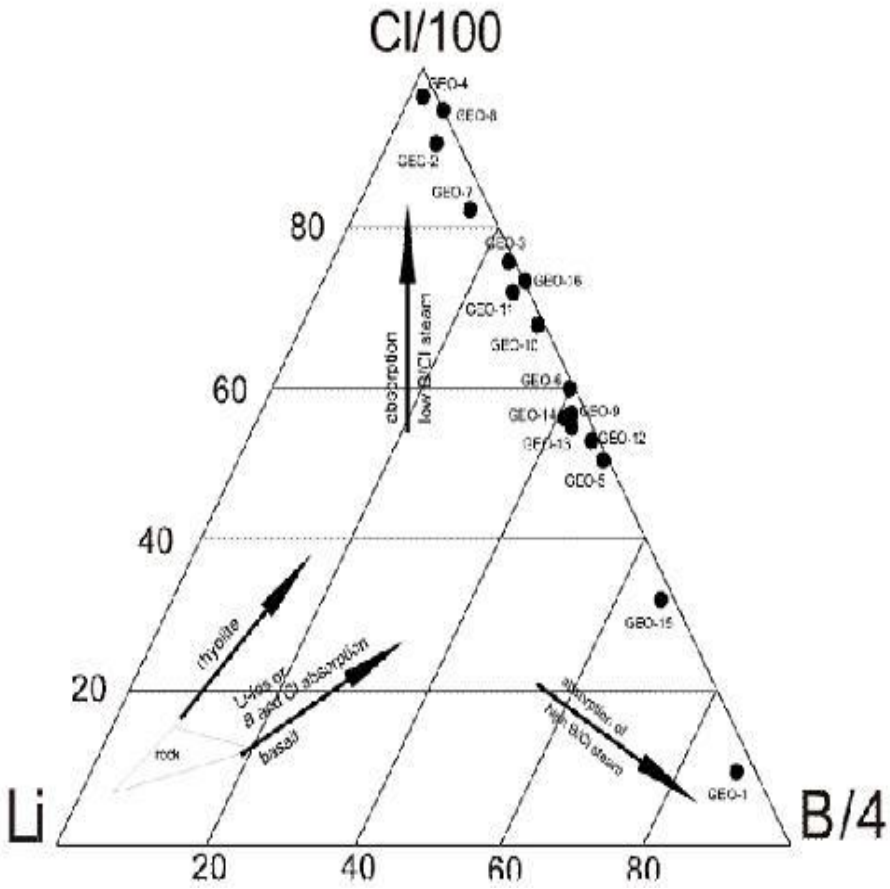

Figure 1. The diagram Cl-B-Li triangle Ungaran geothermal field.

Li, Cl and B are conservative elements in the geothermal system. They are fixed in fluid phase and have not equilibrated. The conservative elements are the best geoindicators of the origin of the geothermal system. B/Cl ratio and Cl-Li-B ternary diagram were used to indicate the source of the fluid. A plot of the relative concentrations of Cl, Li and B is shown in Figure 1. All geothermal waters have high Cl content relative to Li and B, indicating that they are from an old hydrothermal system and that fluid migrated from the old basement rock.

2.1 Classification of the thermal fluids

The average chemical compositions of the geothermal water from the Ungaran are presented in Table 1. The discharge water from Ungaran hot water are of the sodium and acid. A Cl are predominate cations in gedongsongo 2 and Gedongsongo 4 with concentration more than 164 and 176 mg/l respectively. In contrast, hot waters discharged from Diwak 1 hot spring are acid and concentration of carbonate ions are very high (1416 mg/l). The chemical compositions of the waters were classified on the basis of major ions using the Cl-SO4-HCO3 triangular diagram of Giggenbach (Figure 1). All samples plot to area of mature waters and can be classified as sodium-rich geothermal water which formed by the interaction of geothermal fluids with the host rock and dilution with low salinity water at depth (White and Muffler, 1971).

The Ungaran possesses great potentiality for the utilization of geothermal energy. The region has been centre of attraction to a number of visiting national scientists, encouraging them to collect and analyze geothermal water samples at different localities on a sporadic basis. One of such studies has determined the temperature and reservoir characteristic.

2.2 Estimation of Reservoir

Even though the above table suggests that none of the springs have a huge mass flow rate, a number of springs emerging in the vicinity could have lowered the flow rate. Average the water containing chloride concentration lower than 100 mg/l. No high concentration of silica is observed relative to discharge temperature in all spring waters. The waters at Ungaran lying in this region have relatively high sulphate, suggesting that the waters are fairly mature as indicated by the Giggenbach's diagram of concentrations of the major anions, Cl, SO4 and HCO3. This is illustrated in Figure 2. The Ungaran geothermal reservoir characterized by sodium rich and acid sulphat.

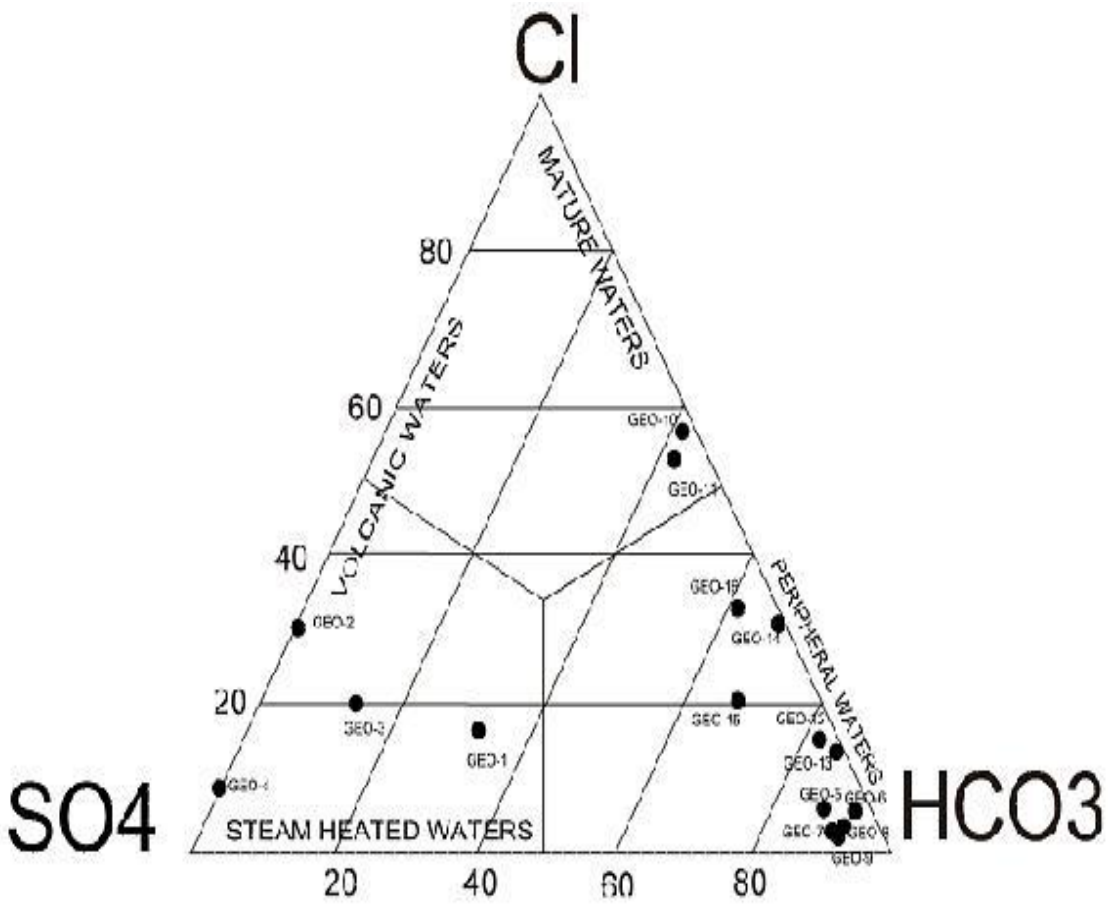

Figure 2. The diagram Cl-HCO3-SO4 triangle Ungaran geothermal field.

2.3. Subsurface Temperature Estimation

Chemical geothermometers are used in order to estimate the reservoir temperature. The important criteria for chemical geothermometer application to thermal spring are the pH, temperature and discharge rate of the spring. Some of them give unreliable results such as either lower than spring temperature or extremely high temperature. These equations are based on geothermometers for chalcedony and quartz, which assume that these minerals used in geothermometers, are not in equilibrium with rock – water interaction in reservoir.

The silica and cation geothermometers were used for the evaluation of subsurface temperature for discharges (Table 2). The Source of temperature equations: T–measured temperature, T: Na-K–Fournier and Truesdell (1973), T: Na-K – Giggenbach (1988), T- Fournier (1977) were used. These give reservoir temperatures ranging 325 - 700^{o}C. The Na-K geothermometer of Giggenbach (1988) suggested reservoir temperature more than 330^{o}C and Fournier (1977) suggested reservoir temperature more than 325^{o}C.

The Na-K-Mg triangular diagram shows the equilibrium between the geothermal fluids and rock and reservoir temperature (Figure 3).

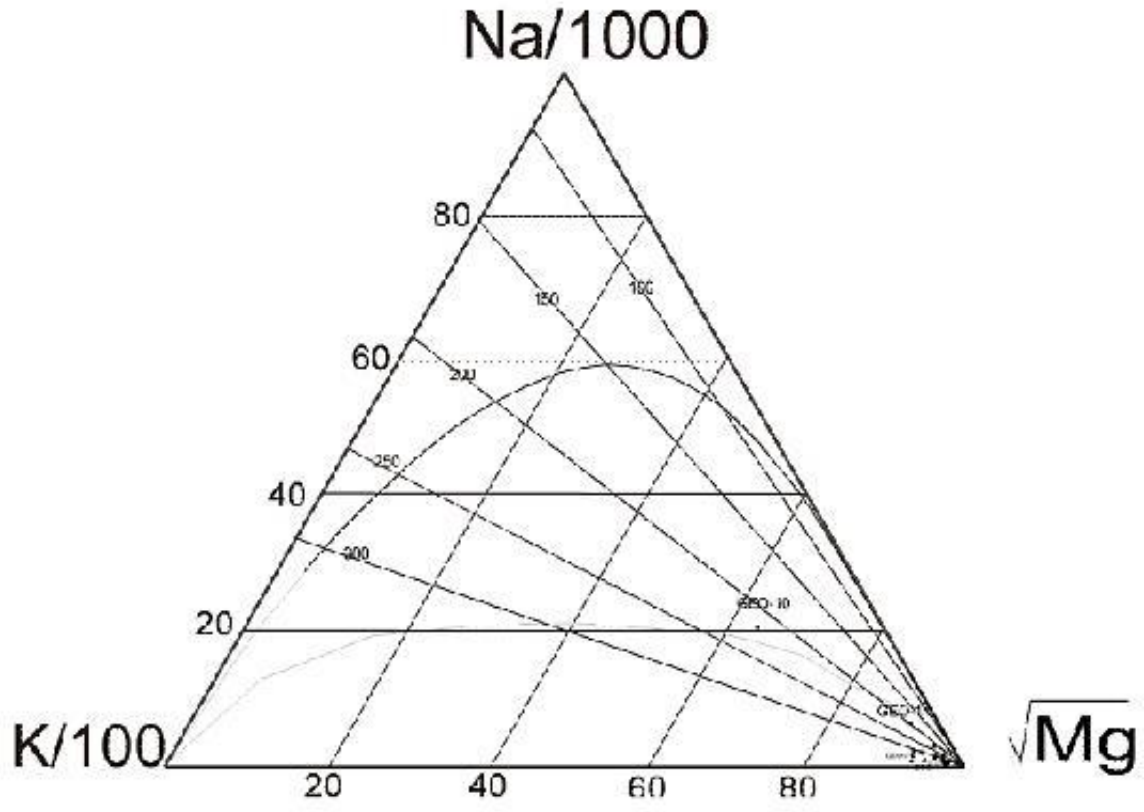

Figur 3. The diagram Na-K-Mg triangle of the temperatures of the Ungaran geothermal reservoir.

Table 2. Na-K Fourier and Giggencbach) from Ungaran geothermal feild

No	LOKASI	Na-K (Fournier)	Na-K (Giggencbach)	Quartz	Chalce dony	Cristo balite	Opal CT
1	Gedongsongo 1	795°C	715 °C	124 °C	96 °C	73 °C	25 °C
2	Gedongsongo 2	689 °C	634 °C	140 °C	114 °C	90 °C	41 °C
3	Gedongsongo 3	834 °C	744 °C	121 °C	93 °C	71 °C	23 °C
4	Gedongsongo 4	872 °C	772 °C	152 °C	127 °C	102 °C	52 °C
5	Gedangan	772 °C	698 °C	90 °C	59 °C	39 °C	6 °C
6	Diwak 1	324 °C	330 °C	116 °C	88 °C	66 °C	18 °C

By considering the diagram presented in Figure 2, the Ungaran hot springs plot in the immature water part, so using the chemical geothermometers is not reliable according to the theory used to establish the diagram. In this Na-K-Mg diagram all the samples have not gained equilibrium with rock, presumably due to fast circulation of fluid through the rock fractures. This causes the water to be immature, considering the ion exchange processes that, equilibrium has not been reached

yet with rock minerals because of circulation flow. Figure 3 shows that samples from studied geothermal wells fall on the full equilibrium line, suggested attainment of the Ungaran 300°C.

3. CONCLUSION

The geothermal waters discharged from Ungaran geothermal field are of sodium-acid type with a high concentration of HCO3 and SO4. Chemical compositions of reservoir waters indicate that the reservoir is located in the liquid dominant zone and geothermal waters come from an old geothermal system. The water composition from Gedongsongo and Diwak is carbonate and sulphate. Thermal fluid is in equilibrium with reservoir rocks, which can be the product of water-rock interaction at high temperature. Common geothermometers have been used for estimating the subsurface temperature. The results from Na-K geothermometers and Na-K-Mg geoindikcator, indicate that the reservoir temperature. The calculated temperatures using Na-K geothermometers and Na-K-Mg geoindikcator is more than 300°C. However, compare with measured temperature further.

4. REFERENCES

Fournier, R. O.: Chemical Geothermometers and Mixing Models for Geothermal System, *Geothermics*, **5**, (1977), 41-50.

Fournier, R., and Truesdell A.: An Empirical Na-K-Ca Geoindicators, *Geochim. Cosmochim. Acta*, **37**, (1973), 1255-1275. Giggenbach, W.: Geothermal Solute Equilibria. Derivation of Na-K-Mg-Ca Geoindicators, *Geochim. Cosmochim. Acta,* **52**, (1988), 2749-2765.

Geocemical indicators of subsurface temperature. U.S. Geol. Survey J. R. 2, (1974), 259-262.

Giggenbach, W. F. Geothermal Gas Equilibria. Geochemica Cosmochemica Acta 31, (1988).

Giggenbach, W.F.: Chemical Techniques in Geothermal Exploration. In: D'Amore, F(coordinator), *Application of geochemistry in geothermal reservoir development.* UNITAR/UNDP publication, Rome, (1991), 119-142.

White, D.E., and Muffler, L.G: Vapour-dominated Hydrothermal System Compared with Hot Water System. *Economic Geology*, **66**, (1971), 75-97.

Design and preliminary evaluation of device for Spectral Induced Polarization measurements in Geophysics Exploration

Suparwoto
Department of Physics, Faculty of Mathematics and Natural Sciences, Gadjah Mada University
Sekip Utara PO BOX BLS.21 Yogyakarta 55281

Abstract

Laboratory experiments to study the induced polarizartion phenomenon on natural and artificial samples are of great importance as they can explain on the cause and nature of the phenomenon.The amplitude and phase characteristics of the voltage and currrent on impedance measurements of the samples is called as Spectral Induced Polarization.

The basic techniques for measuring complex impedance are amplitude voltage measurement, current measurement and phase difference detection between voltage and current as function of frequency. Induced Polarization method measure the variation impedance of the ground or samples with the frequency of the injected current at very low frequency from 0,1 Hz to 1000 Hz. In order to improve the accuracy of the device, the high impedance differential instrumentation amplifier are used. The outputs from voltage amplifier and current amplifier are sent to data logger. Experimental variable frequency measurement on RC circuits were carried out to preliminininary evaluate the performance of the device.

The result obtained by the device were found to be in good agreement with the teoretical computation obtained on RC circuits. Overall mean error of 0,1 % in magnitude and 0,2 ^{o} in phase over frequency range of 0,1 Hz to 1000 Hz. The largest error in phase measurement occured at low frequency below 1 Hz due to electro chemical potential at the electrode.

Keywords : *induced polarization, complex impedance, spectral induced polarization,voltage and current measurement, phase detection, high impedance differential instrumentaion amplifier, data logger, RC circuits,electro chemical potential.*

* Corresponding author.
E-mail address:suparwoto@ugm.ac.id

I. Introduction

Laboratory measurement to study induced polarization phenomenon are of great importance as they can explain on the cause and nature of the phenomenon. Spectral Induced Polarization devices which are portable, low cost ,and capable of performing measurement with adequate accuracy will be highly desirable for this use. This paper describes a novel design of a portable SIP measurement system based on magnitude and phase difference detection.

In resistivity method, low frequency alternating current is introduced into the ground by means of two current electrodes. The resulting potential difference measured by means of two potential electrodes, the apparent resistivity of the ground is proportional to the ratio of the potential difference and the current.

Mineral ore occurs most commonly in nature either in the form of a vein, an ore-shoot or in lense, which causes polarization phenomenon. The frequency depedence of the observed apparent resistivity is strongly controlled by the presence of the mineral ore in nature.

II.The induced polarization method

If an electric current is injected into the ground by means of two current electrodes for several seconds and then intercepted, the voltage across the potential electrodes does not drop to zero instantaneously. It is found that the voltage across the potential electrodes to relax for several seconds starting from an initial value which is a small fraction of the voltage that existed when the current was flowing. This phenomenon has been termed as induced polarization (IP). There are three method of IP survey, i.e. Time Domain IP, Frequency Domain IP and Spectral IP.

Time Domain IP, measures the integrated area under an IP decay curve between t_1 and t_2 normalized by the primary voltage, the parameter is called as chargeability (M). The unit of M is milisecond.

Frequency Domain IP, measure the resistivity of the ground in two frequencies, low frequency (0,1 Hz) and high frequency (10 Hz). The parameter is called Percent Frequency Effect (PFE), i.e.the difference between low frequency resistivity and high frequency resistivity divided by high frequency resistivity multiplied by 100 %, the unit is in percent.
Spectral IP, measures impedance of the ground and phase difference between current and voltage as function of frequency, the frequency range between 0,1 Hz to 1000 Hz. The result of this survey are impedance and phase spectral.

III.The source of polarization

There are two principal effects as origin of induced polarization phenomenon, an electrode polarization and a membrane polarization.

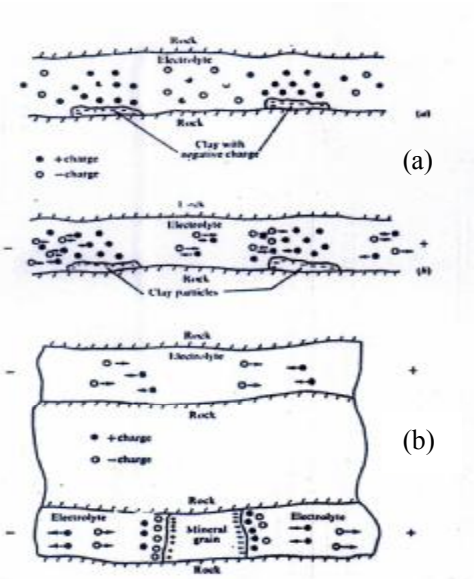

Figure 1. (a) Membrane polarization (a) and (b) electrode polarization

The electric current in the ground normaly carried by ions in the electrolytes present in the pores of rocks. If the passage of these ions is obstructed by conducting mineral particles, wherein current conduction take place by electrons, ionic charges pile up at the particle-electrolyt interface.The particle is said to be polarized if the pile up charges create a voltage thet tends to oppose the flow of electric current across the interface.
When the current is interrupted, a residual voltage continues to exist across the particle, due to the pile up of ionic charges on both side of the particle.
This voltage decreases gradually as the ions slowly diffuse back into the pore electrolytes. This process takes some seconds, and is called the induced polarization effects. This type of polarization is called electrode polarization because it is observed at the surface of the metal electrodes dipped in an electrolyte (Fig.1b).
The presence of clay particles in the ground also gives the IP effect, the phenomenon is termed membrane polarization. The surface of the clay particle is negatively charged and thus attracts positive ions from the electrolytes present in the capillary pores of the clay. When an electric current is flowed through the clay, positive ions are displaced and on interruption of the current the positive ions redistribute themselves in their former equilibrium pattern. This process of re-alignment generates a decaying voltage between two electrodes in contact with the clay (Fig.1 a).
The development of a nett charge at the mineral ore surface affects the distribution of ions in the surrounding interfacial region, resulting in an increased consentration of ions in opposite charge to that of the particle, close to the surface. Thus an electrical double layer exists round each mineral particle. On a bare metal immersed in an electrolyte the double layer capacitance will be 20 to 60 microFarad per centimeter square.
Diffusion process in an electrolyte can create an impedance called the Warburg-impedance. The impedance depends on the frequency, at high frequences the Warburg impedance is small since diffusing reactants don't have to move very far.
The Warburg impedance and electrical double layer capacitance causes the impedance behavior of the ground, the resistance of the ground are depends on the frequency.

IV.Instrument design.

The apparatus for measurement spectral induced polarization is a complex impedance measuring system with facility for wide band current source (0,01 Hz to 10 Khz). The current is sent to modelling tank trough a standard resistor for current sensing element. The signal across the potential electrodes is picked up by a balanced high Common Mode Rejection Ratio amplifier. The configuration of the amplifier is differential instrumentation amplifier with Field Effect Transistor (FET) as input stage to provide a high impedance amplifier. The differntial –input amplifier is formed from two operational amplifier, each op-amp is connected in the non

inverting follower configuration. This circuit is used because the input impedance of the overal amplifier is essentially the input impedance of the device. For a BiMOS op-amp, the input impedance is on the order of 10^{12} ohm. The outputs from potential amplifier and current amplifier are connected to a computerized two channel data logger (Figure 2).

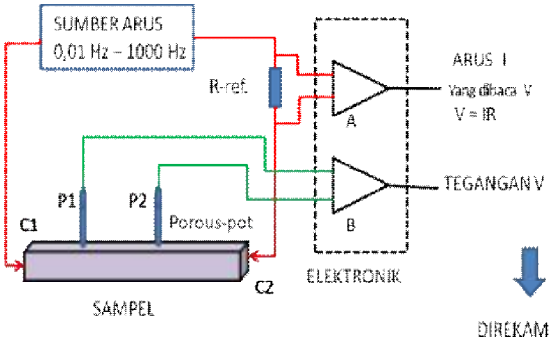

Figure 2. The apparatus for SIP measurement.

V. System calibration

System calibration is very importance in achieving accurate measurements since measurement errors are nearly inevitable. The simple RC circuit (fig.3) were measured using complex impedance measuring system. The RC circuit represent the solution resistance R_S , charge transfer resistance R_{CT} and electrical double layer capacitance $C_{DL.}$, the configuration figure 3 is called the Randle Cells.

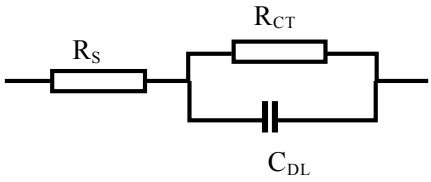

Figure 3. Equivalent circuit of medium.

Two sinus waves represents voltage across the Randle Cell (blue) and current flows through the cell (red), the current leads the voltage (figure 4). Figure 5 is the result of the measuring system, impedance and phase spectra. The lines represent the impedance and phase spectra obtained from teoretical computation, while the circles are the data measured by complex impedance measuring system, with the value of R_S = 1800 ohm, R_{CT} =1800 ohm and C_{DL} = 235 µF.

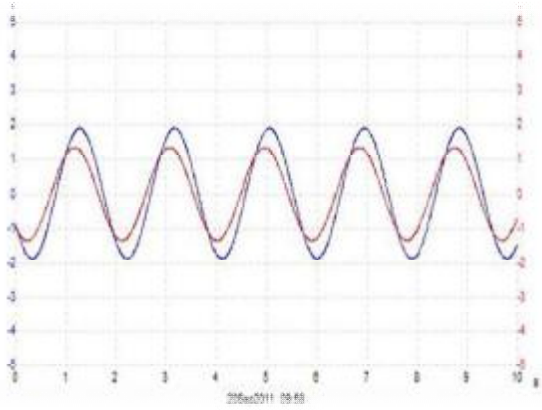

Figure 4. Sinus waves, represent current and across the RC circuit figure 3.

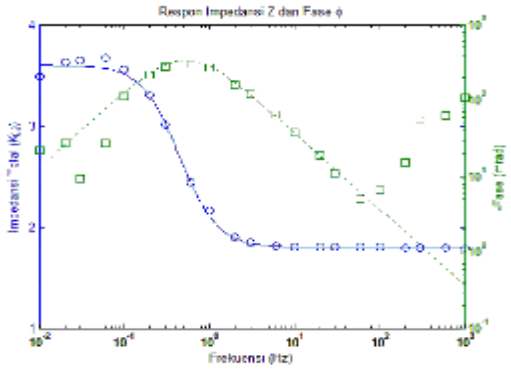

Figure 5. Comparison of SIP data, obtained from teoretical computation and the measurement result.

Figure 6 shows the result of impedance and phase spectra with alumunium sheet immersed in tap water.

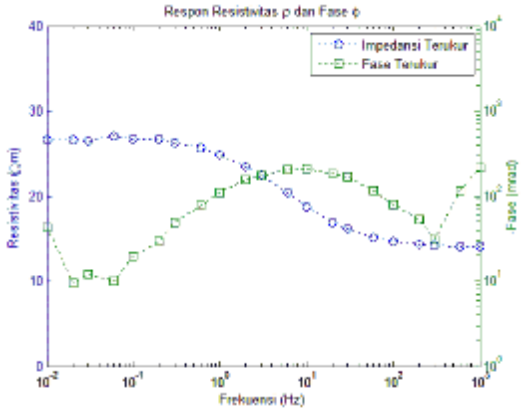

Figure 6. impedance and phase spectra of artificial sample (alumunium sheet).

VI. Conclusion.

The result obtained by the complex impedance measuring device were found to be in good agreement with teoretical computation obtained on RC circuit.
The impedance and phase spectra obtained from artificial sample shows the complex impedance phenomenon as in RC circuit model.

VII.References.

1. Apparao,A, Developments in Geoelectrical Methods, National Geophysical Research Institute ,AA Balkema/Rotterdam /BrookField/1999.
2. Carr,J, Electronic Devices, Glencoe Tech Series, McGraw Hill International Edition, 1991.
3. Vanhala H, Soininen H, Laboratory technique for Spectral Induced Polarization response of Soil samples, Geophysical Prospecting Vol.43,1995.
4. Telford WM, Gerdart, LP, Sherif LP, Applied Geophysics, Cambridge University Press, New York USA, 1990.
5. Ntarlagiannis, D., Doherty, R., dan Williams, K.H., 2010, Spectral induced polarization signatures of abiotic FeS precipition, Geophysics, Vol.75, No.4, hal.F127- F133.

An Analytical Study of Relationship on the Water Saturation, Frequency, Attenuation and Porosity

Sismanto
Geophysics Laboratory, Department of Physics, Faculty of Mathematics and Natural Sciences, Gadjah Mada University, Sekip Utara PO BOX BLS.21 Yogyakarta 55281

Abstract
It has theoretically been derived the water saturation values based on analysis of seismic wave attenuation, frequency and porosity using Biot-Turgut-Yamamoto-Sismanto equation. From the obtained relationship studied, we can see how far the sensitivity of water saturation on seismic wave attenuation parameters, to the frequency and porosity through the cross-plot between these parameters. The results showed that the medium with high water content will be able to attenuate the seismic waves strongly. The higher the water saturation, the lower the frequency seismic waves and the water saturation is more sensitive to changes in porosity, whereas the change in frequency and attenuation make almost no significant changes numerically, so that in practice oil exploration is very difficult to observe.
Keywords *: Water saturation, Wave frequency, Attenuation, Porosity.*

* Corresponding author.
E-mail address: sismanto@ugm.ac.id

I. Introduction

The application of seismic methods in the oil and gas industry today is not only limited to the determination of the geological structures in subsurface, but it has also been utilized for the development of the field, estimates of reserves (reservoir learning) and production, reservoir characterization and determination of volume, pressure, temperature, porosity, permeability, and fluid saturation [1]. Various studies have been conducted to determine the relationship between seismic waves with the reservoir parameters. Sismanto,[2] studied the relationship between the attenuation of seismic waves on the reservoir properties of sedimentary rock such as permeability and water saturation. Sismanto and Ertanti [3] have made a technique to estimates the water saturation based on the analysis of the attenuation of Biot-Turgut-Yamamoto equation. The theoretical results are calibrated against the log data to estimate the water saturation in the same layer in the same field based on porosity logs by cross plot method.

Several papers have discussed the mathematical modeling of elastic wave propagation such as Biot, [4] who started the study with a porous elastic material thoroughly compacted and then developed a theory of linear static and dynamic response to a fluid saturated porous material. Then examined based on the understanding of wave propagation equation in an elastic medium, the fluid saturated porous theoretically for low-frequency waves [4] and high-frequency waves ([5]. Some attenuation measurements under conditions of partial saturation have been done by Mavko and Nur [6]. Some of the curves of the results of these studies indicate that the attenuation increases with increasing saturation. Logarithmic decrement (δ) is used to express the energy dissipation factor, whose value is inversely proportional to the quality factor [1]. Velocity of seismic wave's propagation depends on the properties of the rocks and the density of the rock.

However, not all information of micro physical parameters can be measured directly, such as porosity, permeability, capillary pressure, and so on. The measurements can be done by measuring other physical quantities, and then calculated through the relations involving the micro parameters. Some of the dominant reservoir parameters affect the seismic wave's velocity such as density, permeability, and porosity.

In this study we derive a method of theoretical estimation of water saturation using the analysis of seismic wave attenuation, frequency and porosity of the Biot-Turgut and Yamamoto-Sismanto equation to see the character or the relationships between these parameters.

II. Method

The wave equation of fluid saturated porous medium in [4, 5] gave the concept of the mechanism of wave equations in elastic rocks, porous, and fluid saturation. These rocks are assumed to be homogeneous and isotropic. Turgut and Yamamoto [7] solve the equation with a limitation for the compressed rock

(unconsolidated) in marine sediments such as sandstone, limestone, and porous rock in general that have a high quality factor. The obtained equation is a frequency - wave attenuation relationships in quadratic form, i.e,

$$Q^{-1} \approx \frac{\frac{V_\infty^2}{V_0^2} - 1}{\frac{\tilde{q}_i}{A} + \frac{A}{\tilde{q}_i}.\frac{V_\infty^2}{V_0^2}} \quad (1)$$

where $\tilde{q}_i$ *(=η/k_pω)* or imaginer part of $\tilde{q}$, $A = (\rho m - \rho_f^2)/\rho$, ω is angular frequency *(2πf)*, and V_∞ and V_0 are the velocity of the P wave at high and low frequency and Q^{-1} is the attenuation. In the experiments, Turgut - Yamamoto used ultrasonic wave source, so it is difficult to apply in the seismic exploration that having low frequency less than 200 Hz [2]. For practical purposes, Sismanto [2] made a modification and a development of the equation into a linear form which is more operational as follows;

$$Q^{-1} \approx \frac{2\pi k_p}{\eta}\left(\frac{\rho m - \rho_f^2}{\rho}\right)\left(\frac{V_\infty^2}{V_0^2} - 1\right) f \quad (2)$$

where k_p is the permeability, ρ_f *is* the fluid density, ρ is the density, η is the viscosity, f is the frequency of the P wave, $m = \rho_f \alpha'/\Phi$, $\alpha' = 1.25$ [7, 8] Φ is the porosity. Thus, if the attenuation Q^{-1} is plotted against the frequency f, the density ρ can be obtained by the slope of the straight line in the curve (Q^{-1} - f) is equal to

$$slope \approx \frac{2\pi k_p}{\eta}\left(\frac{\rho m - \rho_f^2}{\rho}\right)\left(\frac{V_\infty^2}{V_0^2} - 1\right) \text{ or } \rho = 4\frac{\frac{2\pi k_p}{\eta}\left(\frac{V_\infty^2}{V_0^2} - 1\right).\rho_f^2}{-4.slope + 5.\frac{2\pi k_p}{\eta}\left(\frac{V_\infty^2}{V_0^2} - 1\right)} \quad (3)$$

We know that the density [9]

$$\rho = (1-\Phi).\rho_m + \Phi\left[S_w.\rho_w + (1-S_w).\rho_g\right] \quad (4)$$

we can calculate the value of water saturation S_w,

$$S_w = \frac{\rho - (1-\Phi).\rho_m - \Phi.\rho_g}{\Phi(\rho_f - \rho_g)}, \quad (5)$$

where ρ_m is the matrix density of the rock, ρ_g is the gas density. When there is no gas, it means that the gas density $\rho_g = 0$, then the saturation is,

$$S_w = \frac{\rho - (1-\Phi).\rho_m}{\Phi\rho_f} \quad (6)$$

by substituting the density equation in equation (3) into equation (6) it can be obtained,

$$S_w = \frac{4\frac{\frac{2\pi k_p}{\eta}\left(\frac{V_\infty^2}{V_0^2} - 1\right).\rho_f^2}{-4.slope + 5.\frac{2\pi k_p}{\eta}\left(\frac{V_\infty^2}{V_0^2} - 1\right)} - (1-\Phi).\rho_m}{\Phi\rho_f} \quad (7)$$

thus if the permeability value of k_p is known, the viscosity η, porosity Φ, V_∞ and V_0 are the velocity of the P wave at high and low frequency and the slope of the attenuation curve of the frequency, the water saturation values can be determined by the equation (7).

At the same time as if, we make a direct substitution without plotting the curve (Q^{-1} - f) or without finding the slope for the gas density is zero by substitution equation (4) into equation (2) it will be obtained the water saturation S_w as,

$$Sw = \frac{1}{2}\left(\frac{-\Phi + \frac{2\pi k_p}{\eta}\left(\frac{V_\infty^2}{V_0^2} - 1\right).f.Q.m.\Phi \pm \sqrt{\begin{array}{l}\Phi^2 - 2\frac{2\pi k_p}{\eta}\left(\frac{V_\infty^2}{V_0^2} - 1\right)f.Q.m.\Phi^2 + \left(\frac{2\pi k_p}{\eta}\right)^2\left(\frac{V_\infty^2}{V_0^2} - 1\right)^2.f^2Q^2m^2\Phi^2 \\ -4\frac{2\pi k_p}{\eta}\left(\frac{V_\infty^2}{V_0^2} - 1\right)f.Q.\rho_m + 4\frac{2\pi k_p}{\eta}\left(\frac{V_\infty^2}{V_0^2} - 1\right)f.Q.\rho_m.\Phi \\ +4\left(\frac{2\pi k_p}{\eta}\right)^2\left(\frac{V_\infty^2}{V_0^2} - 1\right)^2 f^2.Q^2.m.\rho_m - 4\left(\frac{2\pi k_p}{\eta}\right)^2\left(\frac{V_\infty^2}{V_0^2} - 1\right)^2 f^2.Q^2.m.\rho_m.\Phi\end{array}}}{\frac{2\pi k_p}{\eta}\left(\frac{V_\infty^2}{V_0^2} - 1\right)f.Q.\rho_f}\right) \quad (8)$$

where Q is the quality factor (= $1/Q^{-1}$). At this equation (8), there are two water saturations, i.e., water saturation with positive or plus sign (sw1) and negative or minus sign sw2, we will see on the numerical simulation. However, if the equation is derived directly from quadratic equation (1), the theoretical value of water saturation can also be obtained by combining equations (4) with the gas content is not zero and quadratic equation (1), so that the water saturation can be formulated as,

$$Sw = \frac{2\pi k_p mf\rho_m\left(V_\infty^2 - V_0^2 - \phi V_\infty^2 + \phi V_0^2 + \frac{\phi\rho_g V_\infty^2 - \phi\rho_g V_0^2}{\rho_m}\right) + 2\pi k_p \rho_f^2 f\left(V_0^2 - V_\infty^2\right) - Q^{-1}\eta V_0^2 \rho_m\left(1 - \phi + \frac{\phi\rho_g}{\rho_m}\right)}{\left\{Q^{-1}\eta V_0^2 \phi\left(\rho_w - \rho_g\right) - \phi 2\pi k_p mf\left(\rho_w - \rho_g\right)\left(V_\infty^2 - V_0^2\right)\right\}} \quad (9)$$

III. Results and Discussion

In this study the relationship curve of water saturation S_w with porosity reservoir parameters, frequency and wave attenuation based on equation (8) can be constructed, and if the other parameters have been calculated. Then, the graphs are obtained by using the velocity V_p of 5000 m/s are presented as the following equation for sw1 (plus sign) figure 3.1, figure 3.3 and figure 3.5 as well as for sw2 (minus sign) in the figure 3.2, figure 3.4, and figure 3.6.

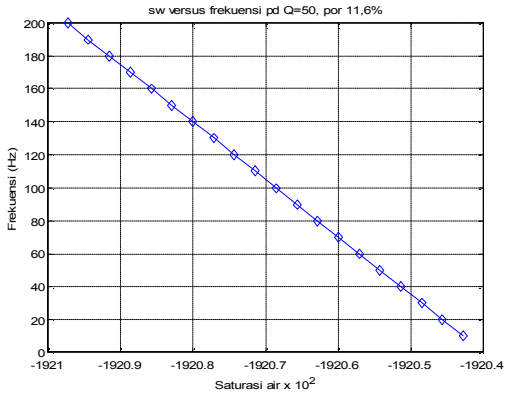

Figure 3.1. The relationship between frequency to water saturation sw1 (plus sign).

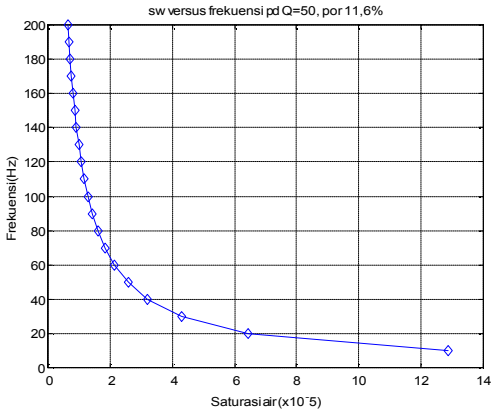

Figure 3.2. The relationship between frequency to water saturation for sw2 (minus sign).

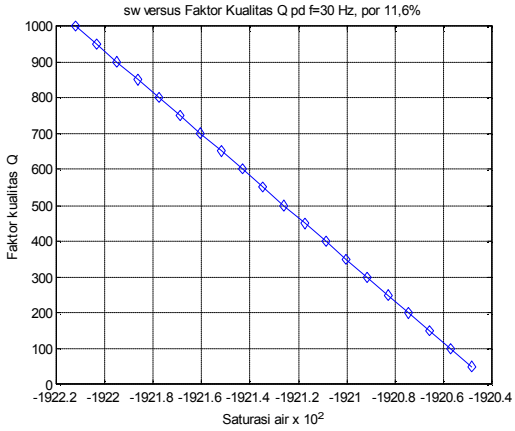

Figure 3.3. The relationship between quality factor Q to water saturation for sw1 (plus sign).

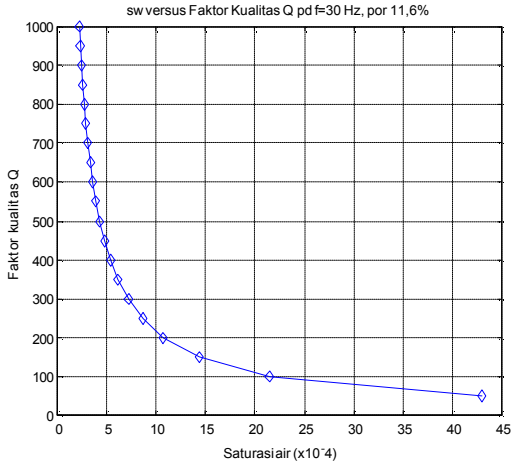

Figure 3.4. The relationship between quality factor Q to water saturation for sw2 (minus sign).

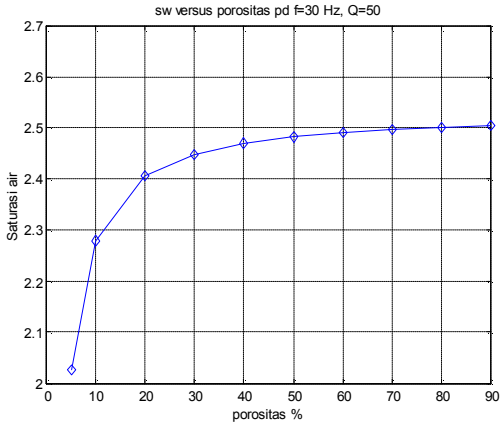

Figure 3.5. The relationship between water saturation to porosity for sw1 (plus sign).

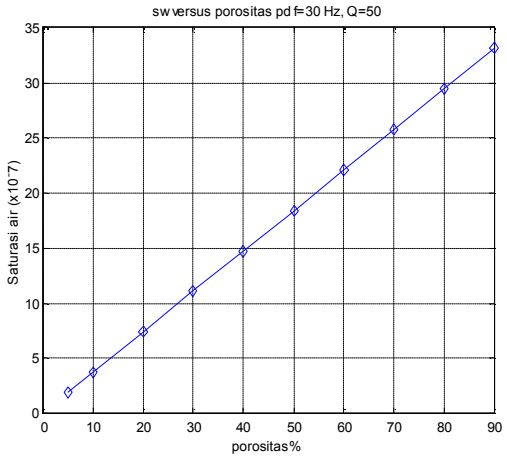

Figure 3.6. The relationship between water saturation to porosity for sw2 (minus sign).

From the curves of each trend parameter relationship is clear. In the curves obtained from the equation with the plus sign and minus sign characters. It appears differently in contrast to when a plus sign have a linear in shape, while those with a minus sign have a curve in shape and vice versa. But the trend curves of the two sign are same, that is declining or ascending, although the numerical values of these parameters did not decrease significantly.

So in general conclusion regardless to the numerical values, that are, when the porosity increases, the water saturation also increases. It is easy to understand, because when the porosity of the medium in higher, the probability of a fluid filled pore space will also be high. After that, if the medium with higher water content will be able to reduce the seismic wave's energy strongly, or by increasing the water saturation, the value of attenuation increases as well (low-quality factor Q). Furthermore, it appears that for the medium with higher water content, the frequency of seismic waves will be smaller or increasing water saturation decreasing the frequency of seismic waves.

Finally, the trends of the relationship between water saturation, porosity, frequency, quality factor or attenuation have been described, but it is numerically obvious that the sensitivity of each is different. Water saturation is more sensitive to changes in porosity, than to the attenuation and frequency changes numerically, so that it is very difficult to observe in the practice of oil exploration.

IV. Conclusion

a. Medium with high water content will be able to attenuate the seismic waves strongly.
b. The higher the water saturation, the lower the frequency seismic waves.
c. The water saturation is more sensitive to changes in porosity, whereas the change in frequency and attenuation is almost no significant changes numerically.

V. References

1. S. Munadi, *Aspek Fisis Seismologi Eksplorasi*, Program Studi Geofisika, Jurusan Fisika-FMIPA UI, Depok. 2000.
2. Sismanto, *Estimasi Permeabilitas Reser-voar Batupasir Tebal dan Homogen Dengan Menggunakan Analisis Atenuasi Inelastik Data Seismik*, Disertasi, Institut Teknologi Bandung. (2003).
3. Sismanto and S. R. Ertanti, *Estimation of Water Saturation Using Crossplot Method Based on Attenuation Analysis of Biot-Turgut-Yamamoto*. International Conferen-ce of Mathematical and Natural Science II, ITB, Bandung 28-30, October (2008).
4. M. A Biot, Theory of Propagation of Elastic Waves in A Fluid Saturated Porous Solid I. Low-Frequency Range, *J. Acoust. Soc. Am.*, 28. (1956).
5. M. A Biot, Theory of Propagation of Elastic Waves in A Fluid Saturated Porous Solid II. Higher Frequency Range, *J. Acoust. Soc. Am.*, 28.(1956).
6. G. M. Mavko, and A. Nur., , Wave Attenuation in Partially Saturated Rocks, *Geophysics,* 44, 161-178. 1979.
7. A. Turgut and Yamamoto, Measurement of acoustic wave velocities and attenuation in marine sediments, *J. Acoust. Soc. Am.,* 87, 2376-2383. (1990).
8. A. Turgut, Approximate expressions for viscous attenuation in marine sediments: Relating Biot's "critical' and "peak" frequencies, *J. Acoust. Soc. Am*., 108, 513 – 518. (2000).
9. G. Asquith and D. Krygowski, *Basic Well Log Analysis*, 2nd Edition, The American Association of Petroleum Geologist, Tulsa, Oklahoma. (2004).

MAGNETC, GRADIENT TEMPERATURE AND GEOCHEMISTRY SURVIE S WITHIN PASEMA AIR KERUH GEOTHERMAL AREA EMPAT LAWANG DISTRICT, SOUTH SUMATERA PROVINCE iNDONESIA

F. Virgo[1, 2], Wahyudi[2], Suharno[3], A. Zaenudin[1] and W. Suryanto[2]

1. Universitas Sriwijaya

2. Universitas Gadjah Mada,

3. Universitas Lampung

ABSTRACT

The Pasema Air Keruh geothermal area situated within the Empat Lawang District, Sumatera Selatan Province. Magnetic, gradient temperature and geochemistry survies conducted within that area, in 9 June 2012. The magnetic and the gradient temperature were not analysed zet. The geochemical analysis using the geothermometer and geoindikator, doe to determine the reservoir characteristic and temperature. The first geothermal exploration activities in Empat Lawang District Sumatera Selatan Province were carried out in the Penantian hot spring field Air Keruh Sub District and Airklinsar hot spring field Ulu Musi Sub District. The discharge test measurements show that chemical composition of the reservoir water was analyzed by standard methods and subsequently classified using Cl-SO4, HCO3 triangular diagram. A Na-K-Mg triangular diagram was used to classify waters according to the state of equilibrium at given temperatures. The geothermal waters are of chloride water type and from a relatively old hydrothermal system. Thermal fluid is in equilibrium with reservoir rocks. The chemical geothermometers were used to predict subsurface temperature. The calculated temperatures using Na-K geothermometers and Na-K-Mg geoindikcator is more than 300^{o}C. However, compare with measured temperature furthere.

Key word: geochemical, geothermometer, geoindicator, geothermal Empat Lawang

1. INTRODUCTION

The Empat Lawang geothermal field is located on one of the major tectonic belts of the Fault Sumatera System. In addition to this, there are volcanic areas spread throughout the country. Therefore, the country has many hot springs with a variety of temperatures ranging up to 98^{o}C. The hot springs are located mainly on major active fractures and volcanic areas one of which is Penantian and Airklinsar.

The Penantian and Airklinsar is one of the prospective areas in Empat Lawang District Sumatera Selatan Province for geothermal exploration which was initiated by Virgo Team are the first in June 2012. The map location is shown in Figure 1.

The Empat Lawang geological extends elongated the Fault Sumatera System between the Bengkulu and Sumatera Selatan.

The Penantian and Airklinsar geothermal field is located near the Gunung Kasih Massif, which is Paleozoic in age. This Massif is mainly composed of metamorphic schists, marble and granite, and forms the basement of the geothermal area covered by Tertiary

volcanic-sedimentary units assumed to be cap rock. The rocks of the Empat Lawang are divided into ten zones that are characterized in Figure 2.

The geothermal manifestation spreads throughout an area including boiling hot springs, travertine and swampy areas formed by hot water emergence and leakage. The results of chemical analysis of hot and cold water samples have been evaluated for fluid using Giggenbach diagrams.

2. CHEMICAL COMPOSITIONS OF THE WATERS

The geochemical study is based on discharge water samples collected from the discharge of two hot water springs. These samples were collected in M June 2012. Samples were untreated and included acidified water. Chemical analyses of Na, K, Ca, Mg, B, Li, and SO4 were carried out in the site laboratory of Lampung University (Bandar Lampung), and the SiO2 pH, Cl, HCO3, in laboratory of Sriwijaya University (Palembang).

Li, Cl and B are conservative elements in the geothermal system. They are fixed in fluid phase and have not equilibrated. The conservative elements are the best geoindicators of the origin of the geothermal system. B/Cl ratio and Cl-Li-B ternary diagram were used to indicate the source of the fluid. A plot of the relative concentrations of Cl, Li and B is shown in Figure 3. All geothermal waters have high Cl content relative to Li and B, indicating that they are from an old hydrothermal system and that fluid migrated from the old basement rock.

3. CLASIFICATION OF THE THERMAL FLUIDS

The average chemical compositions of the geothermal water from the Penantian and Airklinsar are presented in Table 1. The discharge water from Airklinsar hot water are of the chlorate type with alkaline pH (6-7) and with total dissolved solids in range the of 400-700 mg/kg. A Cl are predominate cations with concentration more than 600 mg/l respectively, whereas Mg is present only in trace (0.4-2 mg/l). In contrast, hot waters discharged from Penantian hot spring are neutral (pH-6-7) and concentration of sulfate and carbonate ions are lower. The chemical compositions of the waters were classified on the basis of major ions using the Cl-SO4-HCO3 triangular diagram of Giggenbach (Figure 3). All samples plot to area of mature waters and can be classified as Cl-rich geothermal water which formed by the interaction of geothermal fluids with the host rock and dilution with low salinity water at depth (White and Muffler, 1971).

The Empat Lawang possesses great potentiality for the utilization of geothermal energy. The region has been centre of attraction to a number of visiting national scientists, encouraging them to collect and analyze geothermal water samples at different localities on a sporadic basis. One of such studies has determined the temperature and reservoir characteristic.

4. ESTIMATION OF THE RESERVOIR

Even though the above table suggests that none of the springs have a huge mass flow rate, a number of springs emerging in the vicinity could have lowered the flow rate. Water containing chloride concentration more than 100 ppm. No high concentration of silica is observed relative to discharge temperature in all spring waters. The waters at Airklingsar lying in this region have relatively high chloride, suggesting that the waters are fairly mature as indicated by the Giggenbach's diagram of concentrations of the major anions, Cl, SO4 and HCO3. This is illustrated in Figure 3.

Table 1. Geochemical data from Penantian and Airklingsar hot spring

Sampel	Na	K	Ca	Mg	B	Li	SO4	HCO3	SiO2	Cl
Penantian	15	9	31	0,4	6	0,3	228	190	64	119
Airklingsar	32	9	133	2	17	0,2	340	61	50	664

5. SUBSURFACE TEMPERATURE ESTIMATION

Chemical geothermometers are used in order to estimate the reservoir temperature. The important criteria for chemical geothermometer application to thermal spring are the pH, temperature and discharge rate of the spring. Some of them give unreliable results such as either lower than spring temperature or extremely high temperature. These equations are based on geothermometers for chalcedony and quartz, which assume hat these minerals used in geothermometers, are not in equilibrium with rock – water interaction in reservoir.

The silica and cation geothermometers were used for the evaluation of subsurface temperature for discharges (Table 1). The Source of temperature equations: T–measured temperature, T: Na-K– Fournier and Truesdell (1973), T: Na-K – Giggenbach (1988), T-Fournier (1977) were used. These give reservoir temperatures ranging from 211^{o} to 251C. The Na-K geothermometer of Giggenbach (1988) suggested reservoir temperature in the range of 331^{o}C – 429 ^{o}C and Fournier (1977) suggested reservoir temperature in the range of 271-289oC which is higher than measured temperature. The Na-K-Ca geothermometers (Fournier and Truesdell (1973)) predict anomalously high reservoir temperature (326^{o}C – 438 ^{o}C).

The Na-K-Mg triangular diagram shows the equilibrium between the geothermal fluids and rock and reservoir temperature (Figure 4).

By considering the diagram presented in Figure 5, the Kozakli hot springs plot in the immature water part, so using the chemical geothermometers is not reliable according to the theory used to establish the diagram. In this Na-K-Mg diagram all the samples have not gained equilibrium with rock, presumably due to fast circulation of luid through the rock fractures. This causes the water to be mmature, considering the ion exchange processes that, equilibrium has not been reached yet with rock minerals because of circulation flow. Figure 4 shows that samples from studied geothermal wells fall on the full equilibrium line, suggested attainment of the (Airklinsar) and 350^{o}C (Penantian)

3. CONCLUSION

The geothermal waters discharged from Airklinsar of the Empat Lawang geothermal field are of chlorate type with a high concentration of Cl. Chemical compositions of reservoir waters indicate that the reservoir is located in the liquid dominant zone and geothermal waters come from an old geothermal system. The water composition from Penatian Empat Lawang is carbonate and sulphate. Thermal fluid is in equilibrium with reservoir rocks, which can be the product of water-rock interaction at high temperature. Common geothermometers have been used for estimating the subsurface temperature. The results from Na-K geothermometers and Na-K-Mg geoindikcator, indicate that the reservoir

temperature. The calculated temperatures using Na-K geothermometers and Na-K-Mg geoindikcator is more than 300^{o}C. However, compare with measured temperature furthere.

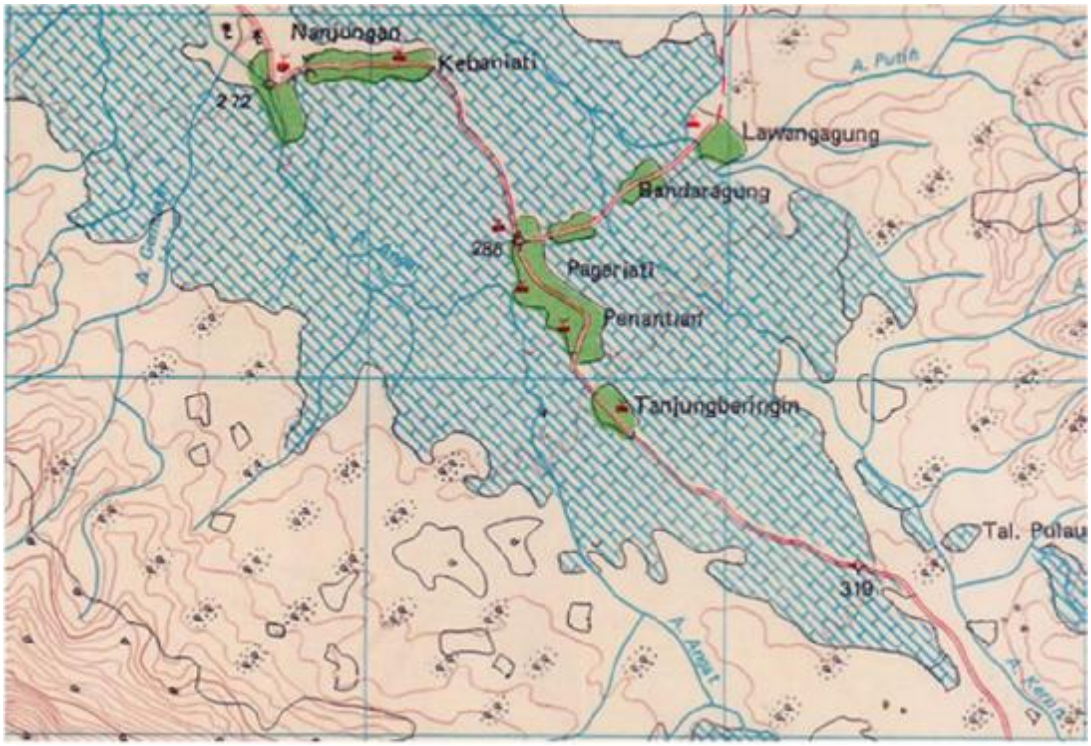

Figure 1. The map location of the Penantian and Airklinsar geothermal field.

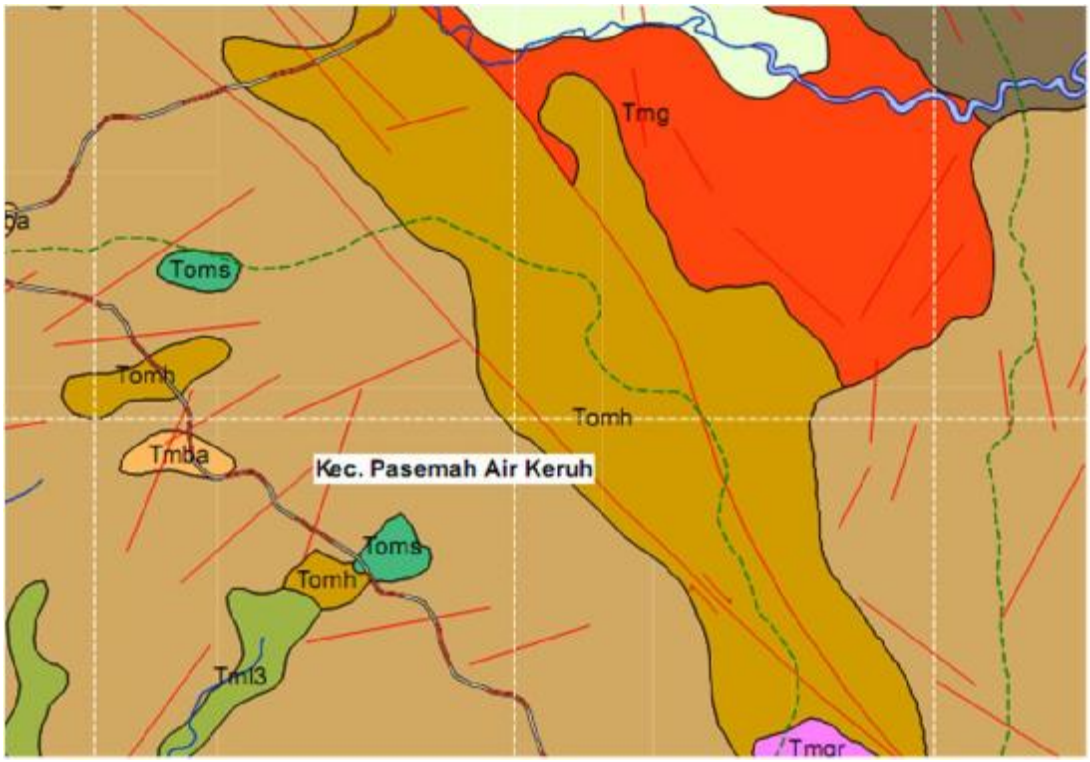

Figure 2. The geological map of the Penantian and Airklinsar geothermal field.

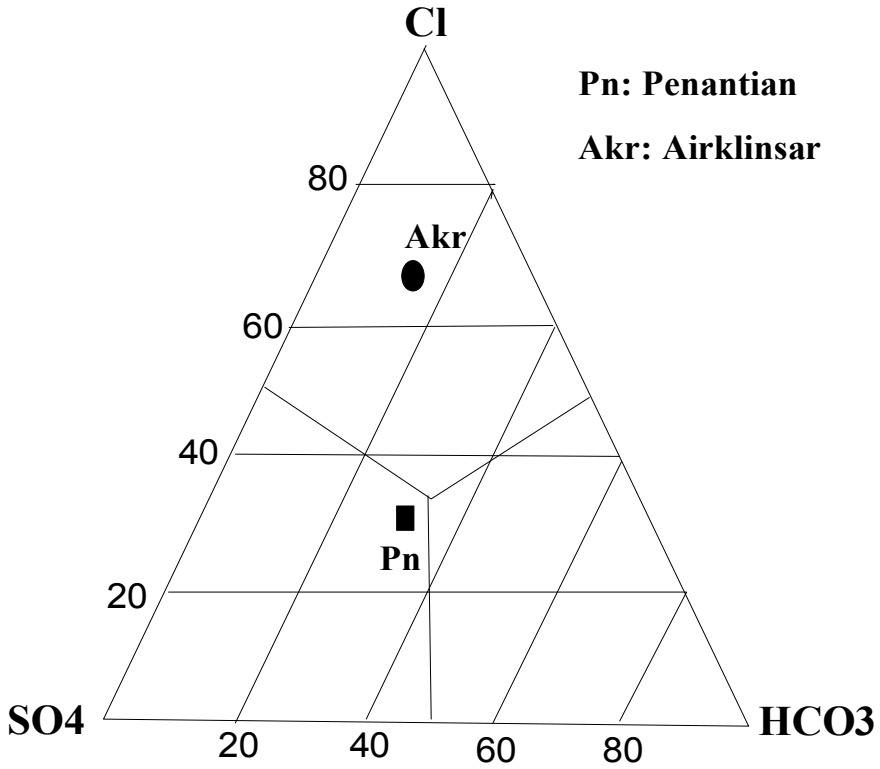

Figur 3. The diagram of the Penantian and Aklinsar reservoir characteristic.

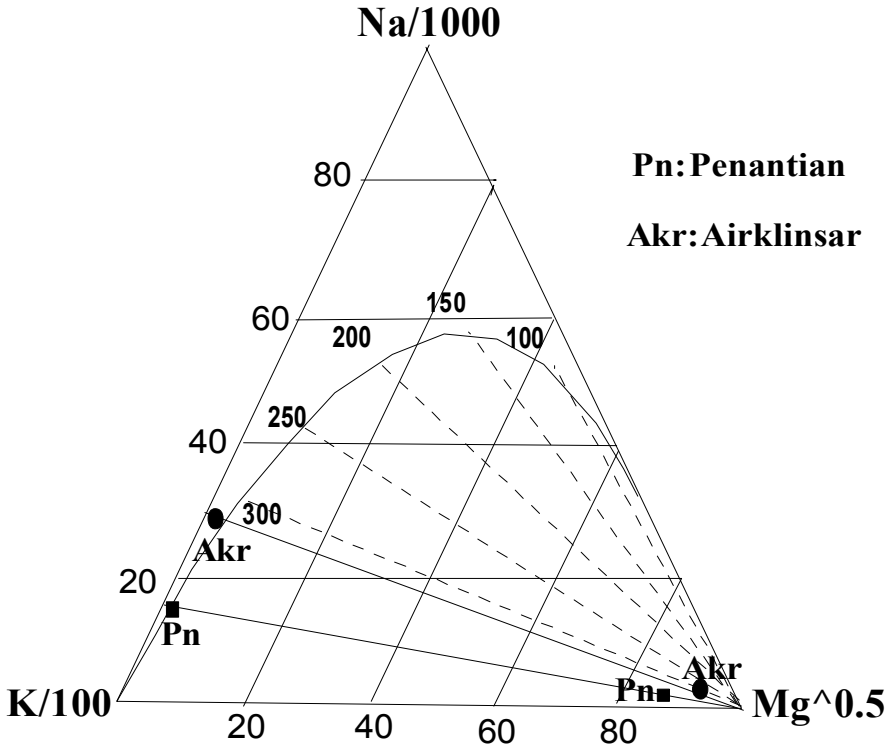

Figur 4. The diagram of the temperatures of the Penantian and Aklinsar geothermal reservoir.

4. REFERENCES

Fournier, R. O.: Chemical Geothermometers and Mixing Models for Geothermal System, *Geothermics*, **5**, (1977), 41-50.

Fournier, R., and Truesdell A.: An Empirical Na-K-Ca Geoindicators, *Geochim. Cosmochim. Acta*, **37**, (1973), 1255-1275. Giggenbach, W.: Geothermal Solute Equilibria. Derivation of Na-K-Mg-Ca Geoindicators, *Geochim. Cosmochim. Acta,* **52**, (1988), 2749-2765.

Geocemical indicators of subsurface temperature. U.S. Geol. Survey J. R. 2, (1974), 259-262.

Giggenbach, W. F. Geothermal Gas Equilibria. Geochemica Cosmochemica Acta 31, (1988).

Giggenbach, W.F.: Chemical Techniques in Geothermal Exploration. In: D'Amore, F(coordinator), *Application of geochemistry in geothermal reservoir development.* UNITAR/UNDP publication, Rome, (1991), 119-142.

White, D.E., and Muffler, L.G: Vapour-dominated Hydrothermal System Compared with Hot Water System. *Economic Geology*, **66**, (1971), 75-97.

High Accuracy Automatic Phase Picking Method in Earthquake and Microearthquake for Earthquake Early Warning System (EEWS) and Geothermal Field in Indonesia

WiwitSuryanto*, Prima Wira Kusuma Wardhani, TheodosiusMarwanIrnaka
Geophysics Sub-Department, Department of Physics, Faculty of Mathematics and Natural Sciences, Gadjah Mada University,Sekip Utara PO BOX BLS.21 Yogyakarta 55281

Abstract

Automatic phase picking in earthquake and microearthquake has become one challenge for every seismologist in Indonesia. Not to mention, rapid growth of seismic network and government awareness of earthquake hazards has become two big issues. Several methods have also been developed by seismologist all around the globe. Two methods that popular are STA/LTA and AR-AIC. STA/LTA is a method based on average value in certain window time; otherwise, AR-AIC is based on auto regressive and akaike information criterion that separate event into two intervals (noise and signal interval). In this paper, those two methods are compared and assess. Three sample of earthquake event acquired at geothermal area is used. Earthquake data with relatively low, medium and high S/N value was selected. The results, AR-AIC have better accuracy than STA/LTA for either low to high S/N ratio and combination of those two method (STA/LTA and AR-AIC) which previously proposed by Akazawa (2004) will give us high accuracy onset time estimation.

Keywords : *automatic, picking, STA/LTA, AR-AIC, earthquake*

* Corresponding author.
E-mail address: wiwit@gadjahmada.edu

I. Introduction

Modern seismic network, either permanent or temporary produce very high amount of data where manual analysis is nearly impossible. One of general process is identifying onset of seismic phase on the data. Traditionally, this work is done by an analyst who checks seismogram; later, P and S-phase onset time estimation is based on their own experience. This process takes a lot of time and very subjective.

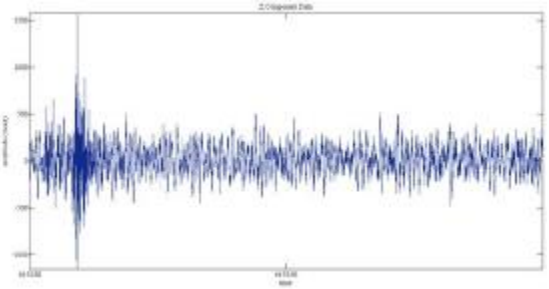

Figure 1. Example of noisy micro-earthquake record at geothermal area

In previous geothermal exploration, during passive seismic investigation, either at high resolution tomography survey or hydrofracturing, small earthquake magnitude is used. Almost of these earthquakes is hard to detect because of low S/N value. In case of microfracture monitoring, aside from noise from borehole environment, hydrofracturing event typically emerge smaller P-wave compared with S-wave. For that reason, P-phase onset time estimation is very important to determine micro-earthquakes location and event azimuth accuracy which mostly depends on the P-wave vector. In other case, high resolution earthquake tomography, large number of small magnitude earthquake event is needed, which are commonly noisy if acquired at urban area. That's why an advanced procedure to estimate P-phase onset accurately is being developed in this research.

Seismic warning system depends on system automation: real-time quasi, detecting procedure, onset picking estimation and signal phase identification in seismogram records. Especially for system that broadcast warning message after the earthquake occurs, accuracy in phase estimation is very important in order to get high accuracy hypocenter.

II. Phase Onset Estimation Method

Many methods to detect and estimate seismic phase and onset time has been developed. Detector has an aim to detect the presence of seismic phase, whereas picker will estimate phase onset time accurately. Traditional approach to

detect seismic phase is applying bandpass filter and then using its absolute value as characteristic function (CF). When Short Term Average (STA) and Long Term Average (LTA) ratio of CF exceed predefined limit, seismic event is found.

Another approach to estimate phase onset time is AR-AIC method. This method is containing two main calculations which are Auto Regressive (AR) and Akaike Information Criterion (AIC). AR is based on assumption that seismogram can be differentiate into locally stationery segments (Sleeman and Eck, 1999). There will be two segments; noise segment, which is located before onset time and signal segment which is located after onset time. Based on this assumption, AIC method is used to estimate P and/or S-phase (Sleeman and Eck, 1999). For AR-AIC picker, AR process sequence must be specific based on trial and error and AR coefficient must be calculated in the both interval. This AR-AIC approach is different compared with AIC method by Maeda (1985). Maeda's AIC method can be calculated directly from the seismogram without any AR coefficient calculation. Unluckily, AIC Maeda's AIC picker will result wrong phase onset time using data with low signal to ratio (S/N) and unclear phase onset time. Later on, AIC picker can identify estimated onset time using pre-determined time window. Akazawa (2004) proposed a method which combines several techniques: STA/LTA ratio, STA/LTA difference and AR-AIC method using strong motion data in Japan. Estimated time accuracy will depends on validity of interval detection and AIC's detection accuracy itself.

III. Phase Onset Estimation Theory

In this paper, only STA/LTA ratio using cumulative envelope, STA/LTA difference, and AR-AIC proposed by Akazawa (2004) that will be compared.

In order to calculate cumulative envelope value, several calculations below need to be done to the data record ($a_{v1}(t)$) (Akazawa, 2004):

$$a_{v2}(t) = \frac{|a_{v1}(t)|}{|a_{v1}|_{max}} - \frac{a_{v1}(t)^2}{{a_{v1}}^2{}_{max}} \quad (1)$$

Then the envelope function $a_{v3}(t)$ is generated from $a_{v2}(t)$ using the following formula:

$$\begin{aligned} a_{v3}(t) &= a_{v2}(t-1) && (if\ a_{v2}(t) \le a_{v2}(t-1)) \\ a_{v3}(t) &= a_{v2}(t) && (if\ a_{v2}(t) > a_{v2}(t-1)) \end{aligned} \quad (2)$$

$a_{v3}(t)$ is the result of cumulative envelope calculation.

STA and LTA value is calculated towards data $b_{v1}(t)$ using the equation below:

$$STA = \frac{\sum_{j=i}^{i+l_1} D_i^2}{l_1}$$
$$LTA = \frac{\sum_{j=i}^{i+l_2} D_i^2}{l_2} \quad (3)$$

STA/LTA ratio (r_i) and STA/LTA difference (d_i) is then calculated using equation 3 as shown:

$$r_i = \frac{STA_i}{LTA_i} \quad (4)$$
$$d_i = STA_i - LTA_i \quad (5)$$

Other approach, which is AR-AIC method, is little more complicated. More parameter is needed to take into. There are two main step two calculate AR-AIC, which are AR and AIC calculation.

In AR calculation, assumes that we have (i) a time series $x_n = \{x_1, \dots, x_n\}$ which includes the onset of seismic signal, and (ii) a first estimate of the onset time. The interval before and after the onset time are assumed to be two different stationery time series (Sleeman, 1999).

At each interval $i = 1,2$, the one preceding and the one including the phase onset, model window is defined in which fit the data to an AR model of order O with coefficient $a_m^i (m = 1, \dots, O)$

$$x_t = \sum_{m=1}^{O} a_m^i x_{t-m} + e_t^i \quad (6)$$

With $t = 1, \dots, M$ for interval 1 (noise interval) and $t = N - M + 1, \dots, N$ for interval 2 (signal interval). The model divides the time series within a model window into a deterministic and a non-deterministic part. The non-deterministic time series e_n^i, or noise, is supposed to be Gaussian, with mean $E\{e_n^i\} = 0$, variance $E\{(e_n^i)^2\} = \sigma_i^2$ and uncorrelated with the deterministic part of the time series: $E\{e_n^i x_{t-m}^i\} = 0$ (Sleeman, 1999).

AIC value is then obtained using the following formula:

$$AIC(k) = (K - M)\log(\sigma_{1,max}^2) + (N - M - K)\ log(\sigma\_(2,max)\text{^}2\ ) + C_2 \quad (7)$$

where K is the division point.

II. Picking Result

Several micro-earthquakes sample data has been processed using both STA/LTA ratio and AR-AIC picker. Figure 2 below is an example of the result from STA/LTA ratio using cumulative envelope as its CF (Figure 2.a.2 and 2.b.2) and AR-AIC calculation (Figure 3.a.3 and 2.b.3). Figure 2.a is attempt to estimate P-phase onset time, the green line (Figure 2.a.1) is P-wave estimation based on AR-AIC method, the black line is P-phase onset time estimation using STA/LTA ratio, the other red line in the back is end event estimation time using S/N mean cumulative ratio.

It is shown that P-phase and S-phase can be estimated using AR-AIC picker, otherwise STA/LTA picker is not very sensitive to data with low-moderate S/N value. However, AR-AIC calculation takes long time to do compare with STA/LTA ratio calculation. It must be noted that AR-AIC calculation will get its best result when the time window is correctly selected and in the time window must contain noise interval and signal interval.

Another attempt to confirm picking

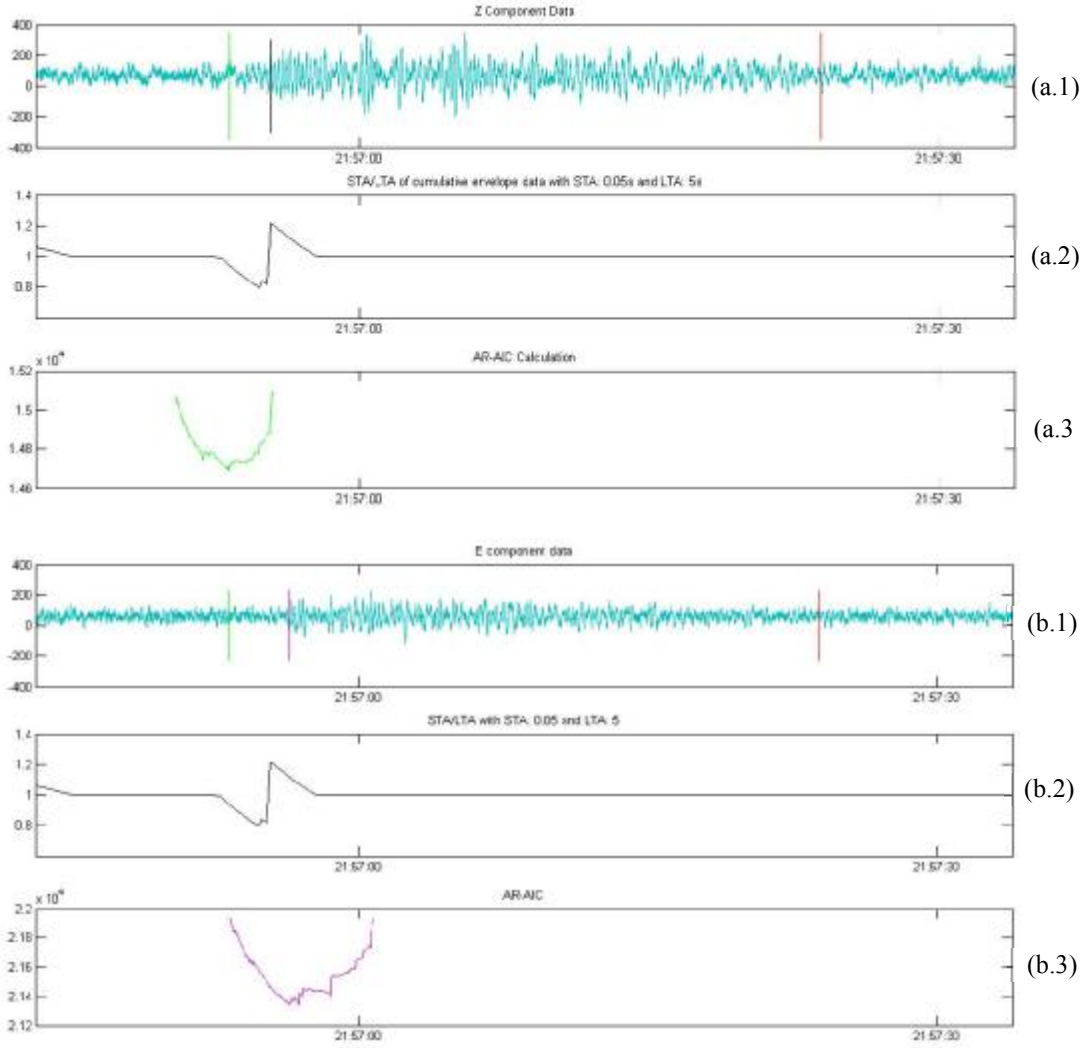

Figure 2. Vertical component data (light blue), P-phase onset estimation using AR-AIC picker (green), P-phase onset estimation using STA/LTA ratio (black), end event time estimation using S/N mean cumulative ratio (red) [2.a.1]. STA/LTA ratio of cumulative envelope on vertical data record [2.a.2].AR-AIC calculation using pre-defined time window (based on figure 2.a.2) [2.a.1]. Horizontal component data (light blue), P-phase onset time estimation using AR-AIC picker (green), S-phase onset time estimation using AR-AIC picker (purple), end event time estimation using S/N mean cumulative ratio (red) [2.b.1]. STA/LTA ratio of cumulative envelope on vertical data record [2.b.2]. AR-AIC calculation using pre-defined time window (based on previous estimated P-phase onset time and STA/LTA information) [2.b.3].

validity of these methods has been done. Figure 3 and Figure 4 are another examples using AR-AIC and STA/LTA picker. AR-AIC picker still resulting better onset time estimation than STA/LTA picker. It is consistent for data with low S/N ratio (Figure 2), medium S/N ratio (Figure 3) to high S/N ratio (Figure 4).

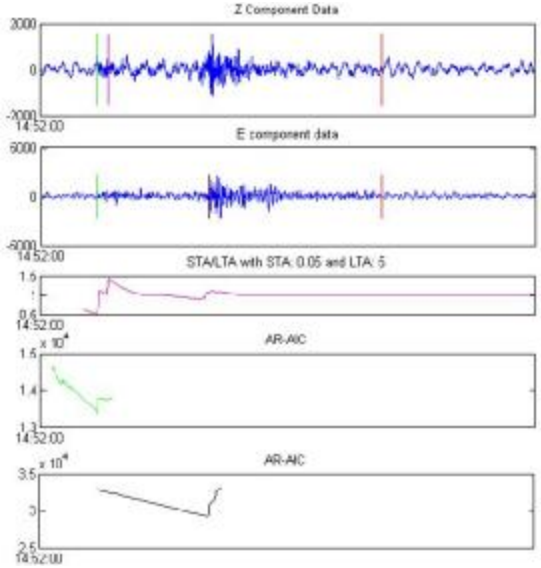

Figure 3. Automatic picking sample using AR-AIC and STA-LTA ratio method. P-phase onset time estimation using AR-AIC is indicated by green line. P-phase onset time estimation using STA/LTA ratio is indicated by purple line in the vertical component. S-phase onset time estimation using AR-AIC is indicated by black line. S-phase onset time estimation using STA/LTA ratio is indicated by purple line in the second top figure. Whereas, red line indicate end event estimation.

III. Conclusion

Both STA/LTA ratio and AR-AIC picker have its own advantages and disadvantages. STA/LTA ratio picker have quicker computation time, but very sensitive to noise. Signal with low S/N ratio will produce bad onset estimation.

On the other side, AR-AIC picker show high accuracy even in low S/N ratio event. But, time window must be pre-defined correctly and as efficient as possible. That's why; AR-AIC picker can't stand on its own. It needs another picker to, at least, estimate pre-estimated onset time. Computation time is also become another challenge using AR-AIC picker. Defining time window which is efficient in computation aspect is a must.

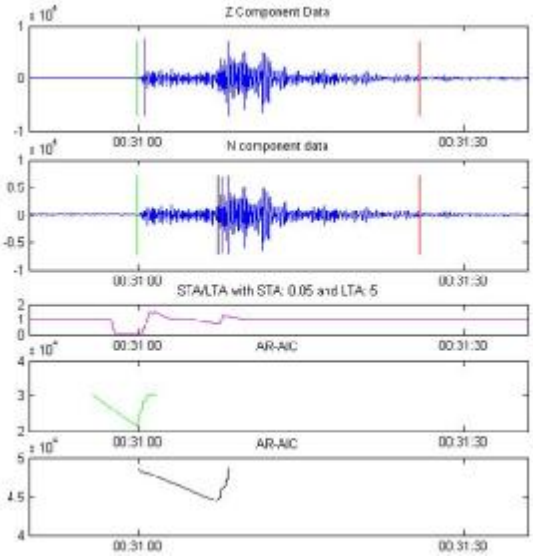

Figure 4. Automatic picking sample using AR-AIC and STA-LTA ratio method. P-phase onset time estimation using AR-AIC is indicated by green line. P-phase onset time estimation using STA/LTA ratio is indicated by purple line in the vertical component. S-phase onset time estimation using AR-AIC is indicated by black line. S-phase onset time estimation using STA/LTA ratio is indicated by purple line in the second top figure. Whereas, red line indicate end event estimation.

Considering seismic event in geothermal area mostly will have low S/N ratio, combination between STA-LTA and AR-AIC that proposed by Akazawa (2004) might be the best choice. For EEWS purpose, this method might become one recommendation. But, since AR-AIC process need high resource computer, the system must be ready and fast enough to do AR-AIC computation in real-time.

V. References

1. Akazawa Takeshi, *A Technique For Automatic Detection of Onset Time of P and S-Phases in Strong Motion Records*, 13th World Conference on Earthquake Engineering (2004)
2. Maeda N., *A method for reading and checking phase times in auto-processing system of seismic wave data*, Zisin = Jishin. 38, 365 (1985)
3. Sleeman R., *Robust Automatic P-Phase Picking: An On-line Implementation in the Analysis of Broad-band Seismogram*, Physics of the Earth and Planetary Interiors. 113, 265 (1999)

Detection of Dissociation and Association Effects of NO_2 – NO Gases by Laser-based Photoacoustic and Wavelength Modulation Spectroscopy Methods

Mitrayana[1*], T. Pierera[2], S. Persijn[2], S.M. Cristescu [2], F.J.M. Harren[2], M.A.J. Wasono[1], and W. Rochmah[3]

1 Atomic and Nuclear Physics Lab. Physics Dept. Gadjah Mada University Indonesia
2 Molecular and Laser Physics Dept. Radboud University of Nijmegen, the Netherlands
3 Medical Faculty of Gadjah Mada University Indonesia

Abstract

Nitrogen dioxide (NO_2) belongs to the family of nitrogen oxides (NO_x). It occurs naturally in the atmosphere, but it is also produced anthropogenically by e.g. burning of gasoline, coal, oil and other fuels as well as in power plants and burning of natural material. Recently, efforts toward the development of simple and reliable devices have been increased with the aim to control air pollution and to detect toxic gases at low levels in the air, in the field of domestic and industrial applications. Laser based trace gas sensors have been used to monitor NO_x emissions from individual vehicles, as well as variations in air pollution over cities, thereby demonstrating that they can make contributions to manage air quality. In this paper, we present a simple, low cost, compact, and standalone NO_2 - NO detection system based on laser photoacoustic and wavelength modulation spectroscopy. The performance of the violet diode and Quantum Cascade laser-driven for photoacoustic and wavelength modulation system, respectively, was explored and the sensors were applied to monitor of the dissociation and association effects of the NO_2 and NO. That's set-up have a detection limit 20 ppbv at STP for NO_2 and 0.8 ppbv for NO.

Keywords: *Photoacoustic spectroscopy, wavelength modulation spectroscopy*

* Corresponding author.
E-mail address: mitrayana@ugm.ac.id

I. Introduction

Nitrogen dioxide (NO_2) belongs to the family of nitrogen oxides (NOx). It occurs naturally in the atmosphere, but it is also produced anthropogenically by e.g. burning of gasoline, coal, oil and other fuels as well as in power plants and burning of natural material [1]. The ambient concentrations of nitrogen dioxide are influenced by meteorological conditions like wind speed, temperature and precipitation, and result in both environmental and health effects [2]. The gas plays an important role in the atmospheric reactions that generate ozone which is an important contributor to air pollution and smog formation. NO_2 promotes the formation of acid aerosols, which pollute water and harm vegetation, as well as buildings. It is also associated with visibility degradation [3]. In The Netherlands, the largest contribution to the emission of NOx is made by traffic (65%).

Nitrogen dioxide is toxic by inhalation. Long-term exposure to NO_2 at concentrations above 40–100 µg/m³ causes adverse health effects that includes irritation of the eyes, skin and the respiratory system. It also affects the immune system resulting in low resistance to infection and cause genetic damage [3]. The current world health organization (WHO) guideline values for NO_2 for Europe are: a 1-hour level of 200 $\mu g/m^3$ (0.11 ppmv) and an annual average of 40 $\mu g/m^3$ (0.021 to 0.026 ppmv). Nitrogen dioxide concentrations in the air have remained around 45$\mu g/m^3$ which equal to the currently maximum allowed recommended concentration. Nitrogen dioxide levels are highest in urban areas and along major road networks. This reflects that vehicle emissions are still the greatest source of NOx gases [4]. Because NO_2 is involved in numerous reactions which affect atmospheric composition, environmental degradation, human health problems and it can be transported over long distances, knowing the concentration of NO_2 in the atmosphere is important.

Recently, efforts toward the development of simple and reliable devices have been increased with the aim to control air pollution and to detect toxic gases at low levels in the air, in the field of domestic and industrial applications. Laser based

trace gas sensors have been used to monitor NOx emissions from individual vehicles [5], as well as variations in air pollution over cities [6, 7], thereby demonstrating that they can make contributions to manage air quality. In this paper, we present a simple, low cost, compact and standalone NO_2 detection system based on resonant photoacoustic spectroscopy (PAS). The performance of the diode laser driven system was explored and the sensor was applied to monitor the NO_2 level in the atmosphere. In addition, NO, as a product of NO_2 dissociations, was monitored using a direct absorption spectroscopy methods on quantum cascade (QCL) laser based detector.

II. Materials & Methods

A sketch of the photoacoustic spectroscopy (PAS) setup is shown in Figure 1. The cell is shown schematically; the real dimensions are given in the text.

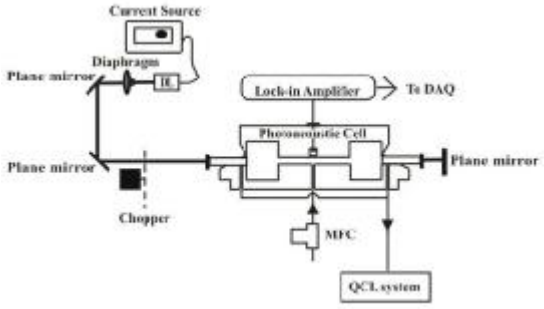

Figure 1 – Photoacoustic spectroscopy (PAS) system experimental setup. The laser beam from the diode laser (DL) is passed twice through the photoacoustic (PA) cell by using a plane mirror behind it. The gas output from PA cell goes to the QCL system. DL: Diode laser, MFC: mass flow controller, DAQ: data acquisition card, QCL: quantum cascade laser

The photoacoustic (PA) cell resonator is cylindrical with buffers attached at both ends and 3 microphones (Knowless EK3024, sensitivity of 22 mV/Pa and electrical noise 29 nV/√Hz) placed near its midpoint. The internal diameter of the resonator is 6 mm and its length is 300 mm. The buffer has a 40 mm diameter and a length 50 mm.. The cell had one inlet and two outlet ports. The gas inlet port was connected to the centre of the resonator via an acoustic notch filter of ¼ λ, in order to suppress the noise in line with the trace gas flow optimally at the resonance frequency of the PA cell.

The detection system of a resonant PA experiment for trace-gas measuring is generally based on synchronous detection with lock-in amplifiers in order to obtain a good signal-to-noise ratio. To determine the resonance frequency of the photoacoustic cell, we varied the modulation frequency f_m to scan the profile of the resonance peak and precisely determine its maximum. The amplitude of the frequency spectrum at the laser-beam chopping frequency f_m was stored and the procedure was repeated for different repetition rates around the cell's resonance with steps adequate for a good definition of the maximum, depending on the cavity *Q*-factor. The recorded amplitude and frequency values determined the PA peak, which shows a Lorentzian profile. For the following experiments the modulation frequency was set to the optimum value found from Figure 2, (565 ± 1) Hz.

The wavelength of the laser is 415 nm. At this wavelength NO_2 is dissociated strongly to NO [8]. To show the dissociation effect we used a direct absorption spectroscopy methods on QCL (Quantum Cascade Laser) system for detection of NO that was generated by the PAS system. For this purpose we connected the gas outlet of the PA cell to multi-pass cell in the QCL system [9]. During the experiments the pressure inside the cell was kept 100 mbar by a pressure controller and a pump. After the absorption cell the laser beam was focused onto a fast, liquid-nitrogen cooled detector (KV-104, Kolmar Technologies).

A schematic arrangement of the wavelength modulation spectroscopy set-up is shown in Figure 2. The QCL has a thermoelectrically cooled housing (Alpes Lasers); the laser is supplied by an external current driver (Keithley 2420). The QCL operates in the wavelength region between 1891.3 and 1907.6 cm^{-1} at an output power ranging from 0.1 mW at 253 K to 26.6 mW at 243 K. The laser is scanned via a function generator and additional home-made electronics; the latter also served as an over-voltage protection for the laser.

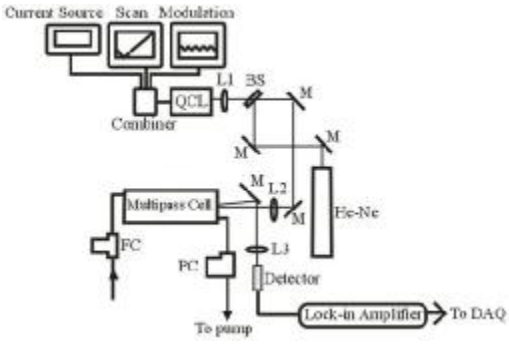

Figure 2 - Schematic diagram of the experimental setup: A combination of a stable current with scanning andmodulating function generators form the laser driver electronics.

For wavelength modulation spectroscopy the modulation depth is determined by optimizing the peak-to-trough values of the 2*f*-signal from the unresolved NO-doublet at 1903.9 cm^{-1} [10]. The modulation frequency *f* was set to 425 kHz and the 2*f* signal was detected with lock-in amplifier (SRS 844, Stanford Research Systems). The integration time of the lock-in amplifier was set to 100 μs, which allowed a scanning rate of 100 Hz over the selected wavelength range of the laser (0.5 cm^{-1}) at a single thermo-electrical temperature. The wavelength scans were stored using a fast data acquisition card (Gage Compuscope 14200). For the detection of NO the laser beam was collimated using a short focus ZnSe collimating lens of ½ - inch (1 inch = 2.54 cm) diameter and focal length and directed into a multiple pass optical cell (Aerodyne, AMAC-76) with an absorption path length of 76 m and a volume of 300 ml. During flow-through experiments the pressure inside the cell was kept at 100 mbar by a pressure controller and a pump (see Figure 1). After the absorption cell the laser beam was focused by a CaF_2 lens of 15 cm focal length onto an infrared photovoltaic detector (PVI-6, Vigo System S.A.). All optics equipment was positioned such that optical interference in the beam path was minimized.

III. Results and Discussions

With this setup (Figure 1) we obtained values for the resonance frequency of the PA cell of 565 ± 1 Hz and a *Q* factor of 13,1 ± 0,2. The laser power in the PA cell is 42 mW. Noise from the electronic equipments and gas flow rate was around 29 nV/$\sqrt{Hz}$. The background signal of the system when filled with N_2 was (180 ± 10) ppbV, so from the noise and background data we get a detection limit of 20 ppbV.

The characterization and calibration of the PA system is shown in Figures 3. From the figures we can infer that dissociation occurs in the PA cell since at the PA signal is reduced at low flow rates. To proof that this effect is due to dissociation we used the QCL system to measure the NO concentration in the gas outlet of the PA cell (Figure 4). From Figure 3 it is clear that by operating the system at a flow rate greater than 10 l/h, our measurement of the atmospheric NO_2 concentration is linear and is not distorted by dissociation effects.

Figure 4 shows the dissociation effect that occurs in the PA cell. This is clear with the NO signal appear in the QCL system when the outlet NO_2 gas from the PA cell is filled in the multiple pass cell in the QCL system, with the following reaction $NO_2 + h\nu \rightarrow NO + O(^3P)$ [10]. We can see that NO signal is not linear to the NO_2 (in the Nitrogen and air) signal. Also we can see the NO signal from NO_2 in N_2 is higher than NO_2 in air, that is because same reaction from $2NO + O_2 \rightarrow 2NO_2$ [10].

Figure 5 shows the results from the parallel measurements between the PAS system and the QCL system from the out side air. Around 3:00 PM we obtained the synchronous signal that is NO_2 signal from the PA system and NO signal from the QCL system.

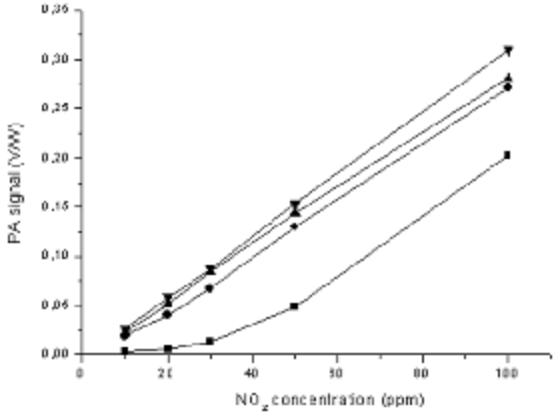

Figure 3 Values of PA signal vs. NO_2 concentration in N_2 at different flow rates at a laser power of 42 mW.■ 2 l/h; ●10 l/h; ▲ 15 l/h; ▼ 20 l/h.

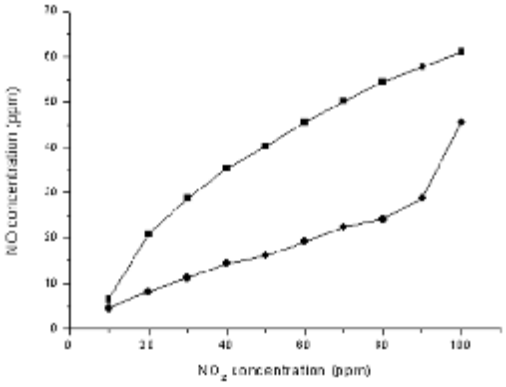

Figure 4 - NO vs. NO_2 concentration measured by the QCL and photoacoustic system, respectively. ■ NO_2 in N_2; ● NO_2 in air. The gas flow rate in the PA system is 15 l/h.

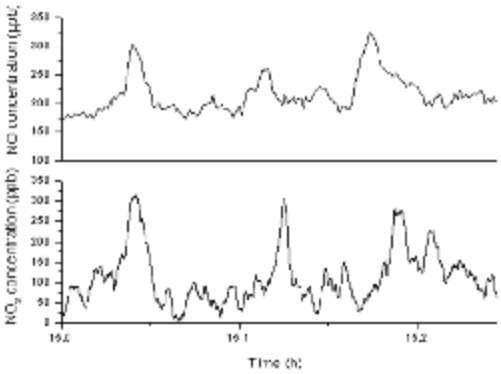

Figure 5 – Values for NO_2 and NO concentration from urban air around 3:00 PM June 15th, 2006.

IV. Conclusion

We have developed the diode laser-based photoacoustic spectroscopy (PAS) system that is simple, low cost, and compact and standalone detection system. The system has a detection limit of 20 ppbv for the NO_2. With this system we were able to detect the NO_2 concentration from urban air near our campus. We have also investigated the NO_2 dissociation effect of the system with NO measurements with a QCL system [9]. Furthermore, trace gas detection using the diode laser-base PAS system has proved to its capability in environmental monitoring and shows promise for other applications in life sciences and medical diagnostics as well.

V. References

1. U.S. environmental protection agency, 1999. Air Pollution and Health Risk. Air Risk Information Support Centre. http://www.epa.gov/ttn/uatw/3_90_022.html

2. World Health Organization (2000) Nitrogen dioxide. In: Air Quality Guidelines for Europe. http://www.who.int/en/

3. Matooane, M (2000): Report on Human Health Risk Assessment of Exposure to Sulphur Dioxide and Nitrogen Dioxide in the Greater Cato Manor-Durban. University of Natal, Durban. Lead Programme in Technologies for Enhanced Environmental Management, Report no. P5-1, Durban.

4. The Environmental Agency, 2006. Environmental facts and figures. http://www.environment-agency.gov.uk/yourenv/eff/1190084/air/1158715/1162725/?lang=_e

5. J. H. Shorter, S. Herndon, M. S. Zahniser, D. D. Nelson, J. Wormhoudt, K. L. Demerjian, and C. E. Kolb. Real-time measurements of nitrogen oxide emissions from in-use New York City transit buses using a chase vehicle. *Environmental Science & Technology*, 39(20):7991–8000, 2005.

6. V. Altuzar, S. A. Tomas, O. Zelaya-angel, and F. Sanchez-Sinencio. Atmospheric pollution profiles inMexico City in two different seasons. *Review of Scientific Instruments*, 74:500–502, 2003.

7. V. Altuzar, S. A. Tomas, O. Zelaya-angel, and F. Sanchez-Sinencio, J.L. Arriaga. Atmospheric ethene concentrations in Mexico City: Indications of strong diurnal and seasonal dependences. *Atmospheric Environment*, 39:5219–5225, 2005.

8. A.M. Coroiu, D.H. Parker, G.C. Groenenboom, J. Barr, I.T. Novalbos, and B.J. Whitaker. Photolysis of NO_2 at multiple wavelengths in the spectral region 200-205 nm. *Eur. Phys. J.D.,* 38, 151 – 162, 2006.

9. B.W.M. Moeskops, S.M. Cristescu, and F.J.M. Harren. Sub-part-per-billion monitoring of nitric oxide by use of wavelength modulation spectroscopy in combination with a thermoelectrically cooled, continuous-wave quantum cascade-laser. *Optics Letters* Vol. 31, No. 6, March 15, 823-825, 2006

10. R. Atkinson, D.L. Baulch, R. A. Cox, J.N. Crowley, R.F. Hampson, R.G. Hynes, M.E. Jenkin, M.J. Rossi, and J. Troe. Evaluated kinetic and photochemical data for atmospheric chemistry: Volume I – gas phase reactions of O_x, HO_x, NO_x and SO_x species. *Atmos. Chem. Phys.,* 4, 1461-1738, 2004

The Study of $H_p(10)$ and $H_p(0.07)$ Responses for Harshaw TLD-100H at Photon Energy of 24–1250 keV

W. Priharti[1] *, S. B. Samat[1], A. B. A. Kadir[2]

1 School of Applied Physics, Faculty of Science and Technology, The National University of Malaysia, 43600 UKM Bangi, Selangor, Malaysia

2 SSDL Malaysia, Nuclear Malaysia Agency, 43000 Kajang, Selangor, Malaysia

Abstract

The absolute, standardized and relative $H_p(10)$ and $H_p(0.07)$ responses of a Harshaw TLD-100H are studied. It is based on the irradiation of the TLD with photons with energy E from 24 to 1250 keV. The type and the thickness of the $H_p(10)$ and $H_p(0.07)$ filters affected the responses. For the absolute responses, results showed that (a) $H_p(0.07)>H_p(10)$ for the lower energy 24−47 keV, (b) $H_p(0.07)<H_p(10)$ for the higher energy 65−662 keV, and (c) $H_p(0.07)<<H_p(10)$ for 1250 keV. Reasons for this, in related with filters type, secondary electron range and the charge particle equilibrium in both TLD and filter are discussed. In overall, the standardized and relative energy responses are in agreement with results obtained by other worker and also in compliance with the ICRP 60 requirement of -33% and 50% acceptance limit.

Keywords : *Harshaw TLD-100H, $H_p(10)$, $H_p(0.07)$, ICRP 60, relative response*

* Corresponding author.
E-mail address: wpriharti@yahoo.com

I. Introduction

The Secondary Standard Dosimetry Laboratory of Malaysia (SSDL Malaysia) has been offering personal monitoring services to local radiation workers since 1985 [1]. The laboratory issues approximately 18,000 dosemeters to 18,000 users, monthly. Of this number, 16,300 dosemeters are of film type whereas the rest are thermoluminescence dosemeters, TLDs. Fewer number of TLD is in used as its price is 10 times higher than a film dosemeter. Despite this, TLD is most sought nowadays. This is due to its advantages such as capability of repeatability annealing and accuracy measuring a dose in a range less than 400 μSv [2]. For this reasons, the SSDL Malaysia has proposed a compulsory use of the TLDs by year 2015.

The SSDL Malaysia currently is using two-element TLD-100H (LiF:Mg,Cu,P) as shown in Figure 1. Element 2 and 3 are to measure $H_p(10)$ and $H_p(0.07)$ respectively. The $H_p(10)$ and $H_p(0.07)$ are the operational quantities of personal dose equivalent at depth 10 mm (deep dose) and 0.07 mm (skin dose) respectively [3, 4]. As part of internal quality assurance (QA) program, SSDL Malaysia routinely evaluates the accuracy of the dose measured by this TLD-100H. This is to ensure that the services provided meet the standard required by the IAEA [5].

The purposes of this work are (a) to compare the two responses of $H_p(10)$ and $H_p(0.07)$ for photon energy E from 24-1250 keV, (b) to evaluate whether these responses satisfy the ICRP 60 [6] requirement for accurate dose measurements, (c) to evaluate whether the results obtained from this work agree with the other published results.

II. Materials and Methods

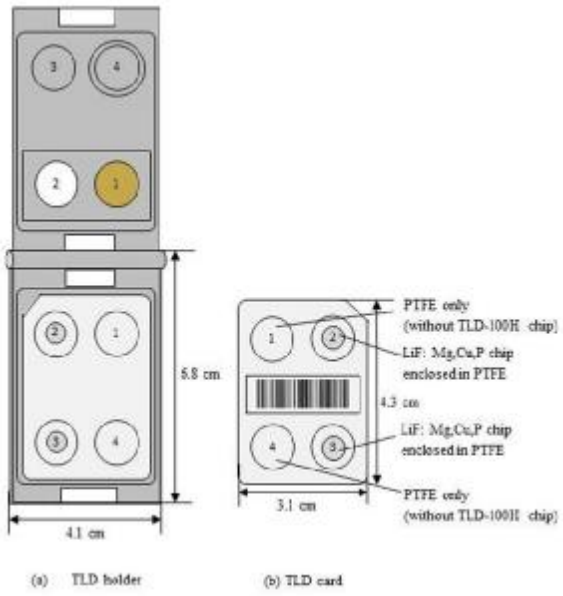

Figure 1. The two-element Harshaw TLD-100H. The element 2 is for $H_p(10)$ and element 3 is for $H_p(0.07)$

(a) The two elements

The two $H_p(10)$ and $H_p(0.07)$ detection elements shown in Figure 1 are circular-shaped chips made from LiF:Mg,Cu,P. These chips are fixed in an aluminium card covered by PTFE wrapping. The cross-section of the $H_p(10)$ and $H_p(0.07)$ and their filters are shown in Figure 2. The $H_p(10)$ detector is located beneath a thick dome made by 107 mg/cm^2 ABS + 893 mg/cm^2 PTFE whereas the $H_p(0.07)$ detector is beneath a sheet of 17 mg/cm^2 Mylar [7].

(b) The signal and background TLD cards

A total of six TLD cards were used. In this work, the same cards were used for all energies. This is to say that batches of TLD were not used for the purpose of reducing uncertainties in the results. Four TLD cards were used to get the signal reading (TLD_{signal} in nC) and the other two were for the background reading ($TLD_{control}$ in nC).

(c) The TLD cards calibration factors

The SSDL Malaysia X-ray machine (ISO 4037-1 quality, narrow spectrum series NSS) and γ ray machine (OB 85) were utilized. These machines provide ten *E* namely 24, 32, 47, 65, 84, 121, 171, 218, 662 and 1250 keV. To get the six cards calibration factors CF (mSv/nC), only 662 keV was used. These cards were put in front of a 30×30×15 cm^3 water phantom, with a source to detector distance (SDD) of 2 m and irradiation time of 5 mins.

(d) The dose delivered to the signal TLD cards

For each irradiation with an *E*, the four signal cards were put in front of a 30×30×15 cm^3 water phantom. In this work, the dose delivered to the cards is fixed to 1 mSv for each E. Therefore in the case of the $H_p(10)$,

$$\text{Delivered dose (mSv)} = H_p(10)_{del} \qquad (1)$$

The method to get this 1 mSv dose for $H_p(10)$ and for each *E* are as follows: The air kerma rate $\dot{K}_{air}$ (mGy/min) was first determined at SDD of 2 m,

$$\dot{K}_{air} = R_i \times N_k \times k_{TP} \qquad (2)$$

where R_i is the charge rate (nC/min) obtained from the M320002(#013) ion chamber, N_k (μGy/nC) is the chamber's calibration coefficient and k_{TP} (no units) is the correction factor for temperature and pressure. Knowing the conversion coefficient from Gy to Sv for $H_p(10)$ for that particular E is $H_p(10)_{CC}$ (in Sv/Gy), the $H_p(10)$ rate $\dot{H}_p(10)$ is calculated from

$$\dot{H}_p(10) = \dot{K}_{air} \times H_p(10)_{CC} \qquad (3)$$

Since $\dot{H}_p(10) = H_p(10)/t$, we can now determine the time needed for the machine to delivered the desired $H_p(10)$. In short, since $H_p(10)$ is fixed to 1 mSv, the irradiation time is calculated from

$$t\,(\text{min}) = 1\ \text{mSv}/[\dot{H}_p(10)\ \text{mSv/min}] \qquad (4)$$

(e) The measured dose by the TLD cards

After irradiation with a fixed dose of 1 mSv for each *E*, the signal TLD cards need to be stored for 24 hours to stabilize the electron trapping process. A Harshaw 4500 TLD reader was used to read the charge (nC). Also in this work, to reduce the uncertainties in the results, same TLD reader was used. During the reading process, the cards undergone a preheating at 165°C for 10 s followed by heating at 260°C for 13.33 s. The heating rate was set to 15°Cs^{-1}. The net dose (mSv) measured by the each card is calculated from [$H_p(10)$ TLD_{signal} (nC) − $H_p(10)$ $TLD_{control}$ (nC)] × $H_p(10)$ CF (mSv/nC). In the case of the $H_p(10)$,

$$\text{Measured dose (mSv)} = H_p(10)_{meas} \qquad (5)$$

Similar calculation could yield the value of $H_p(0.07)_{meas}$ as a function of *E*.

(f) The standardized energy response

For each E, the ratio of eqn (5) to eqn (1) is called the standardized energy response, i.e.

$$H_p(10)_{std,E} = \left[\frac{H_p(10)_{meas}}{H_p(10)_{del}}\right]_E \qquad (6)$$

Similar calculation could be used to get the value of $H_p(0.07)_{std,E}$.

(g) The relative energy response

Relative energy response was obtained by normalizing eqn (6) to $H_p(10)_{std,E}$ = 662 keV (Cs-137), i.e.

$$H_p(10)_{rel,E} = \frac{\left[\frac{H_p(10)_{meas}}{H_p(10)_{del}}\right]_E}{\left[\frac{H_p(10)_{meas}}{H_p(10)_{del}}\right]_{662}} \qquad (7)$$

Similar calculation could be used to get the $H_p(0.07)_{rel,E}$.

III. Results, Discussion and Conclusion

Discussion of the relative responses $H_p(10)_{rel,E}$ and $H_p(0.07)_{rel,E}$ would be easier if the quantity of the measured doses $H_p(10)_{meas}$ and $H_p(0.07)_{meas}$, obtained from eqn (4) were first examined. This is shown in Figure 3. Discussion could be divided into three regions of energy, namely Region I: the lower energy 24−47 keV, where $H_p(0.07)_{meas} > H_p(10)_{meas}$; Region II: the higher energy 65−662 keV, where $H_p(0.07)_{meas} < H_p(10)_{meas}$, and Region III: 1250 keV, where $H_p(0.07)_{meas} << H_p(10)_{meas}$. Discussion would be made easier if we examine the cross-section of the element 3 and 2, respectively for $H_p(0.07)$ and $H_p(10)$, as shown in Figure 2. For Region I, the thin filter of element 3 has allowed the low energy photon to pass through it so that the TLD absorbed most of the energy, in comparison with element 2, fewer low energy photon fluence reaching the TLD as they are attenuated and scattered by the thick filter. For Region II, the thin filter of element 3 is transparent to this high energy. Therefore when this high energy photon was incident on the TLD, the secondary electrons range produced in the TLD has caused a lesser dose absorbed. This is due to the lack of charge particle equilibrium (CPE) in the TLD build-up region. For Region III, (a) for element 3: the more higher photon energy might have caused larger secondary electrons range in the TLD and experienced more forward scattering with TLD electrons, of which these two processes has resulted lesser dose absorbed in the TLD; whereas for element 2: the two processes mentioned earlier did occur in the thick filter, therefore besides the incoming photon reaching the TLD (through the edge of the dome), the outgoing secondary electrons (from the filter) also imparted on the TLD. As shown in Figure 3, this has resulted larger dose being absorbed by the TLD of element 2 for $H_p(10)$.

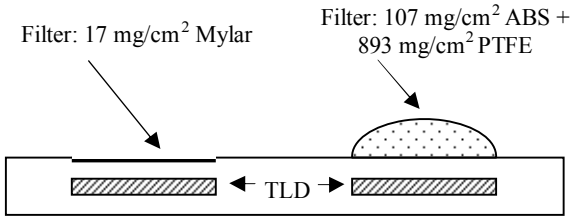

(a) Element 3 for $H_p(0.07)$ (b) Element 2 for $H_p(10)$

Figure 2. The cross-section of the TLD elements

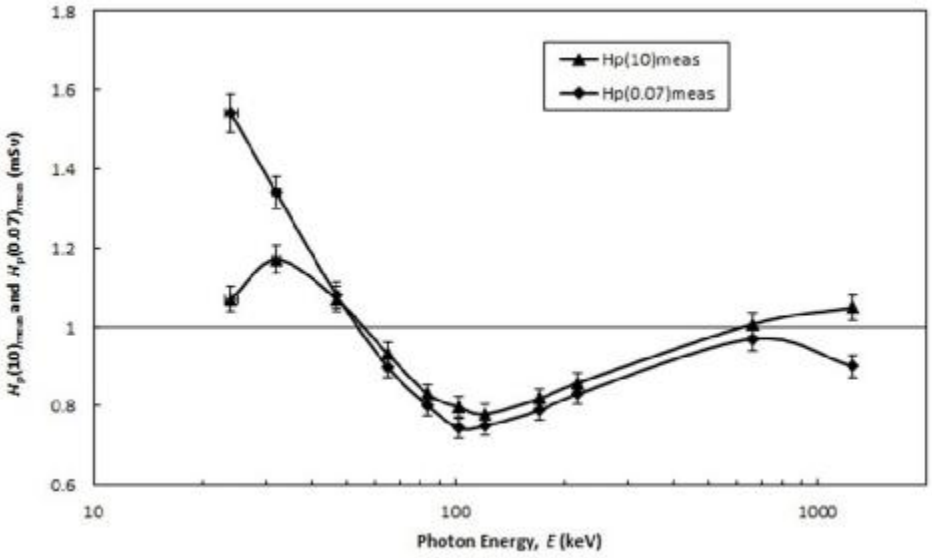

Figure 3. $H_p(10)_{meas}$ and $H_p(0.07)_{meas}$ versus E. The description to get the former is given by eqn (4).

The $H_p(10)$ curve in Figure 3 may be called as the absolute energy response, which has a unit of mSv, and obtained from eqn (5). If this $H_p(10)$ curve is divided by the delivered dose (which is fixed at 1 mSv for all E), as given in eqn (6), we may get the standardized energy response, which figure is not shown here, and has no unit. When the standardized $H_p(10)$ energy response is normalized at $H_p(10)$ at energy 662 keV, as calculated in eqn (7), this curve is called the relative energy response as shown in Figure 4.

It can be seen in Figure 4 that for Regions I and III, both $H_p(10)_{rel,E}$ and $H_p(0.07)_{rel,E}$ curves have a similar shape like what has been obtained in Figure 3. The only difference is that they coincide with each other in Region II. In comparison with the work done by Luo & Rotunda in 2006 [8] which also used the TLD-100H, the present results showed a good degree of agreement.

As it is obvious in Figure 4 that there exists the phenomenon of over-response and under-response, it would be interesting to check whether the results (in Figure 4) comply with the ICRP acceptable limit of -33% and 50%. We found that for both $H_p(10)_{rel,E}$ and $H_p(0.07)_{rel,E}$ are within the limit despite the maximum over-response (16% for $H_p(10)$ and 38% for $H_p(0.07)$) and the maximum under response (23% for both $H_p(10)$ and $H_p(0.07)$).

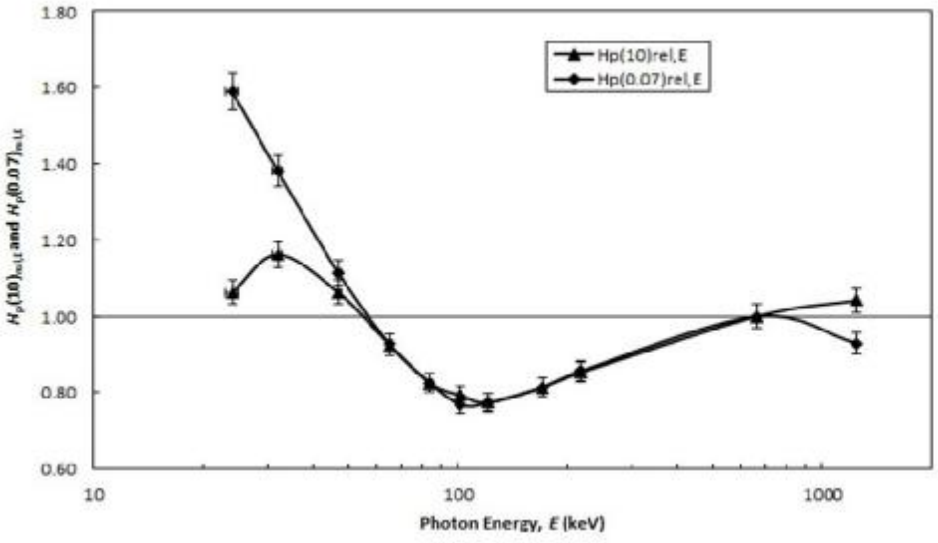

Figure 4. $H_p(10)_{rel,E}$ and $H_p(0.07)_{rel,E.}$ versus E for two-element Harshaw TLD-100H.

IV. Acknowledgement

W.P. wishes to thank The National University of Malaysia for a research grant of UKM-GUP-2011-224 and Ministry of Science and Technology for a research grant of UKM-ST-07-FRGS0154-2010. The collaboration given by the Nuclear Agency Malaysia staff is very much appreciated.

V. References

1. Samat, et al., *Radiation Protection Dosimetry*. 133, 186-191 (2009).
2. MINT, *Radiation Safety*, 2nd ed, Malaysian Institute for Nuclear Technology Research (MINT), Malaysia, 2003.
3. ICRP, *ICRP Publication 60: Recommendations of the International Commission on Radiological Protection*, ICRP, Oxford, 1991.
4. ICRU, *ICRU Report 47: Measurement of Dose Equivalents from External Photon and Electron Radiations*, ICRU, Bethesda, 1992.
5. IAEA, *IAEA Safety Standard: Assesment of Occupational Exposure Due to External Sources of Radiation*, IAEA, Vienna, 1999.
6. ICRP, *ICRP Publication 75: General Principles for the Radiation Protection of Workers*, ICRP, Sweden, 1997.
7. Børretzen and Wohni, *Radiation Protection Dosimetry*. 103, 29-34 (2003).
8. Luo and Rotunda, *Radiation Protection Dosimetry*. 120, 324-330 (2006).

STOPPING POWER AND RANGE OF PROTON IN MEDIUM; A STUDY FOR PROTON RADIOTHERAPY

Eko Sulistya, Kusminarto, Arief Hermanto
Physics Department Faculty of Mathematics and Natural Sciences
Gadjah Mada University, Yogyakarta, Indonesia
sulistya@ugm.ac.id

Abstract

The development of the theory of the interaction between heavy ions with matter has raised hopes on the growing success of radiation therapy for cancer. Relative to the electron, the proton is one of among heavy ions, which have different energy transfer characteristics compared with X-rays, called Bragg curve, a curve that form a flat low line at entry into the medium, and then forming a peak in the final moments before the end. Based on these characteristics, with correct proton energy, radiotherapy with protons is expected to give the maximum effect on the location of cancer and the smallest possible impact on the surrounding healthy tissue.

Deep study of the mechanisms of interaction between protons with the medium in its path has an important role in the planning of radiotherapy with protons. Proton energy should be determined carefully so that the protons stop at cancer sites. Likewise, it should be determined how many protons are fired, to fit the required dosage. This study was conducted by analyzing data from the results of previous studies of the interaction of protons with various elements, then the computation was performed to determine the stopping power and range of protons in the 3 types of body tissues, which is a compound of several elements.

The results were obtained in the form of stopping power data and the range of proton in the three types of tissue, i.e. skin, adipose tissue, and muscle. The results are to be used as a basis for the planning of radiotherapy with protons.

Keywords: stopping power, the projected range, proton radiotherapy, Bragg curve

INTRODUCTION

Radiotherapy with X-rays have been done over the years. X-rays killed tumor cells, but also cause damage to healthy cells in the surrounding tissue. This is due to the nature of X-ray interactions with the medium in its path, namely the exponential decrease in intensity due to the absorption of energy by the medium, so that the greatest damage is in the area near the skin tissue, and this becomes a problem if the tumor is located deep within the body. Because the X-rays did not stop at the location of tumor, the healthy tissue beyond the tumor could also be damaged.

Proton interactions with the medium in its path has different characteristics compared with X-rays. For high energy protons, the largest ionization occurs in the final moments protons will stop in the medium. This trait is an advantage because the energy given by proton to the healthy tissue in its path is very small so as not to ionize the healthy cells. The mechanism of the interaction of protons with a target medium, and how its range in the materials on certain proton energy, determines the level of success of proton radiotherapy.

The interaction between ions with medium is represented by a physical quantity called stopping power. In view of the medium, stopping power is the quantity that determines how adaptable is the medium to stop the incoming ions. For ions that enter into a medium, stopping power is the loss of energy per unit distance of the ions in the

medium. Stopping power of a medium to a specific ion is numerically equal to the stopping power of ions in that medium. The deeper the ions go into the medium, the smaller will be its energy so that the amount of interaction with the electrons in the medium increases. The loss of energy will also greater and reaches its maximum value called the Bragg peak and finally decreases sharply to zero when the ion stops. The distance between the point of entry of ions into the medium to the point where it stops is called the projected range.

Proton, which is H^+ ions, the hydrogen atom that loses electron, can be generated inside the accelerator. Energy is increased gradually up to a certain value and then fired at a target. This target may be another proton beam to investigate the constituent particles of protons, or a human tissue as a means of cancer radiotherapy. Experience with proton radiotherapy began in 1954, conducted at Berkeley, California, USA. The last therapy in Berkeley was performed in 1957 with the number of patients 30. Then continued in Sweden, 1957 to 1976 with the number of patients 73. Currently there are approximately 23 institutions with proton beam radiotherapy, including 3 in Russia, 6 in Japan, 2 in Switzerland, 1 in England, 5 in the USA, 1 in Belgium, 2 in France, 1 in South Africa, 1 in Canada, 1 in Germany and 1 in Italy.

Harald Paganetti and Thomas Bortfeld have written a medical review about radiotherapy with proton beam (Paganetti, 2005). That article did not discuss theories of physics beyond the proton beam radiotherapy, and also did not discussed its computational processes. Jean Paul Font also writes about proton radiotherapy in some tumor cases (Font, 2008), but no mention of its processes and computational physics. One of the roles of physics and computations in the proton radiotherapy is in determining the range of protons in the body tissues, and proper determination of absorbed dose. The range of protons is associated with the amount of stopping power, while the dose is associated with the flux (number) of protons being fired.

Equation of the stopping power for an ion in a homogeneous medium was obtained by Bethe using quantum mechanics (Turner, 2007),

$$-\frac{dE}{dx} = \frac{4\pi k_0^2 z^2 e^4 n}{mc^2\beta^2}\left[\ln\frac{2mc^2\beta^2}{I\left(1-\beta^2\right)} - \beta^2\right] \qquad (1)$$

with k_0 = 8,99 × 10^9 $Nm^2.C^{-2}$, z = atomic number of heavy ion, e = the electron charge, n = number of electrons per unit volume of the medium, m = rest mass of the electron, c = speed of light in vacuum , β = the ratio of the speed of ion to the speed of light, I = mean excitation energy of the medium. Equation (1) is not valid for low-energy ions, when the velocity is much smaller than the speed of the electron orbit. For energies smaller than 25 keV, stopping power equation was proposed by Fermi and Teller, and for energies above 100 keV, Bohr proposed an equation based on the Thomas-Fermi atomic model (Wu, 1961).

Stopping power for protons in a few elements have been obtained experimentally. The data has been matched between experimental results and computational calculations, which is the stopping power equations for all range of energy. Ziegler and Biesarc implement the stopping power formulae to the SRIM program (Ziegler, 2008). The stopping power data for the actual tissue of the human body have not been found, but the computation can be done by replacing the human tissue with a phantom tissue, a compound that is similar to the molecular composition of the tissue composition.

According to ICRP (International Commission on Radiation Protection), human tissues are composed of atoms H, C, N, O, Cl, Na, P, K and S with different compositions for different tissue (Valentin, 2003). Stopping power for different body tissues have different values depending on the constituent elements in the body's tissues. Stopping power per unit mass of the proton in some type of tissue is obtained by using the Bragg summation rule (Getachew, 2007),

$$\left(-\frac{dE}{\rho dx}\right)_{\text{compound}} = \frac{1}{M}\sum_i N_i A_i \left(-\frac{dE}{\rho dx}\right)_i \quad (2)$$

Range is the distance traveled by the proton before stopping. If the stopping power is reversed, the distance is obtained per unit of energy loss, and the range of ion with energy E_0 can be calculated by integrating (2) to zero energy (Getachew, 2007),

$$R(E_0) = \int_0^{E_0} \left(-\frac{dE}{dx}\right)^{-1} dE \quad (3)$$

Range of protons in the medium can be estimated computationally, by selecting certain small values Δx. The iteration is done by adding Δx to the proton distance, calculate the energy loss of the proton by using the stopping power equation, reduced the proton energy and then calculated stopping power for the new proton energy. The procedure is repeated until the value of the proton energy is very small or zero, and the iteration is stopped. Range obtained in this way is called CSDA range (Continuous Slowing Down Approximation), and is always greater than the projected range for proton because its trajectories may not be straight line in the medium, but deflected as an effect of interaction with the medium's atomic nuclei. In the high-energy protons range, above 30 MeV, proton deviates only slightly from the initial trajectory so that its trajectory can be considered as straightline, and the projected range can be approximated by CSDA range. From the stopping power value and the depth of proton we can plot the data to obtain Bragg curve for protons with energies above 30 MeV. Protons with energies between 30 MeV and 60 MeV has a range between 1 to 2.5 cm in the human tissue, which corresponds to the depth of the location of tumor (Mowlavi, 2010).

DISCUSSION

From the data pair of proton energy and stopping power in the constituent atoms of human tissue and from the results of previous studies, regression was performed to find a suitable equation to describe the relationship between the two, and obtained non-linear equations that looks the same for all the atoms of body tissue,

$$-\frac{dE}{dx} = \frac{a + c\ln E + e(\ln E)^2 + g(\ln E)^3 + i(\ln E)^4}{1 + b\ln E + d(\ln E)^2 + f(\ln E)^3 + h(\ln E)^4 + j(\ln E)^5} \quad (4)$$

a, b, c, d, e, f, g, h, i, and *j* is a parameter whose value varies depending on the target atom, and *E* is the kinetic energy of the proton. The equation is needed in the computation so there is no need to choose which equation to use according to the proton energy.

Figure 1 shows the curve of stopping power as a function of the proton energy is calculated with equation (4) and the SRIM program. It appears that computational calculations using the equations resulting from curve fitting is in good agreement with the results from the SRIM program. For the hydrogen atom, there is little difference between the two, which can be corrected by the selection of the target phase, using phase correction depending on whether as a solid or as a gas. For the other elements it can be said that the results of fitting the equation matches with the results of calculations with SRIM.

Figure 2 displays the results of the calculation of proton stopping power in skin, adipose tissue and skeletal muscle with the Bragg addition rules, compared with the results of SRIM program. As for the body tissues, the molecular formula is unknown, but simply stated in percentage, as presented in Table 1. Stopping power curves for the three types of tissues were calculated with Bragg addition rule by using a scale factor. Scale factor is used as a normalization, because the calculation of the Bragg Rule is always greater than the SRIM results. This is caused by the difference in the value of the excitation energy *I*. Bond of the electrons in the compound is stronger than in the pure

element, so that the value of *I* in Bragg addition rule equation would have a lower value, thus generating greater stopping power value. In the SRIM program, the problem is overcome by using a Core and Bond algorithm.

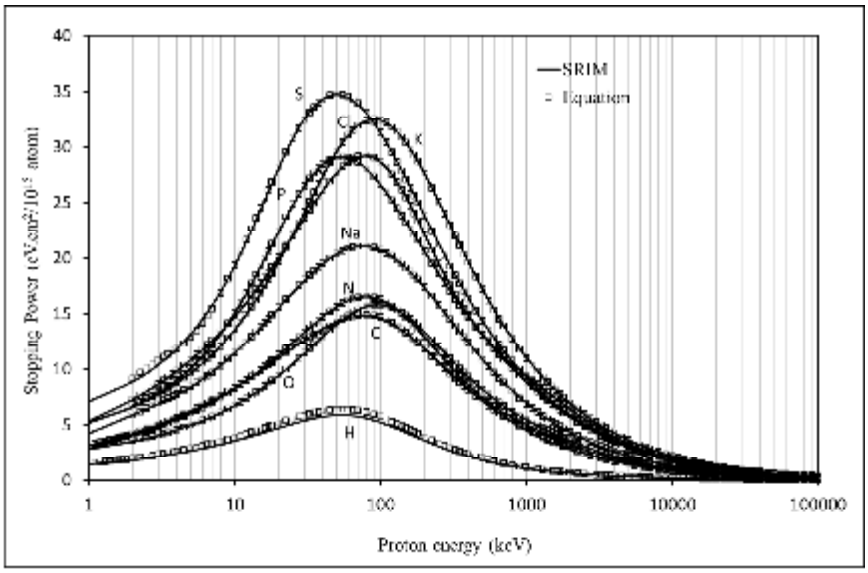

Figure 1. Stopping power curve of constituent elements of the body's tissues to the proton.

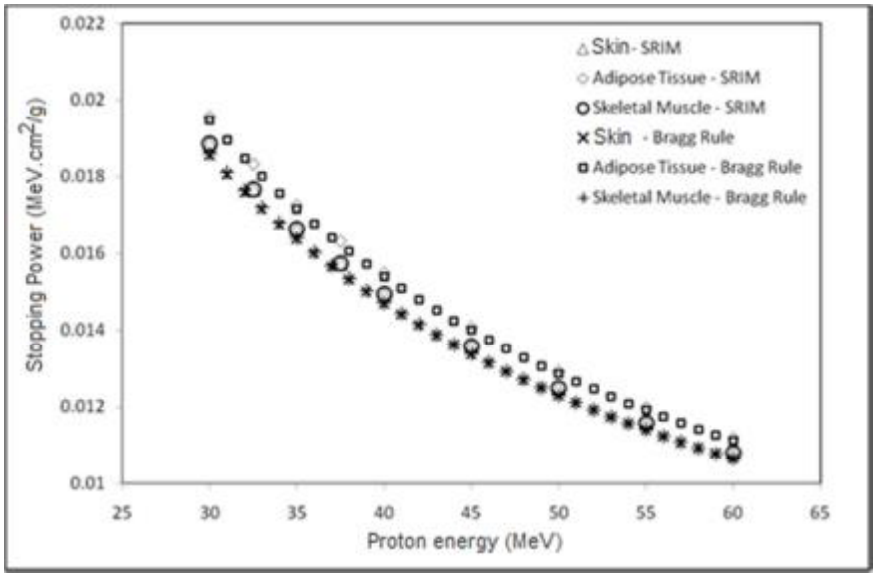

Figure 2. Stopping power of skin, adipose tissue and muscle of the proton, obtained by SRIM program and the Bragg sum rule for proton energies between 30 MeV and 60 MeV

Table 1. Percentage of constituent elements of the skin tissue, adipose and skeletal muscle (Mowlavi, 2010)

Element	Atomic number	Skin (ρ=1,09 g/cm^3)	Adipose tissue (ρ=0,92 g/cm^3)	Muscle (ρ=1,05 g/cm^3)
Hydrogen (H)	1	0,62744	0,63482	0,63169
Carbon (C)	6	0,08237	0,28408	0,07432
Nitrogen (N)	7	0,01654	0,00306	0,01515
Oxygen (O)	8	0,27202	0,07775	0,27703
Sodium (Na)	11	0,00054	0,00012	-
Phosporus (P)	15	-	-	0,0004
Sulfur (S)	16	0,00039	-	0,00058
Clorine (Cl)	17	0,00053	0,00018	0,00018
Potassium (K)	19	0,00016	-	0,00064

Figure 3 shows proton range curve in all three types of tissue for protons energy of 10 MeV to 60 Me. The greatest range is in the adipose tissue. In simulations with proton radiotherapy in cases of thyroid cancer (Mowlavi, 2010), the depth of the thyroid gland cancer is about 1.8 cm. From Figure 3, the range of protons at about 1.8 cm occurs at the proton energies between 40 MeV and 50 MeV for each type of tissue.

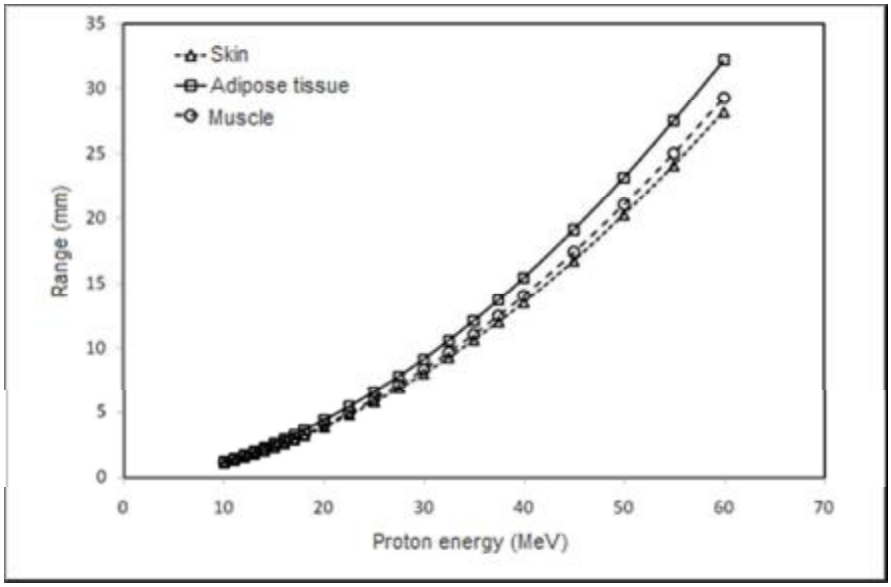

Figure 3. Range of protons in the skin tissue, adipose tissue and muscle.

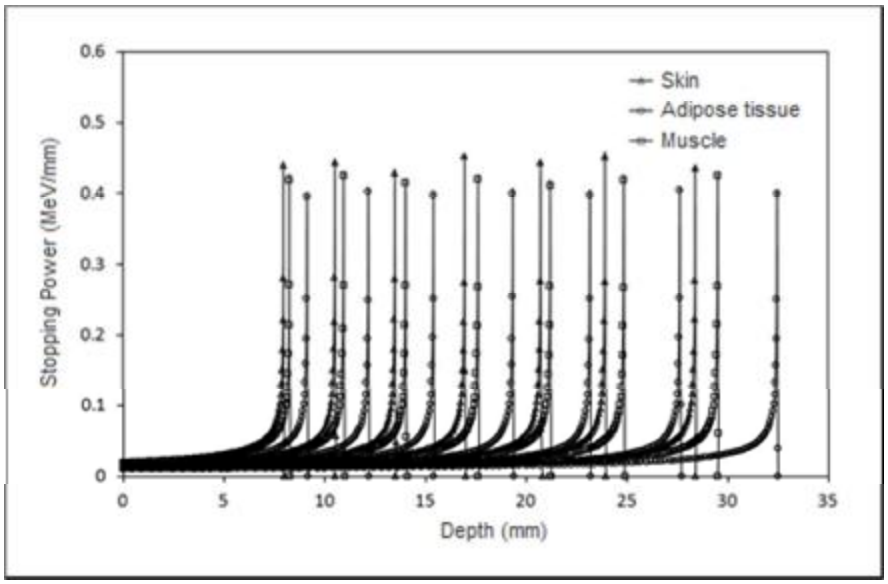

Figure 4. Bragg curves in skin tissue, adipose and muscle for energy 30 MeV protons and 60 MeV at intervals of 5 MeV

In practice, the protons must pass through several layers of different tissue before getting to the location of the cancer. Proton energy left after the exit of the first layer is used for the calculation of stopping power at the next layer. Thus the proton energy must be determined carefully in order to obtain the Bragg peak at the location of the cancer. Figure 4 displays Bragg curve for all three types of tissue, for proton energies ranging

from 30 MeV to 60 MeV at intervals of 5 MeV. The highest peak is in the skin tissue, then in the muscle, and the lowest is adipose tissue. CSDA range can be obtained from Figure 4, which is the point of intersection between the axis and the Bragg curve. According to Figure 3, for the same proton energy, CSDA range is the highest in adipose tissue, then in muscle tissue, and the lowest is in the skin tissue. Bragg peaks for the three tissue are increasing with the increasing energy of proton.

Further analysis of the proton motion in the layered medium can be useful in the planning of radiotherapy with protons.

CONCLUSION

1. Based on the review from the point of view of physics and medical standpoint, radiotherapy with protons could give maximum effect in tumor tissue/cancer target with minimum effect on the surrounding healthy tissue.
2. From the non-linear regression applied to data obtained from SRIM program, a non-linear equation is produced that applies to all energy proton range. This equation has the same form for multiple targets that were examined, but with different parameters. The equation will be very useful in computation involves calculation of stopping power even though it does not contain a specific physical meaning.
3. The results of the calculation of stopping power on the compound using Bragg addition rule is not exactly the same as the calculation of the SRIM program.This is due to the fact that the bonding electrons in the compound is stronger than the bonding electrons in the atom, so that the excitation energy of the compound is higher than the excitation energy of a single atom.
4. Range of proton as a function of proton energy in the 3 human tissues that have been studied can be calculated by computing the value of the stopping power of each element making up the tissue.

REFERENCES

Font, J. P., 2008, *Applications of Proton Beam Radiation*, Grand Rounds Presentation, Dept. of Otolaryngology, University of Texas Medical Branch.

Getachew, A., 2007, *Stopping Power And Range Of Protons Of Various Energies In Different Materials*, Addis Ababa University, Ethiopia.

Mowlavi, A. A. ,Maryam Homaei and Mohammad Alipoor, 2010, *SRIM Code Use for the Evaluation of Optimum Proton Energy Interval for Thyroid Cancer Therapy*, African Physical Review, p.107.

Paganetti, H. and Thomas Bortfeld, 2005, *Proton Beam radiotheraphy – The State of the Art*, New Technologies in Radiation Oncology (Medical Radiology Series), Springer Verlag, Heidelberg, ISBN 3-540-00321-5.

Turner, J. E., 2007, *Atoms, Radiation, and Radiation Protection*, WILEY-VCH Verlag GmbH & Co. KGaA, Weinheim.

Valentin , J., 2003, *Basic Anatomical and Physiological Data for Use in Radiological Protection*: *Reference Values ICRP Publication 89*, ICRP Publishing, Elsevier Science LID.

Yuan, and C.Wu, 1961, *Method of experimental physics*, vol.5, part A, Acadamic press,Inc., New York.

Ziegler, J.F, J.P Biersack, and M.D. Ziegler, 2008, *SRIM – The Stopping and Range of Ions in Matter*, SRIM Co., Chester, Maryland, USA

Dialogue between Science and Faith: A Preliminary Study

Aloysius Rusli
Physics Department, Faculty of Information Technology and Sciences,
Parahyangan Catholic University, Ciumbuleuit 94, Bandung 40141
T: +62 22 204 1964, F: +62 22 204 2141
E: arusli@unpar.ac.id, SMS: 0812 142 5373

Abstract

Awareness of developments in science and of its scientific method, and its increasing influence on society, leads to attention and thoughts on the other major influence on society, i.e. religion and the faith on which it is based. The extent of those influences have caused some notable clashes, e.g. the ongoing clash of scientific precepts and creationism and intelligent design. It is considered important to delve into the basics of both science and faith, as separate from technology and religion, to discover the principles inherent in science and faith, and ways of constructive interaction, to seek a coherent education pattern for the young generation. This is important to attain a coherent and integrated world view, a 21st century aim of integrated science. This report is on preliminary study results, hoping to get further input for continuance of the study. A preliminary result is, that the basic assumptions of science and faith are different, but that the reasoning following those basic assumptions are similar in character, consisting of rationality, consistency and correspondence with observations. It is becoming apparent that there might be some limits for each side, and there should be efforts to uncover the characteristics of those limits, if there are any. The method used is the dialogue method, where every expression from each side is considered in a positive and constructive way, to be able to discern the truth behind the words and the language used.

Keywords : *Science and scientific awareness, science and faith, dialogue*

I. Introduction

Awareness of developments in science and technology [1] clearly shows the effectiveness of the scientific method. This method bases itself on observable things, reflecting on it and hypothezing some explanation or interpretation, which is then checked for reproducibility and consistency with previous and other results and facts.

This success has increasing influence on society, with various consequences. On the positive side, it has helped rationalize behavior and relations between persons and in society. On the negative side, it has caused a belief that everything in this universe can be solved rationally based on the scientific method [2, 3], meaning that only observable things are believed to exist; non-observable things are regarded as non-existent. Other negative effects are, that efforts developed that try to accommodate scientific results with statements by trusted persons or trusted sources which are interpreted in a literal sense, causing the 'creationism' [4] and later on the 'intelligent design' way of thinking [5], the latter trying to see supernatural causes as explanation of various complexities in nature. This has caused clashes between scientists with religious institutions, as these institutions are usually based on religion, and religion is based on faith. By faith is meant the belief in certain precepts or sayings or writings, without always checking for consistency with other things or facts.

II. The Problem

The problem is the possibility of continuing of those clashes, which only shows that the persons involved are unable to understand the other side's thoughts and the principles behind them; or stated in a positive way: The persons involved in those clashes have concluded that theirs are the more valid or the only valid thoughts, while the other side has totally wrong or invalid thoughts and principles. When those clashes are kept at the thought level, the problem will easen; however when those clashes of thoughts lead to physical and destructive action, the welfare or peace of the community and the community members will be disturbed, and this will cause suffering, more so for the weaker or more susceptible people like the sick, the disabled, the aged, and the women and children who have less physical strength.

Until the end of the nineteenth century (counted according to the Common Era), when globalization was just developing, caused by the industrial Revolution, people were still able to isolate themselves on some deserted island or some isolated area. However with the increasing

power of communication, especially with the development of the Internet, the whole human population on Earth got interconnected, and the fact that the whole human race is Earth-locked onto this single fragile planet shows the importance to manage the avoidance of such clashes of thoughts or primarily the resulting physical actions. Since the middle of the twentieth century, the ability to unleash nuclear energy has warned the human race of its ability to self-destruct through globally spread radioactivity if nuclear weapons are launched. The 21st century has started to show that launching 'dirty' (radioactively hazardous) missiles are getting easier and more accessible to people, as are chemical and biogenic weapons. So the importance and urgency of finding ways to make different lines of thought to interact constructively, is becoming increasingly apparent [6].

The more essential, while more intangible problem, is to safeguard the integrity of the human person. The belief that is quite often expressed is, that the human person consists of a physical body, a mental brain-controlled state, and a spiritual mind. That belief especially concerns the existence of the spiritual mind. Observation shows that a 'balanced' person will be a happy and sociable person, and by 'balance' is meant that the three components comprising the human person are in accord with each other, or in other words, there will be integrity of the person. On the other hand, when those three components are not in step, the human person, aware of it or not, is apt to feel unhappiness or 'imbalance'. It has been noted [7] that schools are usually more inclined to train expertise and practical effectiveness to work, while neglecting maturity of mind in an increasingly complex and global world. This is predicted to cause internal psychological, personal and community stresses to build up.

III. The Method

To avoid physical clashes, which are more characteristic of animal behavior, we have to revert to actions which are more characteristic of the human race, which is the method of dialogue, followed if necessary with discussion to discover common ground and practical agreements.

In the Greek era, discussion still has the meaning similar to 'percussion' and 'concussion', with people still feeling appropriate to use physical fighting or wrestling when getting impatient of just exchanging thoughts and seeking mental and practical solutions. However nowadays discussion is seen as fully being at the thought and talking level, without any resort to physical strength.

Dialogue, on the other hand, can be defined as the preliminary of discussion, or the more important activity of meeting (not necessarily agreeing) of minds. This means that in dialogue, the listening aspect is very apparent. And this listening would be followed by reflection, which is thinking about the things heard and trying to understand the meaning of those expressions. Understanding those meanings might lead to understanding the existing differences. And understanding those differences as clear as possible, through questions and answers, will clarify what differences of assumptions are being held. And realizing those differences in assumptions, might clarify the way to reach common ground. This would be fertile ground for starting discussions of more technical nature.

Concretely, this dialogue has been started at the beginning of this year, 2012, using an electronic yahoogroups mailinglist [8], and inviting a score of lecturer friends at the Parahyangan Catholic University to present their viewpoints on the topic of 'dialogue between science and faith'. As an immediate daily sounding board, the participation of physics professor Benedictus Suprapto, with whom the author is sharing office space, has gratefully been obtained. His repeatedly expressed advice has been, that we should primarily listen/read the postings on that mailinglist, and not exert any coercion or guidance or disapproval, and reflect as fully as possible on the meaning of the postings, and try to read between the lines and past the limiting barriers of language, to get at the deeper meanings. Therefore the term 'preliminary' in this paper's title is very appropriate, as this study will need an extended period in time to be able to reach some quite solid conclusions, not to say to get any concrete applicable conclusions.

IV. Some Preliminary Results

From the expressions trolled from the mailinglist postings, and some readings from the literature and the Internet [9], some preliminary results could be reported in this paper:

a. The basic assumptions of science and of faith seem to be different. Science assumes concepts and processes which are based on measureable observations, which should be reproducible. 'Reproducibility' is defined as being able to be repeated in time and in different places, and as long as the other conditions are measureably the same, the results obtained should be the same. Therefore the issue of ghosts, spirits,

'little green Martians', UFOs, in the sense of 'flying saucers' and communications with extra-terrestial aliens, extra-sensory perceptions like *clairvoyance*, future-telling, etc mostly fall outside the area of science. Also outside science is the concept of God and the spiritual universe of angels and devils, as these are, at least for the time being, not measurable at all.

b. The basic assumption of faith is, that some saying, or writing, has been obtained from God or from some human considered to have the proper experience, who is believed to be true and truthful. Based on this premise or axiom or postulate, which is scientifically improvable and assumed not needing any proof, a body of knowledge or rules are developed rationally, and believed to be true.

c. The process of deducing things from the premises are similar, for both science and faith: The common sense of experience, and backed up by mathematics in the science case, are used to derive a body of knowledge. A risk in using common sense too cavalierly is, that it is usually culture-dependent, at least in some measure, so conclusions can differ for different cultures.

d. The condition of reproducibility, or consistency with observations, and rationality, could in some measure be considered to be supportive evidence for the truthfulness of some statement derived from those basic premises. Faith accommodates quite easily the possibility for miracles or 'the hand of God', but science puts very strict demands on experimental proofs.

These are some of the conclusions, very tentatively, which are obtained from reflections on the contributions from the mailinglist, the literature, and the Internet.

V. Conclusion

As a still also tentative conclusion could be offered the following points:

i. The realization of an essential difference in basic premise between science and faith could be considered to support the hope to integrate, or at least mutually support, scientific and faith-based worldviews, and so support the nurturing of a person's integrity in viewing the measureable world around her/him, and the internal/mental/spiritual world inside and around her/him.

ii. The barrier of the limited ability of language to represent truth, and the dependence of language on the culture that is using that language, should be realized appropriately: We should use words carefully, try to realize the various meanings transmitted and connotated by words, and try to neutralize and get at their essential meaning by expressing statements in more than one language; this often helps to sharpen oneself on the meanings contained in the words.

iii. The different human cultures living in this world should be regarded as an asset, not as something to be neglected or dismissed, in the sharpening of meanings of words. This could be regarded also as a contribution of the science of language to the sharpening and rationalization and adaptation of faith to the world of the majority of humans.

Disregarding this might well intensify the stress level of future generations, as they experience the intrusion of science and technology into their daily life, through increasing ability through science to extend lifetimes through education, communication, medicine and food, touching wellbeing, feelings of happiness, and feelings of being an insignificant screw in a gigantic machine which is the nation-state and/or the multinational enterprise.

Acknowledgements

Acknowledged gratefully are:

a. Fruitful ideas and discussions with professor B Suprapto, and contribution of ideas and viewpoints on this theme from members of the electronic mailinglist [8].

b. Financial support from Parahyangan Catholic University, through its Institution of Research and Community Service (LPPM) to attend and present a paper at the Jogjakarta International Conference on Physics (JIPS) 2012 in UGM, 18-19 September 2012.

c. The opportunity given by the Administration of JIPS to present this paper, to obtain input for further studies on this theme.

VI. References

1. A. Rusli, "Science and Scientific Literacy vs Science and Scientific Awareness through Basic Physics Physics Lectures: A Study of Wish and Reality", American Institute of Physics (AIP) Conference Proceedings **1454**, ICPAP 2011, 169-173, 2012. https://edocs.unpar.ac.id/edocs?dn=4ec62709dddd8
2. James Ladyman & Don Ross, with David Spurrett & John Collier, "Everything Must Go – Metaphysics Naturalized", Oxford University Press, New York, 2007.

3. Wallace Matson, ”Grand Theories and Everyday Beliefs – Science, Philosophy, and Their Histories”, Oxford University Press, New York, 2011.
4. Creationism, Wikipedia http://en.wikipedia.org/wiki/Creationism, 6 August 2012.
5. Intelligent Design, Wikipedia (2012), http://en.wikipedia.org/wiki/Intelligent_design, 6 August 2012.
6. John Paul II, “On the Relationship Between Faith and Reason” (‘Fides et Ratio’), Encyclical Letter to the Catholic Bishops, www.vatican.va , 1998.
7. Keith S. Taber, Learning about Science and Religion (LASAR) Project, Faraday Institute for Science and Religion, St Edmund’s College, University of Cambridge, UK, 2012, https://camtools.cam.ac.uk/wiki/site/~kst24/lasar.html
8. Electronic mailinglist “Dialog Ilmu dan Iman”, http://dialogilmudaniman.yahoogroups.com, 2012.
9. *Metanexus Institute on Religion and Science.* Metanexus Global Network Initiative, http://www.metanexus.net/globalnetwork, 2012.

For Science and Scientific Awareness: The Volt Unit and the Alternating Current Josephson Effect

Aloysius Rusli
Physics Department, Faculty of Information Technology and Sciences,
Parahyangan Catholic University, Ciumbuleuit 94, Bandung 40141
T: +62 22 204 1964, F: +62 22 204 2141
E: arusli@unpar.ac.id, SMS: 0812 142 5373

Abstract
To support efforts to increase awareness of science and its scientific method, the process of standardization of the volt unit in electromagnetic theory has been studied. Previous to year 1990, various types of electrolytic cells had been used, but every time it was discovered that the electromotance was drifting away from the initial state. Starting 1 January 1990 the CGPM (General Conference on Weights and Measures) in Paris agreed to opt for the Alternating Current Josephson Effect to produce a standard volt that depends only on fundamental natural constants, i.e. the Planck constant and the electron's electric charge, besides a standard microwave frequency that can be measured with an uncertainty of 1 : 10^{7} or 7 significant digits. This report is on the results of that study, consisting of the historical background, to be aware of the intricacies and also the human factor involved, and the basics of the Josephson Effect, to be aware of a macroscopic, cooperative quantum effect that has produced several other highly accurate instruments, e.g. the SQUID (superconducting quantum interference device) for measuring attotesla magnetic fields. This study is based on information culled from books and the Internet, e.g. the 1973 Nobel Prize Lecture of Brian Josephson, and efforts to systematize and simplify the explanation of the Josephson Effect. This report is expected to be useful to support illustrations in Basic Physics lectures, to help connect lectures with important and more recent scientific discoveries in physics, and the human's role in it.
Keywords: *Science & scientific awareness, volt standard, Josephson Effect, simple model* ***s****.*

I. Introduction

In support of efforts to increase awareness of science and its scientific method, the process of standardization of the volt unit will be reported in this paper. This topic is one component of a string of studies started with an interest in the workings of the International System of Units, well-known as the S.I. [1]. The ongoing effort to prepare the redefinition of the basic S.I. units, then focused attention on the intended redefinition of the kilogram [2], which then drew attention to the standardization of the ohm unit of electrical resistance using the Integer Quantum Hall Effect [3] and then the standardization of the volt unit.

As previously, in a similar vein, the history of the volt will acquaint the student to the human factor in the development of science, so as to become aware that it is the human person, with her/his achievements and limitations, failures and disappointments, and enduring spirit to overcome, that has made possible the various discoveries, interpretations, and inventions. In addition, the process of realizing a standard for the volt, using the so-called Alternating Current Josephson Effect, will acquaint the student to some elements of the science and its scientific method, giving an awareness of its workings and hopefully then also an appreciation of the ability of the human to understand and predict and utilize that science for the benefit of the public community. If this is managed appropriately, a balanced and satisfying appreciation of a Creator behind all this might also be obtained.

II. The Problem with Previous Standards of the Volt

As can be read *e.g.* in Wikipedia [4] or also in a book on Alessandro Volta (1745-1827) [5], it was Luigi Aloisio Galvani (1737-1798) [6] who in the 1780s with his assistant first noted that a metal scalpel touching a main nerve (the sciatic nerve) in a dead frog's leg caused the leg muscles to contract; "animal electricity" he called it, believing that the force came from the frog's muscles, flowing through the nerves. However it was Volta who first realized that it was the fluid in the frog's leg (nowadays called 'electrolyte') which enabled electricity to flow, and not being dependent on the presence of animal or biological muscles but on the metals used. To prove that, Volta eventually (in year 1800) devised the voltaic pile, a series of zinc and copper plates,

interspersed with brine (an electrolyte)-soaked paper, not using any animal parts. This pile could produce a steady current for some time, eventually causing Volta's name to be used for the unit of potential difference which causes electrical current to flow.

The difference in opinion between Galvani and Volta was treated with low profile by Galvani, he just let his nephew defend the idea of animal electricity. This was characteristic of Galvani: He previously abandoned his years of research in the hearing of animals and humans, when a certain rather unethical-behaved professor at the University of Modena, Italy, Antonio Scarpa claimed priority of discovery, even though it appeared that Scarpa was plagiarizing Galvani's results.

The problem with the voltaic pile is the decaying of potential (or 'voltage') difference with time, due to chemical and physical processes. This disqualifies it from being used as a standard for potential difference. In the 1880s [7] the International Electrical Conggress (now named International Electrotechnical Commision, IEC) approved the name 'volt' as the unit, defining it as the potential difference causing a current of one ampere in a conductor to dissipate one watt of power. As electricity became more and more important for industry etc, a practical 'definition' or standard was needed, and in 1893 the international volt was defined as 1/1.4328 of the emf of a Clark cell [8] invented in 1873, using zinc, zinc sulphate, and mercury. This definition of a volt standard was valid for a temperature of 15˚C, and change of temperature caused appreciable deviations, −1.15 mV/°C. In 1908, that definition was replaced by a definition based on the international ohm and international ampere, using Ohm's Law, but in 1948 all these 'reproducible' units were abandoned and the Weston cell became the single standard. The Weston cell (using cadmium, cadmium sulfate, and mercury) was invented in 1893, and since 1911 until 1990 it replaced the Clark cell as standard, as it is more temperature-independent. Its emf was also a convenient 1.018 638 volt, while still having a drift of some 80 microvolts per year [9]. Only when the Josephson Effect was discovered in 1962, a possibility came forward for a better definition of the volt.

III. The Direct Current (DC) Josephson Effect

In 1962, a brilliant graduate student [10] in the Physics Department at Cambridge University, Brian David Josephson (born in 1940), became interested in superconductor behavior when he listened to solid state theory lectures given by Philip Warren Anderson [11] from Bell Laboratories, New Jersey, USA, who was on sabbatical leave, and who showed him some interesting preprints from the highly reputed Physical Review Letters. Josephson then calculated [12] that two superconductors which were separated by a thin insulator film (of thickness a few nanometers), would experience a constant electrical current, tunneling across that junction, with no voltage difference appearing across the junction. This meant that the current was a supercurrent, comprising pairs of 'Cooper' electrons, flowing without any dissipation into heat, even though the insulator film was not a superconductor. This was named the Direct Current Josephson Effect.

Those Cooper electron pairs form inside a metal below its critical temperature, where the metal becomes superconducting. The quantum mechanical wave function of those Cooper pairs (a 'macroscopic' wave function as it describes the density of a macroscopic number of electron pairs) can be described having a phase φ, and the two superconductors comprising the junction have their respective phases φ_1 and φ_2. The so-called first Josephson equation shows [12, 13, 14] that the supercurrent per unit area flowing through the junction, J_S, is simply proportional to the sine of the phase difference:

$$J_S = J_C \sin(\varphi_1 - \varphi_2). \quad (1)$$

It can be seen that zero current indicates that the wave function's phase in the two superconductors will be the same; this is the equilibrium state of lowest energy. However if there is a phase difference, a constant (in direction and magnitude) supercurrent will be flowing between the superconductors. The maximum current J_C is ~650 microampere, comparable to the 'normal' unpaired electron current that will flow if an appropriate voltage is applied able to bridge the small superconductor energy gap (~ a few hundred microvolts [13, p 456]), and so cancelling the superconductive state of the metal [15].

Regarding the Welsh-born (in 1940; [10]) Brian Josephson, his brilliance was already apparent since his school years in Cardiff, Wales, and his undergraduate years in Cambridge University. Anderson, Physics Nobel laureate of year 1977, reminiscensed in 1970 [15], that having Josephson as student in his solid-state lectures was

a very disconcerting experience. Everything he said had to be right or Josephson would meet him after class and politely explain in detail what was wrong and how the correct way would be. Josephson then showed Anderson his calculations on the tunneling supercurrent within a day or two after first making them, as he seemed dubious about the results. Anderson wrote that at that time he already knew Josephson very well, and would have accepted anything else Josephson said on faith, but seeing his doubting, he spent an evening checking some details of the derivation of Eqn (1) above. During the next few weeks, Anderson and Brian Pippard (Josephson's dissertation adviser) kept discussing it with Josephson, all three agreeing with the equations, but very much puzzled by the meaning of the result, that the current depends on the phase difference of the two superconductor wave functions. So it was decided not to send the paper to the very competitive Physical Review Letters, but to the newly established Physics Letters (Vol.1 page 251), with Josephson as sole author, as actually he had done all the detailed calculations himself. And it was this publication that in 1973 won Josephson his Nobel Prize, together with Leo Esaki (Japan) and Ivar Giaever (USA), all three not yet reaching the status of physics professor at that time!

Anderson himself [11] went on becoming theoretical physics professor at Cambridge in 1967, and after doing Nobel Prize level work on magnetic and disordered systems and discovering the concept of localized states caused by disorder, he became interested in the philosophy of science, and highly-cited due to his article of 1972 called "More is Different" in which he emphasized the limitations of reductionism and the existence of hierarchical levels of science, each of which requires its own fundamental principles for advancement (usually known as 'emergent phenomena').

IV. The Alternating Current (AC) Josephson Effect

The second Josephson equation shows how a voltage across the insulating film relates to the rate of change of that phase difference:

$$\Delta V = (1/2\pi)\ (h/2\ e)\ \partial(\varphi_1 - \varphi_2)/\partial t. \quad (2)$$

This relation actually is just an Einstein equation [15], relating the energy of a Cooper pair, $2\ e\ \Delta V$, with a frequency $(h/2\pi)\ \partial(\varphi_1 - \varphi_2)/\partial t$! If a constant electric potential difference is applied to the junction, the phase difference will increase in time,

$$\varphi_1 - \varphi_2 = \Delta V\ 2\pi\ (2\ e/h)\ t. \quad (3)$$

Looking at the first Josephson equation, this means that the supercurrent (as long as the potential difference is smaller than the superconducting energy gap mentioned above) will oscillate with angular frequency

$$f = \Delta V\ (2\ e/h) \quad (4)$$

producing the Alternating Current Josephson Effect. This means that the junction will behave as a (microwave) radiator: The Josephson Effect behaves as a voltage-frequency converter, which is quite useful if the power could be enhanced, as a terahertz microwave radiator. Such radiators are starting to displace X-ray security equipment in airports, as they are non-ionizing radiation.

An interesting note is, when Eqn 4 is written as

$$(h/2\ e)\ f \equiv \Phi_o f = \Delta V. \quad (5)$$

The factor in front of the frequency is recognized as the so-called 'magnetic flux quantum' Φ_o [16] which is the smallest size of magnetic flux, 2.067 833 758 (46) femtoweber (femto, f = 10^{-15}; a recommended S.I. prefix). This quantity appears in the discussion of the Integer Quantum Hall Effect [3] and in an important application of the Josephson Effect, namely the SQUID (Superconducting Quantum Interference Device), a very sensitive magnetometer able to measure attotesla (atto, a = 10^{-18}) magnetic fields, much in use today [17].

Then it turned out [15, 18] that the inverse would also happen: when microwave radiation of frequency f_{ext} is shone on the junction, a DC voltage difference would appear across the junction, proportional to the radiating frequency:

$$\Delta V = (h/2\ e)\ f = \Phi_o f \equiv (1/K_J)\ f, \quad (6)$$

with the proportionality constant depending only on two fundamental natural constants, the electronic charge e and Planck's constant h. The inverse of the proportionality constant was then called Josephson's constant

$$K_{\{J\text{-}90\}} = 2e/h = 1/\Phi_o \quad = 0.483\ 597\ 9\ \text{GHz}/\mu\text{V} \quad (7).$$

The '90' indicates that the value was fixed in year 1990, in this case recommended by the CIPM (International Committee for Weights and Measures) in Sèvres, near Paris. The 18 members of the CIPM are entrusted with deciding on S.I. matters, besides submitting proposals to the CGPM (General Conference on Weights and Measures). So since 1990 the volt was fixed through the values of e and h.

Usually, a microwave frequency of ~80 GHz is used, producing a potential difference of ~124 microvolts. To get a reasonably convenient magnitude of potential difference, a series of ~10 000 Josephson junctions are fabricated, measuring a few millimeters across, so as to be able to be irradiated uniformly, resulting in a convenient voltage of 1,24 volt. Alternatively, various numbers of junctions could be made, to produce exactly constant standards of millivolts, to tens of volts.

The constancy of the microwave frequency was not difficult to control, using the existing standard and definition for the time second, or inverse hertz, up to 7 significant digits. Since year 1967/1968, the time second has been defined based on a transition between two hyperfine levels of the ground state of the Caesium-133 atom at 0 kelvin [19] using 10 significant digits: 1 second = 9.192 631 770 periods of that microwave transition.

Nowadays, various standards have been developed, for alternating voltages at various frequencies, but this will not be discussed as it is more technological than conceptual.

It also can be noted that Josephson was already aware [12, 14, 18] that an external microwave radiation bathing the Josephson junction would cause a DC voltage difference across the junction, and if then some voltage difference be put across the junction, and increased slowly, then on a supercurrent vs applied voltage plot, at definite voltages, resonance-caused, constant voltage 'Shapiro' steps will appear,

$$\Delta V_n = n\,(h/2\,e)\,f_{\text{ext}} = n\,\Phi_o f_{\text{ext}} \quad = n\,(1/K_J) \quad f_{\text{ext}}, \tag{8}$$

which can improve the measurement of h/e, or conversely, as is being proposed for the basic S.I. units, by defining the values of those fundamental constants of nature, the volt standard can be defined up to 7 significant digits.

IV. Conclusion

It has been shown that apparently esoteric science research, like superconductor research at very low temperatures, unexpectedly can produce useful results for technological quantities like voltages. Another conclusion is, that ordinary units like the volt can be related to fundamental natural constants, and so become independent of instrumental problems like temperature, pressure, humidity, etc. This is very important for industry, to be able to produce devices with accurate measurements, reproducible as long as the appropriate laboratories and expertise is present.

It is hoped that this report can contribute to improving awareness of science and the scientific method, for the student and the teacher.

Acknowledgements

Financial support from Parahyangan Catholic University, through its Institution of Research and Community Service (LPPM) to attend and present a paper at the Jogjakarta International Conference on Physics (JIPS) 2012 in UGM, 18-19 September 2012, is acknowledged gratefully.

V. References

1. A. Rusli, "Asal Usul dan Rencana Pengembangan Sistem Internasional (S.I.): Suatu Studi, Prosiding Seminar Nasional Fisika 2011, Pusat Penelitian Fisika-LIPI, Serpong, 12-13 Juli 2011, 774-781, https://edocs.unpar.ac.id/edocs?dn=4ece20af43a75
2. A. Rusli, "Untuk Kesadaran Ilmu dan Ilmiah: Suatu Studi tentang Massa, Usulan Definisi Baru Satuannya, dan Realisasinya", Simposium Fisika Nasional ke 24, ITB, 11 November 2011, https://edocs.unpar.ac.id/edocs?dn=4ece1cfed3d93
3. A. Rusli, "Untuk Kesadaran Ilmu dan Ilmiah: Satuan Hambatan Ohm dan Efek Hall Kuantum", to be published in the Prosiding Simposium Nasional Inovasi Pembelajaran dan Sains 2012, 7-8 June 2012, https://edocs.unpar.ac.id/edocs?dn=50285d5be93fb
4. Alessandro Volta, Wikipedia, http://en.wikipedia.org/wiki/Alessandro_Volta, 8 August 2012.

5. Giuliano Pancaldi, "Volta – Science and Culture in the Age of Enlightment", Princeton University Press, Princeton, 2003.
6. Luigi Galvani, Wikipedia, http://en.wikipedia.org/wiki/Luigi_Galvani, 8 August 2012.
7. Volt standard, Wikipedia, http://en.wikipedia.org/wiki/Volt, 8 August 2012.
8. Clark cell, Wikipedia, http://en.wikipedia.org/wiki/Clark_cell, 8 August 2012.
9. Weston cell, Wikipedia, http://en.wikipedia.org/wiki/Weston_cell, 8 August 2012.
10. Brian David Josephson, Wikipedia, http://en.wikipedia.org/Josephson_Effect, 8 August 2012.
11. Philip Warren Anderson, Wikipedia, http://en.wikipedia.org/wiki/Philip_Warren_Anderson, 10 August 2012.
12. Brian D. Josephson, "The Discovery of Tunneling Supercurrents, Nobel Prize Lecture, 12 December 1973, http://nobelprize/physics/1973, 10 August 2012.
13. Terry P. Orlando & Kevin A Delin, "Foundations of Applied Superconductivity", Addison-Wesley, Reading, Massachusetts, 1991.
14. Paul A. Warburton, "The Josephson Effect: 50 Years of Science and Technology", Physics Education **46** (6) 669-675.
15. Philip W Anderson, "How Josephson discovered his effect", Physics Today (11), November 1970, 23-29.
16. Magnetic Flux Quantum, Wikipedia, http://en.wikipedia.org/wiki/Magnetic_flux_quantum, 10 August 2012.
17. SQUID, Wikipedia, http://en.wikipedia.org/wiki/SQUID, 10 August 2012.
18. Johannes Kohlmann & Ralf Behr, "Development of Josephson Voltage Standards", in "Superconductivity – Theory and Applications, Adir Moysés Luiz (Ed.), 239-260, ISBN 978-953-307-151-0, InTech, available from: http://www.intechopen.com/books/superconductivity-theory-and-applications/development-of-josephson-voltage-standards, 2011.
19. BIPM, Definition of the time second, http://www.bipm.org/en/CGPM/db/13/1/, 10 August 2012.

The Application of Earth and Space Science Lectures Model that Integrated with Multiple Intelligences to Mastery Improvement of Cohesive Earth and Space Science for University Student as a Candidate Earth and Space Science Teacher

W. Liliawati[1*], N. Rustaman[2], D. Herdiwijaya[3], D. Rusdiana[2]

1 Department of Physics Education, Faculty of Mathematics and Natural Sciences Education, Indonesia University of Education, Setiabudhi No 229 Bandung 40154

2 Department of Science Education, Graduate School, Indonesia University of Education, Setiabudhi No 229 Bandung 40154

3 Department of Astronomy, Faculty of Mathematics and Natural Sciences, Institute Technology Bandung, Ganesha No 10 Bandung 40132

Abstract

Earth and Space Science (ESS) is an integrated knowledge from different disciplines such as physics, mathematics, astronomy, meteorology, oceanography, geography, geology and other sciences that studies celestial bodies and natural phenomena in daily life. Through the ESS, students are able to describe natural phenomena and the relationship with its aftermath. However, up till now the ESS study is as if separate the earth and space material. It can be seen from the KTSP curriculum of junior high school in which the ESS is given in two different subjects. Earth learned in social studies and space learned in science studies. Similarly, one of colleges is separating earth and science material in ESS lectures. Moreover students assume that the ESS materials are only memorizing and improving some of multiple intelligences. Therefore we need a lecture model that able to improve the integrated ESS ability by developing a variety of multiple intelligences. This research method is using quasi experiment with 25 students. Lecture theme consists of three themes, namely the celestial body motion, the earth as a planet, and the stars dynamics. Based on the test results of integrated ESS obtained that enhancement to the three themes are included in the medium category. Each has increased the normalized gain value 0.42, 0.44, and 0.42. These results are proves that the designed model can improve the concept mastery of integrated ESS.

.

Keywords : *ESS, multiple intelligences, the concepts mastery*

* Corresponding author.

E-mail address: winny_liliawati@yahoo.co.id

I. Introduction

Earth and Space Sciences (ESS) is an integrated knowledge from different disciplines such as physics, mathematics, astronomy, meteorology, oceanography, geography, geology and other sciences that studies celestial bodies, and the integration of natural phenomena in daily life (Barstow et al., 2002). There is a correlation between the earth and space material with other disciplines that integrated in the study of natural phenomena. Through the ESS, students and university students are able to describe natural phenomena and the relationship with its aftermath. So hopefully they are sensitive with natural phenomena and their impact in daily life. Natural phenomenon and its impact is one unity can't be seperated. Students will be complete, more meaningful, and contextual in concepts understanding. For example, the season differences in many countries. Why did it happen? How to explain the season differences? What about the impact of season differences in a country? Students not only can explain the earth revolution, as well as things related to the impacts that more contextual.

However, up till now ESS study is as if separate the earth and space material. It can be seen on pre-service in the secondary high school curriculum, separation of the ESS material through Natural Science and Social Sciences as well as the material is given in different order, class VII for social sciences and class IX for natural science. Earth learned in social studies and space in science studies. Similarly, one of colleges is separating earth and science material in ESS lectures. Integrated ESS is expected to connected the separation of ESS material between the science and social studies. Student and university students (teachers candidate) assume that the ESS is memorizing and developing some of multiple intelligences. Therefore we need a course model that able to improve the integrated ESS ability by

developing a variety of multiple intelligences. Intelligence is not only language, but also can be seen from kinetic, musical, visual-spatial, interpersonal, intrapersonal, and naturalist aspect. This intelligence types are known as multiple intelligences that classified by Howard Gardner (Gardner, 1983).

Logical-mathematical intelligence indicates a person ability to think inductively and deductively, to think with logical rules, to understand and analyze numbers patterns, and to solve problems with thinking skills. For example, Kepler laws that applied to determine the distance and period of celestial bodies. Linguistic intelligence is shown by the sense of meaning, the word order, and the ability to use language diversely to express and to interpret the complex meaning. For example the ability to describe events such as the occurrence of solar eclipse, the changes of day and night, etc. Musical intelligence indicates a person ability to be sensitive to nonverbal sounds. For example the motion of sky object around the sun in elliptical trajectory periodicly. Visual-spatial intelligence indicates a person ability to understand deeply about relationship between object and space. The ability to imagine a real form then solves the problems. An example student can can distinguish the total solar eclipse and the sun ring eclipse. Kinesthetic intelligence allows the connection between mind and body to succeed in the activity. Kinesthetic intelligence indicates a person ability to actively use the parts or the whole body to communicate and solve problems. For example role plays to explain the planets motion around the sun, the rotation and revolution of earth-moon. Interpersonal intelligence indicates a person ability to be sensitive with own feeling. They tend to understand and interact with others to socialize with environment easily. For example work group experiment to understand sun watch, rainfall, and to determine wind direction. Intrapersonal intelligence indicates person ability to sensitive with own feelings. He tends to recognize his strengths and weaknesses with self-assessment. Naturalist intelligence is the ability to recognize, differentiate, express, and create categories in nature and environment. Naturalist intelligence indicates person ability to be sensitive with natural environment. For example, by applying the concept in daily life, such as when solar eclipse happened students do not see the sun directly, observed changes in moon phases, stars brightness, and the sun movement.

The Standards for Science Teacher Preparation (NSTA, 2003:8) recommended that science teachers of basic education (elementary and junior high schools) have interdisciplinary tendency in science. In addition to demands Unit Level Education Curriculum (Depdiknas, 2006) emphasizes to science, environment, technology, and society learning that integrately with learning experience. Based on these two demands, the need of learning that emphasizes unifying concept and processes. In material terms, there is emphasis material that adapted with common phenomena in Indonesia such as earthquake, tsunami, sighting moon, sun and stars, climate, and storms, so Indonesia students are literate with ESS and its impact wherever they live.

II. **Method**

Research method in this study was quasi-experimental methods. The study design used one group pretest-posttest design. This design is pretest and posttest that implemented in one group without comparison group. The research was conducted during a semester with three major themes, namely the motion of celestial bodies, the earth as a planet, and the dynamics of stars. For the celestial body motion theme is done in six meetings, four meetings to the Earth as a planet theme and 4 meeting to the stars dynamics theme. Population is students that attending in ESS course from even semester of academic year 2011/2012 with 25 students, consisting of 13 females and 12 males. ESS course is compulsory subjects in second semester for students and selection course in the third semester for non-education students. Implementation placed at the Department of Physics Education, FPMIPA UPI.

The instrument used to measure the concept mastery of Integrated ESS with multiple-choice test, consist of 35 questions to the motion of celestial bodies theme, 35 questions to the Earth as a planet theme, and 30 questions to the motion dynamics theme. These questions previously have tested the validity and reliability, with reliability values 0.74, 0.54, and 0.54 in the medium category. Questions cover a variety of disciplines, namely physics, astronomy, biology, chemistry, geography, oceanography, health, environment, etc. To find the improvement in mastery concept of integrated ESS by measuring the normalized gain value with Hake category (Hake, 1998). N-gain calculation aims to avoid errors in interpreting the gain acquisition from a student.

III. Results and Discussion

The course model of this research is Integrated ESS based multiple intelligences with Creative and Productive learning model that has a syntax-oriented exploration-confirmation-re-creations (Kemendikbud, 2011). This study was started to find the problems based on facts or evidence from natural phenomenon, then explored used varied sources, discussion, and re-creation by students in the network diagram themes and papers that contain material report.

Based on the pretest and posttest results for each theme obtained the results as in Table 1. The maximum score to each theme is 35 for the motion of celestial bodies, earth and other planets theme, and 30 for the motion dynamics theme.

Table 1 Recapitulation of Normalized Gain Improvement of Mastery Concept with Integrated ESS to Each Theme

Theme	Average of *Pretest* Score	Average of *Posttest* Score	N-Gain <g>	Category
Motion of Celestial Bodies	6,00	18,16	0,42	Middle
Earth and Planets	14,28	23,40	0,44	Middle
Motion Dynamics	6,88	16,48	0,42	Middle

Based on Table 1, shown that the concepts mastery was increased that measured through normalized gain <g>, it can be said to increase after the applied model of lecture-based Integrated IPBA the medium category of multiple intelligences. The average pretest score for motion of celestial bodies theme is the lowest, because this material is quite difficult to understand and hard to visualize the motion of celestial bodies in the high school (junior and senior high school). However, through Integrated ESS based on multiple intelligences model, there was a significant improvement with 18 average posttest score. In contrast to the Earth and planets theme, students have good initial conception with 14 average pretest score. The Earth and planets theme get a large time portion to learn in the high school. ESS material in high school more focus on earth and solar system material. So the star theme, the initial conception of students was minimal because his material is not given in junior and senior high school.

Questions given for each theme distributed from various disciplines. The following chart states the distribution of student concepts mastery based on the number of students who answered correctly for each discipline in every theme.

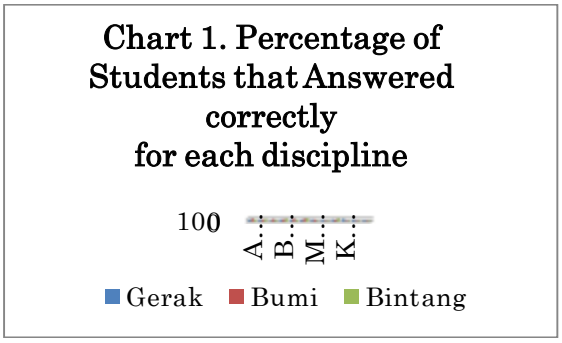

Questions on the motion of celestial bodies theme, the average of all disciplines is below 60% of students who answered correctly except in the health field. The difficult material is related to mathematics, safety and technology. The low math ability affects to the low concepts mastery. Students still do not understand the material as a whole, it is seen from the impact that caused of natural phenomena related to the safety aspect is still low. The Earth as a planet theme has a better acquisition than other themes. Because students are more familiar with this theme and the phenomenon that occurs. But the impact of phenomenon is still low, it is seen from environmental aspect that has the lowest value. The stars dynamics theme has the lowest in the chemistry field that related to stars chemical reactions. However, the aspects relating to the safety impact is very low.

IV. Conclusion

Based on the results and discussion shows that the Integrated ESS with multiple intelligences model can improve the ESS concepts mastery for each theme with normalized gain values 0.42, 0.44, and 0.42. This improvement was included in the medium category. Students are still have trouble to connecting theme with its aftermath, such as safety and environmental aspects. Besides the supporting concepts in other scientific fields is low, such as chemistry and mathematics.

Research suggestion is as an input to design ESS learning material in junior high school. ESS is not stands alone material but integrated with other subjects. So students can get

meaningful knowledge. ESS course is not only memorizing or abstract but contextual material.

V. References

1. Barstow, Daniel and Geary, Ed. (2002). *Revolution in Earth and Space Science Education*. //www.EarthScienceEdRevolution.org
2. Depdiknas. (2006). *Kurikulum Tingkat Satuan Pendidikan SD, SMP dan SMA*
3. Gardner, H. (1983). *Frames of Mind: The Theory of Multiple Intelligences,* New York: Basic Books. The second edition was published in Britain by Fontana Press. 466 + xxix pages.
4. Hake. (*1998). Chapter IV Result* (The *Hake* Factor), (Online). Tersedia: dwb4.unl.edu/Diss/Royuk_Diss_04.pdf (15 Juni 2011)
5. Kemendikbud. (2011). *Peningkatan Kuallitas Pembelajaran*. Kementerian Pendidikan dan Kebudayaan, Direktorat Jenderal Pendidikan Tinggi, Direktorat Pendidik dan Tenaga Kependidikan
6. Liliawati, W dan Ramlan, T. (2010). *Identifikasi Miskonsepsi Materi IPBA bagi Siswa, Guru SMP dan Mahasiswa Calon Guru dalam Upaya Perbaikan dan Pengembangan Program Pembelajaran*. Proceeding Seminar Nasional Penelitian, Pendidikan dan penerapan MIPA, 15 Mei 2010 FMIPA UNY.
7. National Science Teachers Association. 2003. *Standards for Science Teacher Preparation*. http://www.nsta.org/pdfs/NSTAstandards2003.pdf
8. Rustaman, N.Y. (2011). *Pendidikan dan Penelitian Sains dalam Mengembangkan Keterampilan Berpikir Tingkat Tinggi untuk Pembangunan Karakter*. Makalah Utama dipresentasikan dalam Seminar Nasional di Universitas Negeri Surakarta Tanggal 16 Juni 2011 di Solo

DEVELOPING PHYSICS' LECTURING MATERIALS SUPPORTING THE COMPETENCE OF CHEMICAL ENGINEERING – POLBAN'S GRADUATES

I Gede Rasagama[1], Kunlestiowati Hadiningrum[2], Mukhtar Ghozali[3], and Farida Agoes[4]

[1,2,3,4]Politeknik Negri Bandung, INDONESIA

Email: igesagama@polban.ac.id

ABSTRACT

The aim of this research was to know physics materials for lecture which support the competence of D3-Chemical Engineering Study Program, D4-Chemical Engineering-Clean Production Study Program, and D3-Chemical Analyst Study Program in Chemical Engineering Department – Politeknik Negeri Bandung (POLBAN). The subjects of this research consisted of 3 experts in chemical engineering for vocational education and 33 lecturers of Chemical Engineering Department POLBAN. The method used in this research was developing physics materials through experts' validation test and the investigation of stakeholders' views. Expert' validation test was a validation done to a design of lecturing materials from the result of analysis on a number of aspects or documents. Investigation test on the stakeholder's view had the purpose of knowing the stakeholder's views (chemical engineering lecturers) into the design of lecturing materials as the result of expert's validation test. Based on the result of investigation on stakeholders' views, a final product as Physics lecturing program materials could be formulated. The result showed that Physics lecturing program materials for D3-Chemical Engineering Study Program and D4- Chemical Engineering-Clean Production Study Program consist of 8 competences, 8 topics of discussion, 25 sub-topics of discussions, and 4 lecturing aims; and for D3-Chemical Analyst Study Program, they comprises of 8 competences, 8 topics of discussion, 29 sub-topics of discussions and 4 lecturing aims.

Keywords: graduate's competence, chemical engineering department, physics lecturing materials.

INTRODUCTION

Physics, as a branch of science, is the base for mastering various fields of technology, such as information technology, electronics and communication. As the pioneer of the modern knowledge, physics is the result of integration between deductive-inductive analysis relying on empirical observation support based on five senses as the principle validity being developed. As the leader, physics is the base of other knowledge such as chemistry and biology. Physics is also the leader of the knowledge of geography, geology, meteorology, astronomy, oceanography, etc. On the other hand, based on

physics, student's competence can be developed for the need of job. Physics has a great contribution on the development of science and technology and the student's competence.

The competence of Chemical Engineering –PolBan's students is the graduate's ability in improving the value of basic commodity of production, which can be directly obtained from nature. In order to get that ability, students need a variation and special subjects in their lectures. The physics' lecturing program (PLP) as one of subject delivered to the students of Chemical Engineering – PolBan, should be essential and functional in order to be able to raise the graduate's competence. On the other hand, physics is the wide subject and as the result there will be so many competence produced. Not all subject of physics has an effective result and is in accordance with producing the graduate's competence. That is why, the subject of physics should be selected appropriately and should be able to result on the competence which supports the competence of study program's graduates. This is in compliance with Fratt's view (2002) who said that the topic of studying science, including physics is too wide but not deep (a mile wide and an inch deep). Applying the concept of "Less is More", it is necessary for us to reduce the topic based on the research activity.

To obtain the material for lecture as the qualified education product, the activity of development after designing should be executed. Sukmadinata (2006) viewed that the development of education product design was an important step to do due to the product design would have an impact on the knowledge, skill, and attitude of the students before they go to the society. The development should involve the competent persons in their fields and the ones having interest in order to be able to achieve the maximal level of the products' benefit. In this article, the development of one of education product designs having an important role to support establishing the competence of study program-Politeknik's graduate will be discussed.

METHOD OF RESEARCH

Method of research is the development of the lecturing material design through the activity of validation by experts and the investigation of stakeholder's opinions. Validation of the experts is the evaluation done by experts for the consistency of all analysis of physics lecturing program materials design including: the foundation of development, characteristic of physics' materials, analysis result of the graduate's competence meanings; material and concept of functional physics; the result of analysis on syllabus for the advance subject used in study program; physics competence as the result of analysis on functional physics competence; and the aim of lecture as the result of an analysis on physics competence.

The process of validation involves 3 experts on vocational educations, i.e. Prof.Dr. Liliasari, M.Pd – lecturer of SPs IPA (Natural Science) study program – UPI - Bandung. ; Drs. Haryadi, M.Sc.Ph.D – lecturer of Chemical Engineering-PolBan; and Ir. Herawati Budiastuti, M.Eng.SC, Ph.D – lecturer of Chemical Engineering Department. The investigation of stakeholders' view in the collecting of opinions of the Chemical Engineering department's lecturers on the design of lecturing materials,and the result of the experts' validation. In collecting opinions, 14 lecturers of D3-Chemical Engineering study program, 12 lecturers of D4 –Chemical Engineering-Clean Production, and 7 lecturers of D3 –Chemical Analyst of PolBan were involved. Based on the result analysis of the investigation on stakeholders' view, a formulation of the material for physics' lecture as the result of research could be taken.

FINDINGS AND DISCUSSION

Pre-research of "Designing the material for physics lecture which can support the competence of chemical engineering department_PolBan's graduates shows that the component of materials for Physics lecture for 3 study programs of Chemical engineering were: (i) 4 aims of lecture, 16 competence, 16 topics of discussions and 54 sub-topics of discussions of Physics for D3-Chemical Engineering study program as well as D4- Chemical Engineering-Clean Production; (ii) 4 aims of lecture, 9 competences, 9 main topics of discussions, and 32 sub-topics of discussions of physics for D3 Chemical Analyst study program. The development, got from expert validation and investigation of the stakeholders' views, is hoped will be resulted on "The Material of Physics subject which is able to support the competence of Chemical Engineering department –PolBan's graduates.

Design of analysis result validated includes: (i) the foundation of developing materials of lecturing program, i.e.: philosophical, psychological, sociological, scientific-1/Fratt's view and scientific -2 / Reif's view; (ii) the meaning of graduates' competence and the characteristics of materials of physics supporting graduate's competence; (iii)materials and concept of functional physics for advance subject in study program; (iv) the competence of physics; (v) main topic of discussion and the sub-topic, and (vi) the aim of lecture. All of these documents were a range of result analysis to get the design materials for lectures. Its findings and discussions will be explained respectively as follows:

For the first design, the three experts viewed that the result of analysis for every development foundation of the material for lecture has been included into the criteria of 'Correct' for the Scope of designed Concept (SC) and 'Correct' (C) for the Correct Concept (CC) as shown in Table 1. The experts suggested that the foundation of psychological and sociological should be made perfect which is accommodated through revising the related parts.

Table 1. Result of Experts' Evaluation on the Foundation of Developing Materials for Physics Lecturing Program in Chemical Engineering Department.

Foundation of Development	Expert1: LS		Expert2: HY		Expert3: HB		Miscelenous
	SC	CC	SC	CC	SC	CC	
1. Phylosophical foundation	C	C	C	C	C	C	
2. Psychological foundation	C	C	C	C	C	C	LS: More explanation is needed; HB: Year of Jean Peaget's reference
3. Sociological foundation	C	C	C	C	C	C	LS: More explanation is needed;
5. Scientific-2 foundation	C	C	C	C	C	C	
4. Scientific-1 foundation	C	C	C	C	C	C	

Comment:

HB: criteria of age (11 up) is , psychologically,not forj Junior High School students learningPhysics. Mention other reference s

.

Table 2. The Result of Evaluation for the Meaning oh Competence of Study Program's Graduate and the Characteristics of Physics Lecturing Program in Chemical Engineering Department.

Study Program	Competence of Graduate	Meanings						Characteristics of Materials						Miscelenous
		Exp. 1: LS		Exp. 2: HY		Exp.3: HB		Exp. 1: LS		Exp. 2: HY		Exp.3: HB		
		SC	CC	SC	CC	SC	CC	SC	CC	SC	CC	SC	CC	
D3-Chemical Engineering	1. Able to operate main tools and supporting tools in Industrial Process	C	C	C	C	C	C	C	C	C	C	C	C	

	2. Able to maintain and repair tools in Industrial Process	C	C	C	C	C	C	C	C	C	C	C	C
	3. Evaluate the work of Production Process	C	C	C	C	C	C	C	C	C	C	C	C
	4. Understand the System of Industrial Job Safety	C	C	C	C	C	C	C	C	C	C	C	C
	5. Able to Operate Industrial Waste Processing Unit	C	C	C	C	C	C	C	C	C	C	C	C
	6. Able to di business in his / her Field	C	C	C	C	C	C	C	C	C	C	C	W
	Comment:												
	The description of the meaning of graduate's competence should refers to chemical engineering' reference in order to get more formal description.												
	Competence no.6 was not in accordance with the cocncept correctness. Not all physics materials must answer all the expected graduate's competence												
D4-Chemical Engineering-Clean Production	1. Able to operate and maintain the processing equipment in industry well and correctly	C	C	C	C	C	C	C	C	C	C	C	C
	2.Able to evaluate and analyze the work of processing equipment of technical, economical,and environmental aspects	C	C	C	C	C	C	C	C	C	C	C	C
	3. Able to improve the efficency of production using the technical principle of clean production	C	C	C	C	C	C	C	C	C	C	C	C
	4.Able to design the system of production and the system of handling waste.	C	C	C	C	C	C	C	C	C	C	C	C
	5.Able to do managerial supervision and can communicate in Indonesian and English well	C	C	C	C	C	C	C	C	C	C	C	C
	Comment:												
	HB The description of the meaning of graduate's competence should refers to chemical engineering' reference to get more formal description.												
D3-Chemical Analyst	1. Able to do Good Laboratory Practice (GLP) and Good Measurement Practice (GMP)	C	C	C	C	C	C	C	C	C	C	C	C

2. Able to do both conventional chemical anlysis and modern chemical analysis (using instruments)	C	C	C	C	C	C	C	C	C	C	C	C
3. Able to work folowing SOP and considering safety (Health and Safety Safety - HSE) in laboratory of work place.	C	C	C	C	C	C	C	C	C	C	C	C
4. Able to prepare any kind of sample (solid, fluid, gas matters) and determine its methode of analysis.	C	C	C	C	C	C	C	C	C	C	C	C
5. Able to do validation on the method of test.	C	C	C	C	C	C	C	C	C	C	C	C
6. Able to communicate effectively both oral and has a good leadership.	C	C	C	C	C	C	C	C	C	C	C	C
7.Innovative and has a business knowledge	C	C	C	C	C	C	C	C	C	C	C	C

Comment:

LS: being innovative and having a good business knowledge are 2 different things. Being innovative in concept is good, but having a good knowledge on business is special or there should be specific levels or standards.

HB The description of the meaning of graduate's competence should refers to chemical engineering' reference to get more formal description.

Competence no.6 was not in accordance with the cocncept correctness. Not all physics materials must answer all the expected graduate's competence

For the third design, the three experts viewed that the result of analysis of functional physics materials and concepts in advance subject in study program have included into the criteria of 'Correct' for the scope of concept which is defined and 'Correct' for the correctness of the concept , as shown in Table 3. Expert 1: LS (Prof. Dr.Liliasari M.Pd) suggested that to differentiate materials and concepts of functional physics for D4 Chemical Engineering-Clean Production study program and D3-Chemical Engineering could not be accommodated considering that the two study programs were linear and they were different in the level of diploma only. In other word, D4-Chemical Engineering-Clean Production study program was the advance level of D3 –Chemical Engineering Study Program. For disparity of the 2 study programs was only able to do at the level of IQ which could be developed in executing the lecturing strategy.

Table 3: The Result of Evaluation for Materials and Concepts of Functional Physics in Advance Subject in Chemical Engineering Department.

Advance Subject of Study Program	Expert 1: LS		Expert 2: HY		Expert 3: HB		Suggestions
	SC	CC	SC	CC	SC	CC	
1. Chemical Physics	C	C	C	C	C	C	
2. Thermodynamics	C	C	C	C	C	C	
3. Analytic Instrumentation	C	C	C	C	C	C	
4. Instrumentation and Measurement	C	C	C	C	C	C	
5. Knowledge of Materials	C	C	C	C	C	C	HB: Is the elasticity included into the modul provided?
6. Balance of Energy	C	C	C	C	C	C	
7. Fluids Transportations	C	C	C	C	C	C	
8. Heat Transfer	C	C	C	C	C	C	HB: Are properties and kinds of materials for heat transfer included ?
Comment: None	C	C	C	C	C	C	
1. Chemical Physics	C	C	C	C	C	C	
2. Thermodynamics	C	C	C	C	C	C	
3. Analytic Instrumentation	C	C	C	C	C	C	
4. Chemical Physics	C	C	C	C	C	C	
5. Knowledge of Materials	C	C	C	C	C	C	
6. Balance of Energy	C	C	C	C	C	C	
7. Fluids Transportations	C	C	C	C	C	C	
8. Heat Transfer	C	C	C	C	C	C	HB: Are properties and kinds of materials for heat transfer included ?

Comment:

LS: Material and concept of physics are essential for the need for Chemical Engineering-Clean Production should have different specification than Chemicl Engineering.

1. Chemical Physics	C	C	C	C	C	C
2. Instrumentation and Measurement	C	C	C	C	C	C
3. Spectophotometry	C	C	C	C	C	C

Comment: None

For the forth design, the three experts viewed that the result of physics competence analysis for each study program has been included into the criteria of 'Correct' both for the scope of concept defined and the correctness of concept, as shown in Table 4. For suggestion from expert 1:LS (Prof.Dr.Liliasari,M.Pd) in order to have a specification for the need of physics competence for the students of D4-Chemical Engineering-Clean Production compared to D3-Chemical Engineering was not able to be accommodated for the reason as has been mentioned before, i.e. the two study programs were linear and different only at the level of diploma, so its disparity was only able to do at the level of thinking ability (IQ) which developed in lecturing strategy execution.

Table 4: The Result of Physics Competence on chemical Engineering Department's Physics Lecturing Program

Study Program	Physics Competence			Expert 2: BY		Expert 3: HB		Suggestion
		SC	**CC**	**SC**	**CC**	**SC**	**CC**	
D3 Chemical Engineering	1. Mastering physics's unit in IU (International unit), its measurement and its undefiniteness.	**C**	**C**	**C**	**C**	**C**	**C**	-

2. Applying the method of basic calculus	C	C	C	C	C	C	-
3. Mastering the kinematic concept of straight movement and rotated movement	C	C	C	C	C	C	-
4. Mastering the dynamic concept of straight movement and rotated movement	C	C	C	C	C	C	-
5. Mastering the teorema of impuls-momentum	C	C	C	C	C	C	-
6.Mastering teorama of energy power	C	C	C	C	C	C	-
7.Mastering the concept of rotation movement of rigid object	C	C	C	C	C	C	-
8. Mastering the concept of fluids	C	C	C	C	C	C	-
9. Mastering the concept of vibration	C	C	C	C	C	C	-
10. Mastering the concept of sound wave	C	C	C	C	C	C	-
i11. Mastering the concept of electromagnetic wave	C	C	C	C	C	C	-
12. Mastering the concept of temperature and heat	C	C	C	C	C	C	-
13. Mastering the kinetic of gas theory	C	C	C	C	C	C	-
14. Applying the law of thermodynamic	C	C	C	C	C	C	-
15. Mastering the concept of electricity	C	C	C	C	C	C	-
16. Mastering the concept of physical optic	C	C	C	C	C	C	-
Comment: HB: The competence applying specific concept can only be found in basic calculus method (1.2) and the law of thermodynamic							

D4 Chemical Engineering - Clean Production

(6.3). is the component got from laboratory work included into PLP material?							
1. Mastering physics's unit in IU (International unit), its measurement and its undefiniteness	C	C	C	C	C	C	-
2. Applying the method of basic calculus	C	C	C	C	C	C	-
3. Mastering the kinematic concept of straight movement and rotated movement	C	C	C	C	C	C	-
4. Mastering the dynamic concept of straight movement and rotated movement	C	C	C	C	C	C	-
5. Mastering the teorema of impulse - momentum	C	C	C	C	C	C	-
6.Mastering teorama of energy power	C	C	C	C	C	C	-
7.Mastering the concept of rotation movement of rigid object	C	C	C	C	C	C	-
8. Mastering the concept of fluids	C	C	C	C	C	C	-
9. Mastering the concept of vibration	C	C	C	C	C	C	-
10. Mastering the concept of sound wave	C	C	C	C	C	C	-
11. Mastering the concept of electromagnetic wave	C	C	C	C	C	C	-
12. Mastering the concept of temperature and heat	C	C	C	C	C	C	-
13. Mastering the kinetic of gas theory	C	C	C	C	C	C	-
14. Applying the law of thermodynamic	C	C	C	C	C	C	-
15. Mastering the concept of electricity	C	C	C	C	C	C	-
16. Mastering the concept of physical	C	C	C	C	C	C	-

	optic							
	Comment: LS: What is the more specific need of Chemical Engineering- Clean Production (CECP)compared to Chemical Engineering (CE) study program? HB: The competence applying specific concept can only be found in basic calculus method (1.2) and the law of thermodynamic (6.3) Is the competence got from laboratory work included into PLP material?							
D3 Chemical Analyst	1. Mastering physics's unit in IU (International unit), its measurement and its undefiniteness	C	C	C	C	C	C	-
	2. Applying the method of basic calculus	C	C	C	C	C	C	-
	3. Mastering the concept of static fluids	C	C	C	C	C	C	-
	4. Mastering the concept of temperature and heat	C	C	C	C	C	C	-
	5. Mastering the kinetic of gas theory	C	C	C	C	C	C	-
	6. Applying the law of thermodynamic	C	C	C	C	C	C	-
	7. Mastering the concept of electricity	C	C	C	C	C	C	--
	8.. Mastering the concept of electromagnetic wave	C	C	C	C	C	C	-
	9. Mastering the concept of physical optic	C	C	C	C	C	C	-
	Comment: None							

For the fifth design, expert 2: HY (Drs. Haryadi M.Sc.,Ph.D) and expert 3: HB (IR.Hariati Budiastuti, M.Eng, Sc., Ph.D) viewed that the result of analysis on the main topic and sub-topic of discussion of physics has been included into the category of "Correct" both for the scope of concept which is defined and the correctness of the concept. Expert 1: LS (Prof.Dr. Liliasari, M.PD) viewed that only a part of the analysis result on the main topic and sub-topic of discussion were in "Correct" category both for the scope of concept which is defined and the correctness of the concept.

As has been shown in Tabel 5, expert 1 viewed that some of sub-topics of discussion were not so relevant to its main topic. In her comment, she said clearly that "it's not wrong'. It can be concluded that she was not sure in giving her justification. These expert's opinions were accommodated with keep including the sub-topics of discussion in the related main topics. This is done considering that there were still avance activity, i.e. investigation on the stakeholder views to test the validity of the analysis result executed. JTKP lecturers as one of the stakeholders can be considered as the most important one in giving decision on the most suitable material for the need of study program to produce competent graduate as expected.

Table 5: Result of Evaluation on Main Topic and Sub topic of Discussion on Physics Lecturing Program in Chemical Engineering Department

D3-Chemical Engineering

Main Topic	Sub-Topic of Discussion	Expert 1: LS		Expert 2: HY		Expert 3: HB		Miscelanous
		SC	CC	SC	CC	SC	CC	
1.Unit,Measurement, and Undefiniteness	1,Unit , and Dimension	C	C	C	C	C	C	
	2. Measurement and Undefiniteness	C	C	C	C	C	C	
	3. Important Number	C	C	C	C	C	C	
	4. Source of Mistakes and Calibration Tool	C	C	C	C	C	C	
	5.Processing Data (Graph and smallest quadrate)	C	C	C	C	C	C	
2. Basic Calculus	6. Operation of Vector	C	C	C	C	C	C	
	7. Differential and Integral	C	C	C	C	C	C	
3. Kinematics	8. Straight Movement Equation	C	C	C	C	C	C	
	9. Straight Movement Combination	C	C	C	C	C	C	

	10. Rotation Movement Equation	C	C	C	C	C	C
4. Dynamics	11. Friction Energy	W	W	C	C	C	C
	12. Newton's Law	W	W	C	C	C	C
5. Impulse Movement	13. Impulse and Momentum	W	W	C	C	C	C
	14. Theorem of Impulse - Momentum	W	W	C	C	C	C
	15. Law of Linear Momentum Durability	W	W	C	C	C	C
	16. Collision	W	W	C	C	C	C
6.Energy power	17. Force and Energy	C	C	C	C	C	C
	18. Theorem of Force and Energy	C	C	C	C	C	C
	19. Law of Energy Conservation	C	C	C	C	C	C
7. Rotation of Rigid Objects	20. Equation of Rotation Movement	W	W	C	C	C	C
	21. Energizing Moment, Force Moment, Law of Dynamic Rotation	W	W	C	C	C	C
	22. Law of Angular Momentum Durability	W	W		C	C	C
	23. Law of Energy Conversion	W	W	C	C	C	C
	24. Movement of Revolving	W	W	C	C	C	C
8. Fluids	25. Statical Fluids	C	C	C	C	C	C
	26. Dynamical Fluids	C	C	C	C	C	C
9. Vibration	27. Harmonical Vibration	W	W	C	C	C	C

	28. Muffled Vibration	W	W	C	C	C	C
	29. Forced Vibration	W	W	C		C	C
10. Wave of Sound	30. Wave Sound Equation	W	W	C	C	C	C
	31. Intensity and Level of Intensity of Sound	W	W	C	C	C	C
	32. Interference and Soaring of Sound	W	W	C	C	C	C
	33. Doppler Effect	W	W	C	C	C	C
11. Electromagnetic Wave/GEM	34. Equation of Electromagnetic Wave	C	C	C	C	C	C
	35. Electromagnetic Spectrum	C	C	C	C	C	C
	36.POYNTING Vector, Energy, AND GEM energy	C	C	C	C	C	C
12. Temperature & Heat	37. Temperature and Heat	C	C	C	C	C	C
	38. Black Principle	C	C	C	C	C	C
13. Theory of Gas Kinetic	39. Equation fo Ideal Gas	W	W	C	C	C	C
	40. Pressure, Inner Energy, RMS acceleration	W	W	C	C	C	C
	41. Phase Diagram	W	W	C	C	C	C
14. Law of Thermodynamic	42. Power	W	W	C	C	C	C
	43. thermodynamic Process	W	W	C	C	C	C
	44. Law of Thermodynamic	W	W	C	C	C	C
15. Electricity	45. Current in	W	W	C	C	C	C

	Electrolite solution						
	46. Tension,Obstruction, Energy and Electric Power	W	W	C	C	C	C
	47. Capasitor and Inductor	W	W	C	C	C	C
	48. DC Electric Series	W	W	C	C	C	C
	49. AC Electric Series	W	W	C	C	C	C
16. Optical Physics	50. Light Reflection	W	W	C	C	C	C
	51.Light Refraction	W	W	C	C	C	C
	52. Light Interferential	W	W	C	C	C	C
	53. Defraction ofLight	W	W	C	C	C	C
	54. Light Polarisation	W	W	C	C	C	C

Comment:

LS: It is not a mistake not to take notes on concept but it is not relevant to the topic of discussion

Table 5: Result of Evaluation on Main Topic and Sub topic of Discussion on Physics Lecturing Program in JTKP (attachment 1)

D3- Chemical Engineering- Clean Production

Main Topic	Sub-Topic of Discussion	Expert 1: LS		Expert 2: HY		Expert 3: HB		Miscelanous
		SC	CC	SC	CC	SC	CC	
1.Unit,Measurement, and Undefiniteness	1.,Unit , and Dimension	C	C	C	C	C	C	
	2. Measurement and Undefiniteness	C	C	C	C	C	C	
	3. Important Number	C	C	C	C	C	C	
	4. Source of Mistakes and Calibration Tool	C	C	C	C	C	C	
	5.Processing Data (Graph and smallest quadrate)	C	C	C	C	C	C	
2. Basic Calculus	6. Operation of Vector	C	C	C	C	C	C	
	7. Differential and Integral	C	C	C	C	C	C	
3. Kinematics	8. Straight Movement Equation	C	C	C	C	C	C	
	9. Straight Movement Combination	C	C	C	C	C	C	
	10. Rotation Movement Equation	C	C	C	C	C	C	
4. Dynamics	11. Friction Energy	W	W	C	C	C	C	
	12. Newton's Law	W	W	C	C	C	C	
5. Impulse Movement	13. Impulse and Momentum	W	W	C	C	C	C	

	14. Theorem of Impulse - Momentum	W	W	C	C	C	C
	15. Law of Linear Momentum Durability	W	W	C	C	C	C
	16. Collision	W	W	C	C	C	C
6.Energy power	17. Force and Energy	C	C	C	C	C	C
	18. Theorem of Force and Energy	C	C	C	C	C	C
	19. Law of Energy Conservation	C	C	C	C	C	C
7. Rotation of Rigid Objects	20. Equation of Rotation Movement	W	W	C	C	C	C
	21. Energizing Moment, Force Moment, Law of Dynamic Rotation	W	W	C	C	C	C
	22. Law og Angular Momentum Durability	W	W		C	C	C
	23. Law of Energy Conversion	W	W	C	C	C	C
	24. Movement of Revolving	W	W	C	C	C	C
8. Fluids	25. Statical Fluids	C	C	C	C	C	C
	26. Dynamical Fluids	C	C	C	C	C	C
9. Vibration	27. Harmonical Vibration	W	W	C	C	C	C
	28. Muffled Vibration	W	W	C	C	C	C
	29. Forced Vibration	W	W	C		C	C

10. Wave of Sound	30. Wave Sound Equation	W	W	C	C	C	C
	31. Intensity and Level of Intensity of Sound	W	W	C	C	C	C
	32. Interference and Soaring of Sound	W	W	C	C	C	C
	33. Doppler Effect	W	W	C	C	C	C
11. Electromagnetic Wave ?GEM	34. Equation of Electromagnetic Wave	C	C	C	C	C	C
	35. Electromagnetic Spectrum	C	C	C	C	C	C
	36.POYNTING Vector, Energy, AND GEM energy	C	C	C	C	C	C
12. Temperature & Heat	37. Temperature and Heat	C	C	C	C	C	C
	38. Black Principle	C	C	C	C	C	C
13. Theory of Gas Kinetic	39. Equation fo Ideal Gas	C	C	C	C	C	C
	40. Pressure, Inner Energy, RMS acceleration	C	C	C	C	C	C
	41. Phase Diagram	C	C	C	C	C	C
14. Law of Thermodynamic	42. Power	C	C	C	C	C	C
	43. thermodynamic Process	C	C	C	C	C	C
	44. Law of Thermodynamic	C	C	C	C	C	C
15. Electricity	45. Current in	C	C	C	C	C	C

	Electrolite solution							
	46. Tension,Obstruction, Energy and Electric Power	C	C	C	C	C	C	
	47. Capasitor and Inductor	C	C	C	C	C	C	
	48. DC Electric Series	C	C	C	C	C	C	
	49. AC Electric Series	C	C	C	C	C	C	
16. Optical Physics	50. LightReflection	W	W	C	C	C	C	
	51.LightRefraction	W	W	C	C	C	C	
	52. Light Interferential	W	W	C	C	C	C	
	53. Defraction ofLight	W	W	C	C	C	C	
	54. Light Polarisation	W	W	C	C	C	C	
Comment: LS: It is not a mistake not to take notes on concept but it is not relevant to the topic of discussion								

Table 5: Result of Evaluation on Main Topic and Sub topic of Discussion on Physics Lecturing Program in JTKP (attachment 2)

	Main Topic	Sub-Topic of Discussion	Expert 1: LS		Expert 2: HY		Expert 3: HB		Miscelanous
			SC	CC	SC	CC	SC	CC	
D3- Chemical Engineering-Clean Production	1.Unit,Measurement, and Undefiniteness	1. Unit , and Dimension	C	C	C	C	C	C	
		2. Measurement and	C	C	C	C	C	C	

	Undefiniteness						
	3. Important Number	C	C	C	C	C	C
	4. Source of Mistakes and Calibration Tool	C	C	C	C	C	C
	5.Processing Data (Graph and smallest quadrate)	C	C	C	C	C	C
2. Basic Calculus	6. Operation of Vector	C	C	C	C	C	C
	7. Differential and Integral	C	C	C	C	C	C
3. Kinematics	8. Straight Movement Equation	C	C	C	C	C	C
	9. Straight Movement Combination	C	C	C	C	C	C
	10. Rotation Movement Equation	C	C	C	C	C	C
4. Dynamics	11. Friction Energy	W	W	C	C	C	C
	12. Newton's Law	W	W	C	C	C	C
5. Impulse Movement	13. Impulse and Momentum	W	W	C	C	C	C
	14. Theorem of Impulse - Momentum	W	W	C	C	C	C
	15. Law of Linear Momentum Durability	W	W	C	C	C	C
	16. Collision	W	W	C	C	C	C
6.Energy power	17. Force and Energy	C	C	C	C	C	C

	18. Theorem of Force and Energy	C	C	C	C	C	C
	19. Law of Energy Conservation	C	C	C	C	C	C
7. Rotation of Rigid Objects	20. Equation of Rotation Movement	W	W	C	C	C	C
	21. Energizing Moment, Force Moment, Law of Dynamic Rotation	W	W	C	C	C	C
	22. Law og Angular Momentum Durability	W	W		C	C	C
	23. Law of Energy Conversion	W	W	C	C	C	C
	24. Movement of Revolving	W	W	C	C	C	C
8. Fluids	25. Statical Fluids	C	C	C	C	C	C
	26. Dynamical Fluids	C	C	C	C	C	C
9. Vibration	27. Harmonical Vibration	W	W	C	C	C	C
	28. Muffled Vibration	W	W	C	C	C	C
	29. Forced Vibration	W	W	C		C	C
10. Wave of Sound	30. Wave Sound Equation	W	W	C	C	C	C
	31. Intensity and Level of Intensity of Sound	W	W	C	C	C	C
	32. Interference and Soaring of Sound	W	W	C	C	C	C
	33. Doppler Effect	W	W	C	C	C	C

11. Electromagnetic Wave ?GEM	34. Equation of Electromagnetic Wave	C	C	C	C	C	C
	35. Electromagnetic Spectrum	C	C	C	C	C	C
	36.POYNTING Vector, Energy, AND GEM energy	C	C	C	C	C	C
12. Temperature & Heat	37. Temperature and Heat	C	C	C	C	C	C
	38. Black Principle	C	C	C	C	C	C
13. Theory of Gas Kinetic	39. Equation fo Ideal Gas	C	C	C	C	C	C
	40. Pressure, Inner Energy, RMS acceleration	C	C	C	C	C	C
	41. Phase Diagram	C	C	C	C	C	C
14. Law of Thermodynamic	42. Power	C	C	C	C	C	C
	43. thermodynamic Process	C	C	C	C	C	C
	44. Law of Thermodynamic	C	C	C	C	C	C
15. Electricity	45. Current in Electrolite solution	C	C	C	C	C	C
	46. Tension,Obstruction, Energy and Electric Power	C	C	C	C	C	C
	47. Capasitor and Inductor	C	C	C	C	C	C
	48. DC Electric Series	C	C	C	C	C	C
	49. AC Electric Series	C	C	C	C	C	C

16. Optical Physics	50. LightReflection	W	W	C	C	C	C	
	51.LightRefraction	W	W	C	C	C	C	
	52. Light Interferential	W	W	C	C	C	C	
	53. Defraction ofLight	W	W	C	C	C	C	
	54. Light Polarisation	W	W	C	C	C	C	

Comment:
LS: It is not a mistake not to take notes on concept but it is not relevant to the topic of discussion

Table 5. The Result of Evaluation on Main Topic of Discussion and Sub Topic of Discussion in Physics Lecturing Program in JTKP (attachement-2)

D3- Chemical Analyst

Study Program	Main Topic of Discussion	Sub-Topic of Discussion	Expert 1: LS		Expert 2: HY		Expert 3: HB		Miscelaneous
			SC	CC	SC	CC	SC	CC	
	1. Unit, Measurement, and Uncertainty	1. Unit, and dimension	C	C	C	C	C	C	
		2.Measurement and Uncertainty	C	C	C	C	C	C	
		3. Important Number	C	C	C	C	C	C	
		4. Source of Mistakes & Calibration Tool	C	C	C	C	C	C	
		5. Processing Data (Graph, Smallest Quadrate	C	C	C	C	C	C	
	2. Basic Calculus	6. Operation of Vector	C	C	C	C	C	C	
		7. Diferential & Integral	C	C	C	C	C	C	
	3. Statical Fluids	8. MASSA JENIS and Pressure	C	C	C	C	C	C	
		9.Pascal Law & Archimides Law	C	C	C	C	C	C	
		10. Surface Tension	C	C	C	C	C	C	

	11.Capilarity Symptom	C	C	C	C	C	C
4. Temperature & Heat	12.Temperature & Heat	C	C	C	C	C	C
	13. Black Principle	C	C	C	C	C	C
5. Theory of Gas Kinetic	14.Equation of Ideal Gas Condition	C	C	C	C	C	C
	15. Pressure,Inner Energy, RMS Acceleration	C	C	C	C	C	C
	16. Phase of Diagram	C	C	C	C	C	C
6. Law of Thermodynamics	17. Power	C	C	C	C	C	C
	18. Thermodynamics Process	C	C	C	C	C	C
	19.. Thermodynamics Law	C	C	C	C	C	C
7. Electricity	20. Current in Electrolite Solution	C	C	C	C	C	C
	21. Tension,Obstruction, Energy and Electric Power	C	C	C	C	C	C
	22. Capacitor & Inductor	C	C	C	C	C	C
	23.DC Electric Series	C	C	C	C	C	C
	24.AC Electric Series	C	C	C	C	C	C
8. Optical Physics	25.. Light Reflection	C	C	C	C	C	C
	26. Light Refraction	C	C	C	C	C	C
	27. Light Interferential	C	C	C	C	C	C
	28. Defraction ofLight	C	C	C	C	C	C
	29. Light Polarisation	C	C	C	C	C	C
9. Electromagnetic Wave (GEM)	30. Equation of Electromagnetic Wave	W	W	C	C	C	C
	31. Electromagnetic Spectrum	W	W	C	C	C	C
	32.Poynting Vector, Energy, and GEM energy	W	W	C	C	C	C

Comment:

LS: It is not a mistake not to take notes on concept ; It is just not relevant to the topic of discussion.

For the sixth design, the three experts viewed that the result of analysis on physic lecturing aim has been included into the criteria "Correct" both concept scope defined and the correctness of the concept, as shown in Table 6. It means that the frame of thought of the researcher at the beginning of study to obtain the design of lecturing aim is fix to the frame of thought of the experts. There are some strong reasons for the 12 lecturing aims as the result of the beginning of study to be the parts of Physics Lecturing Program. However, for this design, there should be the opinions of stakeholders through investigation in order to get a deeper result of test.

Table 6. Result of Investigation on the Aims of Physics Lecturing Program in JTKP

Study Program	Aims	Expert 1: LS		Expert 2:		Expert 3: HB	Miscelenous
		SC	CC	SC	CC	SC	CC
D3- Chemical Engineering	1.To give an understanding on the concept of basic physics which can support the competence of chemical engineering-Polban's graduates	C	C	C	C	C	C
	2. Students have the ability to apply concept, principle, and law of physics in chemical engineering field of study.	C	C	C	C	C	C
	3. Students have the ability of analyzing parts of implisit physics' concept in equipment	C	C	C	C	C	C

	system related to chemical engineering field of study													
	4. Students have the ability to evaluate a physics' symptom using physics' concept, principle, and law related to chemical engineering field of study	C		C		C	C	C						C

Comment:

There is an inconsistency, for the aim of lecture, in using the Sentence Subject / Phrase. Aim 1 use verb (give an understanding); while for aims 2,3

and 4 use subject of nouns (students). It will be better if the aims are sequenced from understanding, analyzing, evaluating, and then application.

Table 6. Result of Investigation on the Aims of Physics Lecturing Program in JTKP

			Expert 1: LS		Expert 2: HY		Expert 3: HB	Miscelaneous
	Study Program	**Aims**	**SC**	**CC**	**SC**	**CC**	**SC**	
D3- Chemical Engineering-Clean Production		1.To give an understanding on the concept of basic physics which can support the competence of chemical engineering-Polban's graduates	C	C	C	C	C	
		2. Students have the ability to apply	C	C	C	C	C	

	concept, principle, and law of physics in chemical engineering field of study.					
	3. Students have the ability of analyzing parts of implisit physics' concept in equipment system related to chemical engineering field of study	C	C	C	C	C
	4. Students have the ability to evaluate a physics' symptom using physics' concept, principle, and law related to chemical engineering field of study	**C**	**C**	C	C	C
	Comment:					
	HB: Same as the aim of lecture for Chemical Engineering Study Program					

Study Program	**Aims**	**Expert 1: LS**		**Expert 2: HY**		**Expert 3: HB**	**Miscelaneous**
		SC	CC	SC	CC	SC	
D3- Chemical Analyst	1.To give an understanding on the concept of basic physics which can support the competence of chemical engineering-PolBan's graduates	C	C	C	C	C	
	2. Students have the ability to apply concept, principle, and law of physics in	C	C	C	C	C	

chemical engineering field of study.					
3. Students have the ability of analyzing parts of implisit physics' concept in equipment system related to chemical engineering field of study	C	C	C	C	C
4. Students have the ability to evaluate a physics' symptom using physics' concept, principle, and law related to chemical engineering field of study	C	C	C	C	C
Comment:					
HB: Same as the aim of lecture for Chemical Engineering Study Program					

As a whole, validation activity of the expert has affected on the perfectness of the content of the analysis result in achieving product "Designing of Physics Lecturing Program Materials which is able to Support the Competence of Chemical Engineering - PolBan's Graduates"

For main components of lecturing program design, such as competence, main topic of discussion, sub-topic of discussion, and the aim of physics' lecture, experts' validation activity didn't change the content of lecturing program material components. So, the main component of lecturing program design to be viewed by stakeholders are similar to the previous result of study.

Based on the result of investigation on stakeholders' view, it could be determined the lecture's aim, competence, main topic of discussion, sub-topic of discussion, and 8 main topics of essential and functional physics based on the need of chemical engineering study program. Stakeholders' views on the design of lecture aims and physics competence is shown

at Table 7. For D3- Chemical Engineering, seems that the number of respondent agreed to the design of lecture's aims were about 92.86%, D4-Chemical Engineering –Clean Production 95.84%, and D3- Chemical Analyst 100%. It means all designs includes strong foundation as the aims of study program. Lecturers of Chemical Engineering Study Program were sure that this design was suitable for the need of study program. The lecturers agreed that the design of lecture's aim focuses on the activity supporting establishment of study program's competence. Theoretically, the achievement of study program's lecturing program must be determined by the quality and the lecturing strategy type. The specialty of lecturing strategy type very determines the succeed of the lecturing program.

Table 7. Precentage of Stakeholder's Views Agreeing on the Lecture's Aim and the Competence of Physics (Advance)

Study Program	Aim of Lecture	%	Competence of Physics	%
D3-CHEMICAL ENGINEERING	1.To give an understanding on the concept of basic physics which can support the competence of chemical engineering study program - PolBan's graduate	100	1. Mastering physics' International System unit, measurement and uncertainty	100
			2. Applying the method of basic calculus	71.43
			3. Mastering the concept of kinematik ofstraight and rotated movement .	28.57
			4. Mastering the concept of dynamic of straight and rotated movement	28.57
	2. Students have the ability to apply concept, principle, and law of physics in chemical engineering field of study.	100	5.Mastering teorem impulse-momentum	57.14
			6.Mastering teorem power-energy	100
			7. Mastering concept rotated movement of rigid	28.57

			object	
			8. mastering concept of fluids	100
	3.Students have the ability of analyzing parts of implisit physics' concept in equipment system related to chemical engineering field of study	85.71	9. Mastering the concept of fibration	21.43
			10. Mastring the concept of sound wave	21.43
			11. mastering the concept of electromagnetic wave	42.86
			12. Mastering the concept of temperature and heat	100
	4. Students have the ability to evaluate a physics' symptom using physics' concept, principle, and law related to chemical engineering field of study	100	13. Mastering the theory gas kinetic	100
			14. Applying thermodynamic law	100
			15. Mastering the concept of electricity	71.43
			16. Mastering concept of physic optic	50
	1.To give an understanding on the basic physics concept supporting the competence of chemical engineering-clean production study program-PolBan's graduate	100	1. Mastering physics' mulberry, International System unit, measurement and uncertainty	100
			2. Applying the method of basic calculus	83.33
D4-CHEMICAL ENGINEERING-CLEAN PRODUCTION			3. Mastering the concept of kinematik ofstraight and rotated movement .	66.67
			4. Mastering the concept of dynamic of straight and	66.67

			rotated movement	
	2. Students have the ability to apply concept, principle, and law of physics in chemical engineering - clean production field of study.	91.67	5.Mastering teorem impulse-momentum	75
			6.Mastering teorem power-energy	91.67
			7. Mastering concept rotated movement of rigid object	41.67
			8. mastering concept of fluids	100
	3.Students have the ability of analyzing parts of implisit physics' concept in equipment system related to chemical engineering -clean production field of study	91.67	9. Mastering the concept of fibration	50
			10. Mastring the concept of sound wave	25
			11. mastering the concept of electromagnetic wave	25
			12. Mastering the concept of temperature and heat	100
	4. Students have the ability to evaluate a physics' symptom using physics' concept, principle, and law related to chemical engineering -clean production field of study	100	13. Mastering the theory gas kinetic	100
			14. Applying thermodynamic law	100
			15. Mastering the concept of electricity	91.67
			16. Mastering concept of physic optic	50
D3-	1.To give an understanding on the basic physics concept supporting the competence of chemical	100	1. Mastering physics' mulberry, International	100

CHEMICAL ANALYST	analyst study program-PolBan's graduate		System unit, measurement and uncertainty	
			2. Applying the method of basic calculus	42.86
	2. Students have the ability to apply concept, principle, and law of physics in chemical analyst field of study.		3. Mastering the concept of statical fluids	85.71
			4. Mastering the concept of temperature and heat	100
	3.Students have the ability of analyzing parts of implisit physics' concept in equipment system related to chemical analyst field of study	100	5. Mastering the theory gas kinetic	71.43
			6. Applying thermodynamic law	85.71
	4. Students have the ability to evaluate a physics' symptom using physics' concept, principle, and law related to chemical analyst field of study	100	7. Mastering the concept of electricity	100
			8. mastering the concept of electromagnetic wave	100
			9. Mastering concept of physic optic	100

In the category of physics competence design agreed by more than 60% respondents, seems that the lecturers of D3-Chemical Engineering, D4-Chemical Engineering-Clean Production and D3-Chemical Analyst Study Programs, in sequence approximately 50%, 68.75%, and 88.89 %. In other word, D3-Chemical Engineering, D4-Chemical Engineering-Clean Production and D3-Chemical Analyst Study Programs‘ lecturers, in sequence, choose 8,11, and 8 physics’ competence. This design can be the competence of physics as the supporting competence for study program’s graduate. This competence includes the parts of pre-competence which should be mastered by students and with other subjects can produce the competence of graduates as expected by study program.

Table 8. Precentage of Lecturer's View Agreeing on the Design of Physics Main Topic and Sub-Topic.

Study Program	Topic of Discussion	%	Sub-topic of Discussion	%
D3-CHEMICAL ENGINEERING	1. Units	100	1. Unit and Dimesion	100
			2.Measurement and Uncertainty	100
			3. Important Number	100
			4. Source of Mistakes & Calibration Tool	100
			5. Processing Data (Graph, Smallest Quadrate)	85.71
	2. Basic Calculus	64.29	6. Operation of Vector	57.14
			7. Differential & Integral	78.57
	3. Kinematiks	50	8. Equation of Straight Movement	28.57
			9. Combination of Straight Movement	28.57
			10. Equation of Rotated Movement	28.57
	4. Dynamics	50	11.Friction energy	42.86
			12. Law of Newton	71.43
	5. Momentum - Impulse	57.14	13. Impulse and Momentum	57.14
			14. Impulse and Momentum Theorm	50
			15. Law of Linear Momentum Durability	50
			16. Act of colliding	57.14
	6.Energy power	92.86	17. Force and Energy	92.86
			18. Theorem of Force and Energy	78.57
			19. Law of Energy Conservation	100
	7. Rotation of Rigid Objects	35.71	20. Equation of Rotation Movement	21.43
			21. Energizing Moment, Force Moment, Law of Dynamic Rotation	35.71
			22. Law of Angular Momentum Durability	28.57

		23. Law of Energy Conversion	42.86
		24. Movement of Revolving	28.57
8. Fluids	92.86	25. Statical Fluids	100
		26. Dynamical Fluids	100
9. Vibration	21.43	27. Harmonical Vibration	21.43
		28. Muffled Vibration	14.29
		29. Forced Vibration	14.29
10. Wave of Sound	28.57	30. Wave Sound Equation	21.43
		31. Intensity and Level of Intensity of Sound	14.29
		32. Interference and Soaring of Sound	14.29
		33. Doppler Effect	21.43
11. Electromagnetic Wave	42.86	34. Equation of Electromagnetic Wave	42.86
		35. Electromagnetic Spectrum	42.86
		36.POYNTING Vector, Energy, AND GEM energy	28.57
12. Temperature & Heat	100	37. Temperature and Heat	100
		38. Black Principle	100
13. Theory of Gas Kinetic	100	39. Equation fo Ideal Gas	100
		40. Pressure, Inner Energy, RMS acceleration	100
		41. Phase Diagram	100
14. Thermodynamics	100	42. Power	92.86
		43. Thermodynamic Process	92.86
		44. Law of Thermodynamic	100
15. Electricity	78.57	45. Current in Electrolite solution	92.86
		46. Tension, Obstruction, Energy and Electric Power	78.57
		47. Capacitor and Inductor	78.57
		48. DC Electric Series	85.71
		49. AC Electric Series	85.71
16. Optical Physics	50	50. Light Reflection	42.86
		51.Light Refraction	42.86
		52. Light Interferential	35.71

D4-CHEMICAL ENGINEERING-CLEAN PRODUCTION

		53. Defraction of Light	35.71
		54. Light Polarization	35.71
1. Units	100	1. Unit and Dimension	100
		2.Measurement and Uncertainty	91.67
		3. Important Number	91.67
		4. Source of Mistakes & Calibration Tool	100
		5. Processing Data (Graph, Smallest Quadrate)	100
2. Basic Calculus	91.67	6. Operation of Vector	41.67
		7. Differential & Integral	50
3. Kinematiks	75	8. Equation of Straight Movement	50
		9. Combination of Straight Movement	50
		10. Equation of Rotated Movement	41.67
4. Dynamics	91.67	11.Friction energy	58.33
		12. Law of Newton	50
5. Momentum - Impulse	75	13. Impulse and Momentum	50
		14. Impulse and Momentum Theorm	50
		15. Law of Linear Momentum Durability	50
		16. Act of colliding	41.67
6.Energy power	91.67	17. Force and Energy	100
		18. Theorem of Force and Energy	100
		19. Law of Energy Conservation	100
7. Rotation of Rigid Objects	75	20. Equation of Rotation Movement	25
		21. Energizing Moment, Force Moment, Law of Dynamic Rotation	25
		22. Law of Angular Momentum Durability	25
		23. Law of Energy Conversion	25
		24. Movement of Revolving	25
8. Fluids	100	25. Statical Fluids	100
		26. Dynamical Fluids	100

	9. Vibration	58.33	27. Harmonical Vibration	8.33
			28. Muffled Vibration	8.33
			29. Forced Vibration	8.33
	10. Wave of Sound	33.33	30. Wave Sound Equation	25
			31. Intensity and Level of Intensity of Sound	16.67
			32. Interference and Soaring of Sound	16.67
			33. Doppler Effect	33.33
	11. Electromagnetic Wave	41.67	34. Equation of Electromagnetic Wave	33.33
			35. Electromagnetic Spectrum	33.33
			36.POYNTING Vector, Energy, AND GEM energy	33.33
	12. Temperature & Heat	100	37. Temperature and Heat	100
			38. Black Principle	100
	13. Theory of Gas Kinetic	100	39. Equation fo Ideal Gas	91.57
			40. Pressure, Inner Energy, RMS acceleration	91.57
			41. Phase Diagram	91.57
	14. Thermodynamics	100	42. Power	100
			43. thermodynamic Process	100
			44. Law of Thermodynamic	100
	15. Electricity	100	45. Current in Electrolite solution	100
			46. Tension,Obstruction, Energy and Electric Power	100
			47. Capasitor and Inductor	100
			48. DC Electric Series	100
			49. AC Electric Series	100
	16. Optical Physics	50	50. Light Reflection	25
			51.Light Refraction	16.67
			52. Light Interferential	16.67
			53. Defraction of Light	16.67
			54. Light Polarization	16.67
E M IC AL A	1. Unit, Measurement, and	100	1. Unit, and dimension	100

Uncertainty			
		2.Measurement and Uncertainty	100
		3. Important Number	100
		4. Source of Mistakes & Calibration Tool	100
		5. Processing Data (Graph, Smallest Quadrate	100
2. Basic Calculus	42.36	6. Operation of Vector	14.29
		7. Differential & Integral	71.43
3. Statical Fluids	85.71	8. MASSA JENIS and Pressure	100
		9.Pascal Law & Archimides Law	85.71
		10. Surface Tension	100
		11.Capilarity Symptom	100
4. Temperature & Heat	100	12.Temperature & Heat	100
		13. Black Principle	71.43
5. Theory of Gas Kinetic	71.43	14.Equation of Ideal Gas Condition	85.71
		15. Pressure, Inner Energy, RMS Acceleration	85.71
		16. Phase of Diagram	71.43
6. Law of Thermodynamics	85.71	17. Power	71.43
		18. Thermodynamics Process	85.71
		19.. Thermodynamics Law	85.71
7. Electricity	100	20. Current in Electrolite Solution	100
		21. Tension, Obstruction, Energy and Electric Power	85.71
		22. Capacitor & Inductor	71.43
		23.DC Electric Series	85.71
		24.AC Electric Series	85.71
8. Optical Physics	100	25.. Light Reflection	100
		26. Light Refraction	100
		27. Light Interferential	100
		28. Defraction of Light	100
		29. Light Polarization	100
9. Electromagnetic Wave (GEM)	100	30. Equation of Electromagnetic Wave	100

31. Electromagnetic Spectrum	100
32.Poynting Vector, Energy, and GEM energy	42.36

Stakeholder's views on the design of main topics and sub-topics of discussions are shown at Table 8. The category of main topic design were agreed by 60% of respondents. The lectures of D3- Chemical Engineering, D4- Chemical Engineering – Clean Production, and D3- Chemical Analyst respectively chose approximately 56.25%, 62.50%, and 88.89% of the design. In other words, they chose respectively 8,11, ,and 8 designs as topic of discussions which are important to learn by the students of study program. For the design of sub-topic discussion, the lecturers of D3- Chemical Engineering, D4- Chemical Engineering – Clean Production, and D3- Chemical Analyst respectively chose approximately 46.30%, 42.60%, and 93.75%. In other words, they chose respectively 25, 23, and 30 designs as the sub-topics of discussion which need to learn by the students of Chemical Engineering study program.

Table 9. Stakeholders' Opinions on 8 EssentialPhysics' Topic of Discussion in the Category of Being Agreed by 60% Respondents

Study Program	Topic of Discussins	Respondents' Views	
		Included	Not Included
D3-CHEMICAL ENGINEERING	1. Dimension, Units, Measurements , and Uncertainty	100	-
	2. Basic Calculus	64.29	35.71
	3. Force and Energy	100	-
	4. Fluids	100	-
	5. Temperature & Heat	100	-

	6. Theory of Gas Kinetic	92.86	7.14
	7. Law of Thermodynamic	100	-
	8. Electricity	71.43	35.71
D4-CHEMICALENGINEERING-CLEANPRODUCTION	1. Dimension, Units, Measurements , and Uncertainty	100	-
	2. Dynamics	66.67	33.33
	3. Force and Energy	100	-
	4.Fluids	100	-
	5. Temperature & Heat	100	-
	6. Theory of Gas Kinetic	91.67	8.33
	7. Law of Thermodynamic	100	-
	8. Electricity	91.67	8.33
D3-CHEMICAL ANALYST	1.Dimension, Units, Measurements , and Uncertainty	100	-
	2.Static Fluids	85.71	14. 29
	3. Temperature & Heat	100	-

4. Theory of Gas Kinetic	85.71	14. 29
5. Law of Thermodynamics	100	-
6. Electricity	100	-
7. Electromagnetic Wave	100	-
8. Optical Physics	100	-

The understanding of the lecturers into the need of physics material can be measured from their consistency in expressing their opinions. The indicator of consistency is the linearity of respondents' views (agree or disagree) to the choice of competency design, the designs of main topics and sub-topics of physics discussion. Table 7 and 8 show the consistency level of lecturers of D3- Chemical Engineering, D4- Chemical Engineering – Clean Production, and D3- Chemical Analyst respectively 100%, 100%, and 88.89%. It has the meaning that they all were consistent in choosing the competence, main topics of discussions, and sub-topics of discussions from the same cluster. Each lecturer has a good knowledge of the need of materials for physics lecturing program which is suitable with the need of study program. They also have a comprehensive understanding on the relationship between physics lecturing program (PLP) which supports the establishment of study program's graduate competence.

Agreeing with the curriculum, time allocation for physics lecturing program is very limited. In the other side, there are so many topics of discussions. To cope this problem, the essentiality and function of main topics of discussions become the main consideration in determining materials for lecturing program. Eight main topics or 8 physics competence can be made

as an essential-functional indicator. From the result of investigation for lecturer's view as shown in Table 3, the respondents had chosen directly 8 essential topics of discussions from a number of the available topics. This method is in accordance with Reif (1995) view "*Less is More*" and Fratt(2002) "*a mile wide and an inch deep*".

Based on Reif-Fratt's ways of thinking, the relationship concept of the main topics of discussion and competence, the main topics and sub-topics of discussion, physics subject materials as the supporter for study program's graduates' competence, materials and functional concept for the advance subject of the study program, therefore it is determined that the materials or products of physics lecturing program are:

1. All designs of the physics lecturing program (PLP) as the result of validation are the aims of the PLP's research products.

2. Eight main topics of discussions shown at Table 9 are the main topics of the PLP's research products.

3. The eight physics competences related to the 8 essential topics of discussions at Table 7 are the competence of the PLP's research products.

4. Sub-topics of discussions which can be compiled into 8 main topics of essential physics are sub-topic of discussion of the PLP's research products.

All components of the PLP's research products have been included into the category of 'Being agreed by more than 60% of respondents"

CONCLUSION AND SUGGESTIONS

Based on the result of finding and the discussion, it can be concluded that:

1. PLP materials, which had been validated by the experts, are similar to PLP materials which were designed in the pre-study, i.e. 16 competences, 16 main topic of discussions, 54 sub-topic of discussions, 4 aims of physics lecturing program for D3- Chemical Engineering and D4- Chemical Engineering – Clean Production. The materials for D3- Chemical Analyst consist of 9 competences, 9 main topics of discussions, 32 sub-topic of discussions, 4 aims of physics lecturing program.

2. The materials, as the result of the investigation for the stakeholder's views, for D3- Chemical Engineering and D4-

Chemical Engineering – Clean Production consist of 8 competences, 8 main topics of discussions, 25 sub-topics of discussions, 4 aims of physics lecturing program. In other case for D3- Chemical Analyst, they consist of 8 competences of physics, 8 main topics of discussions, 29 sub-topics of discussions, 4 aims of physics lecturing program.

Due to the research has been carried out with involving the scholarly investigation by the experts and stakeholders, it's better for the institution with the same type to apply the product of this research as good as possible.

FINANCIAL RESOURCE

This dissertation is a part of dissemination of multi years "HIBAH BERSAING" or competitive grants financed by Direktorat Penelitian dan Pengabdian Kepada Masyarakat year 2012 SK Direktur PolBan No. 0841/PL/2011 Dated 7 March 2012.

LIST OF BIBLIOGRAPHY

Fratt,L. (2002).*Less is More: Trimming the Overstuffed Curriculum.* AAAS Project 2061.

Reif,F. (1995). Millikan Lecture 1994; *Understanding and Teaching Important Scientific Thought Process*. American Journal of Physics, 63, (l), 17-32.

Sukmadinata, N.S. (2006) *metode Penelitian Pendidikan.* Bandung. Remaja Rosdakarya

Stability Analysis of the Absorbed Dose to Water Calibration Coefficients

A.M. Mukhtar[1*], S.B. Samat[1]
[1] School of Applied Physics, Faculty of Science and Technology, National University of Malaysia, 43600, UKM Bangi, Selangor, Malaysia

Abstract

The stability of the absorbed dose to water calibration coefficients $N_{D,w}$ for seven chambers belonging to the six local radiotherapy centres from year 2004-2012 is studied. The $N_{D,w}$ value for the first calibration was taken as the standard, and the percentage deviations Δ(%) of the consequent $N_{D,w}$ (in comparison with the standard $N_{D,w}$) were then calculated. Then the mean μ, standard error SE and the standard deviation σ_{N-1} of the Δ(%) were obtained. The $N_{D,w}$ of a chamber is said to be stable if $\mu \pm SE$ fulfills the requirement of the IAEA ± 1.5%. Results showed that all chambers fulfilled this requirement. Upon detailed analysis, such as the application of students-t test and the removal of outliers from the original data, better results were obtained. It is concluded that the $N_{D,w}$ for all chambers are stable for the period of eight years.

Keywords : *Stability, ionization chambers, absorbed dose to water calibration coefficients, Malaysian radiotherapy centres.*

* Corresponding author.
E-mail address: atiqahmardziahmukhtar@yahoo.com

I. Introduction

Radiation therapy plays an important role in curing cancer. The purpose of radiation therapy is to maximizing killing cancer cells in a tissue while maximizing or keeping the sparing of healthy cells at acceptable level [1]. To achieve this, ICRU 24 [2] has recommended an accuracy of ±5% at 2σ level in the delivery of absorbed dose to target volume. IAEA 2000 [3] then recommended an uncertainty for an absorbed dose measurement in a phantom be less than 3% at the 1σ level. It is also well known that all factors in radiotherapy procedures contain uncertainties.

When an ionization chamber is used to determine the absorbed dose to water D_w, the ionization chamber's absorbed dose to water calibration coefficient $N_{D,w}$ is needed. The formula that show the relationship between D_w and $N_{D,w}$ is as:

$$D_w = R \times K_{T,P} \times N_{D,w} \quad (1)$$

where R is the charge rate and $K_{T,P}$ is the correction factor for temperature and pressure

IAEA 2002 state that the acceptable limit for $N_{D,w}$ is ±1.5% [4]. NCRP [5] requires an ionization chamber be calibrated every year for the purpose of getting accurate $N_{D,w}$. The SSDL Malaysia is an authorised laboratory for the calibration of $N_{D,w}$. Until now, SSDL Malaysia has calibrated $N_{D,w}$ for 87 ionization chambers belonging to 23 local radiotherapy centres. The calibration frequency f for the N=87 chambers are as follows: (a) N=24, f=1; (b) N=12, f=2 (c) N=14, f=3, (d) N=12, f=4 (e) N=10, f=9 (f) N=9, f=6 (g) N=6, f=7.

The present work analyses the $N_{D,w}$ results for the case of (g) N=6, f=7 , which was performed from year 2004−2012. The N=6 belong to six local radiotherapy centres. It is for the purpose of studying the stability of the $N_{D,w}$ during this period.

II. Materials and Method

Calibration coefficient of a chamber under calibration is obtained from:

$$N_{D,w}^{RC} = \frac{N_{D,w}^{SSDL} \times M_U^{SSDL}}{M^{RC}} \quad (2)$$

where $N_{D,w}^{RC}$ is the calibration coefficient (to be determined) and M^{RC} is corrected electrometer reading of the radiotherapy centre chamber. Also, $N_{D,w}^{SSDL}$ is the calibration coefficient and M_U^{SSDL} is the corrected electrometer reading of the SSDL chamber. Equation (2) is the substitution method recommended by the IAEA [6].

The experimental set-up is shown in Figure 1. Reference standard chamber used by SSDL is NE2571 (#1028) with volume 0.6 cm^3. Apparatus and set-up used in this study are as follows: PMMA water phantom size 30cm×30cm×30cm, perspex sheath (used to

place the ionization chamber inside the phantom), surface to source distance (SSD) = 100 cm, surface to chamber distance (SCD) = 105 cm (with reference point depth = 5 g/cm^2) and field size (FS) = 10 × 10 cm^2. Co-60 was used for irradiation purposes. For each calibration, 15 value of charge rate were taken. The average value was then calculated to get the value of $N_{D,w}$.

The data pairs (year of calibration, $N_{D,w}$) for each chamber (belonging to each radiotherapy centres) were obtained from SSDL Malaysia log book. The $N_{D,w}$ value for the first calibration was taken as the standard, and the percentage deviations $\Delta(\%)$ of the consequent $N_{D,w}$ (in comparison with the standard $N_{D,w}$) were then calculated by equation (3):

$$\%\Delta=\frac{N_{D,w\,(consequent)}-N_{D,w\,(standard)}}{N_{D,w\,(standard)}}\times 100 \quad (3)$$

The mean μ, standard error SE and the standard deviation σ_{N-1} of the $\Delta(\%)$ then calculated [7]. In this work, μ±SE will be used to measure stability of $N_{D,w}$. The $N_{D,w}$ of a chamber is said to be stable if μ±SE lies within the acceptable limit of ±1.5% required by the IAEA [4].

original data of $\mu\pm SE$. It is interesting to check whether $\mu\pm SE$ include the value of zero for each chamber. If it does, we conclude that the result is satisfactory and no evidence that a systematic error occurred in the measurements. On the other hand, if it does not, the student's t-test [8] needs to be done. If the test reveals that no systematic error is occurring, then analysis of the data should be done further for the purpose of identifying the outlier. The aim is to see whether by the removal of the outlier, the newly calculated $\mu\pm SE$ will now include the value of zero.

On examining Table 1 and Figure 2, it is obvious that $\Delta(\%)$ of chamber no. 1, 2, 4, 5 and 6 (except chamber no 3) need to be checked by the student's-t test as their values of $\mu\pm SE$ do not include the value of zero. Upon checking this test (for all the five chambers), it is found that there is no evidence that a systematic errors have occurred in the measurement (of calibration coefficients) at 0.1% confidence level. To demonstrate this test, data for chamber no 2 is chosen as an example. Table 1 yields $\mu\pm SE$ =–1.11±0.21 for this chamber. For 5 degrees of freedom, and a significance level of 0.1%, student's t is 5.893. Since 5.893 × 0.21 is greater than $|-1.11|$, it is concluded that no evidence,

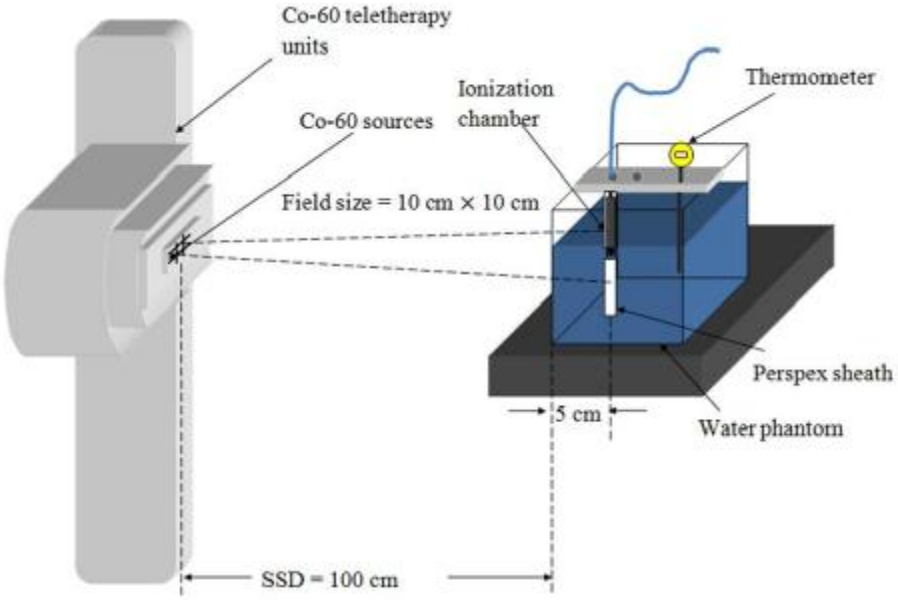

Figure 1: Experimental set-up for the determination of $N_{D,w}$

III. Results, Discussion and Conclusion.

Table 1 shows $\mu\pm SE$ and $\mu\pm\sigma_{N-1}$ of the $\Delta(\%)$ for the six chambers. Discussion will mainly focus on $\mu\pm SE$ in particular. The variation of $\mu\pm SE$ for the six chambers is shown in Figure 2. The solid circles represented the

at the 0.1% level, the chamber no.2 results is systematically lower than the IAEA results.

The next step now is to identify whether the data consist of outliers. The criteria of $1.96\times\sigma_{N-1}$ at 95% confidence interval could be used for this purpose. If a data exceeds this

$1.96\times\sigma_{N-1}$, this data can be treated as an outlier. To demonstrate this, we also take the case of chamber no. 2, as an example. For this chamber, we have f=7 (no. of data =f−1=6) and $\mu\pm\sigma_{N-1}$=−1.11±0.53 (as given in Table 1). The six data of $\Delta(\%)$ are −1.68%, −0.92%, −1.81%, −0.49%, −1.01% and −0.74%. Since for this chamber, $1.98\times\sigma_{N-1}$=1.96×0.53=1.04%, therefore the data of −1.68% and −1.81% can be treated as outliers and subsequently can be omitted. This is left with four data (= 6−2) which now yields new values of the $\mu\pm SE$ and $\mu\pm\sigma_{N-1}$ as shown in Table 1 (now indicate by the hollow circles in Figure 2). Note that by removing the outliers from the original data (solid circles), the new $\mu\pm SE$ (hollow circles) is now approaching $\Delta(\%)$=0. The other effects on the omission of the outliers could also be seen in Figure 1 for chambers no 5 and 6. For chambers no 5 and 6, the new maximum and minimum range of $\mu\pm SE$ now really lie within the IAEA acceptable limit of ±1.5%. In addition for chamber 6, μ±SE now include the value of zero.

In Figure 2, it can be seen that for both cases, i.e. the solid circles (before the outliers are omitted) and hollow circles (omission of outliers), they do lie within the IAEA acceptable limit of ±1.5%. We therefore conclude that the calibration coefficients for the six chambers are stable for the period of eight years.

Table 1: The value of μ±SE and $\mu\pm\sigma_{N-1}$ of the Δ(%) for all six chambers (at one standard deviation, or 68% confidence interval)

Chamber No	$\mu\pm SE$[1]		$\mu\pm\sigma_{N-1}$	
	$\Delta(\%)$[2]	$\Delta(\%)$[3]	$\Delta(\%)$[2]	$\Delta(\%)$[3]
1	-0.16±0.15	-	-0.16±0.36	-
2	-1.11±0.21	-0.79±0.11	-1.11±0.53	-0.79±0.23
3	0.08±0.10	-	0.08±0.24	-
4	-0.59±0.20	-0.44±0.16	-0.59±0.49	-0.44±0.36
5	1.34±1.03	0.32±0.20	1.34±2.53	0.32±0.44
6	-1.16±1.03	-0.25±0.59	-1.16±2.53	-0.25±1.33

[1]$\Delta(\%)^1$ and $\Delta(\%)^2$ are represented as solid and hollow circle respectively in Figure 2
[2]Original data without omission of outlier.
[3]Outlier has been omitted.

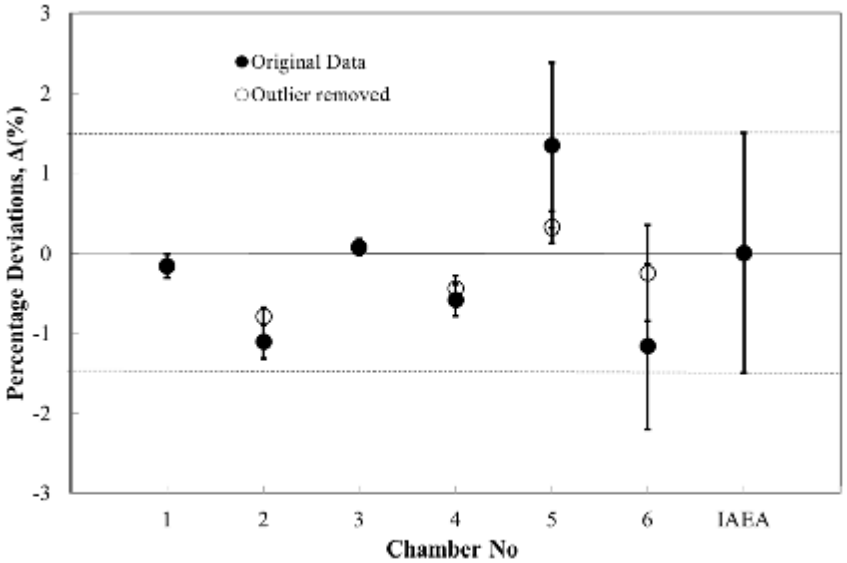

Figure 2: Variation of Δ(%) for μ±SE with chamber number in comparison with the IAEA acceptable limit

IV. Acknowledgements

We gratefully thanked the Ministry of Higher Education for a research grant of UKM-ST-07-FRGS0154-2010 and the Nuclear Malaysia Agency for the cooperation given.

V. References

1. M. Kapanen, Report Series in Physics, HU-P-D163. University of Helsinki, 2009.
2. ICRU, Determination of Absorbed Dose in a Patient Irradiated by beams of X or Gamma Rays in Radiotherapy Procedures, Rep 24, ICRU, Bethesda, 1976.
3. IAEA, Technical Report Series No. 398: Absorbed Dose Determination in External Beam Radiotherapy, Vienna, 2000.
4. IAEA, Calibration of Photon and Beta Ray Sources Used in Brachytherapy: Guidelines on standardized procedures at Secondary Standards Dosimetry Laboratories (SSDLs) and hospitals, Vienna, 2002.
5. NCRP, NCRP Report No. 69: Dosimetry of X-Ray and Gamma Ray Beams for Radiation Therapy in the Energy Range 10 keV TO 50 MeV, National Council on Radiation Protection and Measurements, Washington D.C, 1981.
6. IAEA, Calibration of Dosimeters used in Radiotherapy, Technical Reports Series No. 374, IAEA, Vienna, 1994.
7. S.B. Samat and C.J.Evans, Statistics and Nuclear Counting – Theory, Problems and Solutions, Universiti Putra Malaysia Press, 43400 Serdang, ISBN 967-9952-76-2, 1992.
8. R. Bakeman and B.F. Robinson, Understanding Statistics in the Behavioral Sciences, Lawrence Erlbaum Associates. Inc., New Jersey, 2005.

Effects of the Length and Location of Stack on the Temperature Decrease of a Thermoacoustic Cooler

Ikhsan Setiawan[1,2]*, Agung Bambang Setio-Utomo[1], Makoto Nohtomi[2], and Masafumi Katsuta[2]
[1]*Department of Physics, Faculty of Mathematics and Natural Sciences, Gadjah Mada University*
Sekip Utara PO BOX BLS.21 Yogyakarta 55281, Indonesia
[2]*Graduate School of Environment and Energy Engineering, Waseda University,*
Nishi-tomita 1011, Honjo-city, Saitama pref. Japan

Abstract
Thermoacoustic coolers are environmentally friendly cooling devices because they use harmless gases as working medium instead of chlorofuorocarbons (CFCs) or hydrofluorocarbons (HFCs) as in conventional coolers. They employ sound wave to induce heat transfer in a stack (porous medium), i.e. between working gas and stack material. In this experiment, the working gas was free air at atmospheric pressure and the stacks were parallel plate type made of mica sheets. The stack was installed inside a straight cylindrical 1/4-wavelength resonator of 80 cm in length. An 8" 150 W loudspeaker was used to provide acoustic work. It has been experimentally studied the effects of stack length and stack location in the resonator on the temperature decrease of a thermoacoustic cooler. It was found that each parameter has an optimum value which gave the largest temperature decrease. In this case, the optimum length was 10 cm and the optimum location was at 10 cm of the distance of stack's center measured from the closed end of the resonator. The combination of these optimum values gave a temperature decrease of 11 °C at the cooling point so that the air temperature in this location was down to 19 °C.

Keywords : *Thermoacoustic cooler, stack length, stack location, temperature decrease*

* Corresponding author.
E-mail address: ikhsan_s@ugm.ac.id, ikhsan@asagi.waseda.jp

I. Introduction

Thermoacoustic coolers are environmentally friendly because they use harmless gases like air and noble gases as working medium instead of chlorofuorocarbons (CFCs) and hydrofluorocarbons (HFCs) as in conventional refrigerators. In addition, abundance of the working gas and relatively simple construction make the thermoacoustic coolers as relatively low cost and promising alternative cooling devices in the future compared to the conventional systems.

Thermoacoustic coolers mainly consist of a sound driver (e.g. loudspeaker), a resonator tube, a stack (porous medium), and working gas. The sound driver provides a high power standing sound wave in the working gas inside the resonator tube, and the stack is typically placed near the pressure antinode. The interaction between the expanding and compressing gas with the stack material will result in heat transfer in direction from pressure node to pressure antinode axially in the stack. More detail description on the working principles of thermoacoustic refrigerators can be found elsewhere [1-3].

In this paper we describe an experimental study of the influence of stack length and stack location in the resonator tube on the temperature decrease of a loudspeaker-driven thermoacoustic cooler.

II. Experiment

The experimental set-up is shown schematically in Fig. 1. The thermoacoustic cooler is standing wave type and driven by a loudspeaker. A 1-1/4" PVC (polyvinyl chloride) pipe with length of 80 cm was used as a quarter-wavelength resonator. One end of the pipe is closed and the other end is coupled to an 8" 150 W loudspeaker with its box. A digital audio function generator (AFG) model GFG 8016G was used to provide sinus signal to the loudspeaker after amplified by a 100 W audio amplifier. The input electric current and voltage were measured by an amperemeter (A) and a voltmeter (V), respectively. With free air at atmospheric pressure and room temperature of 30 °C as the working medium, the resonance frequency was calculated as around 106 Hz.

A mic condensor was attached at the closed end of the resonator, and the electric signal generated by the sound in the resonator tube was amplified by a pre-amp and then fed into a sound-

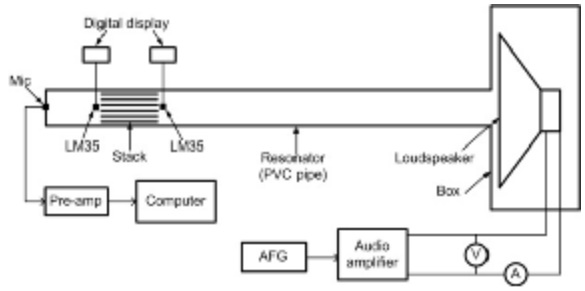

Figure 1. Schematic diagram of experimental set-up. AFG is audio function generator, V is voltmeter, and A is amperemeter.

Figure 2. Parallel plate stack made of mica plastic sheets. The spacer between plates are nylon fishing lines. The stack casing is 1-1/4" PVC pipe.

card of a computer. In the computer, the wave-form and spectrum of the sound wave were monitored in real time by using Oscilloscope 2.51 software.

The stack is parallel plate type made of mica plastic sheets with thickness of 0.5 mm as the plates and nylon fishing lines with 1 mm in diameter as the spacer between plates, as shown in Fig. 2. The fishing lines were glued with 1 cm spacing on the plates. The stack was inserted into its casing which is made of a 1-1/4" PVC pipe, and the diameter of stacks were set to fit into the casing.

One of important parameters for stack in thermoacoustic coolers is the thermal penetration depth (δ_k) which describes the distance that heat can diffuse through a gas during time of $1/\pi f$, where f is the sound frequency. The thermal penetration depth is expressed by [4]

$$\delta_k = \sqrt{K/\pi f \rho c_p} \qquad (1)$$

where K is the thermal conductivity, ρ is the density, c_p is the isobaric specific heat per unit mass of the gas. In this experiment, the thermal penetration depth for free air at 30 °C was calculated around 0.26 mm. Therefore, the plate spacing of 1 mm (i.e. diameter of fishing lines) is around 4 times of the thermal penetration depth. According to Tijani *et al* [4], the stack plate spacing of $4\delta_k$ will lead to the lowest temperature that can be reached by thermoacoustic coolers.

The existance of standing sound wave inside the resonator will pump heat through the stack from the right side to the left side of the stack, resulting in a cooling at the right and heating at the left of the stack (see Fig. 1). We used two digital thermometers with LM35 temperature sensor to measure the temperature at both cooling and heating point.

To study the influence of the stack location on the temperature decrease, we measure the temperature at the cooling point for various distance of the stack center from the closed end of the resonator. To investigate the effect of the stack length on the temperature decrease, we varied the length of stack from 16 cm to 2 cm by cutting the stack by 2 cm for every variation, so that we had 8 different values of the stack length.

III. Results and Discussion

Spectrum of the sound wave in the resonator tube at resonance condition at frequency of 106 Hz is depticted in Fig. 3. It is clearly seen that the first order componen is dominant. A litte shift in resonance frequency from the calculated value is caused by the insertion of stack into the resonator. Therefore, we need to check the resonance condition everytime we change the stack length and the location of the stack in the resonator.

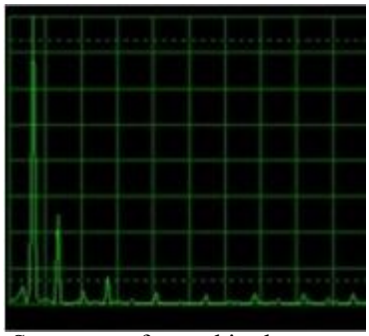

Figure 3. Spectrum of sound in the resonator tube at resonance condition at 106 Hz.

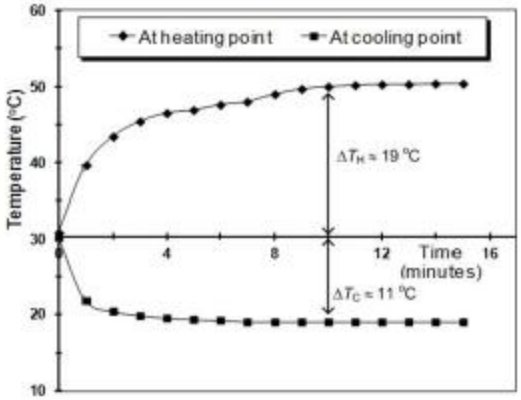

Figure 4. Temperatures of the heating and cooling points as a function of time, for stack length of 10 cm and stack'center location of 10 cm.

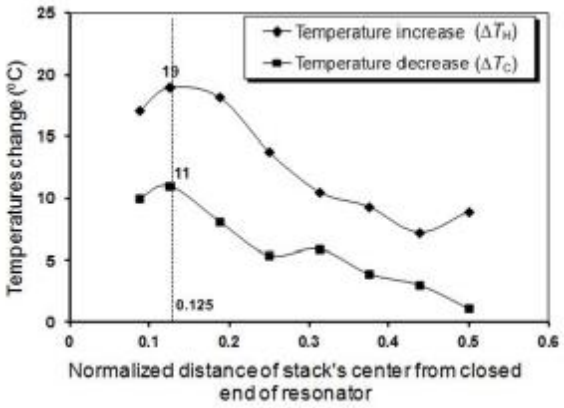

Figure 5. Temperature changes at the heating (ΔT_H) and cooling (ΔT_C) points for various locations of stack. Stack length is 10 cm.

A typical result of temperature measurement at the heating and cooling points as a function of operation time is shown in Fig. 4. In this case, we used stack with 10 cm in length, and the distance of stack's center from the closed end was 10 cm. This result confirms that heat transfer from the cold region to the hot region has occured, indicated by the decreasing and increasing temperatures of the cooling and heating regions, respectively. Initially, both points had the same temperature of 30 °C (T_0), and after 10 minutes operation the temperature at the cooling point (T_C) has decreased as much as 11 °C ($\Delta T_C = T_0 - T_C$) dropped to 19 °C, while the temperature heating point (T_H) has increased as much as 19 °C ($\Delta T_H = T_H - T_0$) up to 49 °C. After that, the air temperatures at both points roughly tended to constant which indicate that thermal equilibrium at both region occured. In addition, the temperature change at the hot region was greater than that of at the cold region due to the volume of the hot region is larger than that of the cold region.

Measurements like above were carried our for various distances of the stack's center location measured from the closed end of resonator. From the results, we can plot the largest temperature changes versus the stack location, as shown in Fig. 5 for which we have used a stack with length of 10 cm. It can be seen in the figure that there is an optimum distance which gives the maximum temperature changes at both heating and cooling points. The largest temperature decerease ($\Delta T_{C,max}$) was 11 °C, while the largest temperature increase ($\Delta T_{H,max}$) was 19 °C. Therefore, the largest temperature different between both ends of stack was 30 °C.

The maximum temperature changes (and temperature different) were occured at normalized distance of 0.125. Recall that the tube length is 80 cm then the optimum stack's center location is 10 cm measured from the closed end of resonator. The fact that the optimum location of stack is near the closed end (pressure antinode) can be understood because it will minimize the viscous dissipation of acoustic power, but standing wave system systems are powerless exactly at the pressure antinode of a standing wave.

Temperature measuments at the heating and cooling points were also conducted for various stack lengths. Figure 6 shows the measurement result in which the largest temperature changes of both heating and cooling points are plotted as functions of stack length. In this case, the stack's center location was at 10 cm from the closed end of resonator. We can see in the figure that there is an optimum length of stack which gives maximum temperature changes. The optimum length was 10 cm related to the maximum temperature decrease of 11 °C and maximum temperature increase of 19 °C.

The existance of the optimum length can be qualitatively explained as follow. A temperature gradient which is created along the stack will be proportional to the difference of the pressure amplitudes at both ends of stack. This pressure difference is larger for the longer stack as long as the stack is placed between the pressure node and antinode. On the other hand, however, the longer is stack, the greater is viscous loss which occures in the stack. When the stack length is less than its optimum value, the shorter stack gives smaller difference of pressure amplitudes at both ends of the stack, creates smaller temperature gradient

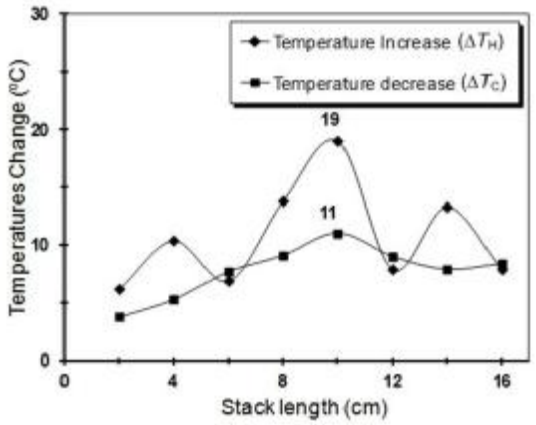

Figure 6. Temperature changes at the heating (ΔT_H) and cooling (ΔT_C) points for various lengths of stack. Stack's center location was at 10 cm from the closed end of resonator.

along stack and therefore the smaller temperature changes at the heating and cooling points. When the stack length is more than its optimum value, the longer stack means that one end of the stack gets closer to the pressure antinode (velocity node) and the other end gets closer to the velocity antinode. The first absorbs only a small acoustic power, and the second causes a larger viscous loss in the stack because of larger velocity.[11] In addition, the longer stack also contributes larger viscous loss due to the longer contact surface between gas and stack channels. These effects, therefore, make the heat transfer from the cold to hot region was not effective enough so that the temperature changes at both regions were smaller.

IV. Conclusion

It can be concluded that there are an optimum stack's length and an optimum location of stack inside resonator tube which are resulting in a maximum temperature decrease at the cooling point of a thermoacoustic cooler.

In this experiment, the optimum stack's length was 10 cm and the optimum location of the stack' center was at a distance of 10 cm measured from the closed end of the resonator. This optimum combination has given a temperature decrease of 11 °C so that the temperature at the cooling point has been lowered to 19 °C.

V. Acknowledgement

This research was supported financially by Community Fund of Faculty of Mathematics and Natural Sciences, Gadjah Mada University.

VI. References

1. G.W. Swift, J. Acoust. Soc. Am. 84, 1145 (1988).
2. G.W. Swift, *Thermoacoustics: A unifying perspective for some engines and refrigerators*, Acoustical Society of America, New York, 2002.
3. D.A. Russell and P. Weibull, Am. J. Phys. 70, 1231 (2002).
4. M.E.H. Tijani, J.C.H. Zeegers, and A.T.A.M. de Waele, J. Acoust. Soc. Am. 112, 128 (2002).

Discrimination of Coffee Aroma using Electronic Nose based on Gas Sensor Array and Principal Component Analysis

Radi[1*], M.Rivai[2], M.H. Purnomo[2], D. Hardiono[3], R. Kurniawan[3]

1 Doctoral Student, Department of Electrical Engineering, Faculty of Industrial Technology, Institut Teknologi Sepuluh Nopember, Kampus ITS Sukolilo Surabaya

2 Department of Electrical Engineering, Faculty of Industrial Technology, Institut Teknologi Sepuluh Nopember, Kampus ITS Sukolilo Surabaya

3 Bachelor students, Department of Agricultural Engineering, Faculty of Agricultural Technology, Gadjah Mada University

Abstract

Electronic nose is an instrument developed as an artificial model of the biological olfactory system. Since the weaknesses of human quality control are known well, researchers provide an alternative solution by developing this device. The device is especially needed for industries which use aroma as a quality attribute of their product, such as coffee industry. Although electronic nose has been developed in recent decades, but its implementation as an identifier of coffee aroma requires some extensive researches. Beside because of the complexity of the coffee aroma, it is also limited by the availability of related sensors. This study aims to analyze the ability of an electronic nose based on gas sensor array as an identifier system of coffee. Some coffee powders produced from different brands were tested. The potentiality of this electronic nose was evaluated by Principal Component Analysis (PCA). 2D mapping based on this analysis beside provided the information of discrimination level of each sample also gave an overview of this instrument when used to identify aroma of coffee sample. The level of discrimination evaluated with variation of aroma pattern described in this paper.

Keywords*: electronic nose, coffee aroma, discrimination, PCA*

* Corresponding author.
E-mail address: radi-tep@ugm.ac.id

I. Introduction

Aroma is a major quality attributes of coffee products. As a beverage, consumers prefer this product one because of its aroma. The smell of coffee gives a special sensation for the audiences who are very interested in consuming of the product. Coffee industries create a number of product diversification competitively and try to offer this product with various aroma and flavors. Because of the importance of aroma as a quality parameter, generally the coffee industries conduct closely monitoring system for this attribute in all stages of their coffee processing. This monitoring system is started from the receipt of raw materials into the packaging process. Old method conducted by industries for this assessment is known as sensory testing.

Sensory testing is conducted by involving some panelists for every analysis. A number of samples are conditioned with a standard procedure before evaluated. Experts or panelists assess the samples by providing a score for each sample tested. The combined score of all panelists for a sample presents the quality of the product. The accuracy of this assessment results is determined by the ability of panelists. The best results are obtained by involving many trained panelists. Each panelist should practice regularly in order to maintain his sensory ability. This rule causes this test expensive. In addition, the assessment provide by human is also be influenced by psychological factors and subjective perception. Besides, the physical condition of panelists and environmental condition can also affect to the final result of the test. Aware with this weakness, researchers develop an electronic nose as an alternative in assessing of the aroma of coffee.

Electronic nose is a model of artificial olfaction inspired by biological olfactory system. Electronic nose is commonly developed to detect, identify and classify an aroma (odor) of a sample by simulating the identifying process of odor by human olfactory system (Pierce, 2003). In basic manner, identification process of aroma by biological olfactory system in human or animal can generally be described as follows. Volatile compound of aroma entering our nasal cavity will be absorbed by smell-sensitive receptors located in

the cavity. Chemical signals released by the receptor are transmitted to the brain as the center of the olfactory nerve to be identified.

Additionally, Pierce (2003) explained that the physicochemical attributes sensed of smell are not identified correctly, as well as the receptors that respond to the presence of the volatile compounds. Some literature stated that not all of the receptors in the nasal cavity respond to the presence of the compounds. Only receptors those are sensitive to a certain volatile issue a physicochemical signal. Thus, the experts argue that the aroma should be translated into a distinctive fingerprint pattern first before identified. The assurance underlies the expert to develop an artificial olfactory system by applying several sensors in one array as a pattern generator of aroma sample. Although the entire sensors respond to the exposure of fragrance, but the difference responses allow to be processed into a typical fingerprint pattern.

The working principle of an electronic nose based on gas sensor array can be described as follows. The sample to be detected should be entered into a chamber containing the sensor array. The response of each sensor is acquired and processed into the form of aroma pattern. Then the pattern is identified by a pattern recognition algorithm used in the system to determine the types of fragrance analyzed.

Based on the principle, an electronic nose has four main sections. These sections are odor handling and delivery system, detector (sensor), signal conditioning and preprocessing, and pattern analysis and identification system. The function of the first part is to prepare and provide a sample into the detector. The detector will respond to the presence of the sample. The response depends on the amount of volatile compound contained in the sample. The responses of all detectors should be processed into a special pattern (aroma pattern) that can be used to represent the aroma of coffee sample. The pattern is then interpreted by a smart system used, which can be either a database or other intelligent systems such as neural nets. The more typical of aroma pattern produced from each sample, the higher opportunity for researcher to use this instrument.

Although the principle is easy but the implementation of an electronic nose as an identifier system of coffee aroma needs a dept-research. Many factors affect to the early success of this system in coffee aroma recognition. Complexity of coffee aroma compounds is one factor that inhibits the use of the electronic nose. Researchers have investigated the components of coffee aroma. Previous research has concluded that coffee contains more than 800 compounds. These compound interact each other to form the profile of aroma. It is also influenced by the amount of natural aroma compounds contained in the coffee beans after harvesting and the process conducted in secondary processing. This fact beside makes the coffee aroma has a complex dimension also causes some laboratory analyses cannot be used to represent the profile of coffee aroma. Therefore effort of aroma pattern recognition is more precise in classifying of the coffee quality.

Study of the coffee quality from sensory aspect has been done by Bhumiratana (2010). This study attempted to analyze the sensory aspects that are important in secondary coffee processing started from the receipt of raw materials to final result of end product. This quality attribute resulted in this study is became a challenge should be solved in the development of the electronic nose. In advance, the electronic nose should be developed in order to assist or replace the fuction of panelist in sensory testing. In addition, studies about laboratories analysis for coffee aroma have also been thoroughly investigated.

Research on the implementation of an electronic nose as aroma pattern identification has been reported by investigators. Electronic nose based on semiconductor sensor array in quality monitoring of tomato during storage and mandarin maturity have been reported by Gomes, et.al (2006), in evaluating of harvesting time of apple has been reported by Saevels, et.al (2003), in identification of the grade of tea has been published by Yu, et.al (2008), in monitoring of quality degradation of meat during storage combined with color analysis has been reported by Cunshe, et.al (2007). Electronic nose used to recognize the aroma of coffee has also been reported by several researchers. Pardo, et.al (2001) reported a study on the use of an electronic nose for quality control of coffee. This study tries to classify the quality of coffee sample using an electronic nose, and the results were compared with the result of sensory testing.

The results of these researches indicate that there are needed some depth studies related to the implementation of an electronic nose as an identifier system of coffee aroma. The main point in determining of the aroma identification is the uniqueness of the aroma pattern formed by the

signal combination of the sensor array. The specificity of aroma pattern determines the ability of the intelligent system in this device. Therefore, designing an electronic nose should be started by peculiarity evaluation of sample aroma patterns to be classified. The specificity pattern of aroma can be evaluated by the level of discrimination of each pattern. PCA is one method that can be used to show the level of discrimination pattern of each sample. This study aimed to evaluate the opportunities of an electronic nose as an identifier device of coffee aroma with PCA analysis.

II. Method

A. Device Setup

This study used an electronic nose based on gas sensor array. Schematically designed hardware is presented in Fig. 1. The device has four main parts, i.e. odor handling and delivery system, detector, signal conditioning, and data acquisition devices. The detector was designed by 8 gas sensors coupled in one array. The sensors used were MQ135, MQ136, MQ137, MQ138, MQ2, MQ3, TGS822, and TGS2620.

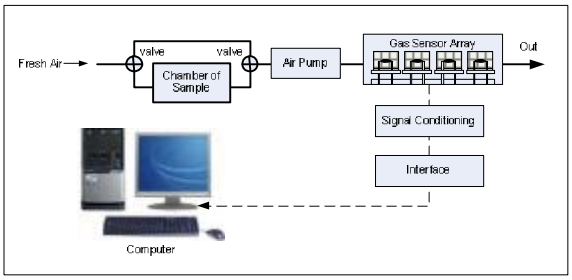

Figure 1. Device setup

B. Material

Samples of coffee powder processed from two varieties of Arabica and Robusta coffee either in pure powder or blending were evaluated in this study. The samples also reflected the difference of origin. There were 14 samples tested in this study.

C. Experiment procedure

This research was carried out by the following procedure. The smell of coffee was brought by the odor sampling and delivery system into the head of the sensor array (detector). Detectors gave response to the exposure of the aroma sample by changing of their conductivity. With a signal conditioner, these changes could be converted into a voltage that makes it possible to be acquired. The level of the voltage represented the exposure of aroma volatile compound in the sensor headspace. Then, the voltage was recorded and analyzed into pattern of aroma. The discrimination of all samples was evaluated by PCA. The level of discrimination was evaluated through a 2D mapping by taking the first principal component as an absis and the second principal component as an ordinate. Schematically, the data analysis procedure can be presented on Fig. 2.

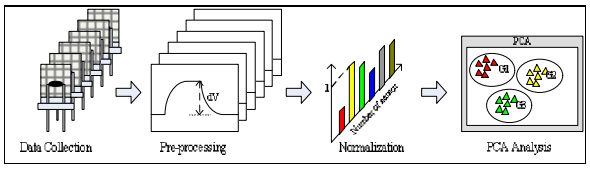

Figure 2. Data analysis procedure

The analysis was started by the process of data acquisition, continued to the process of aroma pattern formation, and finally pattern evaluation. To determine the pattern that provide the best level of discrimination, this study implemented three methods of pattern formation, they were aroma pattern formed from the absolute voltage of the gas sensor array, aroma pattern formed from effective change of the sensor conductivity, and the aroma pattern formed from the change of relative conductivity of the sensor array. The aroma pattern should be formed in normalized pattern in order to eliminate the effect of the amount of samples analyzed. Besides, in this study also conducted with time variation of data sampling.

III. Result and Discussion

After the device was assembled and tested, the next step was collecting data needed. Sample was prepared in the sample chamber at room temperature. The aroma of coffee sample was flowed from the chamber to the detector with a constant velocity. Exposure of this aroma compound led to change the conductivity of all sensors that can be presented on Fig. 3.

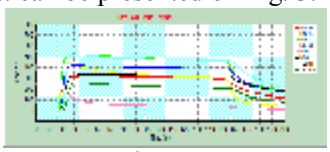

Figure 3. Response of gas sensor array when the sample was exposed

Fig. 3 shows the voltage of the gas sensor array as a function of time by exposing of the sample. The pattern was formed with 3 variations of time sampling, i.e with duration of 50-60s, 75-85s, and 100-110s for three variations of pattern formation method as described in previous section. The distribution of coffee aroma pattern analyzed by PCA could be described as follows.

A. Aroma pattern based on absolute voltage of sensor

Visualization of the distribution of the pattern formed by absolute voltage of sensor array in 2D systems with PCA analysis for all variations of sampling time were presented in Fig. 4.

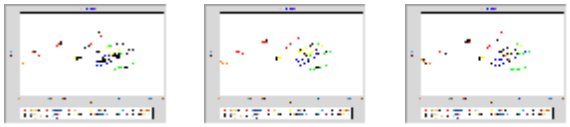

(a) (b) (c)

Figure 4. Distribution of coffee aroma pattern formed by absolute voltage with PCA analysis, (a) sampling time of 50-60s, (b) sampling time of 75-85s, (c) sampling time of 100-110s

The pattern distribution presented on Fig. 4 explained most of the samples collected in one group and only a small number was able to be classified clearly for overall variations of the sampling time.

B. Aroma pattern based on the change of voltage of sensor

Discrimination of all sample patterns formed by the second method was presented on Fig. 5. Compared with the first analysis, there are more sample can be clustered clearly. From this result, it can be inferred that the pattern formed by this method provides a better level of discrimination.

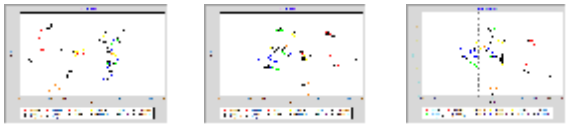

(a) (b) (c)

Figure 5. Distribution of coffee aroma pattern based on the change of sensor conductivity with PCA analysis, (a) sampling time of 50-60s, (b) sampling time of 75-85s, (c) sampling time of 100-110s.

C. Aroma pattern based on the change of relative conductivity of sensor

In this method, the aroma patterns were formed by changes in sensor conductivity relative to the initial conductivity. The discrimination mapping for each pattern analyzed by PCA was presented on Fig. 6. The 2D mapping shows the distribution pattern of all data evaluated. This mapping presents a better separation than the two previous methods. Some samples were able be discriminated clearly with this method.

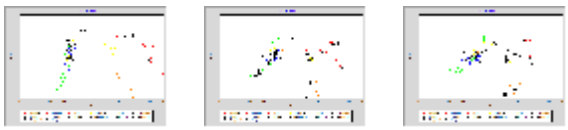

(a) (b) (c)

Figure 6. 2D mapping of coffee aroma pattern based on relative conductivity of sensor analyzed by PCA, (a) sampling time of 50-60 s, (b) sampling time of 75-85 s, (c) sampling time of 100-110s

The 2D visualization provided the information about discrimination level between patterns that possible to be classified with this device. This result also explains an overview of the identity of sample giving high opportunity to be identified successfully when the electronic nose is implemented. This analysis is important because with the result we are able to choose which one of the samples that could be analyzed with this system. Only patterns separated well on the mapping allowed to be recognized successfully by this model. When connected with the variety of coffee samples tested, the discrimination pattern presented on Fig. 6 had able to distinguish the sample into two groups, samples processed from Arabica were clustered on the right side, while coffee produced from Robusta and combination of Robusta and Arabica (blended coffee) were separated on the other side. Meanwhile, when viewed from the origin, the discrimination pattern showed on Fig. 6 couldn't be used to explain it properly.

IV. Conclusion

This study has evaluated the distribution mapping of coffee aroma pattern formed by using an electronic nose based on gas sensor array. The sensor array consists of eight types of semiconductor sensor placed inside a chamber. PCA was used to visualize the distribution of aroma pattern of coffee samples. Analysis results showed that some of the coffee samples capable to be classified properly, while others were not clustered well. Based on the sample tested, mostly samples processed from two varieties of coffee, tends to produce a similar pattern. Therefore, this study needs to be continued with laboratories analysis of all samples tested as comparison.

Acknowledgment

This research was supported by Gadjah Mada University (Grant no. LPPM-UGM/309/BID.I/2012). Special thank for PT. Aneka Coffee Industry, Mr. Saikhul, Mr. Sugeng, and others for their contribution in this work.

References

1. Bhumiratana, N., Adhikari, K., Edgar Chambers IV, E. 2011. Evolution of sensory aroma attributes from coffee beans to brewed coffee. Journal of LWT - Food Science and Technology. doi:10.1016/j.lwt.2011.07.001.
2. Freitas, A.M.C., Parreira, C., Vilas-Boas, L. 2001. The Use of an Electronic Aroma-Sensing Device to Assess Coffee Differentiation – Comparison with SPME Gas Chromatography-Mass Spectrometry Aroma Pattern. Journal of Food Composition and Analysis 14 p: 513-522.
3. Korhonova, M., Hron, K., Klimcíkova, D., Müller, L., Bednár, P., Barták, P. 2009. Coffee aroma—Statistical analysis of compositional data, Journal of Talanta 80 p:710–715. http://www.elsevier.com/locate/talanta.
4. Mulato, S. and Suharyanto, E., 2011. Post Harvest Coffee Processing in Indonesia an Introduction to Good Manufacturing Practices. 2nd edition. Indonesian Coffee and Cocoa Research Institute. Jember. Indonesia.
5. Mulato, S., Suharyanto, E., Kaswanto. 2010. Product Development of Coffee. Indonesian Coffee and Cocoa Research Institute. Jember. Indonesia.
6. Pardo, M., Faglia, G., Sberveglieri, G., Quercia, L. 2001. Electronic Nose for coffee quality control. In Proceeding of IEEE Instrumentation and Measurement Technology Conference. Budapest, Hungary. 0-7803-6646-8/01/$10.00200 01 IEEE.
7. Pearce, T. C.; Schiffman, S. S.; Nagle, H.T.; dan Gardner, J.W., 2003. Handbook of Machine Olfaction. WILEY-VCH Verlag GmbH & Co. KGaA, Weinheim, Germany.
8. Pornpanomchai, C., Jurangboon, K., Jantarase, K. 2010. Instan Coffee Classification by Electronic Noses. In Procceding of 2nd International Conferencee on Mechanical and Electronic Engineering (ICMEE 2010). Volume 1. 978-1-4244-7481-3/$26.00 © 2010 IEEE.
9. Radi, Rivai, M., Purnomo, M.H. 2011. Multi-Thread Constructive Back Propagation Neural Network for Aroma Pattern Classification. In Proceding of 2011 IFSA-AFSS International Conference.
10. Radi, Rois, M., Rivai, M., Purnomo, M.H. 2011. Identifikasi Aroma Tembakau dengan Deret Sensor Gas dan Jaring saraf Tiruan. Proceeding of National Perteta Conference 2011, Jember. Indonesia.
11. Rivai, M. 2007. Pengaruh *Principle Component Analysis* Terhadap Tingkat Identifikasi *Neural Network* Pada Sistem Sensor Gas. TELKOMNIKA Vol. 5, No. 3, Desember 2007 : 159 – 167.

Development of coloured-light mixer for teaching coloured light and colour perception concepts

SuchaiNopparatjamjomras[1,2], Ratchapak Chitaree[2], and Thasaneeya R. Nopparatjamjomras[1*]
1Institute for Innovative Learning, Mahidol University, Phuthamonthon 4 Rd., Salaya, Phuthamonthon Nakhonpathom 73170 Thailand
2Department of Physics, Mahidol University, Rama VI Rd, University, Bangkok, 10400, Thailand

Abstract

Coloured light and colour perception concepts are taught in secondary and/or high school levels. However, many misconceptions are held by a number of students [1], i.e. 1) the mixing of coloured lights follow the same rules as those of coloured paints and pigments also the primary colours of light are the same as the primary colours of paints and pigments used by artists (red, yellow and blue); 2) when a coloured light illuminates a coloured object, the colour of the light mixes with the colour of the object. Many coloured-light mixers [2-13] have been developed in terms of a light source (filament lamp, projector, sunlight, laser and LED) and a size of the mixer to help students improve their understanding about coloured light and colour perception. The teaching technique used with these mixers was demonstration, which students could only perceived about primary coloured light mixing. Students did not inquire what coloured lights are the primary coloured lights. In addition, to modify light sources and to provide dimly lit or dark rooms in schools were presented as limitations of those mixers. To teach primary coloured lights in an inquiry way, which students are engaged to inquire the primary coloured lights, a new mixer is required. The new mixer needs to have more than 3 coloured lights (red, green, and blue) as presented in general mixers. Therefore, researchers developed the new mixer having 4 buttons to control 4 coloured-light sources; red, green, blue, and yellow. In addition, the new mixer is able to generate, in a normally-lit room, bright and clear coloured lights without any modification to the light sources. Moreover, researchers designed a PODS (Predict-Observe-Discuss-Synthesize) [14] based activity to help students discover the primary coloured light by themselves.

Keywords : *Coloured light Mixer, Primary coloured light*

* Corresponding author.
E-mail address: Thasaneeya.rat@mahidol.ac.th

I. Introduction

Primary coloured lights and their mixing is a basic concept to understand a coloured light and colour perception. This concept is also applied to many everyday life phenomena such a an Light-Emitting Diode (LED) traffic light or sign board, colour monitor, and stage lighting. A basic instrument for teaching primary coloured lights and their mixing is a coloured light mixer. Therefore, it has been developed by many researchers [4, 6, 10, 13, 15-18].

These researchers tried to develop their mixer in terms of a light source (filament lamp, projector, sunlight, laser, and LED) and a size of the mixer. Their mixers could help students memorize the results of primary coloured lights mixing better than reading from a book or looking at the primary coloured lights mixing chart (see Figure 1). However, the question of "Why are the primary coloured lights not red, yellow, and blue?" could not be solved by the previous mixers. They were designed as a "demonstration" tool. Students could only perceive the results of primary coloured lights mixing.

Figure 1 *Primary coloured lights mixing chart*

To help students get the answer of the above question, the mixer having more than 3 coloured lights (red, green, and blue) as presented in the general mixers is required. The detail of

how many and what coloured lights should be used for the new mixer will be described in the second section.

As many researchers mentioned about the disadvantage of using a traditional passive teaching method i.e., 1) it only requires students to memorize facts and properties without developing much understanding of the underlying physics principles [1, 19, 20] 2) what they are taught is separated from what they are familiar in their everyday life 3) students could not link what they learn in a science classroom to the applications in real life situations. Those researchers also mentioned that traditional passive teaching method could lead students to confuse the ideas and have misconceptions. Therefore, a PODS (Predict-Observe-Discuss-Synthesize) [14] based activity used with the new mixer was designed to help students discover the primary coloured lights by themselves.

In addition, the other benefit of the new mixer is the ability to generate, in a normally-lit room, bright and clear coloured lights without any modification to the light sources.

II. The new colured light mixer

As mentioned in the introduction that the new mixer has to have more than 3 coloured lights (red, green, and blue). However, it appears true that the more coloured lights used with the mixer, the more difficult for students to find the primary coloured lights. To optimize the number of coloured lights used with the mixer and what they are, the misconceptions as "the primary colours used by artists (red, yellow and blue) are the same as the primary colours for all colour mixing" [1] was used as a guideline to choose red, green, blue, and yellow coloured lights for the mixer.

There are 11 possible combinations of these four coloured lights of maximum intensities as shown in Table 1. However, to correct students' misconception about the primary colours of light as mentioned in the above paragraph (yellow is not a primary colour of light) and to learn about the mixing of primary coloured lights, students need to observe only four combinations (1^{st} to 4^{th}). In addition, the 5^{th} combination could help students correct their misconception as "The mixing of coloured paints and pigments follow the same rules as the mixing of coloured lights" [1]; students who have this misconception always give a response as a green colour.

Table l. All possible combinations of these four coloured lights of maximum intensities

Combination	Mixing of coloured light
1	Red and green
2	Red and blue
3	Blue and green
4	Red, green, and blue
5	Blue and yellow
6	Red and yellow
7	Green and yellow
8	Red, green, and yellow
9	Red, blue, and yellow
10	Green, blue, and yellow
11	Red, green, blue, and yellow

Therefore, a microcontroller was used to control the three tiny LEDs (red, green, and blue) individually to 1) limit the output of the mixer as only the 1^{st} to 5^{th} combinations are available (other combinations will produce no colured lights from the mixer) 2) create a yellow light which is a mixing of red and green lights with the same intensities. Moreover, the mixer was designed to introduce an idea of "colour shading" to students by integrating a tuning circuit to make the green LED change its intensity. Therefore, students were able to perceive an orange colour from the mixer. The mixer and the coloured lights generated by the mixer are shown in Figure 2 and 3 respectively.

Figure 2 *The mixer*

Figure 3 *Coloured lights generated by the mixer*

III. The activity

The PODS learning cycle was used as a guideline to design the activity to help students correct their misconception about primary coloured lights and their mixing. The PODS is a short form of Predict, Observe, Discuss, and Synthesize [14].

In the activity, students were encouraged to share with the class about their definition of primary colours which was "primary coloured lights cannot be generated from other coloured lights and also that it cannot be separated into other coloured lights. Students then had to choose which one of the four alternatives is a set primary colours of light; a) red, green, and blue b) red, yellow, and blue c) cyan, magenta, and yellow d) red, orange, yellow, green, blue, indigo, and violet. After that, students were encouraged to make a prediction and observation about the mixing of coloured lights as shown in a Table 2.

Questions	Predict	Observe
1. The colour of light produced by the mixing of red light and blue lights with the maximum intensity is……		
2. The colour of light produced by the mixing of red light and green lights with the maximum intensity is……		
3. The colour of light produced by the mixing of green light and blue lights with the maximum intensity is……		
4. The colour of light produced by the mixing of blue light and yellow lights with the maximum intensity is……		
5. The colour of light produced by the mixing of red light, green light and blue lights with the maximum intensity is……		
6. The colour of light produced by the mixing of red light and green with the green intensity is less than red intensity is……		

Students then discussed in a group to solve any conflict between prediction and observation. This discussion could help students correct their misconceptions such as students would learn that yellow is not a primary colour of light because it could be generated by the mixing of red and green lights (the 2nd question).

Finally, students synthesized the coloured lights mixing data to conclude that 1) the mixing of coloured paints and pigments do not follow the same rules as the mixing of coloured lights 2) yellow is not a primary colours of light.

IV. Conclusion

The previous coloured light mixers were designed as a demonstration tool so students did not have a chance to find the reason why the primary colours of light are not the same as that of paint.

The new mixer was designed as an inquiry tool to give students a chance to find out the primary colours of light based on their existing knowledge about the definition of primary colours.

Some technologies were used to 1) eliminate many problems or difficults found in the previous research such as the ability of a surface mount LED to generate, in a normally-lit room, bright and clear coloured lights without any modification to the light sources 2) reduce some students' difficult i.e., a microcontroller to limit the output of the mixer as only the 1st to 5th combinations are available.

V. References

1. Beaty, B. *Children's misconceptions about science (including colour misconceptions) can be found on Bill Beaty's web site*. 1998 23 May 2008]; Available from: http://www.amasci.com/miscon/opphys.html or http://www.eskimo.com/~billb/miscon/ophys.html
2. Bartels, R.A., *Using a video projector for color-mixing demonstrations.* The Physics Teacher, 1982. **20**(4): p. 247-248.
3. Bartels, R.A., *A hallway display of additive color mixing.* The Physics Teacher, 1986. **24**(9): p. 564-565.
4. Butler, W.A., A.D. Davis, and J.C.E. Miller, *Color mixing for a large audience.* The Physics Teacher, 1979. **17**(1): p. 43-43.
5. Chiaverina, C., *The Ping-Pong Ball Color Mixer Revisited.* The Physics Teacher, 2007. **45**(2): p. 120-120.
6. Cockman, J., *A Bright Color Mixer.* The Physics Teacher, 2002. **40**(9): p. 553-553.
7. Greenslade, J.T.B., *The von Nardroff Color Mixing Apparatus.* The Physics Teacher, 2005. **43**(9): p. 602-602.

8. Heilemann, J.J., *A Lantern Slide Color Mixer*. The American Physics Teacher, 1935. **3**(4): p. 184-184.
9. Heilemann, J.J., *An Indicating Lantern Slide Color Mixer*. The American Physics Teacher, 1936. **4**(4): p. 211-211.
10. Luttikhuizen, M.G., *Color mixing using a single projector*. The Physics Teacher, 1988. **26**(5): p. 296-297.
11. Maroto, J.A., C.M.P. Valverde, and J.E.B.-G. Tejero, *Description of additive colour mixing exhibits by using PC-designed Maxwell discs*. Physics Education, 2006. **41**(5): p. 448-452.
12. Parsons, L., *As easy as R, G, B*. The Physics Teacher, 1998. **36**(6): p. 347-348.
13. Planinšič, G., *Color Mixer for Every Student*. The Physics Teacher, 2004. **42**(3): p. 138-142.
14. Lakhadar, Z.B., et al., *Active Learning in Optics and Photonics Training Manual*2006, Paris: UNESCO.
15. Cortel, A., *Simple Experiments on Perception of Color Using Cardboard Turbines*. The Physics Teacher, 2004. **42**(6): p. 377-377.
16. Holtsmark, T., *A Demonstration of Additive Color Mixing Rules under the Influence of Color Contrast*. American Journal of Physics, 1969. **37**(6): p. 662-664.
17. Palmquist, B.C., *Interactive spectra demonstration*. The Physics Teacher, 2002. **40**(3): p. 140-142.
18. Wyrembeck, E.P., *A Student-Centered Interactive Color Quiz*. The Physics Teacher, 2003. **41**(9): p. 531-533.
19. Hake, R.R., *Interactive-engagement versus traditional methods: A six-thousand-student survey of mechanics test data for introductory physics courses*. American Journal of Physics, 1998. **66**(1): p. 64-74.
20. Thornton, R.K. and D.R. Sokoloff, *Assessing student learning of Newton's laws: The Force and Motion Conceptual Evaluation and the Evaluation of Active Learning Laboratory and Lecture Curricula*. American Journal of Physics, 1998. **66**(4): p. 338-352.

Partial Double Wall Incubator for Proposed Optimal Thermoregulator Supporting Media of Newborn Care

Ruri Agung W.[1*], Nailil Dahliyah[1], Irana Eka P.[1], Tri Dedi S.[2], Ridho Hantoro[1]
1 Department of Engineering Physics, Institut Teknologi Sepuluh Nopember
Jl. Arief Rahman Hakim 60111, Sukolilo, Surabaya
2 Thermal Laboratory, Medical Equipment and Calibration Center (BPFK) Surabaya
Jl. Karangmenjangan No. 22 60286, Surabaya

Abstract

Incubator should provide neutral temperature environment (NTE) to achieve the thermal comfort so that the newborn will not suffer hypothermia due to higher heat losses. The presence of double wall inside the incubator is hypothetically capable to reduce the heat loss of newborn nursed in incubator. This study was conducted by numerical computation that aims to analyze the effect of partial double wall to the heat loss of a newborn constrained to radiant and convective heat losses. Computational Fluid Dynamics (CFD) was used to evaluate the aspects of thermal comfort including temperature – airflow distribution and heat losses in three setting of air temperature (32, 33 and 35°C). Based on the result of numerical calculation, temperature distribution could be improved however the average chamber temperature decrease down to 0.25°C. The average magnitude of airflow close to newborn's body is 0,00304ms^{-1} that induces lower evaporative heat loss. The partial double wall incubator can reduce the dry heat losses down to 6.99 – 9.87W m^{-2} or 30.8 – 43.38% compared to single wall incubator. All in all, the partial double wall can be proposed for further development of infant incubator providing optimal NTE.

Keywords: *Double wall incubator, NTE, Newborn, Dry heat loss.*

* Corresponding author.
E-mail address: r_agung_w@ep.its.ac.id

I. Introduction

Keeping newborns warm is important for their survival since they have incomplete skin tissue and organs as the normal newborn [1]. Consequently the ability to avoid excessive heat loss to the environment and to maintain its body temperature is weak. This condition will affect to high risk to suffer hypothermia. The risk of hypothermia is important for newborn related to its thermoregulation [2]. Hypothermia causes imbalance metabolism, IQ and growth problem, cold trauma and death [2, 3]. A worse baby's body thermoregulation is caused by imbalance of heat production and heat loss since thermal environmental is not optimum for nursing.

Nursing newborn baby needs the neutral temperature environment (NTE) for avoiding thermal stress [4]. The condition of NTE is achieved while the setting environmental temperature is able to maintain the body temperature in normal range and induce minimum energy (O_2) consumption [3, 4]. Hypothermia, cold stress, might be induced by improper nursing method and media. The problem remains in nursing media is the biggest problem compared to nursing method. Incubator, one of nursing media for newborn baby, is widely used for a baby to spend the time until the health back to normal. Unfortunately most of incubators have a problem of temperature distribution which much accumulated in the mattress. The problem of temperature distribution can induce undesired thermal comfort that causes abnormality of baby's thermoregulation.

In order to provide optimum thermal environment inside the incubator, modification to the geometry has been studied by experiment and/or numerical method. To overcome this, baby incubators were developed by using double wall where the hot air stream is passed between the two walls. This modification is hypothetically shown to have the advantage of reducing the excess evaporative heat loss, reduce heat production, and reduce radiant heat loss compared to an incubator with a single wall [5 - 7]. In this research, numerical study based on Computational Fluid Dynamics (CFD) is proposed to analyze the dry heat loss of newborn baby nursed in double wall incubator since recent simulation result of neonatology modeling is quite satisfying [8, 9].

II. Method

The study of dry heat loss is conducted by numerical method. All numerical calculations

have been performed using the commercial computational fluid dynamics (CFD). Numerical calculations have been calculated for three different air setting temperatures, 32, 33 and 35°C. The incubator geometry design is refer to the geometry of trapezoidal top walled incubator AMECARE in the Department of Medical Instrument and Calibration Surabaya. Double wall as the modification is added 3 cm from the front to back side of incubator. The study is based on measurement data.

2.1. Thermoregulation and Dry Heat Loss

Thermoregulation of newborn is widely defined as physiological control of the body to maintain the balance of heat production and heat loss. The main objective of thermoregulation is to keep the environment achieves NTE and minimize the energy loss. Based on empirical study, the heat production of a baby is determined as follow [8]:

$$\dot{Q}_M = 0.0522 m\, p + 1{,}64 \quad (1)$$

where m is mass of newborn (kg) and p is newborn's age (days). The modes of heat loss for nursing baby are heat loss by conduction, radiation, evaporation, and convection [10]. All of modes, except evaporation, are dry heat loss.

2.2. Mathematical Model

Numerical method is built by employing the governing equations such as conservation of energy, momentum and continuity [11]. Energy conservation is determined as equation below.

$$\frac{\partial}{\partial t}(\rho E) + \nabla.(\vec{v}(\rho E + p)) = \nabla.k_{eff}\nabla T + \nabla.(\bar{\bar{\tau}}_{eff}.\vec{v}) + S_h \quad (2)$$

where k_{eff} is effective conductivity which the value is equal to sum of k and k_t (thermal conductivity for the presence of turbulence). The two term on the right side represent the energy transfer by conduction and viscosity dissipation. For the solid region (i.e. newborn body), energy transfer is calculated by employing equation as follow:

$$\frac{\partial}{\partial t}(\rho h) + \nabla.(\vec{v}\rho h) = \nabla.(k\nabla T) + S_h \quad (3)$$

where ρ is solid density, h is sensible enthalpy, k is conductivity constant of newborn, T is newborn skin temperature, and S_h is volumetric heat source.

The equation (2) and (3) are complemented by continuity and conservation of momentum defined below [8]:

$$\nabla.u = 0 \quad (4)$$

$$\rho\frac{du}{dt} = F - \nabla p + \mu\nabla^2 u \quad (5)$$

where p is normal pressure (N/m^2), F is body force on solid region (nursed baby).

For natural-convection flows, faster convergence of numerical calculation can be retained with the Boussinesq model. It sets the fluid density as a function of temperature. The Boussinesq model is represented by equation below [11]:

$$\rho = \rho_0(1 - \beta(T - T_0)) \quad (6)$$

where β is thermal expansion coefficient (1/K), T_0 dan ρ_0 represent the operational parameter. This model is valid if satisfying for $\beta(T - T_0) << 1$.

Radiant heat transfer is modeled with the presence of absorptive and dispersive medium by this following equation.

$$\frac{dI(\vec{r},\vec{s})}{ds} + (\alpha + \sigma_s)I(\vec{r},\vec{s}) = \alpha n^2\frac{\sigma T^4}{\pi} + \frac{\sigma_s}{4\pi}\int_0^{4\pi} I(\vec{r},\vec{s})\Phi(\vec{s}\cdot\vec{s}')d\Omega' \quad (7)$$

where $\vec{r}$ is vector of position, $\vec{s}$ is directional vector, $\vec{s}'$ is scattering vector, s is path length, α is absorption coefficient, n is refractive index, σ_s is scattering coefficient, σ is Stefan-Boltzmann constant (5,672 x 10^{-8} W/m^2.K^4), I is radiance intensity, T is temperature, Φ is phase function and Ω is solid angle to solid region.

2.3. Numerical Method on CFD

There are three main stages must be completed in CFD simulation. They are preprocessing, solving, and post processing. The preprocessing consists of CAD drawing of incubator geometry, meshing the 3D model, defining the boundary condition and domain.

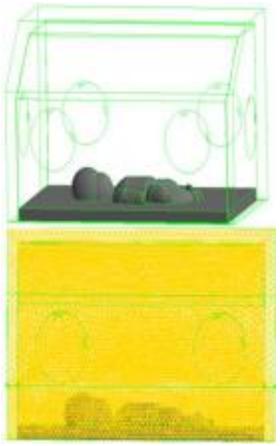

(a) (b)

Fig 1. (a) 3D model of double wall incubator and (b) meshed incubator with tetrahedral type.

It is shown in Fig 1 that incubator can be modeled by simplify several details of the geometry. The incubator is meshed using tetrahedral type and the worse element is less than 0.85 which indicate the successful meshing. The physical parameter of boundary condition defined in preprocessing is given as follow.

Table 1. Physical parameter of boundary condition in three environmental temperatures based on measurement.

Boundary Condition	Value of Parameter		
	32°C	33°C	35°C
Airflow inlet (m/s)	0.15	0.14	0.09
Inlet Temperature (K)	305.75	306.93	309.50
Outlet Temperature (K)	304.23	305.46	308.51
Wall Temperature (K)	304.42	305.50	307.50
Double Wall (K) *	304,51	305,76	307,92

*) Incubator with inner wall

The solving stage employs 3ddp (3 dimensions double precision) method. The control solution of all of chosen equation is coupled pressure-velocity simple mode and the discretization is chosen to be second order upwind. There are no changes on convergence limit (under relaxation factor) from the default.

Visualization (post processing) is done by figuring contour of temperature, path line of airflow, radiant heat flux, and wall temperature coefficient. Convective heat loss is determined by multiplying the average wall temperature coefficient, convective area of newborn body and temperature different between the body and air in surrounding.

III. Result and Discussion

The first analysis before focused on the dry heat loss is about the first validation to the CFD performance. The result of simulation for k-omega SST based is well validated by experimental data on empty chamber of single wall incubator. The range of error on temperature distribution is 0.36 – 2.37% and error on airflow distribution is 3.37 – 5.50%. Based on 5% error criteria, the result of simulation is accepted.

Temperature distribution is important to be analyzed since it is one of parameter that induces high or low heat loss of nursed baby. The temperature distribution of the incubator chamber in both of incubator is shown as Fig 2. A better temperature distribution is possessed in single wall incubator (see Fig 2). However the typical contours of temperature of both incubators are alike. The average chamber temperature of double wall incubator is lower than the average temperature of single wall incubator. The deviation of average chamber temperature compared to set point temperature in double wall incubator is 0.3 – 1.94 °C higher than the single wall incubator has.

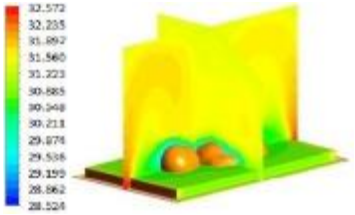

(a)

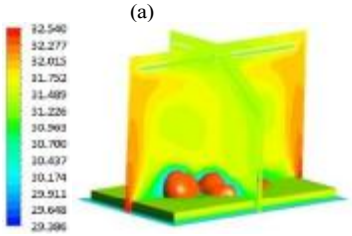

(b)

Fig 2. Temperature distribution (°C) on an infant incubator (a) single wall and (b) partial double wall for 32°C environment temperature.

The presence of double wall implies higher magnitude of air velocity which flow back to newborn body. It is caused by increase of air momentum since molecules of air collides to the solid material (inner wall). In higher environment temperature, the amount of airflow's path line inside the chamber decrease significantly as the heated air (lighter density) is accumulated in the area between the top outer wall and inner wall.

The result of radiant heat loss can be seen in Fig 3. Radiant heat flux as the hat loss by radiation mode is represented by contour of color in the body. Incubator with double wall can reduce the radiant heat flux due to the red color (indicate highest heat loss) is getting fade.

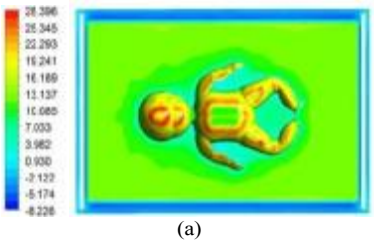

(a)

(b)

Fig 3. Radiant heat flux (W/m^2) on an infant incubator (a) single wall and (b) partial double wall for 32^{o}C environment temperature.

Both of incubators have almost the same trend of radiant heat loss related to increasing environment temperature. However the radiant heat loss in a double wall incubator is lower of 7 – 12.5 Watt/m^2 than single wall incubator. The convective heat loss is represented by the contour of wall heat transfer coefficient figured below.

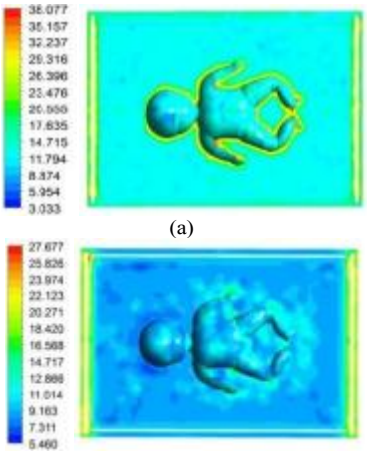

(a)

(b)

Fig 4. Convective heat transfer coefficient (W/m^{2}K) on an infant incubator (a) single wall and (b) partial double wall for 32^{o}C environment temperature.

Fig 4 shows that there is significant different of wall heat transfer coefficient's contour in both of incubator. Comparing to radiant heat loss, the magnitude of convective heat loss is relative low. This is caused by the very low airflow inside incubator, the insignificant temperature different of body and air so that the calculation does not result the big magnitude of convective heat loss at all of environment temperature. The numerical calculation is verified as the evidence that the simulation really represent the real physical condition. The result of CFD simulation is validated with experimental study conducted by Hey and Katz [2]. The newborns observed in their experiment are nursed in single wall incubator. The verification can be seen as follow.

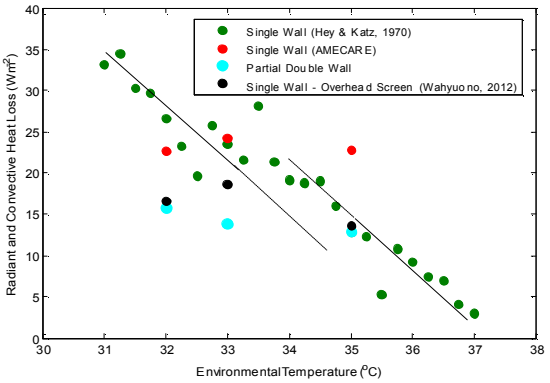

Fig 5. Dry heat loss of partial double wall incubator comparing to single wall incubator and single wall incubator with overhead screen

Based on all of analysis as mentioned before, the additional double wall can reduce the total dry heat loss of newborn nursed in incubator more than the incubator with overhead screen in the previous study [11]. However the analysis of dry heat loss due to presence of double wall is only performed for one condition, i.e. 3 cm stuck from the outer wall. It probably will affect much different dry heat loss if the double (inner) wall is installed in varies of distance from top wall incubator. Thus for further study, it's important to analyze the effect of double wall distance from outer wall of incubator to its reduction of dry heat loss so that it can be defined the optimum distance for installing overhead screen.

IV. Conclusion

The dry heat loss of newborn nursed in double wall incubator has been performed by numerical study employing CFD. The result of dry heat loss has been verified and show the improvement of thermal condition to the single wall incubator with overhead screen as the hypothesis mentioned in the background. Hence partial double wall incubator with overhead screen is recommended to be developed as optimum thermoregulation supporting media for nursing newborn.

V. References

1. E. B. Elabbassi, K. Belghazi, S. Delanaud and J. P. Libert, *European Journal Applied Physiology*. 92, 679 – 682 (2004).
2. E. N. Hey and G. Katz. Archieves of Disease in Childhood. 45, 328 – 334 (1970).
3. McCall E.M., Alderdice F. A., Halliday H. L., Jenkins J. G., Vohra S. *Evidence-Based Child Health*. 1, 287 – 324 (2006).
4. P. J. Sauer, H. J. Dane, H. K. Viser. *Archives of Disease in Childhood*. 59, 18 – 22 (1984).

5. Yeh, T. F., S. Voora, L. D. Lilien, J. Matwynshyn, G. Srinivasan, R.S. Pildes, The Journal of Pediatrics, 97, 967-971 (1980).
6. Chessex, P., S. Blouet and J. Vaucher. *The Journal of Pediatrics*. 113, 373-380 (1998).
7. Laroia N, Phelps D. L, Roy J. *Cochrane Database Syst* Rev. 18, CD004215 (2007).
8. M. K. Ginalski, A. J. Nowak, L. C. Wrobel. *Medical Engineering & Physics*. 29, 531 – 541 (2007).
9. L. C. Wrobel, M. K. Ginalski, A. J. Nowak, D. B. Ingham, A. M. Fic. *Phil. Transaction of The Royal Society A*. 328, 2817 – 2834 (2010).
10. S. Dollberg and S. B. Hoath. *NeoReviews.* 2, 282 – 291 (2001).
11. R. A. Wahyuono, R. Hantoro, G. Nugroho. *Proceeding SITIA 2012 - ITS, Indonesia*.

High Temperature Oxidation Behavior of Niobium Containing Zirconium Alloy Zr-Nb-Mo-Ge

Bernardus BANDRIYANA[1], H. Ismoyo AGUS[2], PARIKIN,[3] Hadi P., DJOKO[4]
1,,2,3 PTBIN-BATAN, Puspiptek, Tangerang
4 PTNBR-BATAN, Bandung

Abstract

Zirconium alloys (zircaloys) were widely used for fuel cladding in Nuclear Power Plants (NPP) because they have low neutron absorption, good mechanical and corrosion resistance properties. Researchs on zirconium alloys were now developed to improve the high temperature oxidation resistance regarding to the increasing of steam temperature during condition in loss of coolant accident (LOCA). Improvement of the corrosion resistance can be performed by using niobium element in the syntesis of zirconium alloys. Syntesis of a new niobium containing zirconium alloy of Zr-Nb-Mo-Ge was developed in PTBIN-BATAN and obtained a good characteristic in mechanical properties. Oxidation tests in steam were performed to evaluate high temperature oxidation behavior of the Zr-Nb-Mo-Ge alloy. Effects of niobium content to the high temperature oxidation behavior were investigated. Three specimens with 1% , 2% and 3% Nb content were oxidized in flowing steam at temperature of 500 ^{o}C and 700^{o}C for the duration for 1, 4 and 8 hours. The oxidation behavior was evaluated by determining the weight gain and measuring the oxide layer thickness. Oxidation kinetics of the specimens were evaluated and the microstructural properties after steam oxidation were also characterized. The different oxidation behaviors in the examined temperature of 700^{o}C were considered to be due to the niobium content. It was obtained that the characteristic of high temperature oxidation for the specimen had similar properties with the commercial cladding materials of Zircaloy 4

Keywords : *zirconium-alloy, niobium, high-temperature, oxidation*

* Corresponding author.
E-mail address: bandriyana2005@yahoo.com

I. Introduction

Zirconium alloys (zircaloys) were widely used for fuel cladding in Nuclear Power Plants (NPP) because they have low neutron absorption, good mechanical and corrosion resistance properties [1]. Since the fuel cladding was functioned to prevent leakage of radioactive materials into the coolant, the structural integrity under normal and accident condition should be considered to guarantee the safety. The main problem experienced in the fuel cladding during accident condition such as loss of coolant accident (LOCA), was the high temperature oxidation by increasing steam temperature causing the deformation. Safety design requirement of fuel cladding for LOCA condition stated that the equivalent cladding reacted (ECR) must not exceed the 17 % criterion and the peak cladding temperature (ECR) should be below 1200 ^{o}C [2].

Commercial zirconium alloy Zircaloy-4 was a famous material used for fuel cladding of NPPs presurized water reactor (PWR) type for a long time [3]. However, at high burn up as now developed in some NPPs by increasing the operating temperature, some high temperature oxidation problems have been reported. Therefore, the zirconium alloys used for cladding material was necessary developed especially to improve the oxidation resistance in high temperature. Improvement of the corrosion and high temperature oxidation resistance has been developed by adding niobium into the Zr-based alloys. For example, niobium containing alloy of zircaloy (Zr-1%Nb) has been used in Russia for cladding materials for many years [4]. The Zircaloy-4 has also developed into Nb containing zirconium alloy Zirlo with composition of (wt pct) 1.8 Nb, 1.2 Sn and 0.1 Fe and Bal. Zr [5].

Development of cladding material was also performed in BATAN by carried out some researchs on syntesis of new zirconium alloy Zr-Nb-Mo-Ge using melting process in high temperature furnace. This alloy has good mechanical properties with high strength and hardness obtained by the formation of Zr-Ge

precipitation during the melting process [6]. The high temperature oxidation test of this alloy was necessary carried out, especially to optimize the effect of Nb content for its oxidation resistance. According to safety analysys, oxidation kinetics in high temperature should also be determined. The oxidation kinetic behavior was used to evaluate the most important problem according to the heat generation and hydrogen production in fuel cladding.

In this present study, high temperature oxidation testing of Zr-Nb-Mo-Ge was carried out to investigate the effect of Nb content to the high temperature oxidation rate. The oxidation kinetic was evaluated and the microstructural properties after steam oxidation were also characterized.

II. Experimental procedure

Sample Preparation

The specimens were prepared by machining ingot of Zr-Nb-Mo-Ge which resulted from the syntesis of the alloy in the arc melting furnace. After cleaning with acetone, dimentions and initial weights of the specimens were measured. The chemical composition of specimens are showed in Table 1.

Table 1. Specimens used in oxidation test

Specimen	Composition (weight %)			
	Nb	Mo	Ge	Zr
Nb1	1	1.3	0.5	Bal
Nb2	2	1.3	0.5	Bal
Nb3	3	1.3	0.5	Bal

Apparatus and Test Procedure

Fig. 1 shows a schematic of oxidation test apparatus. The apparatus consisted of quartz tube, electrical resistance furnace, temperature controll with thermocouple, steam generator and argon tank. Steam from the steam generator was pushed and pressured by argon gas flowing from the pressurized argon gas tank. The specimens put on a ceramic boats were then inserted into the midpoint of the tube and oxidized in flowing steam. Oxidation temperature was measured with K-type thermocouple at the midpoint of the tube and maintened constant with a temperature control. After obtaining the determined oxidation time, the specimens were cooled and then pulled out from the tube. The mass or weight change after oxidation was measured to calculate the weight gain, than the characteristic of microstructure was evaluated based on the observation result from optic and SEM microstructure testing.

Oxidation test was carried out for the 3 specimens at the same temperature of 500 ^{o}C and 700^{o}C to simulate the normal and LOCA condition. The duration of tests were 1, 4 and 8 hours. After oxidation test, the weight of each specimen was measured using micro balance apparatus and the weight gains per unit area of each specimens were calculated. Microstructure observation of the specimens cross section was carried out and the thickness of the oxidation layers were measured.

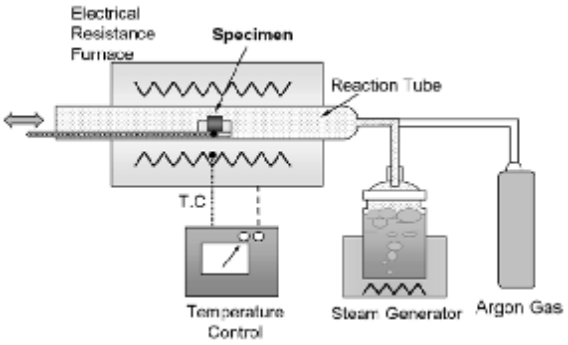

Fig 1. Schematic of Oxidation Test apparatus

III. Results and Discussion

Behavior of oxidation

The continous weight gains of the specimen in steam atmosphere at temperature of 500 ^{o}C and 700^{o}C were plotted as a function of oxidation time and showed in Fig 2. In the temperature testing, the weight gains at early stage tended to increase considering the diffusion of oxygen ions through the oxidation layer. There was a diffrent value of weight gains observed at 500 ^{o}C and 700^{o}C on each of Nb content alloy. In a range of 1 % to 3% Nb content, additon of this element will decrease the weight gains. Therefore, additional Nb into the Zr-Nb-Mo-Ge alloy will increase its oxidation resistance. Increasing the weight gain observed in the curve was similar to the oxidation behavior of Zircaloy-4 and agreed to the parabolic rate law [7]. Hypotesis of Nb element additioning that increase the oxidation resistance may caused by stabilizing of the β–Zr phase which observed in the microstructure testing.

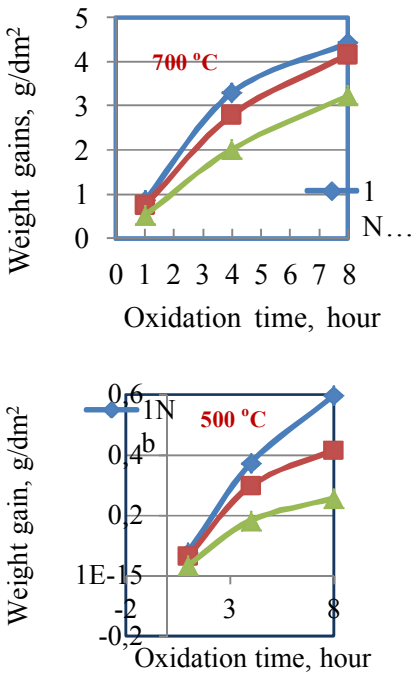

Fig. 2. Oxidation behavior at 700°C and 500 °C

Oxidation Kinetic

The relationship between the weight gain and reaction time can be generalized in terms of the oxidation temperature as follows [5]:

$W^n = K_n \cdot t$ ..... *(1)*

where : K_n : is the oxidation rate constant $(mg/dm^2)^n/s$, n : is the oxidation rate exponent and t : is oxidation reaction time (s).

This oxidation rate exponent *(n)* of these specimens developed from equation *(1)* in terms of oxidation temperature was shown in Fig. 3.

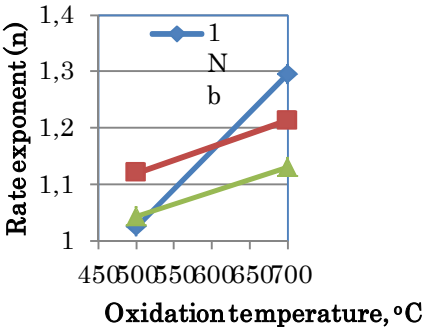

Fig. 3 Oxidation rate exponent for temperature 500 °C and 700 °C

The rate of exponent at 500 °C oxidation temperature were 1.025, 1.20 and 1.044 for the specimen with 1%, 2% and 3% Nb content respectively. These rates tended to increase with increasing temperature in the range temperature of 500 °C and 700°C.

In case of the oxidation kinetics agreed with the parabolic rate law, the oxidation rate constant (K_n) can be expressed as follows [5]:

$K_n = A \exp(-Q/RT)$ ..... *(2)*

where : A is a constanta $(mg/dm^2)n / s$, Q and R are the activation energy and universal gas constant (cal/mol °K) respectively , and T : is the oxidation temperature (°K). Based on equations *(1)* and *(2)* the curve can be ploted in linear relation between oxidation rate constant (K_n) and temperature $(1/T)$ and showed that increasing of the oxidation temperature will increase the rate constant of the specimen. It was also found that the oxidation rate constant (K_n) at temperature of 700 °C was increase by increasing of the Nb content in alloy.

Microstructure

The microstructure and oxidation layer of the specimens after oxidation were shown in Fig 5. The oxidation rate is reduced by the existance of the layer formed during oxidation process. Observation of the microstructure showed that the oxygen-stabilized α-Zr phase was formed near the surface since the oxygen diffused from the oxide layer. The β –Zr phase was formed in the central region because of the suppression of the oxygen diffusion.

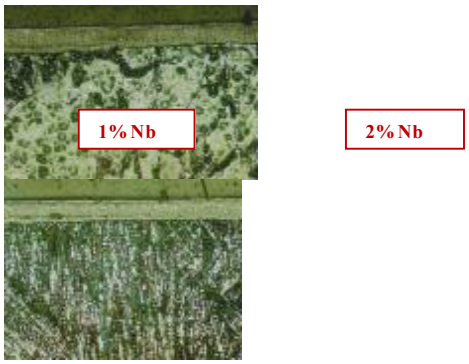

Fig 5. Microstructure of Zr-Nb-Mo-Ge alloy, 500x

The layer thickness for 700 °C oxidation temperature can be measured based on the microstructures observed by SEM as shown in Fig 6. There were two layers observed in the specimens which were predicted as zircon oxide in the lower part and a spinel in the upper part near the surface.

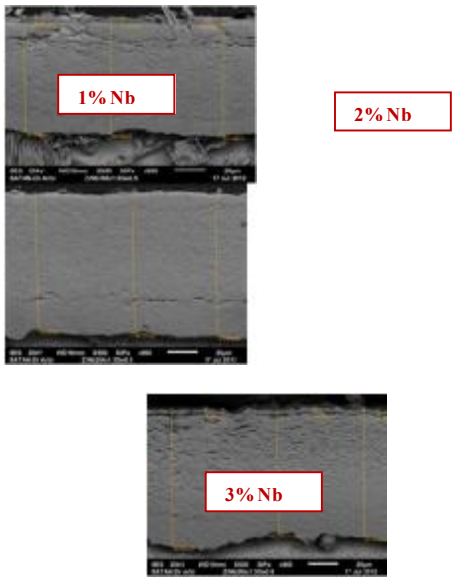

Fig 6 . Layer thickness measurement by SEM

The layer thicknes of specimen with 1%Nb was 80.252 µm with spinnel thickness of 5.337 µm. For the specimen with 2%Nb the layer thicknes was 92.604 µm but there was no spinnel. For 3% Nb specimen the layer thickness was 85.610 µm with 4.252 µm spinnel thickness. It can be observed that the layer thikness was increased by increasing of the Nb content followed by the oxidation resistance. However, in case of the 2%Nb content increased, the layer thickness was bigger while the spinnel was not formed in the surface. Analysis of the layer formation mechanism and oxidation layer composition were necessaryly performed to explain the effect of each element to the oxidation behavior, but it was not yet studied in this experiment.

IV. Conclusion

The oxidation behaviors for Zr-Nb-Mo-Ge alloy with variation of Nb content in the temperature of 500 °C and 700°C under steam supply condition were investigated. The results showed the weight gains of the specimens were depend on the Nb content and oxidation temperature test. Additional Nb into the Zr-Nb-Mo-Ge alloys decreased the weight gain and increase their oxidation resistance being believed to contribute to the stabilization of β-Zr phase. The oxidation layers were observed in microstructure characteristic followed by the spinnel formed near the surface. It was obtained that the characteristic of high temperature oxidation for the specimens were good enough and similar to the commercial zirconium alloy of Zircaloy 4 used for the cladding material of PWR type Nuclear Power Plant.

ACKNOWLEDGEMENT

This research was conducted as part of PKPP 2012 research program organized by the Indonesian Ministry of Research and Technology. The authors would like to acknowledge and express their appreciation for time and effort devoted by engineers,researchers and technicians in KPTF and BBIN-BATAN.

REFFRENCES

[1] Lustman,B., Kerze JR., "The Metallurgy of Zirconium", 1st edition, Mc. Graw-Hill Book *Co.,* New York, 1955.

[2] Paul M., Clifford, **"**Strategy for Revising Fuel Cladding Acceptance Criteria**,"** U.S. NRC Regulatory Information Conference**,** Division of Safety Systems, Nuclear Reactor Regulation,Washington, March 11 – 13, 2008

[3] Prayitno,D.H., "Uniform of Zircaloy-4 under Isothermal Oxidation at High Temperature", International Conference at Neutron Scattering, BATAN, 2007.

[4] Steiburg, M., et.all, "Status of studies on high temperature oxidation and quench behavior of Zircaloy-4 and E110 cladding alloys", The 3rd Europen Review Meeting on Severe Accident Research (ERMSAR-2008), 2008.

[5] Hyung Hoon Kim, et.al, "High Temperature Oxidation Behavior of Zircaloy-4 and Zirlo in Steam Ambient", Journal of Material Science and Technology, 2010

[6] B.Bandriyana, Agus Hadi Ismoyo, Parikin,

"Penelitian dan Pengembangan Paduan Zirkonium untuk Material Kelongsong PLTN," Prosiding Seminar Nasional Pengembangan Energi Nuklir V, P2EN-BATAN, 2012

[7] Toshinori, C., Fumihisa,N., Toyosi F., "High temperature Oxidation of Nb-Containing Zr alloy Cladding in LOCA Condition," Nuclear Engineering and Technology, Vol. 41, No. 2, March 2009, Special Issue on the Water Reactor Fuel performance Meeting 2008.

Preliminary Study of Synthesis of TiO_2-Dispersed Steel by Mechanical Alloying

Abu Khalid Rivai[1*], Devi Anggraini[2], Arbi Dimyati[1], Marzuki Silalahi[1]
[1]PTBIN-BATAN, Kawasan PUSPIPTEK Gedung 71 Tangerang Selatan Banten, Indonesia
[2]Dept. Fisika-UNSRI, Jl. Palembang-Prabumulih Km 32 Sumatera Selatan, Indonesia

Abstract

Preliminary study of synthesis of TiO_2-dispersed steel by mechanical alloying has been done. TiO_2-dispersed steel is one type of ODS (Oxide Dispersion Strengthened) steels. ODS steels type is projected to be used for a system that is operated at high temperature such as advanced nuclear reactors. In this study, TiO_2 particles have been attempted to be dispersed inside the steel`s matrix using mechanical alloying method. First, elemental powders of the steel`s constituent materials i.e. Fe, Cr, Ti and TiO_2 particles were blended using HEM (High Energy ball Milling) tool. Then, the mixed powder was compacted become a pellet. Afterward, the pellet was sintered inside the furnace under an argon gas atmosphere. The samples were characterized using SEM-EDS (Scanning Electron Microscope-Energy Dispersive Spectroscope) to analyze the microstructure characteristics. XRD (X-ray Diffraction) analysis was also performed to analyze the powder after milling. The present results showed that fine distribution of TiO_2 particles inside the matrix of the steel has not been achieved. Nevertheless, improvement of the synthesis of the steel by modification of mechanical alloying, degassing and sintering procedures has been achieved. Further improvements of synthesis procedures are needed to achieve fine and homogeneous dispersion of TiO_2 particles inside the matrix of the steel.

Keywords: *synthesis, steel, TiO_2, ODS, mechanical alloying*

* Corresponding author.
E-mail address: rivai.abukhalid@batan.go.id

I. Introduction

Recently, many fields of industry tend to increase their operation temperature for increasing the efficiency. As a direct consequence, development of high temperature materials is absolutely required. Oxide dispersion strengthened (ODS) steels are one type of steel-based high temperature material candidates which are proposed for that purpose. Up today ODS steels are mostly developed for advanced nuclear fission reactors (so-called Generation IV reactors) and nuclear fusion reactors [1-8]. ODS steels are intensively investigated for fission and fusion nuclear reactors applications in United States, Japan and Europe followed by Korea, India and China [1-8]. ODS steels are one of the promising materials to be utilized at high temperature under severe irradiation exposure environment.

Up to now in many countries ODS steels have been developed by powder metallurgy method using mechanical alloying technique to obtain a dispersion of oxide particles in a steel matrix. Mechanical alloying is a technique to acquire homogeneous materials from elemental powder materials. The technique is started from blended the powders using milling tools e.g. HEM-high energy ball milling tool. During mechanical alloying recurred welding, breaking, and re-welding process of powder particles occur in a high-energy milling. ODS steels were reported exhibit excellent creep strength at elevated temperatures environment because of pinning mobile dislocations [2, 5]. This characteristic is obtained from fine dispersion of oxide particles inside the steel`s matrix. Y_2O_3 and/or TiO_2 particles with nanometer in size are mostly used as the dispersion particles [1-8]. In this paper preliminary study of TiO_2-dispersed steel synthesized by mechanical alloying is described.

II. Experiment and Procedures

II.1. Material

Elemental metal powders of Fe, Cr, Ti, and TiO_2 were used as the constituent materials. The purities of the powders were higher than 99%. Figure 1 shows SEM micrograph of the TiO_2 powder. The TiO_2 powder was commercial chemicals made by Degussa Chemicals Company. Average size of TiO_2 powder was in nanometer.

Two samples were prepared using electro-micro balance. The designed compositions of sample-1 and sample-2 were Fe-9Cr-1Ti-1TiO_2 and Fe-15Cr-1.5Ti-1TiO_2 in weight percent, respectively.

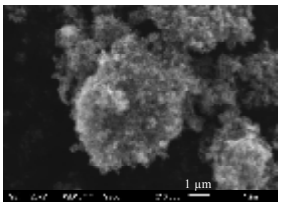

Fig. 3. SEM micrograph of TiO_2 powder

II. 2. Experimental Method

Schematic of experimental procedure is shown in Fig. 2. The elemental powders were milled using HEM-high energy ball milling. The mechanical alloying tools are shown in Figs. 3.

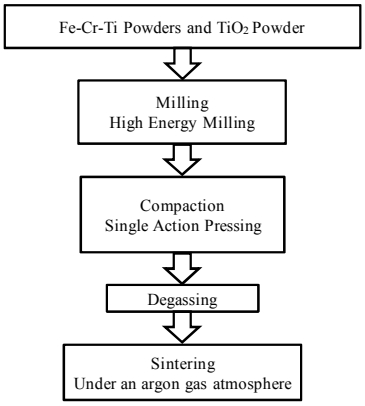

Fig. 2. Schematic of experimental procedure

Fig. 3. Mechanical alloying tools (a) steel balls (b) vial (c) HEM-high energy ball milling

Sample-1 was synthesized and analyzed previously before sample-2. The experimental procedure for sample-2 was an improvement of sample-1 experimental procedure.

Ball-to-powder mass ratios of sample-1 and sample-2 were 2:1 and 5:1, respectively. The speeds and milling times of HEM were 1000 rpm-8 hours and 300 rpm-40 hours for sample-1 and sample-2, respectively. Then, the milled powders were compacted using single action pressing (6000-7000 psi of pressure) with 1 inch-dias (mould). Figure 4(a) shows the pellet of sample-1 after compaction. Afterward, the pellets of sample-1 and sample-2 were degassed at 140°C for 180 minutes and at 400°C for 180 minutes, respectively. Finally, the pellets were sintered under an argon gas atmosphere at 1150°C for 120 minutes and 1350°C for 180 minutes for sample-1 and sample-2, respectively. Figure 4(b) shows the pellet of sample-2 after sintering.

Fig. 4. Photos of samples pellet (a) sample-1 after compaction (b) sample-2 after sintering

SEM (Scanning Electron Microscope)-EDS (Energy Dispersive Spectrometer) and also XRD (X-ray Diffraction) were used to analyze the samples. For SEM-EDS analysis, the samples were cut in the middle, and then polished. Afterward, the samples were etched before SEM-EDS analysis.

III. Results and Discussion

Figures 5 show SEM micrographs of cross section of sample-1 after sintering. Some inhomogeneous parts were observed in the matrix of sample-1 as shown in Fig. 5(a). Fig. 5(b) as larger magnification for indicated circle in Fig. 5(a) shows the inhomogeneous parts in detail. The inhomogeneous parts with grain particles in shape were observed inside the matrix. The grain particles were less than 1µm in diameter. The grain particles might be formed during sintering process, or some powder particles did not sintered well. EDS was used to analyze the elements and compositions of the grain particles. Fig. 6(a) shows the indicated area of sample-1 for EDS analysis. Fig. 6(b) shows the EDS analysis graph for area. High peaks of iron, chromium and titanium were observed as shown in Fig. 6(b). The peaks of carbon and oxygen were also observed. It is predicted that the impurities were produced during preparation and milling process. Therefore in order to suppress the impurities production in powders because of heat and friction among the balls during milling, a toluene liquid was added and the HEM speed was decreased for synthesizing of sample-2. Figure 6(c) shows the weight and atomic percentage analyses of

chromium and titanium. The figure shows that the amount of chromium and titanium was almost similar with the amount of the starting elemental powders for area analysis. However, the amount of chromium and titanium were smaller than the amount of starting elemental powders for point 1 analysis. On the other hand, the amount of chromium and titanium was higher than the amount of starting elemental powders for point 2 analysis. The results showed that the grain particle components were mainly consist of chromium and titanium. Furthermore, Fig. 5(c) also shows high percentage of oxygen. Therefore, it was estimated that TiO_2 was one of grain particle components. TiO_2 particles were dispersed inside the matrix together with other grain particle components.

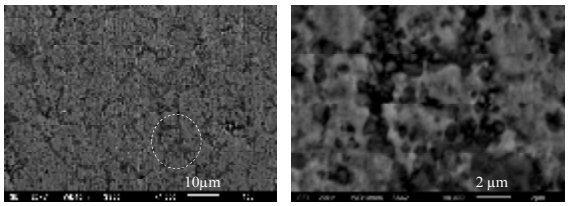

(a)

(b)

Fig. 5. SEM micrographs of sample-1 cross section (a) 1500 times magnification (b) 8000 times magnification

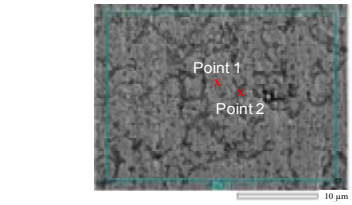

(a)

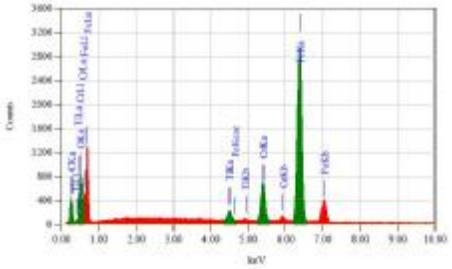

(b)

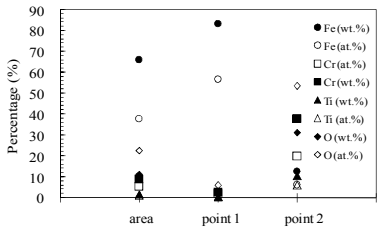

(c)

Fig. 6. EDS analysis of sample-1 after sintering (a) indicated area (b) area analysis (c) percentage analysis

The phenomena occurred at least because of two reasons. First, the milling time might be not long enough to produce homogeneous powders. Second, the sintering temperature might be not high enough to produce homogeneous matrix of the steel. Therefore, as improvement for sample-2 the milling time was increased to 40 hours and the sintering temperature was increased to 1350°C. Moreover, degassing temperature for sample-2 was increased to 400°C to achieve optimum removal of trapped gases inside the sample that might be occurred during milling process.

Figure 7 shows SEM micrograph of sample-2 (Fe-15Cr-1.5Ti-1TiO_2) powder after milling for 40 hours. In general, the figure shows homogenous shape and fine grain of the powder. Nevertheless, small amount of lamellar shape of the powder were observed. It was estimated that the milling time was still not long enough or the milling speed was not fast enough. Figure 8 shows XRD analysis of the powder after milling. The figure shows the peaks for FeCr phase or might be Fe and Cr. The XRD peaks among FeCr, Fe and Cr are difficult to be distinguished because of similarity in crystallographic structure. However, it was predicted that FeCr will be formed in the powder during the mechanical alloying process.

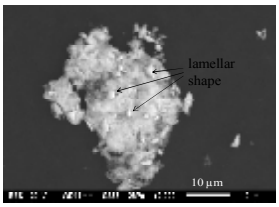

Fig. 7. SEM micrograph of sample-2 powder after milling for 40 hours

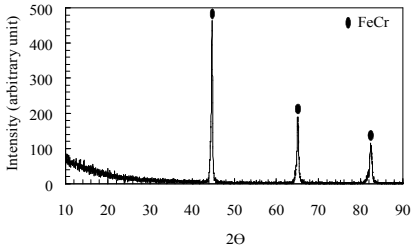

Fig. 8. XRD analysis of sample-2 powders after milling for 40 hours

Figures 9 show SEM micrographs of cross section of sample-2 after sintering.

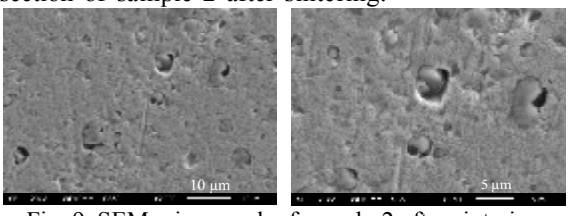

Fig. 9. SEM micrograph of sample-2 after sintering

Figures 9 show that no inhomogeneous part with grain particle in shape such as in sample-1 was observed in sample-2. It means that increasing the milling time and the sintering temperature was effective to suppress the grain particles formation. Moreover, homogenous area was dominant in the matrix. However, some inhomogeneous parts like agglomeration dispersed inside the matrix of sample-2 were observed.

Figures 10 show the weight and atomic percentage of EDS analyses of iron, chromium and titanium for sample-2. The amount of chromium and titanium was almost similar with the amount of the starting element powders for area analysis. Moreover, there were no significant impurities observed. Therefore, addition of the liquid toluene was effective to suppress the impurities formation. However, the amount of chromium and titanium were smaller than the amount of starting element powders for point 1 analysis. On the contrary, the amount of chromium and titanium was higher than the starting element powders for point 2 analysis. The results showed that the inhomogeneous parts mainly consist of chromium and titanium. Moreover, Fig. 10 also shows high percentage of oxygen. Therefore, it was estimated that TiO_2 was one of inhomogeneous part components. TiO_2 particles were dispersed inside the matrix together with other inhomogeneous part components. It was analyzed that the inhomogeneous parts were formed because of agglomeration of titania, titanium and chromium during mechanical alloying process. The lamellar shape parts of the sample-2 powder after milling, as shown in Fig.7, were possibly the agglomerations.

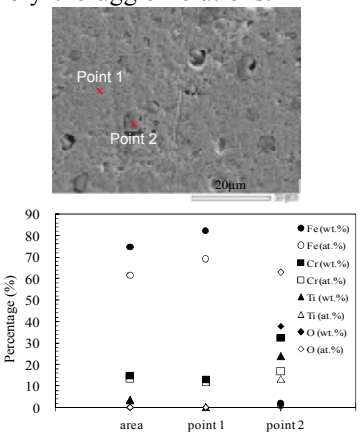

Fig. 10. EDS analysis of sample-2 after sintering

Fine distribution of oxide particles as the dispersoid particles inside the matrix of ODS steels is one of the requirements for a high quality of ODS steels [1-8]. To achieve that condition, powder metallurgy method and mechanical alloying technique have been developed in many countries. In this study, fine distribution of TiO_2 particles inside the matrix of the steel has not been achieved. However, improvement of synthesis of the steel from sample-1 to sample-2 has been achieved. Therefore, optimum synthesis procedures are necessary for further improvement.

IV. Conclusion

Preliminary study of synthesis of TiO_2-dispersed steel by mechanical alloying has been done. The results showed that fine distribution of TiO_2 particles inside the matrix of the steel has not been achieved. Nevertheless, from this study improvement of the synthesis process of the steel by modification of mechanical alloying, degassing and sintering procedures has been done and understood. Therefore, for the next step further improvements of synthesis procedures will be performed to achieve fine and homogeneous dispersion of TiO_2 particles in the steel`s matrix.

Acknowledgements

This study was funded by Riset Insentif Ristek no. RT-2012-660.

V. References

1. S. Ukai, M, Harada, H. Okada, M. Inoue, T. Nishida, and M. Fujiwara, Journal of Nuclear Materials 204, 65-73 (1993).
2. Shigeharu Ukai, and Masayuki Fujiwara, Journal of Nuclear Materials 307–311, 749–757 (2002).
3. K. Verhiest, A. Almazouzi, N. De Wispelaere, R. Petrov, and S. Claessens, Journal of Nuclear Materials 385, 308–311 (2009).
4. Yingli Xu, Zhangjian Zhou, Ming Li, and Pei He, Journal of Nuclear Materials 417, 283–285, (2011).
5. S. Saroja, A. Dasgupta, R. Divakar, S. Raju, E. Mohandas, M. Vijayalakshmi, K. Bhanu Sankara Rao, and Baldev Raj, Journal of Nuclear Materials 409, 131–139 (2011).
6. M. Bodart, R. Baccino, and E. Moret, Journal de Physique IV Colloque sup plement for Journal de Physique III, Volume 3, 709-714, (1993).
7. Jung-Ho Ahn, Hyungseop Shin, and Seung Joon Hwang, Rev. Adv. Mater. Sci. 18, 335-338 (2008).
8. S. Ohtsuka, S. Ukai, M. Fujiwara, T. Kaito, and T. Narita, Journal of Physics and Chemistry of Solids 66, 571-575 (2005).

Resistivity Imaging and Interpretation of the Rawa Dano Ground Water Basin, Banten, Indonesia

Syuhada[1*], Titi Anggono[1], Bogie Soedjatmiko[1]
1 Research Center for Physics, Indonesian Institute of Sciences (LIPI)
Kawasan Puspiptek Serpong, Tangerang Selatan Indonesia

Abstract
Resistivity survey was carried out to infer subsurface information at the Rawa Dano Ground Water Basin. 20 soundings using Schlumberger array were conducted with current electrode spacing (AB/2) up to 400 meters. The data were processed and quantitatively interpreted using a vertical resistivity distribution model assumption and lateral resistivity distributions generated with triangle-based linear interpolation algorithm at a particular depth. The interpretation result showed that the study area consists of three main layers. A very low resistivity zone (< 10 ohm.m) detected in this study area may be caused by the presence of clay rich structure in the formations, while the sandy tuff formation is characterized by resistivity values ranging from 10 ohm.m to 25 ohm.m.
Keywords : *Resistivity survey, Schlumberger array, Ground water basin*

* Corresponding author.
E-mail address: syuhada@lipi.go.id

I. Introduction

The electrical properties of upper Earth's material mainly depend upon the rock type, the existence of fluid, porosity and the salinity of the rock. For example, the resistivity of saturated rock layers is generally lower than the unsaturated ones, and coarse-grained, well-consolidated sandstones generally have lower resistivity than unconsolidated fine-grained silt of the comparable porosity [1]. The presence of clay and conductive mineral also can lower the resistivity of rock. Thus, geoelectrical method is suggested to be successful method for characterizing shallow geological targets [2], imaging faults [3], detection of geothermal reservoir [4], investigation of ground water potential as well as detection of contaminants [5,6].

The main objectives of this research are to image the subsurface resistivity distribution and to characterize the potential aquifers in the Rawa Dano ground water basin with their boundaries.

II. Geological Setting

Direct current electrical survey was carried out in the Rawa Dano groundwater basin of the western part of Banten province with an area of about 216 km^2. The study area is situated in the Plio-Pleistocene caldera of the Dano volcanic complex bounded with caldera rim and adjacent high volcanic terrain with the highest peak reaching around 1778 asl (above sea level) in Mt. Karang (Figure 1). The basin was formed in a number of eruptive phases resulting in the thick volcanic deposits well known as the Banten pumice tuff. The steep rim in northern part of the caldera was formed mainly by andesitic lava and volcanoclastics, while alluvium deposit dominates the formation of younger volcanic cones in southern part of the basin [7,8]. The geomorphology within the caldera is characterized by the youngest sedimentation derived from the southern volcanic slopes and deposited in alluvial fans and fluvial system in the caldera [9,10].

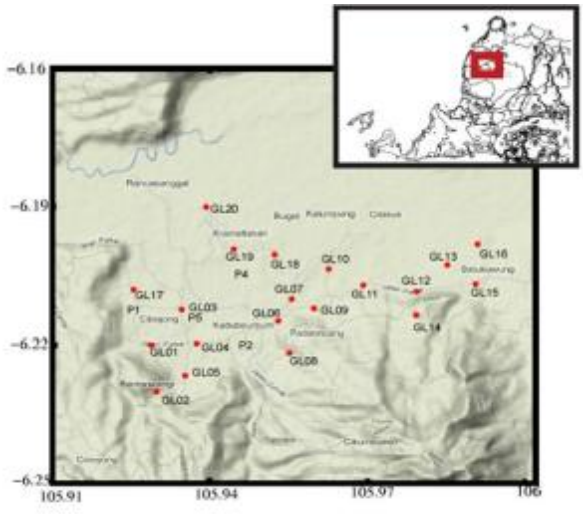

Figure 1. Map showing the sounding locations. The sounding points are represented by the red solid circles.

III. Data

Geoelectrical measurements were conducted using Schlumberger array configuration, with half current electrode spacing (AB/2) ranging from 5 meters to 400 meters. This spacing is expected to be sufficient to penetrate adequate depths of the groundwater aquifer in the area of investigation. A total of 20 vertical resistivity sounding points were completed for the whole area of investigation (Figure 1). The data obtained from the survey were initially interpreted using an automatic interpretation program [i.e. 11] to produce a model of subsurface rock layering in term of electrical resistivity values and its corresponding thickness (n-layered model, Figure 2). The results were then used to construct a geoelectrical cross sections along the various profiles using available geological information and lateral resistivity distributions generated with triangle-based linear interpolation algorithm [12] at a selected depth.

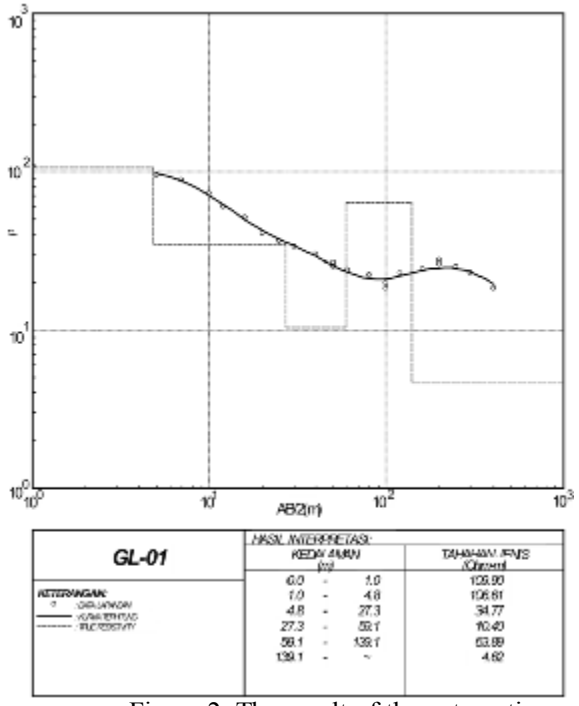

Figure 2. The result of the automatic interpretation generating n-layered model of the subsurface rock.

IV. Result and Discussion

In this study, two selected cross sections are generated from sounding interpretation and presented in Figures 3 and 4. Figure 3 shows the east-west geoelectric cross section and it consists of eight sounding points (GL01, GL04, GL06, GL09, GL11, GL12, GL13 and GL16). Figure 4 represents the profiling surveys that are oriented predominantly south-north from high to low altitude consisting of three vertical sounding points GL08, GL06, GL19 and GL20.

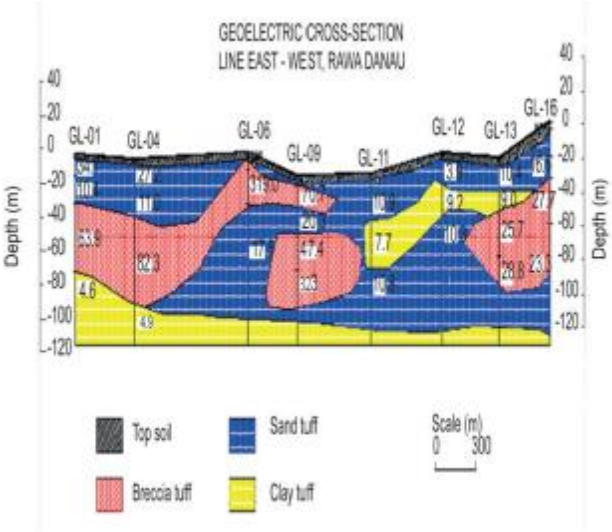

Figure 3. Line east-west interpreted resistivity cross section.

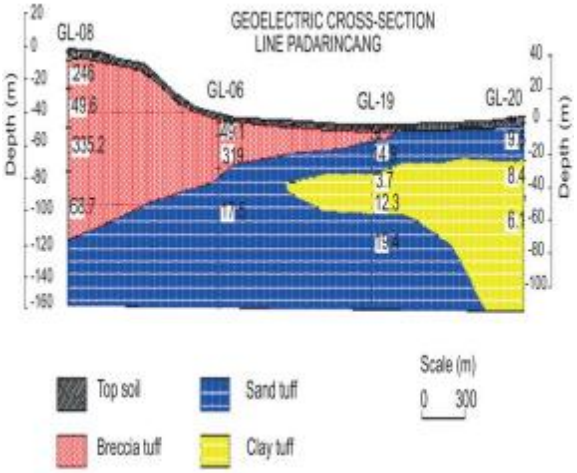

Figure 4. Selected line south-north interpreted resistivity cross section.

In general, the study area is covered mainly by low and moderate resistivity materials and consists of three to four major layers. The top layers show high variations in resistivity values above 100 Ohm-m, and it can be interpreted as topsoil. The thickness of this layer varies from 0.5 to 5 m. The breccias tuff layers may presence in these profiles, having resistivity values ranging from 25 Ohm-m to 70 Ohm-m (i.e. in Figure 4. under soundings GL-08, GL-06 and GL-19 at depth 20 to 120 m). The next layer is probably

formed from sandy tuff which is characterized by relatively low electrical resistivity values (10-25 Ohm.m) and it may be considered as the water-bearing aquifers. This material extends greater than 140 m depth as depicted on Figure 4. Another layer formed from clay tuff, which may serve as aquiclude. It has a relatively very low resistivity no greater than 10 Ohm-m with thickness ranging from 20 to 80 m (Figure 3 and 4). These findings are in good agreement with the borehole data constructed previously in the investigation area [10]. The data shows that the deeper basin deposits (> 10 m) mainly consists of sand with intercalation of clay, while the breccias deposits found in the shallower part of the basin.

Figure 5 shows maps of interpreted resistivity at a particular depth generated by sampling geoelectrical sounding interpretations at a selected depth by the difference between the surface elevation at that sounding and the desired depth (i.e [6]). The sampled resistivity values were then interpolated into grid using triangle-based linear interpolation [12].

(a)

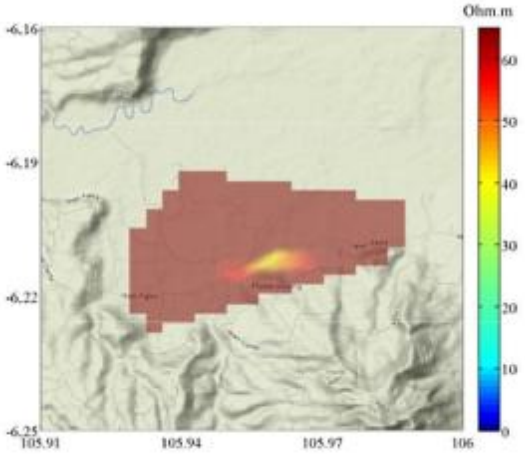

(b)

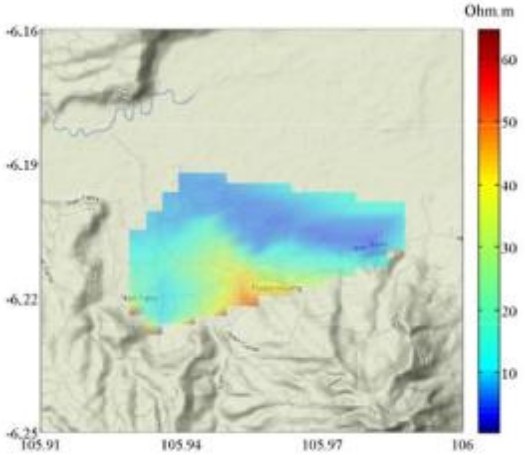

(c)

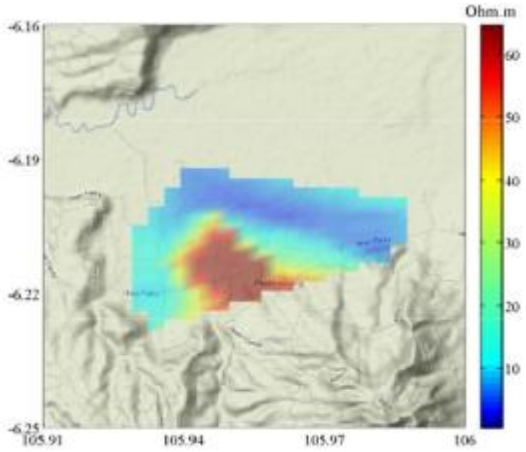

(d)

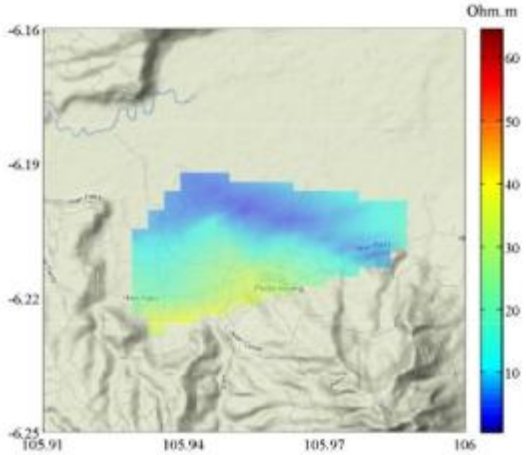

Figure 5. Map of restivity distribution at depth (a) z = 0.1 m, (b) z = 10 m, (c) z = 40 m, and (d) z = 70 m.

The surface resistivity map distribution (depth=0.1 m) suggests the fairly uniform covering of the top soil marked by relatively high resistivity values (> 70 ohm.m) throughout the study area. At shallow depth (10 m), the resistivity map reflects the low and very low resistivity zones covering the study area. The very low resistivity (<10 ohm.m) zone marked by blue colour in northern part of the map suggests the indicative of increased clay content or water content. This feature also appears on the resistivity at deeper depth (40 and 70 m). The low resistivity zone (cyan colour: 10 to 25 ohm.m) interpreted as sandy tuff covers mainly on the western part of the maps. The moderate resistivity zone (> 25 ohm.m) just covers small portion in the south of the

investigation area at shallow depth. However, the feature is more prominent and becomes broader reflecting the extent of breccias tuff deposit at 40 m depth.

V. Conclusion

DC sounding electricity survey was conducted and interpreted to create interpreted cross sections and map of resistivity distribution at various selected depths. This technique was successfully to reveal the main structural and lithological information beneath the Rawa Dano ground water basin.

In general, the resistivity results reveal the presence of three main distinct zones of the resistivity values namely: the very low, low and moderate resistivity zones. These zones reflect the various lithologic types and geological structure of the study area which are interpreted as clay tuff, sandy tuff and breccias tuff formations, respectively.

VI. Acknowledgments

Financial support of this study was provided from the PKPP research grant Kemenristek. The contribution of Banten province local government especially from Balitbangda and Bappeda staffs are gratefully acknowledged. The authors would like also to extend their thanks to Mr. Jauhari and Mr. Hardijaya for their assistants during data acquisition.

VII. References

1. M.A. Sabet, “Vertical Electrical Resistivity Soundings to Locate Groundwater Resources: A Feasibilty Study”, VPI-WRRC-Bull 73, Virginia Polytechnic Institute and State University, Blacksburg, Virginia, 1975.
2. J.D. Abaraham, and J.E. Lucius, USGS Open-File Report 2004-1319.
3. D. Demanent, F. Renardy, K. Vanneste, D. Jongmans, T. Camelbeeck, and M. Meghraoui, Geophysics. 66, 78 (2001).
4. I. Caglar, and M. Demirorer, Geothermics 28, 803 (1999).
5. W.K. Kosinski, and W.E. Kelly, Ground Water 19, 2 (1981).
6. R. J. Bisdorf, and D. V. Fitterman, USGS Open-File Report 2004-1053.
7. R.W. Van Bemmelen. “The Geology of Indonesia” , vol. 1. 1A, 1B. Government Printing Office, Den Haag, 1949.
8. E. Rusmana, K. Suwitodirdjo, and Suharsono, “Geology of the Serang Quadrangle, Jawa. Scale 1:100.000. Explanatory notes and Geological map. Geological Research and Development Center, Bandung, 1991.
9. S. Van Der Kaars, D. Penny, J. Tibby, J. Fluin, R.A.C Dam, and P. Suparan. Palaeogeography, Palaeoclimatology, Palaeoecology 171, 185-212(2001).
10. H. D. Said, Djuwahir and H. Danaryanto, “Potensi Sumber Airtanah Cekungan Rawa Danau Bagi Penyediaan Air Daerah Cilegon, Kabupaten Serang, Jawa Barat”, Direktorat Geologi Tata lingkungan, Bandung, 1985.
11. A. A. R. Zohdy, Geophysics 54, 2 (1989)
12. D. F. Watson, "Contouring: A guide to the analysis and display of spacial data", Pergamon, 1994.

NUMERICAL ANALYSES OF RAYLEIGH WAVES IN 3D MEDIUM CONSIDERING CALDERA-LIKE FORMATION BASED ON FINITE DIFFERENCE USING STAGGERED GRID SCHEME

Titi Anggono

Research Center for Physics, Indonesian Institute of Science,
Kompleks Puspiptek Serpong, Tangerang, 15310
Phone: (+62) 21 7560570, Fax: (+62) 21 7560554

Abstract

Numerical analyses of seismic wave propagation considering flat topography as free surface has provided important information on the characteristics of wave propagation in the medium. However, tectonic or volcanic activities cause mountainous region or caldera formations that change the shape of the topography. We carry out 3D numerical analyses using finite difference method to investigate the behavior of Rayleigh waves when a caldera is formed due to volcanic activities. Cells of the 3D medium are constructed based on the staggered grid scheme, in which the normal stress is embedded in the medium cell and shear stresses are located on the face of each cell. The collapsed caldera is modeled with half-spherical boundary and flat surface at the bottom of the caldera. We compare the behavior of the Rayleigh waves before and after encountering the caldera boundary. From the analyses, we suggest that the Rayleigh waves propagation is strongly affected by the caldera boundary at wavelength comparable to the geometry of the caldera.

Keywords: *Rayleigh waves, Finite difference, caldera formation .*

Corresponding author
E-mail address: titi.anggono@gmail.com

I. Introduction

The earth surface acts as boundary that reflects upcoming seismic energy and produce surface waves. Irregular free surface can lead to complex wave propagation. Because of the difficulty of the free surface boundary condition in the finite-difference method in the presence of topography, realistic topography was not frequently considered in the simulation. However, there have been a number of numerical simulations of the effect of topography on ground motion based on two-dimensional (2D) [1, 2] or three-dimensional (3D) calculation [e.g. 3, 4]. *Fuyuki and Matsumoto* using trench model showed that amplitude and phase of Rayleigh waves are affected due to topographical changes [1]. *Snieder* estimated that the topographical surface with a mountain-like model with 1 km height affect the fundamental mode phase velocity up to 1 per cent at period 15 – 30 s [5] .

Topographical changes not only lead to surface wave scattering, but also influence the propagation of the direct wave surface waves. To investigate the effect of topography to seismic wave propagation, studies have been conducted such as finite difference [e.g. 6, 1]. However, the schemes used in these studies have been limited to simple geometries. Other studies use method of boundary element method [2, 3]. *Jih et al.* (1988) used rotational rotation technique to implement free boundary condition by using a rotated coordinate system parallel to the inclined boundary [7]. *Tesmer et al.* (1992) used pseudospectral technique to investigate the propagation of seismic wave in the global scale [8]. More recently, spectral element method has been used to study the seismic wave propagation in the 3D medium [e.g. 9, 10].

In the active volcano, when a volcano erupts it sometimes causes a caldera formation. A formed caldera causes changes in the topography. In this study, we investigate the behavior of surface wave (Rayleigh wave) when a caldera formed on the flat topography. A half spherical boundary is selected as a caldera model to simplify the boundary condition. *Ohminato and Chouet* (1997) implemented the 3D elastic wave equation with topography using finite difference method [4]. They used staggered grid scheme of elastic wave equation where the location for the free surface is chosen so that it follows a staircase approximating the topographic surface. In this study, we use the method introduced by *Ohminato and Chouet* (1997) to implement free-surface boundary condition to the caldera topography.

II. Method

II.1 Equations of motion of elastic waves

Equations of motion describing wave propagation within 3D, isotropic media can be written as equations of momentum conservation and stress-strain relations. For velocity stress formulation, equations of momentum conservations can be written as

$$\rho \frac{\partial u^i}{\partial t} = \sum_{j=1,3} \frac{\partial T^{ij}}{\partial x^j} + F^i \qquad (1)$$

and stress-strain relation can be written as

$$\frac{\partial T^{ij}}{\partial t} = \lambda \frac{\partial u^k}{\partial x^k} \delta^{ij} + \mu \left(\frac{\partial u^i}{\partial x^j} + \frac{\partial u^j}{\partial x^i} \right) \qquad (2)$$

where i, j, k refer to the coordinate directions, e.g. x, y, and z, u is velocity component, t is time, x is spatial dimensions, T is stress, λ and μ are Lame coefficients, ρ is density, F is force component and δ^{ij} is Kronecker delta.

We solve the equation motion above using a staggered-grid scheme following *Ohminato and Chouet* (1997) (Figure 1). The coefficient λ is defined at the same position as the normal stress T^{ii} (i = x, y, z) and μ is defined at position where both normal and shear stresses are defined.

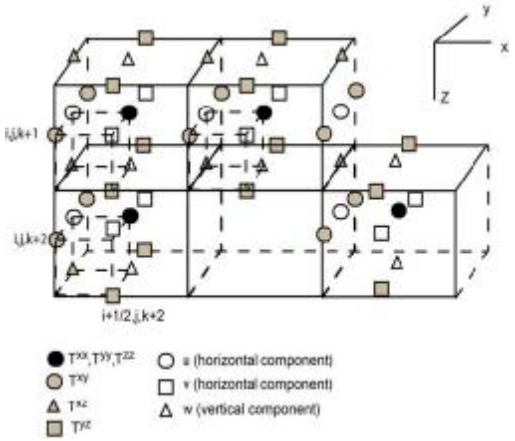

Figure 1. Staggered grid scheme for 3D elastic wave equation considering a collapse caldera boundary as free surface.

II.2 Finite difference method to the equations of motion

We approximate the time derivatives of the velocity at time level m using central-difference formula over the time step Δt, and the time derivative of the stress-tensor at the time level $m+1/2$. We use a second-order approximation for the time and spatial derivatives, where the grid spacing is set at h. The second-order velocity-stress finite difference scheme can be written as

$$\begin{aligned}
u^{m+\frac{1}{2}}_{i,j+\frac{1}{2},k} &= u^{m-\frac{1}{2}}_{i,j+\frac{1}{2},k} + \frac{\Delta t}{\rho} F^{x,m}_{i,j+\frac{1}{2},k} + \frac{\Delta t}{h\rho}\Big(T^{xx,m}_{i+\frac{1}{2},j+\frac{1}{2},k} - \\
&\quad T^{xx,m}_{i-\frac{1}{2},j+\frac{1}{2},k} + T^{xy,m}_{i,j+1,k} - T^{xy,m}_{i,j+\frac{1}{2},k+\frac{1}{2}} + \\
&\quad T^{xz,m}_{i,j+\frac{1}{2},k+\frac{1}{2}} - T^{xz,m}_{i,j+\frac{1}{2},k-\frac{1}{2}} \Big) \\
v^{m+\frac{1}{2}}_{i+\frac{1}{2},j,k} &= v^{m-\frac{1}{2}}_{i+\frac{1}{2},j,k} + \frac{\Delta t}{\rho} F^{y,m}_{i+\frac{1}{2},j,k} + \frac{\Delta t}{h\rho}\Big(T^{xy,m}_{i+1,j,k} - \\
&\quad T^{xy,m}_{i,j,k} + T^{yy,m}_{i+\frac{1}{2},j+\frac{1}{2},k} - T^{yy,m}_{i+\frac{1}{2},j-\frac{1}{2},k} + \\
&\quad T^{yz,m}_{i+\frac{1}{2},j,k+\frac{1}{2}} - T^{xz,m}_{i+\frac{1}{2},j,k-\frac{1}{2}} \Big) \\
w^{m+\frac{1}{2}}_{i+\frac{1}{2},j+\frac{1}{2},k+\frac{1}{2}} &= w^{m-\frac{1}{2}}_{i+\frac{1}{2},j+\frac{1}{2},k+\frac{1}{2}} + \frac{\Delta t}{\rho} F^{z,m}_{i+\frac{1}{2},j+\frac{1}{2},k+\frac{1}{2}} + \\
&\quad \frac{\Delta t}{h\rho}\Big(T^{xz,m}_{i+1,j+\frac{1}{2},k+\frac{1}{2}} - T^{xz,m}_{i,j+\frac{1}{2},k+\frac{1}{2}} + \\
&\quad T^{yz,m}_{i+\frac{1}{2},j+1,k+\frac{1}{2}} - T^{yz,m}_{i+\frac{1}{2},j,k+\frac{1}{2}} + \\
&\quad T^{zz,m}_{i+\frac{1}{2},j+\frac{1}{2},k+1} - T^{zz,m}_{i+\frac{1}{2},j+\frac{1}{2},k} \Big)
\end{aligned} \qquad (3)$$

for the velocity component of x, y, and z directions, and

$$\begin{aligned}
T^{xx,m+1}_{i+\frac{1}{2},j+\frac{1}{2},k} &= T^{xx,m}_{i+\frac{1}{2},j+\frac{1}{2},k} + \frac{\Delta t}{h}(\lambda + 2\mu)\Big(u^{m+\frac{1}{2}}_{i+1,j+\frac{1}{2},k} - \\
&\quad u^{m+\frac{1}{2}}_{i+\frac{1}{2},j+\frac{1}{2},k} \Big) + \Big(\frac{\Delta t}{h}\Big)\lambda\Big(v^{m+\frac{1}{2}}_{i+1,j+1,k} - \\
&\quad v^{m+\frac{1}{2}}_{i+\frac{1}{2},j,k} \Big) + \Big(\frac{\Delta t}{h}\Big)\lambda\Big(w^{m+\frac{1}{2}}_{i+\frac{1}{2},j+1,k+\frac{1}{2}} - \\
&\quad w^{m+\frac{1}{2}}_{i+\frac{1}{2},j+\frac{1}{2},k-\frac{1}{2}} \Big) \\
T^{yy,m+1}_{i+\frac{1}{2},j+\frac{1}{2},k} &= T^{yy,m}_{i+\frac{1}{2},j+\frac{1}{2},k} + \frac{\Delta t}{h}(\lambda + 2\mu)\Big(v^{m+\frac{1}{2}}_{i+1/2,j+1,k} - \\
&\quad v^{m+\frac{1}{2}}_{i+\frac{1}{2},j,k} \Big) + \Big(\frac{\Delta t}{h}\Big)\lambda\Big(u^{m+\frac{1}{2}}_{i+1,j+1/2,k} - \\
&\quad u^{m+\frac{1}{2}}_{i+\frac{1}{2},j,k} \Big) + \Big(\frac{\Delta t}{h}\Big)\lambda\Big(w^{m+\frac{1}{2}}_{i+\frac{1}{2},j+1,k+\frac{1}{2}} - \\
&\quad w^{m+\frac{1}{2}}_{i+\frac{1}{2},j+\frac{1}{2},k-\frac{1}{2}} \Big)
\end{aligned}$$

$$T^{zz,m+1}_{i+\frac{1}{2},j+\frac{1}{2},k} = T^{zz,m}_{i+\frac{1}{2},j+\frac{1}{2},k} + \frac{\Delta t}{h}(\lambda+2\mu)\left(w^{m+\frac{1}{2}}_{i+\frac{1}{2},j+\frac{1}{2},k+\frac{1}{2}} - w^{m+\frac{1}{2}}_{i+\frac{1}{2},j+\frac{1}{2},k-\frac{1}{2}}\right) + \left(\frac{\Delta t}{h}\right)\lambda\left(u^{m+\frac{1}{2}}_{i+1,j+\frac{1}{2},k} - u^{m+\frac{1}{2}}_{i,j+\frac{1}{2},k}\right) + \left(\frac{\Delta t}{h}\right)\lambda\left(v^{m+\frac{1}{2}}_{i+\frac{1}{2},j+1,k} - v^{m+\frac{1}{2}}_{i+\frac{1}{2},j,k}\right)$$

$$T^{xy,m+1}_{i,j,k} = T^{xy,m}_{i,j,k} + \frac{\Delta t}{h}\mu\left(u^{m+\frac{1}{2}}_{i,j+\frac{1}{2},k} - u^{m+\frac{1}{2}}_{i,j-\frac{1}{2},k}\right) + \left(\frac{\Delta t}{h}\right)\mu\left(v^{m+\frac{1}{2}}_{i+\frac{1}{2},j,k} - v^{m+\frac{1}{2}}_{i-\frac{1}{2},j,k}\right) \quad (4)$$

$$T^{xz,m+1}_{i,j+\frac{1}{2},k+\frac{1}{2}} = T^{xz,m}_{i,j+\frac{1}{2},k+\frac{1}{2}} + \frac{\Delta t}{h}\mu\left(u^{m+\frac{1}{2}}_{i,j+\frac{1}{2},k+1} - u^{m+\frac{1}{2}}_{i,j+\frac{1}{2},k}\right) + \left(\frac{\Delta t}{h}\right)\mu\left(w^{m+\frac{1}{2}}_{i+\frac{1}{2},j+1,k+\frac{1}{2}} - w^{m+\frac{1}{2}}_{i-\frac{1}{2},j+\frac{1}{2},k+\frac{1}{2}}\right)$$

$$T^{yz,m+1}_{i+\frac{1}{2},j,k+1/2} = T^{yz,m}_{i+\frac{1}{2},j,k+1/2} + \frac{\Delta t}{h}\mu\left(v^{m+\frac{1}{2}}_{i+1/2,j,k} - v^{m+\frac{1}{2}}_{i+1/2,j,k}\right) + \left(\frac{\Delta t}{h}\right)\mu\left(w^{m+\frac{1}{2}}_{i+\frac{1}{2},j+\frac{1}{2},k+1/2} - w^{m+\frac{1}{2}}_{i+\frac{1}{2},j-\frac{1}{2},k+1/2}\right)$$

for the stresses. The subscripts refer to the spatial indices and the superscripts refer to the time index. As shown in equation (3), the velocities at time $(m+1/2)\Delta t$ is determined from the velocities at time $(m-1/2)\Delta t$ and the stresses at the time $m\Delta t$. At time $(m+1)\Delta t$ the stress is updated based on equation (4) from the stress field at time $m\Delta t$ and the previously updated velocities at time $(m+1/2)\Delta t$.

We set the free surface boundary condition at the top of the medium, and at the wall and bottom of the caldera. The 3D topography of the caldera is modeled as a staircase by stacking unit material cell so that those horizontal and vertical free surfaces always coincide with a face of unit material. Using this model, we obtain that only shear stresses appear on the free surface, while the normal stresses are always within the medium. Based on the zero-stress condition at the free surface where there is no traction, we can directly set shear stresses to be zero as the boundary conditions. To avoid artificial reflections from the edges of the boundary of the numerical domain, we apply an absorbing boundary condition based on paraxial (one-way) wave equation [11].

III. Results and discussion

We represent the topography with caldera formation by a half-spherical-like form with a radius of 800 m and a flat bottom surface at a depth of 500 m (Figure 2). P-wave velocity of 2.0 km/s, S-wave velocity of 1.1 km/s, and density of 2200 kg/m^3 are assumed for the medium. These elastic properties are selected to explain the observed group velocity of Rayleigh waves. Homogeneous medium with a dimension of 16 km x 16 km x 8 km is set with a grid size h of 40 m. We apply a vertical single force with a source time function represented by Ricker wavelet with a central frequency of 0.5 Hz on the surface. We update the simulation with a time step Δt of 1 ms. The source location is set at 3.0 km from the caldera boundary and two stations (R1 and R2) are placed in the opposite side at 1.2 km and 2.2 km from the boundary of the caldera.

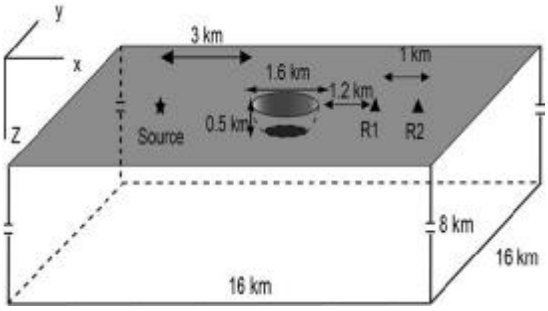

Figure 2. Staggered grid scheme for 3D elastic wave equation considering a collapse caldera boundary as free surface.

Figure 3 shows snapshots of vertical component (w) seismic wave at the top medium for flat topography and topography with caldera at time 5s after the source is excited. As the Ricker wavelet used for the source contains two troughs and one peak in time dependence, three distinct wave fronts are observed, two of which are black and one white. The shallow source expects to generate surface waves that dominate the wave field.

Wave front of the seismic waves are partly stretched and contracted as the waves travel along the caldera (Figure 3b). The change of wave front is due to interaction of the waves with the caldera boundary. The interaction causes scattering that may result in the reflection and diffraction of the seismic waves. Propagation

of seismic wave along the caldera boundary can yield delay of peak amplitude of the surface waves, in this case Rayleigh waves. The reflection of some energy of the Rayleigh waves can decrease in amplitude of the surface waves.

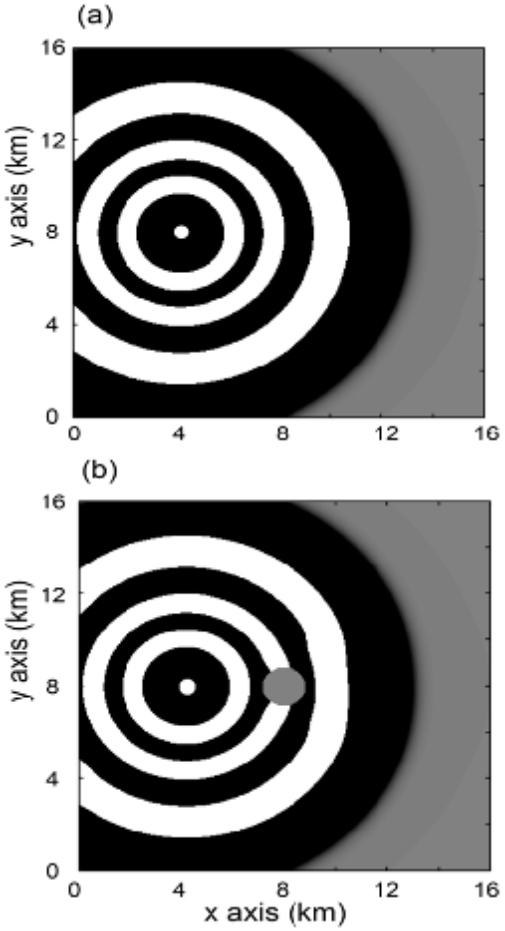

Figure 3. Snapshot of vertical component of seismic wave at 5 s after the source excited for (a) flat topography and (b) topography with collapse caldera.

Figure 4 shows seismograms at the receivers R1 and R2. Black lines show seismic waves that are simulated using a medium with a flat topography, while dashed lines are seismic waves for the structure with the caldera. Each trace is normalized by the maximum amplitude of each waveform. We observe phase delays (delay of arrival times) at both the R1 and R2 for Rayleigh wave after the collapse caldera. These delays could be generated because a longer time is needed for the surface waves to travel from the source to the receivers. We estimate the travel time increases of about 2.5 % and 1.9 % for station R1 and R2, respectively. The phase delay decreases as the station distance from the caldera increases due to the wave front healing.

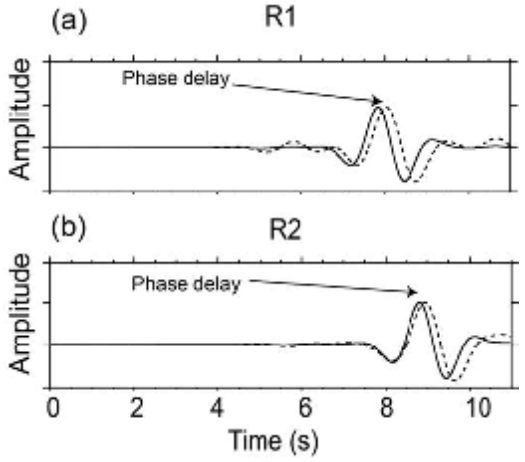

Figure 4. Seismograms simulated with flat topography (solid line) and caldera-like topography (dashed line) at receivers (a) R1 and (b) R2. Phase delays are observed at phase around maximum amplitude for seismograms simulated with caldera-like topography.

IV. Conclusion

We presented numerical analyses on the effect of topographical changes to the seismic wave propagation using a caldera-like formation. Wave fronts changes are observed when seismic waves interact with the caldera boundary.

V. Referencese

1. Fuyuki, M., dan Y. Matsumoto, *Bull. Seismol. Soc. Am.* 70(6), 2051 (1980).
2. Kawase, H., *Bull. Seismol. Soc. Am*. 78, 1415 (1988).
3. Bouchon, M., C. Schultz, dan M. Toksoz, *J. Geophys. Res*. 101, 5835 (1996).
4. Ohminato, T. dan B. A. Chouet, *Bull. Seism. Soc. Am*., 87, 494 (1997).
5. Snieder, R., *Bull. Seismol. Soc. Am.* 76 (5), 1385 (1986).
6. Munasinghe, M., and G. W. Farnell, *J. Geophys. Res.* 78, 2454 (1973).
7. Jih, Rong-Song, K. L. McLaughlin, and Zoltan A. Der, *Geophysics* 53, 1045 (1988).
8. Tessmer, E., D. Kosloff, and A. Behle, *Geophys. J. Int.* 108, 621 (1992).
9. Chaljub, E., and B. Valette, *Geophys. J. Int.* 158, 131 (2004).
10. Komatitsch, D., Q. Liu, J. Tromp, P. Süss, C. Stidham, and J. H. Shaw, *Bull. Seismol. Soc. Am.* 94, 187 (2004).

11. Clayton, R., dan B. Engquist, *Bull. Seismol. Soc. Am.* 67(6) 1529 (1977).